Characterisation of sympathetic neurons and cardiomyocytes derived from human pluripotent stem cells and their therapeutic mechanism



Ni Li

Thesis submitted for the degree of

Doctor of Philosophy

University of Oxford

Hilary Term 2024

Merton College

University of Oxford

Abstract

Heightened sympathetic drive is a powerful negative prognostic indicator for morbidity and mortality associated with arrhythmia and sudden cardiac death. In the heart, cardiac channelopathy, in particular catecholaminergic polymorphic ventricular tachycardia (CPVT), underpin a significant portion of lethal arrhythmia triggered by adrenergic stimulation. However, the molecular targets underlying dysautonomia remain unclear, and no therapeutic pathways have been validated against human tissue. Human induced pluripotent stem cells (hiPSCs) offer an unprecedented opportunity to generate a potentially unlimited source of cells to develop model systems that facilitate a mechanistic understanding of human disease.

Chapter 1 introduces the autonomic innervation of the heart and how sympathetic dysfunction is related to cardiac arrhythmia in cardiac channelopathies. Intracellular calcium ($[Ca^{2+}]$) is a critical modulator of neuronal function, which is subjected to cyclic nucleotides and membrane potential regulation. The development of hiPSCs is also reviewed, leading to the main of the aim of the thesis, which is concerned with testing the hypothesis that CPVT is also a disease of cardiac sympathetic neurons.

Chapter 2 explains the methods used in the following results chapters. While primary human LQTS/CPVT cells are largely unavailable, hiPSCs have emerged as a tool to model inherited arrhythmias. In this chapter, methods for efficient and replicable induction of hiPSC-CMs and -SNs and phenotyping of these cells are provided.

Chapter 3 depicts the physiological phenotypes of cardiac myocytes and sympathetic neurons derived from hiPSCs. They morphologically resemble primary cells, expressing tissue-specific markers. The electrophysiological properties of myocytes and the neurotransmission of sympathetic neurons are investigated.

Chapter 4 demonstrates a model of cardiac hypertrophy using iPSC-CMs. Healthy iPSC-CMs develop anatomical alteration and beta hyper-responsiveness with angiotensin II. The results validate the utility of hiPSC in disease modelling when compared against a rat model.

Chapter 5 Monocultures and co-cultures were made from hiPSC with a CPVT genotype (and isogenic pairing) to generate a model of triggered arrhythmia. Neuronal Ca^{2+} transients were enhanced in CPVT cells, which inspired further investigation into underlying dysregulated molecules, in particular cyclic nucleotide signalling (cAMP) and membrane excitability (M current).

Chapter 6 provides a single-cell RNA sequencing dataset profiling transcriptome of hiPSC-differentiated cardiac myocytes and sympathetic neurons. Differential gene expression analysis discovered dysregulated genes in the CPVT sympathetic neurons.

Chapter 7 is the concluding discussion that summarizes all the results, suggesting the applicability of hiPSC in disease modelling and the triggering role of sympathetic neurons in CPVT. It also highlights potential pathways for therapeutic intervention.

Awards and Prizes arising from this thesis

DPAG Sherrington Talk 2022 Prize Winner

Oxford BHF CRE Annual Symposium 2022 Student Best Poster

CAMS-OXFORD Institute Network Conference 2023 Best Flash Talk

Oxford University Peter Beaconsfield Prize Winner 2023

Publications

1. **Li N**, Edel M, Liu K, Denning C, Betts J, Neely OC, Li D, Paterson DJ. Human induced pluripotent stem cell-derived cardiac myocytes and sympathetic neurons in disease modelling. Philos Trans R Soc Lond B Biol Sci. 2023;378(1879):20220173.
2. Li D, Liu K, Davis H, Robertson C, Neely OC, Tarafdar A, **Li N**, Lefkimmiatis K, Zaccolo M, Paterson DJ. Abnormal Cyclic Nucleotide Signaling at the Outer Mitochondrial Membrane In Sympathetic Neurons During the Early Stages of Hypertension. Hypertension. 2022;79(7):1374-1384.
3. Davis H, Liu K, **Li N**, Li D, Paterson DJ. Healthy cardiac myocytes can decrease sympathetic hyperexcitability in the early stages of hypertension. Front Synaptic Neurosci. 2022;14:949150.
4. Wang D, Liu K, Zhong J, Li X, Zhang J, Wang G, **Li N**, Li T, Davis H, El-Gaby I, Hao G, Ye H, Li D. Molecular Correlates of Early Onset of Diabetic Cardiomyopathy: Possible Therapeutic Targets. Oxid Med Cell Longev. 2022;2022:9014155.

Oral presentation:

Poster, Europhysiology 2022 conference, Copenhagen, Denmark

Oral report, DPAG Cardiac Symposium 2022

Poster, Oxford BHF CRE Annual Symposium 2022

Poster, American Physiology Summit 2023, Long Beach, USA

Flash talk, CAMS-OXFORD Institute Network Conference 2023, Chengdu, China

Acknowledgements

It has been a long journey for my DPhil life to come to the last page. I would like to extend my sincere gratitude to all those who helped me in this process without whom this could not be accomplished.

My heartful thanks go first and foremost to Professor David James Paterson, my supervisor, for his invaluable guidance, insightful feedback, and exceptional support throughout this research. His expertise and mentorship have been instrumental in shaping the direction and quality of this work. His encouragement during seminars and presentations has inspired me to pursue more academic progress.

I am deeply grateful to my other supervisor Professor Dan Li, who not only provided professional guidance during laboratory experiments but also offered significant support in my personal life, facilitating my integration into the academic and social fabric of the community.

I extend my sincere appreciation to all the group members and collaborators, especially Dr. Kun Liu, Dr. Harvey Davis and Dr. Oliver Neely, for their support and assistance in the lab work. Their contribution eased my pressure in achieving the objectives of this thesis.

I would also like to acknowledge the generous funding from the China Scholarship Council-Chinese Academy of Medical Sciences Oxford Institute (CSC-COI). Their financial support has been crucial in enabling me to pursue this project effectively.

Finally, special thanks to my family and friends who have offered their support, advice, and encouragement during this endeavor. Your belief in me has become my source of strength over challenging times.

Table of Contents

Abstract **1**

Acknowledgements **3**

List of Abbreviations **8**

Chapter 1： Introduction **9**

1.1 Autonomic nervous system 9
1.1.1 Anatomy 9
1.1.2 Autonomic neurotransmitters 12
1.2 Autonomic innervation of the heart 13
1.2.1 Sympathetic neurotransmitter cardiac effect 16
1.3 Regulatory mechanism of autonomic activity 18
1.4 Autonomic dysregulation and cardiac arrhythmia 19
1.4.1 Sympathetic dysfunction 19
1.4.2 Pathological changes in postganglionic neurons 21
1.5 Cardiac myocyte electrophysiology 27
1.5.1 Cardiac action potential 27
1.5.2 Cardiac myocytes calcium signalling 29
1.5.3 Cardiac excitation contraction coupling 31
1.6 Cardiac channelopathy 32
1.6.1 Long QT syndrome 33
1.6.2 Catecholaminergic polymorphic ventricular tachycardia 35
1.6.3 Brugada syndrome 41
1.6.4 Sympathetic denervation improves the prognosis of cardiac channelopathy 43
1.7. Human induced pluripotent stem cell 44
1.7.1 Model development from the rat to human iPSCs 44
1.7.2 hiPSC differentiated cardiac myocytes 45
1.7.3 hiPSC differentiated sympathetic neurons 48
1.7.4 Co-culture of sympathetic neurons and cardiomyocytes derived from hiPSCs 50
1.8. Rationale in using human induced pluripotent stem cell to study sympathetic neurons in cardiac channelopathy 51
1.9 Hypothesis 52
1.10 Aims of this thesis 52

Chapter 2: General methods **54**

2.1 Solutions and reagents 54
2.2 Animal model 54
2.2.1 Wistar Rats 54

2.2.2 Schedule-1 54
2.2.3 Rat ventricular myocytes isolation 55
2.3 Human induced pluripotent stem cell modelling 55
2.3.1 Ethics and cell lines used....58
2.3.2 Maintenance and differentiation of human induce pluripotent cell....60
2.4 Cell plating for experiments....63
2.5 Immunofluorescence staining 65
2.5.1 Sample preparation....68
2.5.2 Staining....68
2.6 Flow cytometry 69
2.6.1 Gating 72
2.6.2 Compensation 75
2.6.3 Methodology....75
2.7 RT-qPCR....77
2.7.1 Methodology....79
2.8 Enzyme-linked immunosorbent assay....80
2.8.1 Methodology....81
2.9 Förster resonance energy transfer (FRET) imaging....82
2.9.1 cAMP sensors....83
2.9.2 Cell transfection....84
2.9.3 FRET measurement....85
2.10 Calcium imaging 90
2.10.1 Methodology....92
2.11 Electrical mapping....95
2.11.1 Methodology....96
2.11.2 Data analysis....96
2.12 Single RNA sequencing 98
2.13 Statistical analysis 103

Chapter 3：Phenotyping human induced pluripotent stem cell derived cardiac myocytes and sympathetic neuron 104

3.1 Introduction 104
3.1.1 General introduction of the hiPS cell evolution 104
3.1.2 Understanding cardiac hypertrophy....106
3.1.3 Cardiac myocytes are non-generative cells 107
3.1.4 Induced pluripotent stem cells emerging as a powerful tool....107
3.2 Methods....108
3.2.1 Flow cytometry....108
3.2.2 Immunofluorescence 109
3.2.3 qRT-PCR 110

3.2.4 Electrical mapping 111
3.2.5 Calcium imaging 112
3.2.6 Förster resonance energy transfer 112
3.2.7 Enzyme-linked immunosorbent assay 113
3.2.8 In vitro cardiomyocyte hypertrophy induction 113
3.2.9 Cell size and nuclear size measurement 114
3.2.10 Myocytes hypertrophic marker gene expression 115
3.2.11 proBNP secretion 115
3.2.12 Cytosolic cAMP measurement 116
3.3 Results 117
3.3.1 Cardiac myocyte and sympathetic neuron induction from hiPSCs 117
3.3.2 Morphological phenotype of hiPSC, hiPSC-CM and hiPSC-SN 121
3.3.3 Functional phenotype of hiSPC-CM and hiPSC-SN 126
3.3.4 Cardiac hypertrophy modelling using hiPSC-cardiac myocyte 131
3.3.5 Neurocardiac coculture establishment 138
3.4 Discussion 140
3.4.1 hiPSC cardiac myocyte differentiation and characterization 140
3.4.2 hiPSC sympathetic neuron differentiation and characterization 142
3.4.3 hiPSC-CM recapitulate cardiac hypertrophy *in vitro* 143
3.4.4 Neural-cardiac signalling in co-culture 145
3.5 Limitations 146

CHAPTER 4: Catecholaminergic polymorphic ventricular tachycardia disease modelling using hiPSC-derived cardiac myocytes and sympathetic neuron 148

4.1 Background 148
4.1.1 Catecholaminergic polymorphic ventricular tachycardia: a disease of the sarcoplasmic reticulum calcium release channel 148
4.1.2 Exercise and activation of the sympathetic nervous system facilitates the onset of CPVT 148
4.1.3 Disease in a dish: Human cell modelling of CPVT 149
4.2 Methods 150
4.2.1 Flow cytometry 150
4.2.2 Immunofluorescence imaging 151
4.2.3 Calcium imaging 152
4.2.4 Förster resonance energy transfer 152
4.2.5 Electrical mapping 153
4.2.6 Noradrenaline release assay 154
4.3 Results 155
4.3.1 Differentiation efficiency of cardiac myocytes and sympathetic neurons 155
4.3.2 Morphological phenotyping of hiPSC-CM and hiPSC-SN between genotypes 158

4.3.3 CPVT calcium dysregulation....163
4.3.4 Noradrenaline released from CPVT and control neurons 167
....168
4.3.5 Cyclic nucleotides signalling....168
4.3.6 Neurocardiac coculture....172
4.3.7 Electrical mapping....176
4.4 Discussion 184
4.5 Future direction 188

Chapter 5: Target discovery to attenuate neurotransmission in catecholaminergic polymorphic ventricular tachycardia neurons....191

5.1 Introduction 191
5.1.1 Rationale for target discovery....191
5.1.2 Application of RNA sequencing in target discovery....192
5.2 Methods....193
5.2.1 Sample preparation....193
5.2.2 Dead cell removal....194
5.2.3 Single cell RNA sequencing and data analysis 195
5.3 Results....195
5.3.1 Key marker gene expression identified cardiac myocytes and sympathetic neurons 195
5.3.2 Dysregulated gene expression in the sympathetic neuron due to genotype 198
5.4 Discussion 202
5.5 Limitations 205

Chapter 6: Concluding Discussion 206

6.1 The main findings of this thesis 206
6.2 Cardiac myocyte and sympathetic neuron induction from hiPSC 207
6.3 Application of hiPSC in disease modelling: pathological cardiac hypertrophy....208
6.4 CPVT disease modelling with hiPSC-CM and hiPSC-SN 209
6.4.1 Cardiac myocytes calcium leakage....210
6.4.2 Hyperactive calcium discharge in CPVT sympathetic neuron....210
6.5 Transcript profile of cardiac myocyte and sympathetic neuron differentiation from CPVT vs WT hiPSC....211
6.5.1 *SERPINA3* gene expression downregulated in CPVT hiPSC-SN....212

References....213

List of Abbreviations

AC	=	Adenylyl Cyclase
AngII	=	Angiotensin II
ANS	=	Autonomic Nervous system
APD	=	Action Potential Duration
BrS	=	Brugada Syndrome
CASQ	=	Calsequestrin
CICR	=	Calcium Induced Calcium Release
CNS	=	Central Nervous System
CPVT	=	Catecholaminergic Polymorphic Ventricular Tachycardia
cTnT	=	cardiac Troponin T
DAD	=	Delayed After Depolarization
FACS	=	Fluorescence-Activated Cell Sorting
FKBP	=	FK506 Binding Protein
FPD	=	Field Potential Duration
FRET	=	Förster Resonance Energy Transfer
FSK	=	Forskolin
hiPSC	=	human induced Pluripotent Stem Cell
hiPSC-CM	=	hiSPC derived Cardiac Myocyte
hiPSC-SN	=	hiPSC derived Sympathetic Neuron
IBMX	=	3-Isobutyl-1-Methyl-Xanthine
ICD	=	Implantable Cardioverter-Defibrillators
IP3R	=	Inositol Triphosphate Receptor
Iso	=	Isoprenaline
LCSD	=	Left Cardiac Sympathetic Denervation
LQTS	=	Long QT Syndrome
LTCC	=	L-Type Calcium Channel
MEA	=	Microelectrode Array
NA	=	Noradrenaline
nAChR	=	nicotinic Acetylcholine Receptor
NCX	=	Sodium-Calcium Exchanger
NOS1	=	Nitric oxide synthase 1
NOS1AP	=	Nitric oxide synthase 1 Adaptor Protein
PDE	=	Phosphodiesterase
PNS	=	Peripheral Nervous System
PRPH	=	Peripherin
RYR2	=	Ryanodine 2 Receptor
SCD	=	Sudden Cardiac Death
SERCA	=	Sarcoplasmic/endoplasmic Reticulum Calcium ATPase
Syn	=	Synapsin
TH	=	Tyrosine Hydroxylase

Chapter 1：Introduction

1.1 Autonomic nervous system

The sympathetic nervous system (SNS), constituting one of the two divisions of the autonomic nervous system (ANS), significantly contributes to orchestrating the body's preparation for 'fight or flight' responses and the maintenance of systemic homeostasis. This dynamic interplay between the SNS and its counterpart, the parasympathetic nervous system (PNS), underscores their integral roles in regulating various bodily functions.

The SNS operates in direct opposition to the PNS, creating a finely tuned balance that governs diverse physiological processes. While the SNS primes the body for heightened activity and responsiveness during stress or challenging situations, the PNS, in contrast, assumes a predominant role in fostering a state of relaxation and facilitating digestive processes under normal, non-stressful conditions.

This duality, where the SNS and PNS act as counterparts, is crucial for maintaining overall equilibrium in the autonomic nervous system. The harmonious interaction between these two systems ensures adaptive responses to the varying demands of the internal and external environment, showcasing the remarkable complexity and precision of autonomic control in the human body.

1.1.1 Anatomy

Sympathetic regulation of bodily functions requires the establishment of anatomical and functional connections between axons of postganglionic sympathetic neurons and peripheral organs distributed throughout the body. The preganglionic neurons of the SNS arise from the intermediolateral column of T1 to L2 or L3 segments of the spinal cord and project axons

through T1 to L2 spinal nerves to form synapses with the postganglionic sympathetic neurons arranged at the paravertebral ganglia (Fig. 1.1), including three cervical, twelve thoracic, four lumbar and five sacral, although number may vary individually, and the inferior cervical ganglion may fuse with the first, and occasionally second, thoracic ganglion to form stellate ganglion[1]. These postganglionic neurons then travel to their target organs through splanchnic nerves innervating viscera in the thoracic, abdominal, and pelvic cavities. To be noted, nerves innervating the abdominal and pelvic viscera pass through the paraganglia without synapsing, but synapse in prevertebral ganglia which also belong to sympathetic ganglia.

Although both the SNS and PNS are composed of pre- and postganglionic neurons, the first-order neurons of the PNS are much longer than the SNS as they synapse with postganglionic neurons in ganglia at or near the effector organs. Preganglionic PNS neurons originate from brainstem nuclei, specifically the dorsal nucleus, nucleus ambiguous, nucleus solitarius, and spinal trigeminal nucleus of the medulla oblongata, and the S2 to S4 segments sacral spinal cord, and exit the central nervous system (CNS) through cranial nerves III, VII, IX and X, and exit the sacral cord joining the pelvic splanchnic nerve. The vagus nerve (X) is the most influential of the PNS as it comprises 75% of the PNS fibers[2].

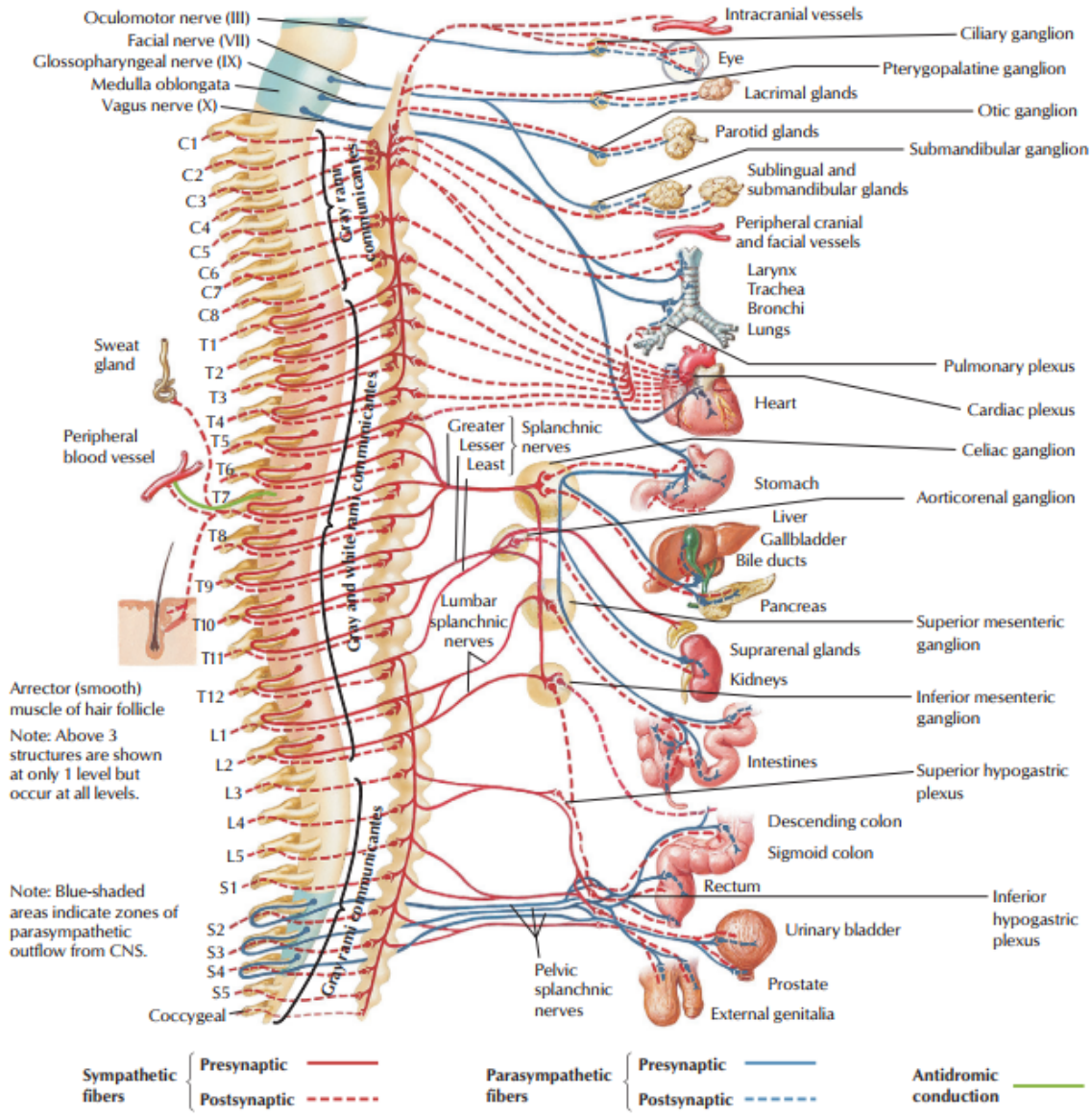


Figure 1.1 The anatomy of the autonomic nervous system, highlighting the sympathetic pathway in red and the parasympathetic pathway in blue. Sympathetic preganglionic neurons are situated in the T1-L2 spinal segment, and their axonal extensions in spinal nerves synapse with postganglionic neurons in both paravertebral and prevertebral ganglia. The cardiopulmonary nerve contains sympathetic postsynaptic fibers, while the thoracic (Greater, Lesser, Least) splanchnic nerve, lumbar splanchnic nerve, and sacral splanchnic nerve contain sympathetic presynaptic fibers. On the other hand, parasympathetic pathways originate from the brain stem and sacral spinal cord, with synapses occurring in ganglia located around target tissues and organs. The visual representation credits attributed to Netters Atlas of Human Neuroscience.

1.1.2 Autonomic neurotransmitters

Acetylcholine is the neurotransmitter from preganglionic neurons of both the SNS and PNS, which activates the nicotinic receptors (N2 receptor) located in the postganglionic cell bodies. The postganglionic neurons of the SNS are mainly adrenergic while PNS are still cholinergic. Most postganglionic sympathetic neurons release noradrenaline as the primary neurotransmitter along with one or more peptides such as neuropeptide Y or somatostatin that serve as modulators of the response to the primary neurotransmitter[1]. Sympathetic innervation of the sweat gland and the arrestor's pili muscles use acetylcholine as the postganglionic neurotransmitter. Noradrenaline activates adrenergic receptors, including alpha-1 (Gq-coupled), alpha-2 (Gi-coupled), and beta 1, beta 2, and beta 3 (Gs-coupled) receptors located on different tissues, which leads to a state of overall enhanced activity (Table 1).

Table 1 Adrenergic receptors summary

Receptor	α		β		
	α_1	α_2	β_1	β_2	β_3
Predominant tissues	Smooth muscle	Presynaptic nerve terminal	Cardiac muscle	Smooth muscle (bronchial, vascular)	Adipose tissue
Main effects	Vasoconstriction	Inhibit NE release	Increase cardiac output (chronotropy, inotropy, dromotropy, lusitropy)	Bronchodilation, vasodilation	Lipolysis, thermogenesis
Agonist	Noradrenaline+++ Adrenaline++	Noradrenaline Adrenaline	Adrenaline+++ Noradrenaline++ Isoprenaline+++	Adrenaline+++ Noradrenaline+ Isoprenaline+++	Noradrenaline Adrenaline
G protein coupled	Gq	Gi	Gs	Gs (Gi in some cases)	Gs (Gi in some cases)
Second messenger	IP_3, DAG	cAMP	cAMP	cAMP	cAMP, Nitric oxide

Table contents summarized from Bylund 2013[3] and Kuhar et al. 1999[4].

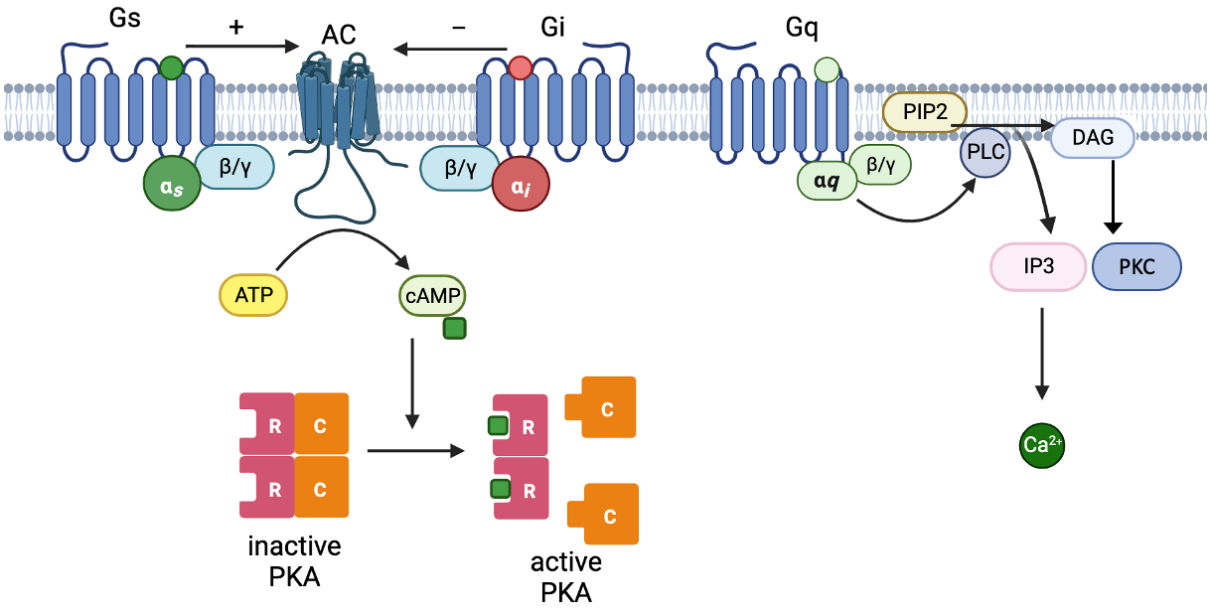


Figure 1.2 G protein-coupled receptor signalling. G protein-coupled receptor (GPCR) is a seven-transmembrane domain receptor coupled to a trimeric G protein (Gαβγ), mediating the majority of cell responses to external stimuli. The cAMP/PKA pathway and IP3/DAG pathway are two principal signaling pathways associated with GPCR[5]. Ligands binding with the GPCR cause a conformational change of the receptor and promote GTP exchange with GDP of Gα, which can then be dissociated from β and γ subunit and mediate downstream signaling activities depending on the α subunit type (αs, αi, and αq). The Gαs and Gαi exert opposite effects on adenylyl cyclase (AC), which catalyzes the generation of cAMP. cAMP as a second messenger modulates many biological processes via the second effector protein kinase A[6]. PKA comprises one regulatory (R) dimer and 2 catalytic (C) subunits, and binding of cAMP to the R subunit promotes the release of the C subunit which phosphorylates target proteins. Gαq activates phospholipase C (PLC) that cleave phosphatidylinositol 4,5-biphosphotate (PIP2) to inositol triphosphate (IP3) and diacylglycerol (DAG). IP3 binds to the IP3 receptor on the ER membrane allows the release of Ca2+ from the internal store, and DAG activates protein kinase C (PKC) along plasma membrane.

1.2 Autonomic innervation of the heart

The heart is precisely regulated by both the sympathetic and parasympathetic nerves so as to reliably deliver oxygenated blood according to the perfusion demand of the organisms. In the intrinsic conduction system, spontaneous depolarization originates from the sinoatrial node (SA node) then the electric signal is conveyed along the internodal pathway to the AV node,

AV bundle, the left and right branches of the bundle of His, and finally the Purkinje Fibre, which locate in the inner ventricular wall of the heart and is responsible for depolarizing the whole ventricle simultaneously to generate a synchronized and effective contraction. Without autonomic regulation, the SA nodal myocytes depolarize at an intrinsic rate between 60-100 beats per minute (bpm)[7], which is regarded as the normal heart rate. The cardiac output should vary in response to the changing requirements under different circumstances so as to secure enough oxygen supply. Autonomic control plays a significant role in this regulation.

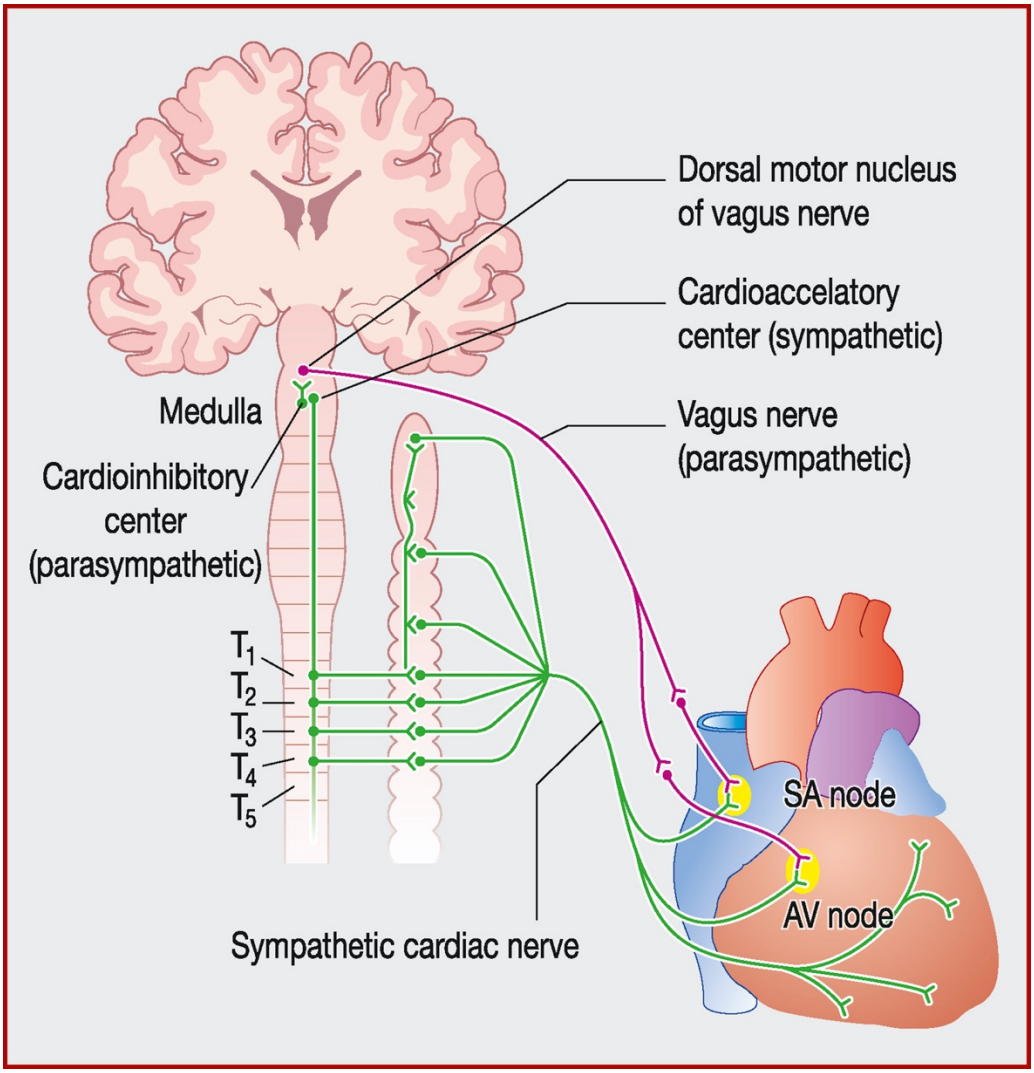


Figure 1.3 Anatomy of cardiac autonomic innervation. Sympathetic innervation is composed of preganglionic neurons originating from the T1-T5/6 spinal cord and postganglionic neurons mainly in the stellate ganglion. Preganglionic parasympathetic neurons located in the dorsal motor nucleus and nucleus are ambiguous and provide efferent fibre to the heart via the vagus nerve and synapse with postganglionic neurons around the heart. Image credit: Scridon A, Şerban RC, Chevalier P. Atrial fibrillation: Neurogenic or myogenic? Arch Cardiovasc Dis. 2018 Jan;111(1):59-69.

Preganglionic sympathetic neurons innervating the heart are confined to T1-T5/6 segments of the spinal cord, from where they extend fibres to the stellate ganglion as the main postganglionic sympathetic innervation to the heart, and middle cervical ganglion as the sporadic observation that also contains cardiac destined fibres in human[8]. During development,

cardiac tissues also release neurotrophic factors to regulate the distribution and maturation of the neuron[9]. Sympathetic activation causes an increased heart rate (chronotropy), rate of conduction, and contraction force (inotropy) through the action of noradrenaline and adrenaline. Electrical and photogenic stimulation of the stellate ganglion can replicate these effects[10]. The acceleration of heart rate is the result of adrenergic activation on the SA node and conduction system, whereas the increased contractile force is a direct action on ventricular myocytes.

On the contrary, vagal nerve stimulation slows down the heart rate and reduces contractile force via the action of acetylcholine, which is the primary parasympathetic neurotransmitter. Both the SNS and PNS contribute to the basal heart rate by functioning in opposite ways to maintain homeostasis.

1.2.1 Sympathetic neurotransmitter cardiac effect

Noradrenaline acts on the β1 adrenoreceptor on the cardiac myocyte plasma membrane, which activates the downstream signalling cascade to regulate cardiac excitation-contraction coupling. With agonist binding to β1 adrenoreceptor, the alpha subunit of the Gs protein exchanges GDP for GTP and gets activated, which in turn, binds to and activates the membrane-bound enzyme adenylyl cyclase (AC). AC then catalyses the conversion of ATP to cAMP, which is an intracellular second messenger that activates protein kinase A (PKA) by dissociating the regulatory subunit from the catalytic subunit[11]. PKA then phosphorylate numerous target proteins such as ion channels and other enzymes. In cardiac myocytes, PKA phosphorylates L-type Ca^{2+} channel (LTCC, Cav1.2), phospholamban (PLB), and ryanodine receptor type 2 (RyR2) to increase cardiac inotropy (Fig. 1.4)[12]. Phosphorylation of LTCC enhances channel activity and increase calcium current; phosphorylation of PLB relieves its inhibition on sarcoendoplasmic reticulum (SR) calcium transport ATPase (SERCA) and therefore increase

Ca^{2+} reuptake and SR calcium load; RyR2 phosphorylation induces the open state of channel and promote calcium release. All of these increase calcium availability during systole. PKA phosphorylation of cardiac troponin I (cTnI) enhances cardiac lusitropy which reduces Ca^{2+} affinity of cardiac troponin T (cTnT) and thus promotes the dissociation of calcium from the myofilament during diastole[13]; Cardiac myosin binding protein C (cMyBP-C) phosphorylation increases both inotropy and lusitropy[14]. Phosphorylated cMyBP-C increases the interaction of myosin head with the thin filaments through weakening the cMyBP-C mediated inhibition of myosin, thus increases contractile force generation (inotropy)[15]. Phosphorylated cMyBP-C also increases the rate of cardiac relaxation (lusitropy) as it accelerates the cross-bridge detachment[10]. PKA also regulates cardiac chronotropy, which is achieved through the phosphorylation of Ca^{2+} cyclin proteins in cardiac pacemaker cells.

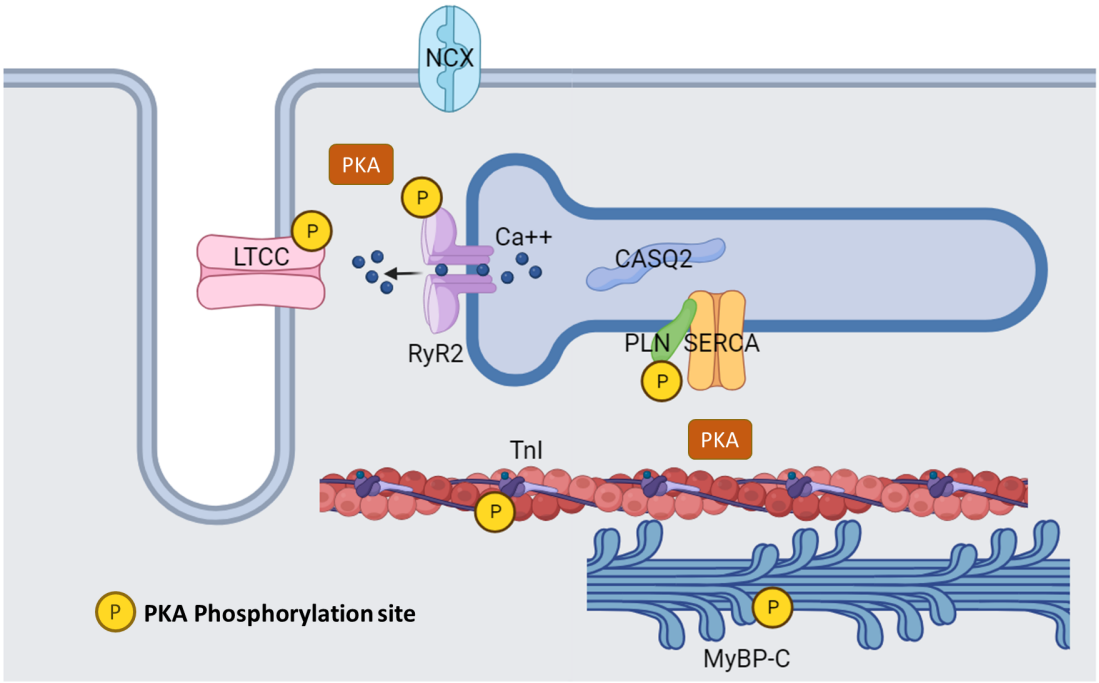


Figure 1.4 Main PKA targets in cardiac myocytes. PKA phosphorylates calcium handling channels including L-type calcium channel (LTCC), ryanodine receptor (RyR2) and phospholamban that modulate the activity of SERCA, and cardiac troponin I (cTnI) and cardiac myosin binding protein C (cMyBP-C) that regulate myofilament contraction.

1.3 Regulatory mechanism of autonomic activity

The autonomic control of the heart undergoes precise regulation through reflex circuits. Sensory signals, primarily mechanical information such as alterations in blood pressure (baroreceptors, situated in the aortic arch and carotid sinuses), along with secondary chemical cues like blood oxygen and carbon dioxide levels (chemoreceptors, found in carotid bodies and aortic bodies), are consistently transmitted to the brain stem centre via afferent fibres within the autonomic pathways[16].

Baroreceptors, located in major blood vessels, respond to vessel wall deformation and become active during vessel distension, correlating with increased blood pressure. Activation of baroreceptors fine-tunes the sympathetic nervous system (SNS) and parasympathetic nervous system (PNS) tone, resulting in a reduction in cardiac output through negative inotropic and chronotropic regulation, and a decrease in total peripheral resistance through vasodilation. Simultaneously, chemoreceptor cells in the carotid bodies and aortic bodies monitor changes in oxygen and carbon dioxide partial pressure in arterial blood, along with sensitivity to surrounding pH. Afferent information from alterations in blood pressure and blood gas levels modulates the activity of relevant sympathetic and parasympathetic nervous systems, ultimately influencing the function of end target tissues and organs. Disruptions in autonomic balance, often characterized by sympathetic overdrive, can contribute to cardiovascular issues such as hypertension, arrhythmia, and myocardial infarction. On the other hand, in cases of chronic myocardial infarction, morphological and functional remodelling of stellate ganglia has been observed, associated with an increased risk of ventricular tachycardia[17].

Apart from autonomic regulation, the concept of the Intracardiac nervous system (ICNS) has been raised and studied for decades[18] which is believed to be a complicated local regulation centre integrating autonomic input. It is comprised of several subpopulations of neurons

forming intracardiac ganglia and a local circuit that function as a short cardio-cardia feedback control loop.

1.4 Autonomic dysregulation and cardiac arrhythmia

1.4.1 Sympathetic dysfunction

The occurrence of arrhythmia necessitates a triggering event to generate an extra stimulus and a substrate to propagate the ectopic stimulus. Arrhythmic triggers, such as afterdepolarization and abnormal automaticity, must occur beyond the refractory period of cardiac myocytes to reactivate the cells. The substrate for the propagation of ectopic beats can be either structural, resulting from cardiac remodelling after certain cardiovascular diseases such as myocardial infarction, or electrophysiological, as observed in hereditary ion channelopathies[19].

All the steps in the generation of ectopic beats are under the ANS regulation. The distribution and density of sympathetic and parasympathetic innervation of the heart are finely arranged. The imbalance between these two branches is pro-arrhythmic, with enhanced sympathetic influence being the mainstay[20]. In cardiac disease states such as myocardial infarction (MI) and heart failure (HF), sympathetic innervation undergoes significant adverse remodelling, resulting in sympathetic nerve heterogeneity which is thought to predispose to VT[21,22]. Increased sympathetic drive can exacerbate pre-existing hazardous cardiac conditions such as ischemia or rhythmic abnormality to induce the onset of arrhythmia[23].

Sympathetic activation elevates cytosolic [Ca^{2+}] through PKA phosphorylation of calcium-modulating proteins, including LTCC, enhancing calcium current. It also affects the RyR2 receptor, leading to increased release of SR calcium stores, and phosphorylates phospholamban to remove the inhibition of the SERCA pump for calcium reuptake. The resulting calcium

overload poses a risk for delayed afterdepolarization by driving the Na-Ca exchanger current, depolarizing the membrane potential towards the action potential threshold.

Early afterdepolarizations (EAD) are more likely during prolonged action potential duration (APD) when inward current exceeds outward current. $I_{Ca\text{-}L}$ and I_{NCX} are two major currents potentially responsible for the membrane potential upstroke in the EAD voltage range[24]. Therefore, calcium overload during sympathetic activation could increase the risk of EAD by enhancing LTCC and NCX. While EAD classically occurs in bradycardia, it can also manifest in tachycardia with an APD that fails to shorten, such as in LQT1 where I_{ks} is not enhanced by sympathetic activation.

Beyond afterdepolarization, beta-adrenergic receptor stimulation increases action potential frequency, shortens the refractory period by enhancing Iks, and reduces APD, favouring conditions for re-entry.

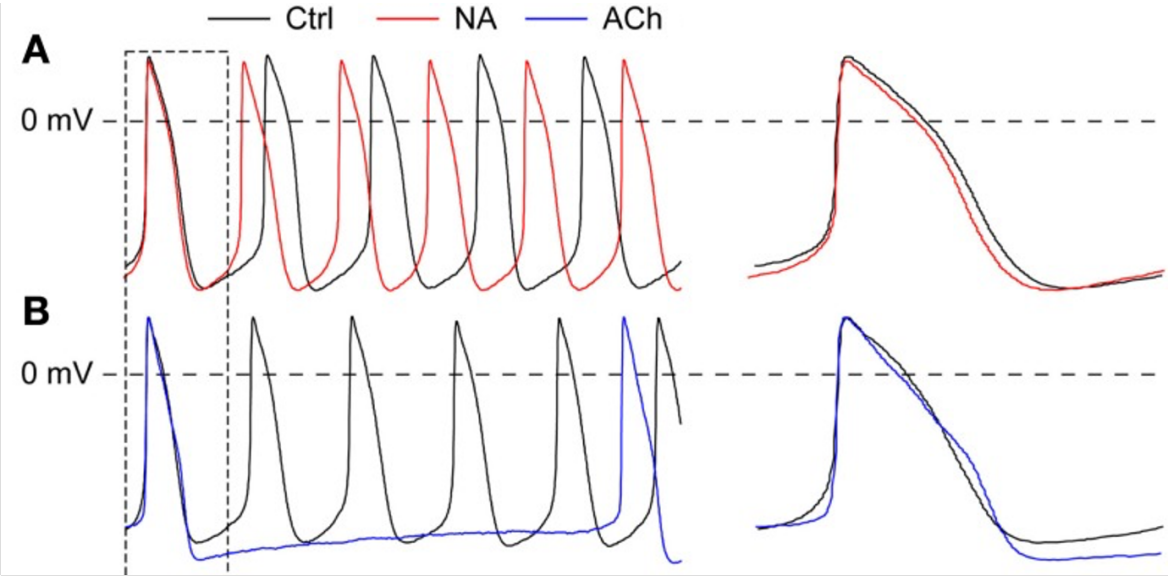


Figure 1.5 Adrenergic vs cholinergic effects on action potential (SA node). Noradrenaline as a sympathetic simulator shortened action potential duration and increased action potential frequency, whereas acetylcholine which mimics parasympathetic activation prolonged AP duration and reduced the frequency. Image credit: Verkerk AO, Geuzebroek GS, Veldkamp MW, Wilders R. Effects of acetylcholine and noradrenalin on action potentials of isolated rabbit sinoatrial and atrial myocytes. *Front Physiol*. 2012; 3:174.

1.4.2 Pathological changes in postganglionic neurons

As increased sympathetic firing can potentially induce arrhythmias, understanding the pathological changes in sympathetic neurons associated with elevated neurotransmission becomes crucial in deciphering the underlying mechanisms triggering arrhythmias. While existing evidence supports the idea that the heterogeneity of sympathetic innervation, influenced by cardiac injury-induced remodeling, increases the risk of arrhythmia, and cardiac sympathetic denervation exhibits potent antiarrhythmic effects, the specific molecular mechanisms within sympathetic neurons remain largely unexplored.

Rizzo et al. highlighted distinct inflammatory infiltrates in the left stellate ganglion of 12 catecholaminergic polymorphic ventricular tachycardia or long QT syndrome (CPVT/LQTS) patients, emphasizing the pathological changes occurring in neurons[25]. Additionally, neuronal nitric oxide synthase adaptor protein (NOS1AP) was identified as a genetic modifier of LQTS, with genetic variations in NOS1AP contributing to QT interval prolongation and sudden cardiac death[26]. NOS1AP encodes the nitric oxide synthase 1 adaptor protein, also known as the carboxyl-terminal PDZ ligand of neuronal nitric oxide synthase protein (CAPON), predominantly expressed in nerve tissue. CAPON plays a regulatory role in neurotransmission alongside neuronal nitric oxide synthase (nNOS). Increased nNOS expression has been linked to a reduction in noradrenaline release from sympathetic neurons and the facilitation of acetylcholine release from parasympathetic neurons[27]. The nNOS-mediated inhibition of sympathetic neurotransmission is associated with cGMP-cAMP crosstalk (Fig. 1.6), resulting in decreased intracellular calcium concentration ($[Ca^{2+}]_i$) and consequently suppressing the exocytosis of neurotransmitters.

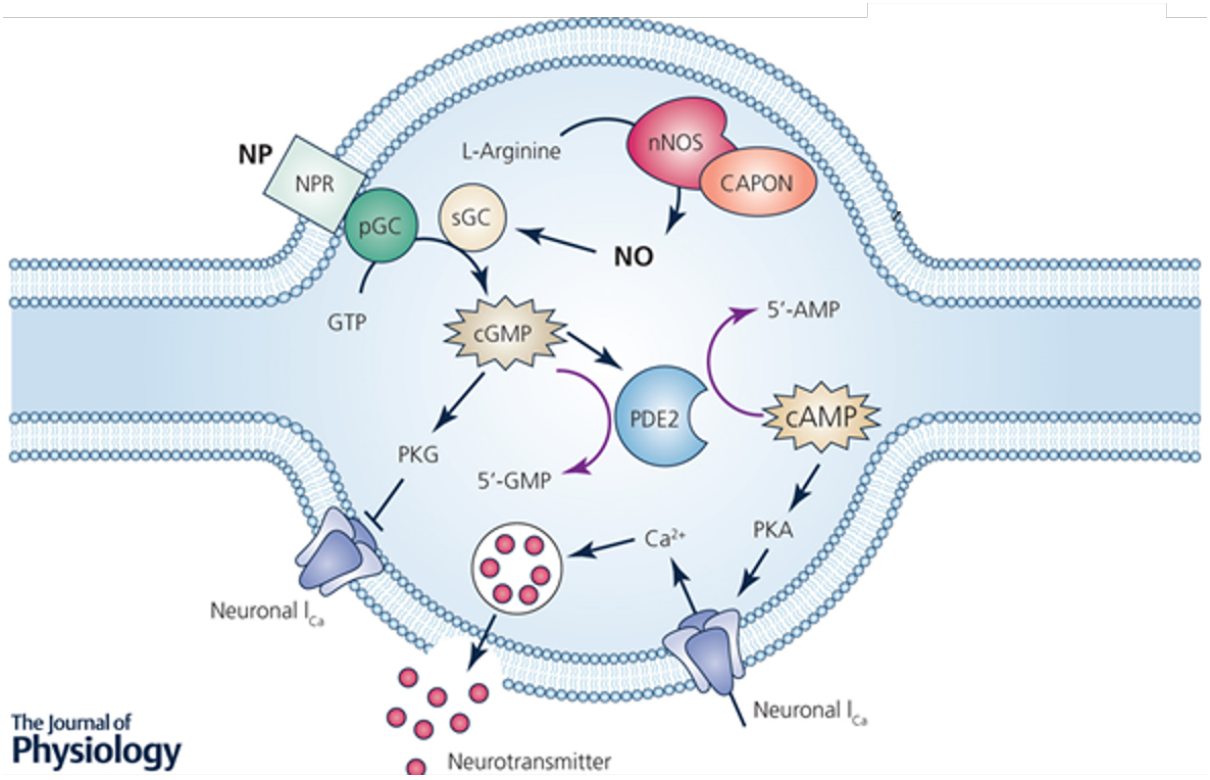


Figure 1.6 Example of cAMP-cGMP crosstalk in postganglionic neuron. Nitric oxide-activated guanylyl cyclase catalyzes the conversion of GTP to cGMP, initiating a signaling cascade that activates PKG. PKG, in turn, inhibits LTCC, contributing to the regulation of intracellular calcium levels. In contrast, the cAMP/PKA pathway stimulates LTCC, enhancing the influx of calcium ions and facilitating the fusion of neurotransmitter vesicles with the plasma membrane, ultimately influencing neurotransmission processes. PDE2 hydrolyses both cGMP and cAMP. An increase in cGMP level stimulates PDE2 activity and therefore accelerates the breakdown of cAMP, reducing neurotransmission. Image credits to Li D, Paterson DJ. Cyclic nucleotide regulation of cardiac sympatho-vagal responsiveness. J Physiol. 2016;594(14):3993-4008.

1.4.2.1 Critical role of calcium in postganglionic neurons

Calcium plays a crucial role in the physiological functioning of neurons, influencing neurotransmitter release, neural plasticity, and neuronal survival. Neuronal calcium concentration is meticulously controlled by various calcium ion transporters, including ion channels, exchangers, and pumps located in the plasma membrane, endoplasmic reticulum (ER), mitochondria, Golgi apparatus, and nuclear envelope. Key systems responsible for

increasing calcium level include voltage-gated calcium channels, ligand-gated calcium channels, store-operated calcium channels on the plasma membrane, as well as ryanodine receptors (RyRs) and inositol-1,4,5-tris-phosphate receptors (IP3Rs) on the ER membrane. Activation of transient receptor potential (TRP) channels[28] and arachidonic acid-regulated calcium (ARC) channels[29] also allows calcium influx through the plasma membrane. Notably, all three subtypes of RyRs are expressed in neuronal tissue, with RyR2 being the predominant one in the brain[30,31].

For maintaining calcium homeostasis, plasma membrane Ca^{2+} ATPase (PMCA) and Na^{+}-Ca^{2+} exchanger (NCX) on the plasma membrane, as well as sarco/endoplasmic reticulum calcium ATPase (SERCA) and mitochondrial uniporter, participate in the removal and reuptake of calcium to restore basal cytosolic calcium levels. These channels are subject to feedback control from calcium through calcium-modulating proteins like calmodulin and G-protein-coupled receptors such as beta-adrenergic receptors. Any disruption in the balance between calcium release and elimination can lead to calcium mishandling.

The release of neurotransmitters is highly dependent on [Ca^{2+}]. Neurotransmitters are released from the axonal terminal of one neuron, diffusing across the synaptic cleft to the dendrite or body of the adjacent neuron, through which an electrical signal can be conveyed to the next neuron crossing the spatial distance in the form of a chemical signal. Upon axonal membrane depolarization, calcium ions influx from activated voltage-gated calcium channels and promote the binding of synaptic vesicles enclosing neurotransmitters with the presynaptic membrane and the emptying of their contents into the synaptic cleft. The postsynaptic membrane of the dendrite contains a high density of neurotransmitter receptors to receive and transfer signals. Excess neurotransmitters will be reabsorbed or digested in the cleft to cease the signalling process.

1.4.2.2 Regulation of neuronal Ca^{2+} channels

All the neuronal calcium channels or pumps are under the regulation of different ligands or mechanisms. For example, a voltage-gated calcium channel is regulated by PKA, CaMK-II and PI3K-Akt, which modulate either the gating or the expression of the channel. IP3R is targeted by phosphokinases such as PKA and PKC, CaMK-II and calcium itself[32]. Ryanodine receptor has a series of associated proteins involved in the proper gating of this channel, such as FK506 binding protein (FKBP), junctin and triadin, and it is also a target of phosphokinase. Among all these regulations, phosphorylation of the channel by protein kinases is of critical importance. Various subtypes of neuronal calcium channels were found in neuronal tissue, including L-type (Cav1.2-Cav1.4), N-type (Cav2.2), P/Q-type (Cav2.1), R-type (Cav2.3) and T-type (Cav3.1-3.3) [33], which is determined by the primary functioning unit α1 subunit of the heterotetrameric channel. The α1 subunit forms the calcium ion-conducting pore with voltage sensing and ligand binding function. Each subtype of calcium channel serves a distinct role in cell physiological functioning due to their identical electrical properties[34]. N-type calcium channel is the predominant subtype in the presynaptic neuron that mediates synaptogenesis[35] and postganglionic sympathetic neuron that controls the release of noradrenaline[36]. Current evidence suggests that phosphorylation of the neuronal calcium channels by protein kinase G (PKG) inhibits the channel[37], whereas PKA phosphorylation results in channel activation.

1.4.2.3 cAMP/PKA signalling and cGMP/PKG signalling

The functionality of PKA and PKG is orchestrated through cyclic nucleotides cAMP and cGMP. cAMP, the first identified second messenger[38], transmits signals from extracellular neurotransmitters or hormones into the cytosol and nucleus. Intracellular cAMP levels are

regulated by adenylyl cyclase (AC), which synthesizes cAMP from ATP, and phosphodiesterase (PDE), which degrades cAMP. Transmembrane AC activity is modulated by ligands binding to G-protein coupled receptors, with the Gs protein activating ACs and the Gi protein inhibiting ACs (Fig. 2).

On the other hand, cGMP is synthesized by nitric oxide-activated guanylyl cyclase (GC) from GTP and degraded by PDEs. PDEs, divided into 11 families, exhibit varying affinities to cAMP and cGMP and display distinct tissue-specific expression patterns and subcellular compartmentalization. The effects of cAMP and cGMP largely hinge on the downstream activation of PKA and PKG, along with their regulatory impact on calcium channels. Both PKA and PKG are serine/threonine kinases. While a plethora of metabolic enzymes and transcription factors have been identified as substrates for phosphorylation by PKA, the substrates of PKG are comparatively less well characterized. The crosstalk between cAMP and cGMP intercorrelates their downstream regulation of various cell biological process including but not limited to metabolism, immune function, neuronal signaling, cardiac contraction and gene expression[39].

1.4.2.4 cAMP-cGMP crosstalk

Phosphokinase and phosphodiesterase both exhibit a degree of cross-selectivity for cAMP and cGMP. While cAMP and cGMP generally preferentially activate PKA and PKG, respectively, there are instances where phosphokinase can be enhanced by the 'opposite' cyclic nucleotide and participate in the biological actions of that cyclic nucleotide[40–42].

Among the 11 PDE families, PDE4, PDE7, and PDE8 exclusively hydrolyze cAMP, PDE5, PDE6, and PDE9 are specific to cGMP, while PDE1, PDE2, PDE3, PDE10, and PDE11 exhibit

dual specificity for both cAMP and cGMP. Crosstalk between cAMP and cGMP at PDE catalysis occurs in two aspects: competition for binding to enzyme active sites and direct activation or inhibition of the enzyme. In non-stimulated cells, the basal concentration of cAMP is 10-100 times higher than cGMP, occupying most of the PDE hydrolysis capacity in controlling the baseline amplitude of cAMP[43,44]. Elevated cGMP levels compete with cAMP in the hydrolytic domains of dual-specificity PDEs, affecting the concentration of cAMP. In addition to competitive inhibition, cGMP activates PDE2 and PDE5 through allosteric modification[45], while cAMP boosts the activity of PDE3, PDE4, and PDE5 through PKA-mediated activation[46]. For example, Isidori et al. reported that increased cGMP activates PDE2, enhancing cAMP hydrolysis and reducing cAMP levels[47].

The overall influence of cGMP on cAMP and vice versa depends on the origin and localization of the cyclic nucleotide pool, as different PDE subtypes reside in various subcellular compartments to regulate local cyclic nucleotide levels. For instance, the hydrophobicity difference in the three isoforms of PDE2, decided by the amino-terminal regions, allocates the enzyme as either membrane-bound or soluble. In addition to physical localization, various pools of cyclic nucleotides originate from specific ligand stimulation are subject to degradation by different PDEs. For instance, PDE2 and PDE4 are implicated in the hydrolysis of β-AR-stimulated cAMP pools[45,48]. Consequently, disruption in either of these cyclic-nucleotide signaling pathways can have a positive or negative influence on the other, depending on cell types, subcellular compartmentalization, and other interacting effectors.

Concerning sympathetic neurotransmission, dysregulation in the nNOS/cGMP/PKG pathway has the potential to impact cAMP levels and result in calcium mishandling, thereby disrupting the normal release of neurotransmitters. The interplay between cAMP and cGMP highlights the nNOS/cGMP/PKG pathway as a promising therapeutic target for modulating sympathetic activity.

1.4.2.5 M current

In addition to second messengers, dysfunction in ion channels, particularly downregulation of the M current, has been identified as a contributing factor to abnormal excitability in sympathetic neural firing[49]. The M current (*Kv7/KCNQ* family) is a noninactivating potassium current active at the resting membrane potential and even more active during depolarization, playing a crucial role in maintaining the resting membrane potential of neurons and keeping the cells at a negative voltage[50]. Early studies have established a correlation between M current and sympathetic activity, as the activation of M current by the channel opener retigabine significantly reduces firing rates in sympathetic neurons of spontaneously hypertensive rats (SHR) and hyperpolarizes the membrane potential[49]. Moreover, up-regulation of neuronal Kv7/M-current impedes catecholamine release in SHR sympathetic neurons[51]. Conversely, the loss of M current increased firing rates in Wistar neurons, mimicking the SHR phenotype. Single-cell RNA sequencing confirmed the conservation of Kv7 expression in human stellate ganglia[49]. Consequently, targeting the M channel presents another potential therapeutic avenue for reducing sympathetic neurotransmission in CPVT.

1.5 Cardiac myocyte electrophysiology

1.5.1 Cardiac action potential

Electrical activities of cardiac myocytes control and coordinate cardiac contraction and relaxation, which features different shapes in atria, ventricles and conduction cells that are determined by specific membrane ion channels. Ventricular action potential consists of five major phases[52] (Fig. 1.7). In phase 0, which is the phase of rapid depolarization, the threshold potential of about -70mV for sodium channel opening is reached by the propagation of action

potential from neighbouring cells through gap junctions. Activated sodium channels (Nav1.5) allow a large influx of sodium that rapidly increases membrane potential to a positive voltage range. In phase 1, the sodium channel is inactivated due to the close of the inactivation gate by increased membrane potential. Meanwhile, cardiac transient outward potassium channels rapidly open and close, letting out potassium ions (transient outward potassium current, Ito) that give rise to phase 1 repolarization. Phase 2 is also called the plateau phase, during which the membrane potential remains nearly constant due to the balance of charge crossing the cell membrane inwardly through L-type calcium channel (LTCC, Cav1.2) and outwardly through slow delayed rectifier potassium channel (Kv7.1, Iks). Influx calcium ions activate ryanodine receptors on the sarcoplasmic reticulum (SR) membrane that allow more storage calcium to be released from SR. During phase 3, LTCCs close while slow rectifier potassium channels remain open, and also rapid delayed rectifier potassium channel (Kv11.1, Ikr) and inwardly rectifier channel (Kir, Ik1) are activated due to potential drop. Therefore, the net outward positive current restores membrane potential to the resting stage. Delayed rectifier potassium channels close at the end of repolarization, while Ik1 remain active and plays a role in maintaining resting membrane potential in phase 4. During phase 4, ion equilibriums are restored by different ion pumps, such as sodium-potassium pumps and sodium-calcium exchangers, which re-establish electrochemical gradients across the membrane after action potential and also maintain resting membrane potential.

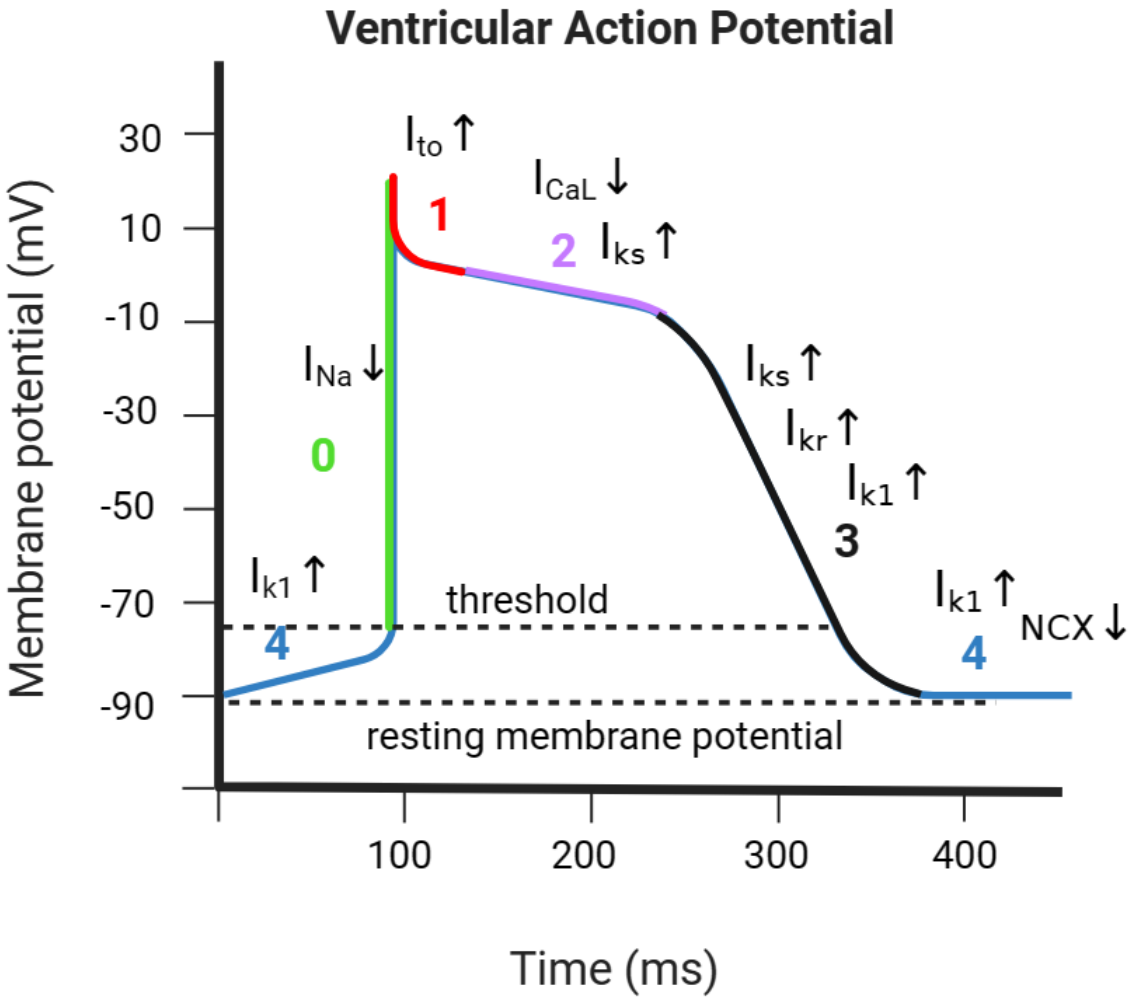


Figure 1.7 Ventricular action potential. The ventricular action potential comprises 4 phases, including phase 4 resting membrane potential at -90mV, phase 0 rapid depolarization when the membrane potential reaches the threshold for sodium channel opening, phase 1 rapid repolarization, phase 2 plateau phase when calcium influx counteracts potassium efflux and phase 3 repolarization which restores membrane potential.

1.5.2 Cardiac myocytes calcium signalling

The heart's vital function of conducting blood supply to the entire body is achieved through the highly organized excitation-contraction (EC) coupling, describing the connection between membrane depolarization of muscle cells and the generation of force by myofilament gliding. Calcium ions play a pivotal role in this process, responding to membrane depolarization and

facilitating cross-bridge formation. In cardiac myocytes, the action potential (AP) initiates myocardial membrane depolarization through the influx of sodium ions via the Nav1.5 channel. This activates the L-type calcium channel, allowing calcium influx (calcium current). The local increase in intracellular calcium concentration ($[Ca^{2+}]_i$) opens the RyR2 receptor on the sarcoplasmic reticulum (SR) membrane, a phenomenon known as calcium-induced calcium release (CICR).

The cardiac dyad, where the transverse tubule is closely associated with the SR membrane, provides the structural basis for CICR and calcium transients. Extracellular calcium influx during each AP in each cleft is sufficient to open at least one of approximately 100 RyR2 channels[53]. The opening of a single RyR2 recruits nearby channels to open. These local release events are synchronized by the rapidly spreading AP throughout the sarcolemma, a critical aspect for functional EC coupling. The spatiotemporal summation of these local Ca-release events constitutes the ECC Ca transient.

Released calcium binds to troponin C on the actin filament, inducing a conformational change that removes tropomyosin and exposes the active actin site. This allows the binding of myosin heads to actin, initiating the power stroke using energy from ATP hydrolysis. When stimulation ceases, calcium diffuses away, some is pumped out by the sodium-calcium exchanger (NCX), and the rest is restored to the SR through the sarco/endoplasmic reticulum calcium ATPase (SERCA) pump.

In the absence of a calcium current, stochastic opening of RyR2 can cause spontaneous calcium release events known as calcium sparks. The opening of RyR2 is a complex process influenced by $[Ca^{2+}]_i$, $[Ca^{2+}]_{SR}$, and various modifications such as phosphorylation and disease-related mutations. There is a spontaneously open probability of RyR2. Normally, these discrete calcium sparks do not propagate to the next junction to activate calcium release, forming

calcium waves, because calcium concentration is too low. However, an increase in calcium load or RyR2 excitability can lead to the occurrence of calcium waves without external stimulation, potentially becoming arrhythmogenic.

Table 2 Membrane ion channels that generate ventricular action potential

Current		Description	Channel	Gene	AP phase
I_{to} / I_{to1}	$I_{to, f}$	Transient outward potassium current, fast	Kv4.2/Kv4.3	KCND2/KCND3	Phase 1
	$I_{to, s}$	Transient outward potassium current, slow	Kv1.4	KCNA4	
I_{ks}		Slow delayed rectifier	Kv7.1	KCNQ1/KCNE1	Phase 2&3
I_{kr}		Rapid delayed rectifier	Kv11.1	KCNH2/hERG	Phase 3
I_{k1}		Inward rectifier potassium current	Kir	KCNJ2(Kir2.1)/ KCNJ12(Kir2.2)	Phase 3&4
I_{Na}		Sodium current	Nav1.5	SCN5A	Phase 0
I_{ca-L}		L-type calcium current	Cav1.2	CACNA1C	Phase 2

1.5.3 Cardiac excitation contraction coupling

Excitation-contraction coupling refers to the process by which action potential generated at the muscle cell membrane causes muscle contraction and force generation. Calcium mobilization plays a central role in the process. When an action potential from self-depolarizing cells is conducted to ventricular myocyte via gap junctions, it travels along the cell membrane into the T-tubule and the depolarization leads to the opening of L-type calcium channels on the membrane of the T-tubule, which are positioned in proximity to ryanodine receptors on the junctional SR forming the diad structure. Influxed Ca^{2+} through activated LTCC causes a local increase in intracellular Ca^{2+}, which activates ryanodine receptors by calcium-induced calcium release (CICR). Activated RyR2 receptors allow calcium storage in SR to be released into the

cytosol, giving rise to sporadic calcium sparks. Synchronous activation of RyR2 receptors at the cell-wide level through AP propagation results in a calcium transient as a summation of calcium sparks[54]. The elevated Ca^{2+} binds to troponin C (TnC) on the actin filament, causing a conformational change of the troponin complex that removes tropomyosin from the actin-binding site. This allows the myosin head to bind to actin and form the cross bridge, after which the myosin can hydrolyse ATP and generate the power stroke. The binding of another ATP to myosin detaches the myosin head from actin and another cross-bridge cycle can occur if calcium increases. Released calcium is actively pumped back to SR by SERCA, fluxed from the cell by NCX and plasma membrane calcium ATPase, and taken up by mitochondria through uniporter. When calcium returns to resting level, Ca^{2+} ions dissociate from TnC and tropomyosin covers the myosin binding site on the actin filament again, which ceases myocyte contraction.

1.6 Cardiac channelopathy

Genetic mutations affecting ion channels in myocardial cell membranes, crucial for cardiac action potential generation and propagation, can predispose individuals to life-threatening arrhythmias such as ventricular tachycardia (VT) and ventricular fibrillation (VF), ultimately leading to sudden cardiac death (SCD). Major cardiac channelopathies linked to different genetic disorders involving cardiac ion channels or associated proteins include Long QT syndrome (LQTS), catecholaminergic polymorphic ventricular tachycardia (CPVT), Brugada syndrome (BrS), and short QT syndrome (SQTS)[55].

In general, cardiac channelopathies are characterized by the sudden onset of lethal arrhythmias in structurally normal hearts, primarily affecting the young-adult population. It's noteworthy that most cases of SCD in patients over 40 are attributable to ischemic heart events, while

arrhythmia syndromes typically manifest in the younger demographic[56–58]. Given the often-asymptomatic nature of cardiac channelopathies, the clinical identification of genetic risk factors in family members of sudden death becomes crucial.

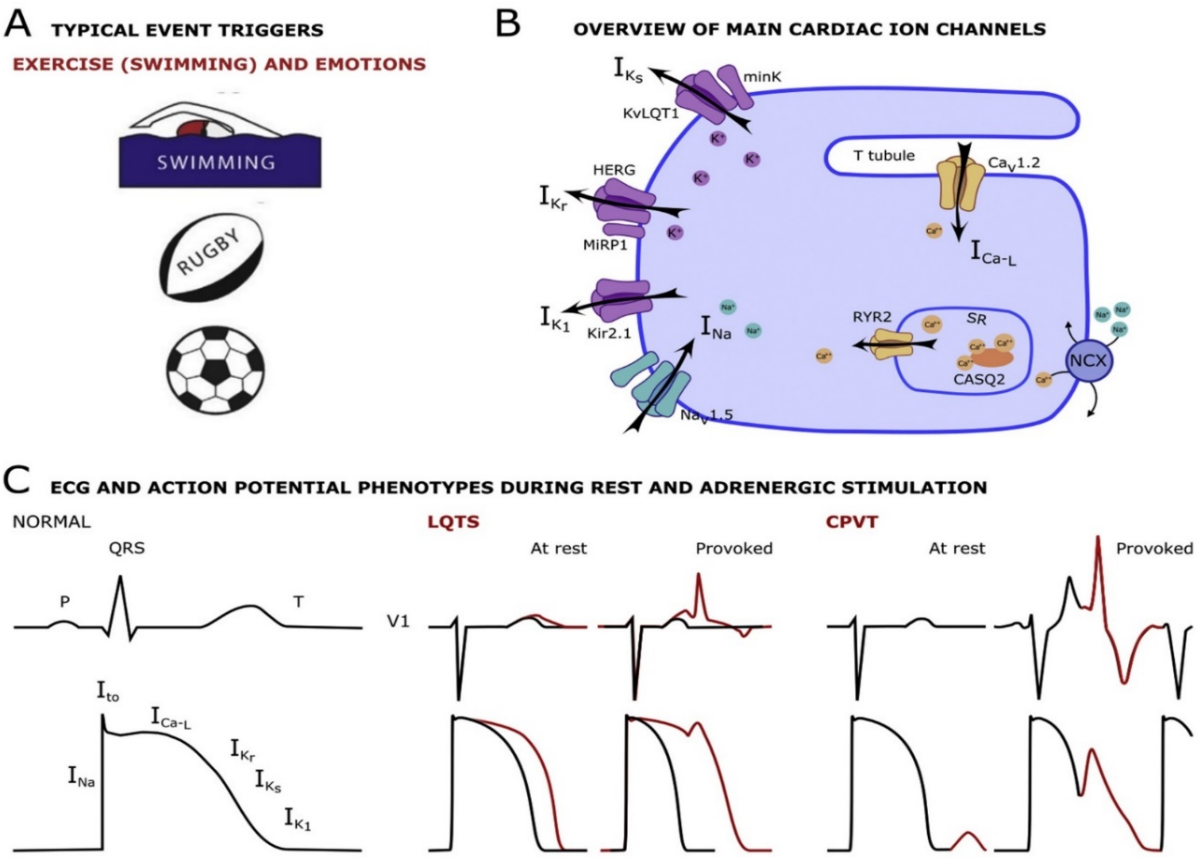


Figure 1.8 A: Both LQTS and CPVT are triggered by sympathetic activation. **B:** Ion channel**s** involved in the maintenance of cardiac action potential and intracellular calcium homeostasis. **C:** represent ECG patterns (top row) and ventricular action potentials (bottom row) of LQTS (loss of function mutation K^+ channels) and CPVT (gain of function in RyR2 Ca^{2+} release). (Adapted from Winbo & Paterson 2020)

1.6.1 Long QT syndrome

Long QT syndrome (LQTS) is a disorder that affects the repolarization phase of the heart, manifesting as an abnormally prolonged QT interval in the electrocardiogram (ECG). This prolonged QT interval heightens the risk of triggered action potentials during extended

repolarization, leading to ectopic heartbeats. Individuals with LQTS may experience syncope or cardiac arrest, often triggered by emotional or physical stress. The estimated prevalence of LQTS varies between populations, ranging from 1 in 2000 to 1 in 5000[59], with a higher prevalence in females than males[60]. If left untreated, the mortality rate within one year since the first onset of syncope could be as high as 21%, but proper management can reduce it to around 1%[61]. Hence, timely diagnosis and treatment are crucial for individuals with LQTS.

Long QT syndrome can be inherited as genetic defects in cardiac ion channels or developed later in life due to certain medications or electrolyte imbalances such as hypokalaemia or hypomagnesemia. However, it is likely that these patients also carry a silent mutation in one of the genes responsible for inherited LQTS.

The QT interval, reflecting the repolarization phase of the action potential, can be prolonged due to either a reduction in outward potassium currents or an increase in inward calcium or sodium currents. The three primary genes associated with Long QT Syndrome (LQTS) are *KCNQ1* (LQT1), *KCNH2* (LQT2), and *SCN5A* (LQT3), collectively accounting for approximately 90% of all hereditary cases[61]. *KCNQ1* encodes the α-subunit of the K+ channel Kv7.1, crucial for QT adaptation during increased heart rate, as it is physiologically enhanced by sympathetic activation[62]. *KCNH2*, encoding the Kv11.1 channel carrying the rapid delayed rectifier current, contributes to the terminal phase of repolarization, and mutations in *KCNH2* lead to prolonged QT interval similar to LQT1. *SCN5A*, the third common LQTS gene, encodes the α-subunit of the cardiac sodium channel Nav1.5, responsible for the outward depolarizing I_{Na} current[63]. Variants in *SCN5A* prolong the QT interval by slowing sodium channel inactivation, increasing the late sodium inward current. SCN5A variants altering other features of the I_{Na} current can result in different phenotypes of arrhythmic diseases. Romano-Ward syndrome (RWS), encompassing LQTS types 1 to 6 and types 9-15, is the most common form

of LQTS. RWS is distinguished from other LQTS subtypes by being a pure cardiac electrophysiological disorder and inherited in an autosomal dominant manner, while other subtypes of LQTS present with different comorbidities[64].

Prolonged QT interval increases the risk of ventricular tachycardia, which usually is the Torsade-de-Pointes that underlies the cardiac events of LQTS. As repolarization is abnormally longer, it is likely for the trigger of ectopic action potential to be in the form of early afterdepolarization that happens before the plasma membrane is fully repolarized while sodium and calcium channels are reactivated[24]. However, delayed afterdepolarization and re-entry were also implicated in the genesis of polymorphic ventricular tachycardia in LQTS.

Patients diagnosed with LQTS should carefully avoid drugs that can further prolong QT interval. Beta-adrenergic blockers have been evidenced to reduce the arrhythmic risks in all three major types of LQTS, although efficacy differed. Left cardiac sympathetic denervation (LCSD) and implantable cardioverter defibrillator are surgical options for LQTS based on risk stratification[65]. Also, bilateral cardiac sympathetic denervation (BCSD) provides extra benefits in decreasing the incidence of ventricular arrhythmia when a patient fails to respond to other therapeutic options[66].

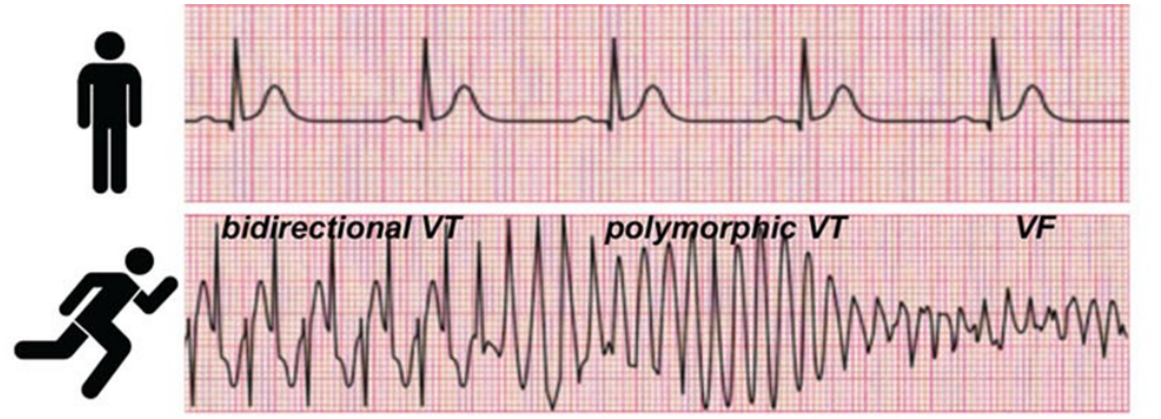
1.6.2 Catecholaminergic polymorphic ventricular tachycardia

1.6.2.1 General information

CPVT, akin to Long QT Syndrome (LQTS), is an inherited disorder that predisposes carriers of the genetic variant to potentially life-threatening arrhythmias. The onset of ventricular tachycardia or ventricular fibrillation typically occurs during periods of physical exertion or heightened emotional stress. CPVT stands out as a significant contributor to sudden cardiac

death, particularly among the young demographic. Despite its relatively low prevalence, estimated at 1 in 5,000 to 10,000 individuals, the untreated mortality rate can range between 30% and 50% by the age of 40[67].

The root cause of CPVT lies in genetic mutations that impact the sarcoplasmic membrane calcium release compartment. This compartment comprises the RyR2 receptor, serving as the primary calcium channel, along with other modulator proteins like triadin, junctin, calmodulin, and calsequestrin. Together, these proteins play a crucial role in regulating calcium concentration within cardiac muscle cells.



Park et al. (2019) *Circulation* 140:390-404

Figure 1.9 CPVT patient has a normal ECG at rest, but triggered VT by physical exertion or emotional stress.

1.6.2.2 Clinical manifestation

Individuals afflicted with CPVT typically exhibit normal heart structure and a baseline electrocardiogram (ECG) at rest. This normal appearance can obscure early detection, impeding timely diagnosis and hindering effective management to prevent the progression of the disease. The disease's onset is marked by episodic palpitations or syncope episodes occurring during periods of physical exertion or heightened emotional stress.

The initial occurrence of CPVT often manifests at a young age, with the mean onset typically ranging from 7 to 12 years old. While these arrhythmias may be self-terminated, severe cases can lead to sudden cardiac death, especially in instances of acute sympathetic hyperactivity. It is noteworthy that cardiac arrest may serve as the inaugural manifestation of CPVT, underscoring the critical importance of recognizing and addressing this condition promptly.

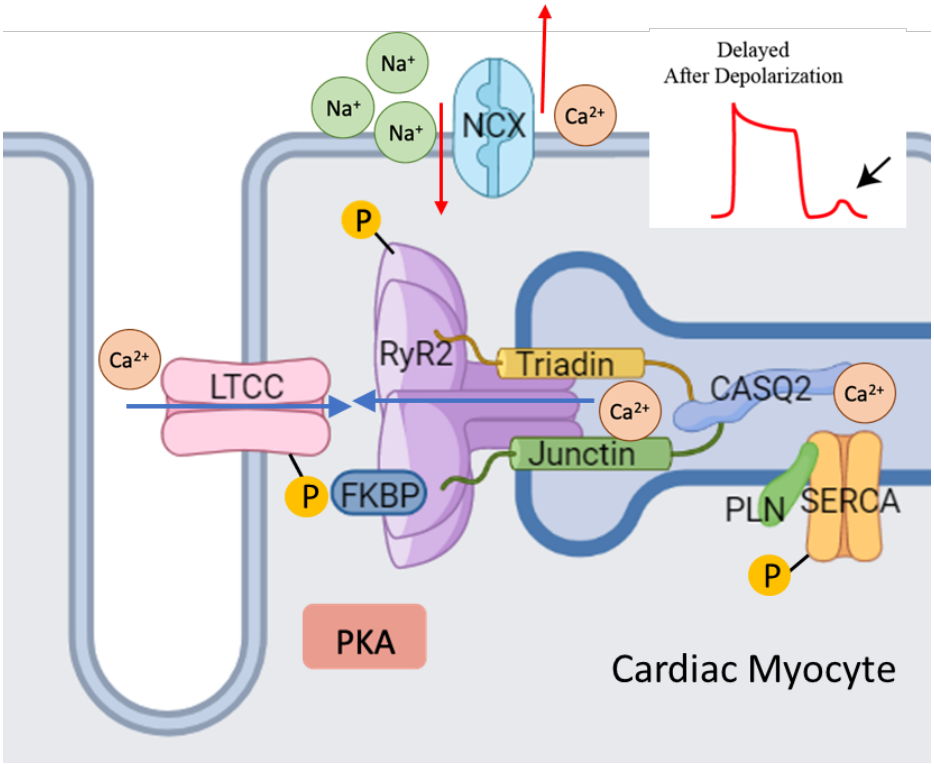


Figure 1.10 Schematic of SR calcium-releasing compartment in cardiac myocytes. The RyR2 receptor forms complexes with triadin, junctin, and FKBP, collectively regulating the gating of the channel. Additionally, calsequestrin associates with RyR2 inside the SR, contributing to the molecular basis of luminal calcium sensing in the RyR2 receptor. Calcium release from the RyR2 is induced by calcium influx through the L-type calcium channel (LTCC). Excess calcium released may be exported via sodium-calcium exchange (NCX), potentially leading to afterdepolarizations due to a net inward sodium current. Despite these intricate molecular interactions, the cellular mechanisms that underlie the sympathetic triggering of CPVT arrhythmia are not fully characterized, presenting an area where further research is needed for a comprehensive understanding.

1.6.2.3 Genetic pathophysiology

1.6.2.3.1 Gain-of-function RYR2 mutation

The triggered tachycardia results from extra calcium release during diastole from the sarcoplasmic reticulum through the ryanodine channel complex (Fig. 1.10), due to the instability of the receptor and associated regulatory proteins. Over 75% of inherited CPVT were found to have gain-of-function mutation in the *RYR2* gene (CPVT1) that encodes the ryanodine receptor[67], which is most abundantly expressed in cardiac tissue and secondly in neurons[31]. Ryanodine receptors are arranged in line with LTCCs on T-tubules and are activated when calcium influx through LTCC during action potential increases local calcium concentration around the receptors. Thus, it plays a significant role in calcium-induced calcium release (CICR) and excitation-contraction coupling (EC coupling). The underlying mechanisms of *RYR2* mutations promoting calcium release have been proposed to be related to lowering the receptor opening calcium threshold, preventing FKBP12/12.6 binding to RyR2 receptor and 'unzipping' RyR2 receptor domains, all of which increase the open probability of receptor. Although the functional effects of FKBP on the RyR2 receptor are disputed[68], disruption of the interaction is arrhythmogenic[69].

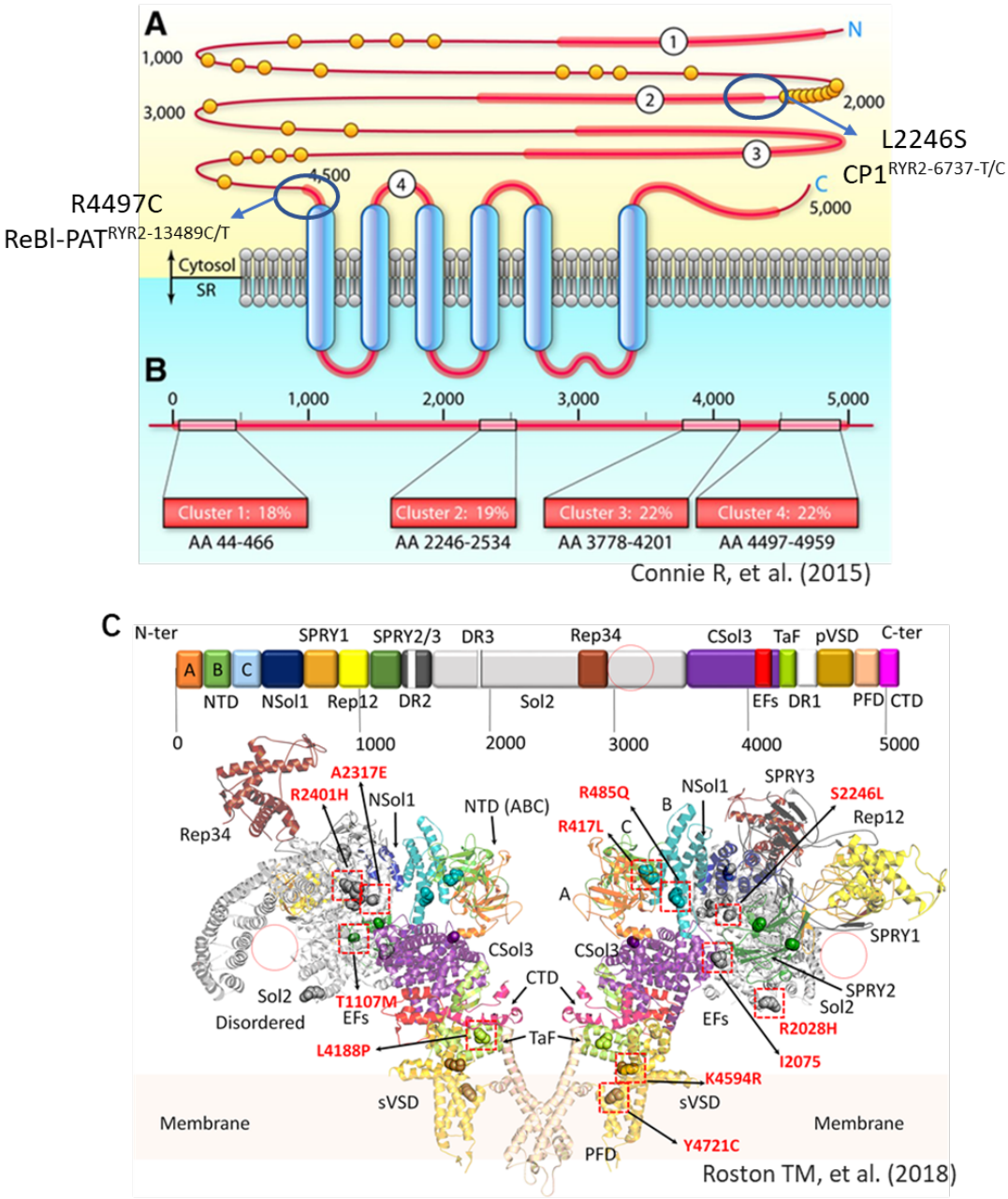


Figure 1.11 Schematic structure of RyR2 channel with frequent mutation clusters. A. Numbered red lines represented frequent mutation clusters on a RyR2 monomer. The frequency of these mutations and their location on the peptides are illustrated in **B**. **C: Domain architecture of RyR2 receptor.** The nomenclature of domains was adapted from des Georges A, et al 2016. The point mutation of the two CPVT cell lines used in this thesis, CP1$^{RYR2\text{-}6737\text{-}T/C}$ (L2246S) and ReBl-PAT$^{RYR2\text{-}13489C/T}$ (R4497C), were denoted in figure A. Amino acid 2246 located on the cytosol segment is part of the bridging solenoid, which is reported to be involved in receptor gating. (Image credit: A&B: Connie R et al. 2015 C: Roston TM et al. 2018)

1.6.2.3.2 Other CPVT genetic defects

The CASQ gene, encoding calsequestrin, a critical calcium buffer within the sarcoplasmic reticulum (SR), is implicated in approximately 5% of CPVT cases, denoted as type 2 CPVT (CPVT2). Normally, calsequestrin interacts with the RyR2 receptor via triadin and junctin, modulating the gating behaviour of the receptor. Dysfunction in calsequestrin diminishes the SR's calcium buffering capacity and destabilizes the receptor[70,71].

Other genetic disorders identified in proteins that play a role in stabilizing the RyR2 receptor or immobilizing calcium, include calmodulin (CALM), Trans-2,3-enoyl-CoA reductase-like protein (TECRL), triadin (TRDN), and junctin (JCN). Calmodulin regulates the RyR2 receptor in a calcium-dependent manner; the binding of Ca^{2+}-CaM induces a conformational change leading to pore closure of the calcium-activated channel[72].

The first family study of a malignant form of CPVT devoid of *RYR2* and *CASQ* mutations, yet featuring a *TECRL* mutation, was reported in 2007 and was termed CPVT3[73]. However, given the limited number of case reports describing *TECRL* mutation-associated arrhythmia[74], the investigation into the phenotype and genotype-phenotype correlation has only recently commenced. This underscores the emerging nature of our understanding of TECRL-related CPVT and the need for further research in this domain.

1.6.2.4 Arrhythmogenic mechanism

Calcium overload during diastole from the leaky ryanodine receptor predisposes to delayed afterdepolarization (DAD) through sodium-calcium exchanger which generates net outward positive current. DAD can trigger a premature action potential if the amplitude reaches the voltage threshold for sodium channel opening.

1.6.2.5 Management

The mainstays of treatment for CPVT patient are beta blockers, which act as competitive antagonists with catecholamine at adrenergic receptors. Beta blockers effectively prevent cardiac events in CPVT patients, but over 30% patients still develop arrhythmias in long term follow-up.[75] Flecainide, a class Ic antiarrhythmic drugs that blocks sodium channel, has been proposed to be a therapeutic option for patient with CPVT refractory to beta blockers. Clinical observations proved its efficacy in reducing onset of arrhythmia in CPVT. Its mechanism of action in CPVT was reported to be combined actions of sodium channel blockage and direct inhibition of RyR2 receptor, but contrary opinions suggesting that Flecainide does not interact with RyR2 receptor.[76] Left side cardiac denervation (LSCD) and ICD can be used in patients experience persistent arrhythmia despite pharmacological treatments.

1.6.3 Brugada syndrome

Brugada syndrome (BrS) is a rare arrhythmic disease with a prevalence of about three to five per 10,000 people. Initially identified and named by Pedro and Josep Brugada in 1992[77], the syndrome is characterized by a distinct electrocardiogram (ECG) pattern showcasing ST-segment elevation in leads V1-V3. Symptoms encompass syncope, ventricular tachycardia (VT), ventricular fibrillation (VF), cardiac arrest, and sudden cardiac death (SCD). Notably, both the ECG features and associated symptoms are relatively specific to Brugada syndrome.

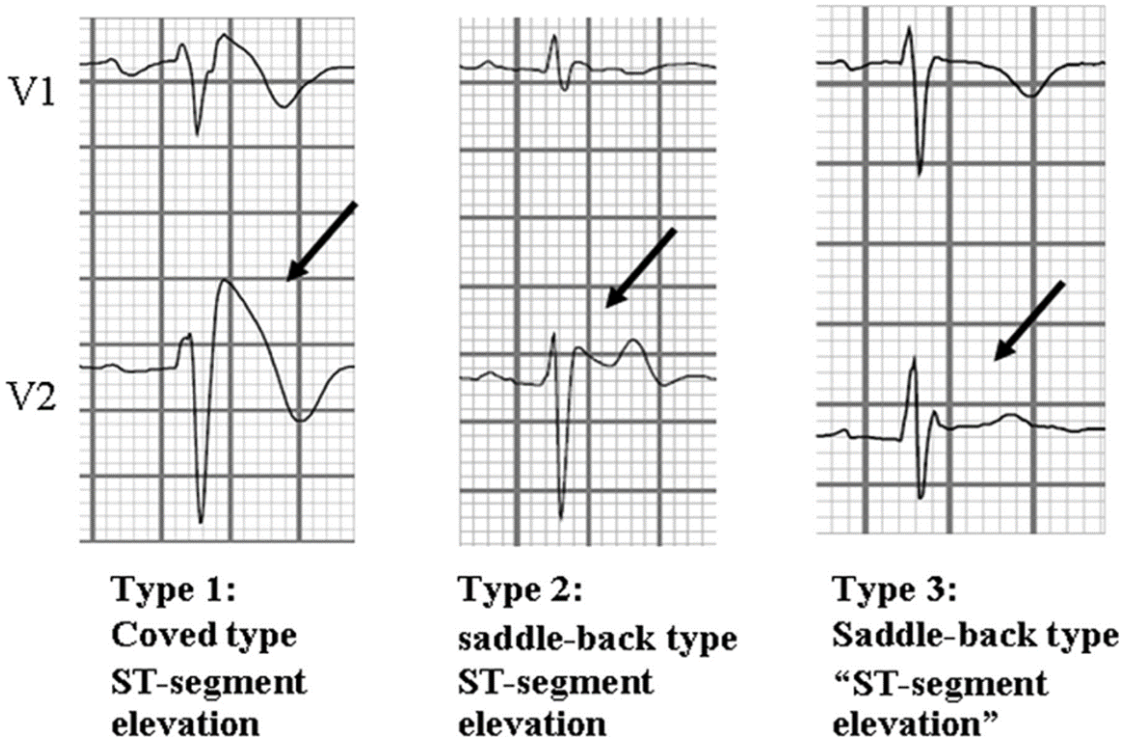


Figure 1.12 Brugada syndrome ECG patterns. Type 1 is characterized as coved type ST-segment elevation ≥2 mm followed by inversion T wave in lead V1 or V2. Type 1 ECG is diagnostic for Brugada syndrome. Type 2 marks the saddle-back shape ST-segment elevation with J point elevation ≥2 mm, which gives rise to a gradually descending ST segment with the terminal portion elevated ≥1 mm. Type 3 refers to ST-segment elevation that fails to meet the type 1 or type 2 criteria. Image credit: Yuka Mizusawa. Circulation: Arrhythmia and Electrophysiology. Brugada Syndrome, Volume: 5, Issue: 3, Pages: 606-616.

The first genetic mutation identified in BrS was *SCN5A* encoding for the α-subunit of cardiac voltage-gated sodium channel, which was reported to be responsible for 20-30% of inherited BrS[78]. A number of other mutations in calcium channels and potassium channels were also suggested to be associated with BrS, many with undecided role in causing the disease. Even in *SCN5A*, over 100 variants have been detected in BrS and could demonstrate incomplete penetrance and variably expressivity[79].

The exact mechanism of BrS remains to be clarified. Functional studies of *SCN5A* mutation in BrS revealed a loss of function of the sodium channel that impairs phase 0 depolarization and

reduces the conduction velocity of the action potential. However, whether *SCN5A* mutation is the sole causal factor remains unclear due to the broad range of variants in genetics and phenotypes[80]. Some acquired factors such as certain drugs and electrolyte imbalance can induce Brugada ECG patterns which cannot be diagnosed as BrS if typical symptoms or family history are absent.

For patients with Brugada syndrome who have suffered from syncope or VT/VF, or have survived cardiac arrest, the first line treatment is implantable cardioverter-defibrillator (ICD). An alternative pharmacological treatment with quinidine could be considered for BrS patients with contraindications for ICD placement.

1.6.4 Sympathetic denervation improves the prognosis of cardiac channelopathy

Cardiac sympathetic denervation (CSD) has been demonstrated to be effective for LQTS and CPVT in reducing the onset of cardiac events and ICD shocks. A multicentre retrospective study evaluated the outcomes of CSD in patients suffering refractory VT or VT storm, which reported a decreased recurrence of sustained VT with ICD shock-free survival of 50% at 1 year.

This study also found that bilateral CSD was more beneficial than left CSD in reducing the burden of ICD shock (Fig. 1.13.)[81,82].

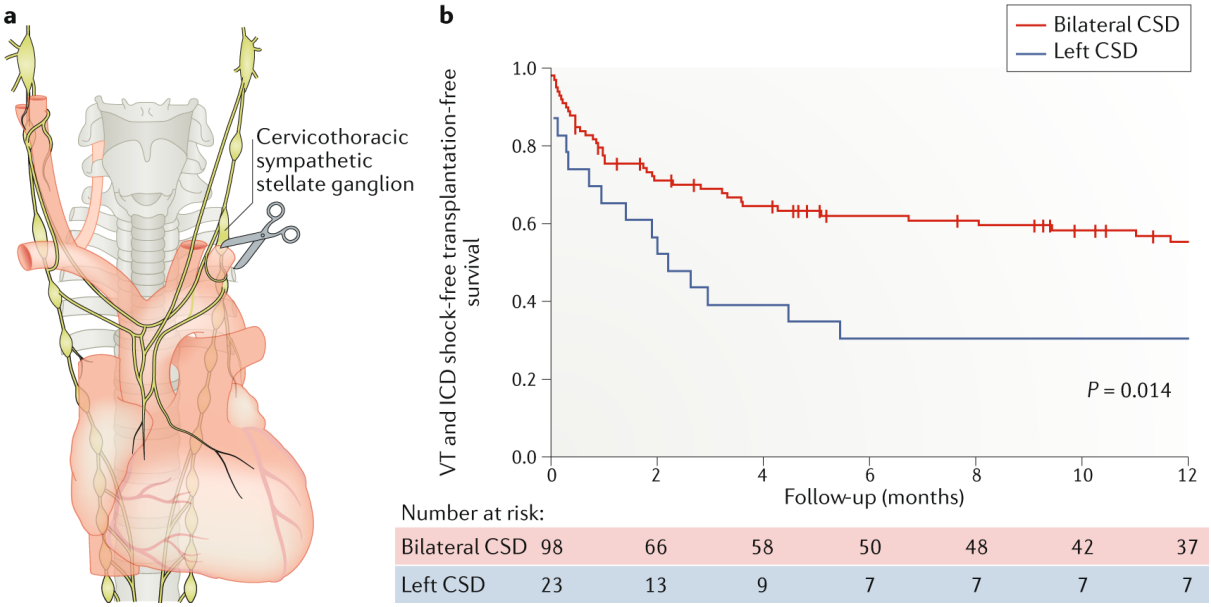


Figure 1.13 A. Schematic illustration of left cardiac sympathetic denervation. **B.** Patients who underwent bilateral cardiac sympathetic denervation have longer VT and ICD shock-free survival compared to the left-sided procedures. Adapted from: Herring, Kalla, & Paterson, Nat Rev Cardiol 16, 707–726 (2019).

1.7. Human induced pluripotent stem cell

1.7.1 Model development from the rat to human iPSCs

A major drawback of animal models is the interspecies differences in ion channel distribution, electrophysiological properties and contractile features that make rat models less representative for recapitulating the human cell response. Primary human cardiomyocytes and sympathetic neurons are of limited supply for disease pathophysiological studies due to their lack of regenerative capacity and the invasive procedures required for the collection from patients. Thus, human stem cells including embryonic stem cells and induced pluripotent stem cells have

emerged as a promising tool that overcome the inter-species genetic heterogeneity and offer unlimited somatic cells. There is a long history of research in nuclear transfer cloning[83,84], the discovery of reprogramming transcription factors[85] and embryonic stem cell culture, which laid a foundation for the concept of introducing key transcription factors into somatic cells to reactivate pluripotency[86].

In the past few decades, human induced pluripotent stem cell (hiPSC) has become a research focus in disease modelling due to their potential to provide unlimited sources of human somatic cells. The reprogramming of fibroblasts to a pluripotent state was first reported in 2006 by Takahashi et al by overexpressing 4 transcription factors, Oct3/4, Sox2, c-Myc, and Klf4[87]. The reprogrammed cells obtained similar morphology and growth properties to embryonic stem cells and express stem cell markers, which can be further differentiated to different somatic cells. Human iPSC technology provides a useful platform for the study of human genetic disease especially those involving the interaction of two or more cell types, as multiple somatic cell types can be differentiated from the same stem cell carrying the same genetic information[87,88].

1.7.2 hiPSC differentiated cardiac myocytes

1.7.2.1 Advancements in induction protocol

Since the pioneering derivation of human embryonic stem cells (hESC) in 1998[89], the process of cardiac myocyte differentiation from hESC and later hiPSC has undergone a significant transformation. Initially characterized by uncontrolled conditions, the evolution of differentiation protocols has advanced towards simplified, defined, and relatively robust methodologies. The foundational understanding of signalling pathways regulating differentiation has been instrumental in this progression.

The induction of cardiac myocytes from human stem cells began with embryonic stem cells (hESC) via embryoid bodies (EB) formation[90]. Early stages required fetal bovine serum (FBS) and a mouse embryonic fibroblast feeder layer for hESC culture[89]. Subsequently, these were replaced by a formula medium supplemented with fibroblast growth factor 2 (FGF2) and Matrigel coating, achieving a serum-free, feeder-free culture condition[91]. The efficiency of cardiac differentiation was enhanced by incorporating growth factors such as FGF2, activin A, and BMP4 at specific stages[92].

In 2007, a monolayer-based direct differentiation method emerged as an alternative to the EB-based approach, offering improved survival and purification of derived cardiac myocytes[93]. This method utilized activin A and BMP4 with RPMI/B27 medium and laid the groundwork for the development of the GiWi small-molecule method[94]. Over the subsequent decade, the GiWi protocol, employing Gsk3 inhibitors and Wnt signaling inhibitors in a stage-specific manner, became the predominant approach[95], modulating the Wnt/β-catenin pathway identified as a crucial regulator in cardiac myocyte differentiation[96].

Ongoing efforts focus on enhancing myocyte maturation, yield, and reproducibility by fine-tuning medium components and the concentration of small molecules[97–100]. Additionally, the field explores tissue engineering using hiPSC-derived cardiac myocytes, such as three-dimensional cardiac organoids, showing promise in recapitulating pathophysiological properties akin to a real heart[101]. Continued optimization of cardiac differentiation protocols is essential to ensure reproducibility across diverse cell lines, achieve myocyte maturation, and enhance cost efficiency.

1.7.2.2 Cardiac investigations for disease modelling

The application of hiPSCs-CMs in the study of human disease has incompatible advantages over primary cells with limited sources or animal models that are less clinically transferable.

Human iPSCs-induced cardiomyocytes were first applied in the mechanistic study of long QT syndrome (LQTS) in 2010[102]. Moretti et al generated cardiac myocytes from hiPSC with *KCNQ1* mutation, which displayed prolonged action potential and 70 to 80% reduction in Iks current, which suggests patients-derived cells were capable of recapitulating disease phenotypes.

Since then, numerous studies have refined the techniques using hiPSC-CMs in modelling cardiac diseases, mostly channelopathies and cardiomyopathy. Besides the first LQTS1 report, works on LQTS2 also identified decreased Ikr current stem cell-derived cardiac myocytes with *KCNH2* mutation, as well as increased frequency of afterdepolarization and triggered activity[103,104]. Pierre et al. modelled LQTS 3 through the expression of LQTS3 variants Nav1.5/delQKP in Nav1.5 knockout iPSC-CMs and detected persistent sodium current from the dysfunctional sodium channel and prolonged AP duration as characterized in LQT3 patients[105].

CPVT is another channelopathy that has been extensively explored using hiPSC-CMs[106–108]. Cardiac myocytes derived from CPVT hiPSCs exhibit abnormal calcium handling, characterized by increased adrenergic-induced intracellular calcium concentration ($[Ca^{2+}]_i$) and a heightened frequency of calcium sparks. Additionally, these cells demonstrate arrhythmogenic membrane potential features, including delayed afterdepolarization, oscillatory prepotentials, and triggered arrhythmia. These abnormalities align with the behaviours observed in the hearts of individuals affected by CPVT, providing valuable insights into the pathophysiology of the disease.

The development of the hiPSC-CMs model benefits the investigation of BrS with disputed pathogenesis. Comparison between mice and hiPSC-CMs model carrying SCN5A mutation demonstrated hiPSC-CM an appropriate model for cardiac sodium channel diseases[109].

Reduction in I_{Na} density and upstroke velocity of action potential have been detected in BrS patients specific hiPSC-CMs in many previous works on BrS[110–112]. Dysregulated calcium transient and abnormal conduction was also reported[110,111].

Also, the *in vitro* differentiation allows investigation into the early developmental stage of the heart which is otherwise impossible. Lewis-Israeli et al reported that heart organoids generated from human iPSCs exhibited transcriptomes, heart field development, action potential and calcium activity comparable to the main cardiac developmental stage. Their model system recapitulated hallmarks of pregestational diabetes-induced congenital heart disease at structural, electrophysiological, and metabolic levels[113].

1.7.3 hiPSC differentiated sympathetic neurons

Adrenergic sympathetic neurons are derived from neural crest cells and migrate from the neural tube to the periphery directed by a series of molecules that turn on and off related signalling pathways at certain stages over the development. For example, stem cell factor (SCF) keeps the neural crest cells (NCSs) alive while the addition of nerve growth factor (NGF), brain-derived neurotrophic factor (BDNF) and neurotrophin-3 cause NCS apoptosis but promote the growth of melanogenic cells[114]. The significant roles of growth factors, WNT signalling, SHH signalling, and bone morphogenetic (BMP) signalling in promoting ANS development have long been studied, although not thoroughly clarified and more interconnections are being added to the map.

Based on the biomolecular understanding of sympathetic nervous system development, *in vitro* induction of sympathetic neurons has been attempted using hiPSCs. Although much utilization with hiPSC has been made since the reprogramming was achieved, especially with hiPSC-

induced cardiac cells, hepatocytes, blood cells and neurons of the central nervous system, experiences with peripheral neuron induction are still limited. Dual inhibition of SMAD signalling was reported to be effective in generating neural crest cells[115], based on which Oh et al. reported the first differentiation protocol for sympathetic neurons with multiple genetic reporters to monitor the differentiation and isolate sympathetic neuron progenitors[116]. By monitoring the expression of fluorescent reporters, they confirmed that activation of WNT signalling followed by SHH signalling promoted the generation of sympathetic progenitors. They generated DBH+ TH+ PRPH+ neurons that can regulate mouse ventricular myocytes' beating rate. Later, Zeltner et al. published an ANS induction protocol with similar strategies that modify NC development-related signalling pathway and induce sympathetic neurons from neural crest spheroid using SOX10::GFP-reporter cell line and FACS sorting to purify neural crest cells before sympathetic neuron differentiation[117]. They continuously optimized their protocol to a feeder-free chemically defined differentiation protocol without the need for cell sorting[118]. Winbo et al. generalized the above protocols and proposed a small molecule feeder-free protocol with 12-day differentiation plus 28-day maturation which was adopted in this thesis[119]. Takayama et al. presented an optimization for ANS lineage neural crest derivation by subsequent WNT inhibition, SHH inhibition and BMP activation following the conventional NC induction steps. Besides sympathetic neurons, they also presented data on parasympathetic neurons derived from the ANS lineage neural crest cells with low cell density and high neurotrophic factor. Single-cell RNAseq identified sympathetic and parasympathetic markers, and the two populations function oppositely on cardiomyocyte beating rate[120].

1.7.4 Co-culture of sympathetic neurons and cardiomyocytes derived from hiPSCs

Sympathetic innervation plays a crucial role in influencing cardiac function under normal physiological conditions, but its heightened activity is linked to a diverse spectrum of cardiovascular diseases. Elevated β-adrenergic signalling is implicated in the development of hypertension, cardiac remodelling following myocardial infarction, and the initiation of various life-threatening arrhythmias, particularly in individuals with Long QT Syndrome and Catecholaminergic Polymorphic Ventricular Tachycardia.

Due to the potent ability of the sympathetic nervous system to induce arrhythmias in individuals with cardiac channelopathies, recent attention has been directed toward developing neuronal-cardiac co-culture systems. These systems, employing either animal cells or stem cells, aim to facilitate the exploration of neurocardiac interactions, and some success has been achieved in this endeavour.

Oh et al. were pioneers in reporting functional coupling evidence, demonstrating that noradrenaline-secreting sympathetic neurons in co-culture could drive the heart rate of neonatal cardiac myocytes when stimulated either pharmacologically or optogenetically[116]. Likewise, other studies have shown that the selective induction of healthy human sympathetic neurons allows for precise control of cardiac myocyte beating[119,120].

While the development of a diseased cardiac-neural co-culture system has not been firmly established, Winbo et al. recently reported increased excitability and neurotransmission in sympathetic-derived neurons from a Long QT Syndrome type 1 (LQT1) patient with *KCNQ1* loss-of-function variants[121]. Whether a human induced pluripotent stem cell (hiPSC) cardiac-neural co-culture system can replicate and mimic cardiac-neural responses observed in other mammalian systems remains an area that requires further investigation.

1.8. Rationale in using human induced pluripotent stem cell to study sympathetic neurons in cardiac channelopathy

Elevated sympathetic drive is a hallmark feature of numerous cardiovascular diseases, serving as a potent prognostic indicator for morbidity and mortality associated with arrhythmias and sudden cardiac death (SCD). Despite its recognized significance, the molecular targets underlying this dysautonomia remain inadequately understood. Notably, our research has unveiled some key proteins, including neuronal PDE2A[122,123] and adaptor protein NOS1-AP[124] within cardiac sympathetic neurons, contributing to abnormal neurotransmission and amplifying cardiac excitability. These neurons emerge as formidable drivers of life-threatening arrhythmias, particularly evident in individuals with channelopathies—disorders stemming from dysregulated ion channel subunits or their regulating proteins.

Conditions such as long QT syndrome (LQTS) and catecholaminergic polymorphic ventricular tachycardia (CPVT) are precipitated by ion channel mutations in the heart, constituting a significant proportion of sudden cardiac deaths in those under 40 years old. Sympathetic nervous system responses to physical or emotional stress typically trigger these arrhythmias. Although treatments like beta-adrenergic blockade and cardiac stellectomy have shown benefits, they do not fully prevent SCD and are burdened with off-target effects and undesired side effects. Additionally, achieving site-specific targeting of sympathetic neurons has proven challenging, and validating therapeutic pathways against human tissue remains elusive.

While primary human LQTS/CPVT cells are generally unavailable, human induced pluripotent stem cells (hiPSCs) have emerged as a valuable tool for modelling inherited arrhythmias. Cardiomyocytes differentiated from LQTS hiPSCs faithfully replicate the disease phenotype, demonstrating a pathological response when exposed to sympathomimetics. Although extensive studies have examined cardiac myocytes derived from hiPSCs with CPVT genetic

defects, research on the autonomic regulation of arrhythmia onset using hiPSC modelling systems is lacking. Understanding autonomic function is pivotal for preventing sudden cardiac death in individuals with cardiac channelopathies.

Therefore, the overall objective of my thesis is to identify cellular neurocardiac arrhythmia mechanisms that underpin life-threatening cardiac events in CPVT using a human-derived co-culture model.

1.9 Hypothesis

CPVT patients are usually asymptomatic until increased sympathetic tone such as exercise or emotional stress triggers the lethal arrhythmia. Increased sympathetic tone phosphorylates RyR2 receptors to facilitate the opening of the channel through cAMP/PKA signalling, which exacerbates calcium release and predisposes to delayed afterdepolarizations. Little was known about the role of the sympathetic neuron itself in the pathogenesis of CPVT. Given the growing evidence showing the role of hyperactivated sympathetic tone in cardiovascular diseases such as hypertension and long QT syndrome, I hypothesize that CPVT sympathetic neurons also harbor abnormalities that enhance adrenergic neurotransmission. Identifying these dysregulated molecules could lead to new therapeutic options.

1.10 Aims of this thesis

The first objective was to derive cardiac myocytes and sympathetic neurons from human-induced pluripotent cell lines and verify the recapitulation of physiological phenotypes in hiPSC-derived cardiac myocytes and sympathetic neurons.

Secondly, to apply hiPSC-CM in the modelling of cardiac hypertrophy with a comparison using hypertrophic neonatal ventricular myocytes from the rat.

Thirdly, to establish a hiPSC-derived neurocardiac coculture and verify the morphological and functional connection between the two cell types.

Finally, to apply CPVT hiPSC-CM and -SN monoculture and co-culture model in the mechanistic study of the disease, with a focus on the role of sympathetic neurons in triggering arrhythmia.

Some work on hiPSC phenotyping (Chapter Three) and modelling of cardiac hypertrophy (Chapter Four) have been published[125].

Chapter 2: General methods

2.1 Solutions and reagents

The catalogue number and formula of all solutions and reagents used in this thesis are given in each experimental chapter.

2.2 Animal model

All experiments were approved by Oxford University's Animal Ethics Committee and carried out in accordance with the UK Home Office Animals Scientific Procedures Act, 1986 (P707EB251 (DJP)).

2.2.1 Wistar Rats

Wistar rats are the most widely used laboratory outbred rat model for medical and biological research. Cardiac myocytes taken from Wistar neonatal rats (1-2 days old) ventricles were used in the cardiac myocytes hypertrophic modelling experiments as interspecies comparison for the human iPS cell model.

2.2.2 Schedule-1

Schedule 1 of the Animals (Scientific Procedures) Act, 1986 listed the methods of humane killing for particular research animals, including confirmation of permanent cessation of the circulation, destruction of the brain, dislocation of the neck, exsanguination, confirming the onset of rigour mortis and instantaneous destruction of the body by a macerator. The only animal model applied in this research was neonatal rat, which was subject to rodents up to 500g, so dislocation of the neck was the method used as indicated.

2.2.3 Rat ventricular myocytes isolation

Animal use adhered to the University of Oxford Local Ethical Guidelines and aligned with the Guide for the Care and Use of Laboratory Animals by the US National Institutes of Health (Publication No. 85-23, revised 2011) and the Animals (Scientific Procedures) Act 1986 in the United Kingdom. The experiments were conducted under the British Home Office Project License [P707EB251 (DJP)].

Ventricles were extracted from 1-3-day Wistar neonatal rats, following the approved Schedule 1 killing procedure by dislocation of the neck. Subsequently, the ventricles were digested for 20 minutes with stirring in Tyrode solution comprising collagenase (Roche, 10103586001) and pancreatin (Sigma, P1750) at 37 ℃, repeated five times. After each 20-minute digestion period, supernatants containing cardiac myocytes were collected, centrifuged, and the cell pellets were resuspended. Following digestion, all cell suspensions were combined and centrifuged at 1250 rpm for five minutes at 4 ℃. The resulting pellet, containing cardiomyocytes, was resuspended in culture medium (DMEM high glucose plus 17.5% M199, 10% horse serum, 5% newborn calf serum, 2mM glutamine, 0.1% penicillin/streptomycin) and seeded on a cell culture dish for one hour to eliminate fibroblasts and endothelial cells. Unattached myocytes were then collected from the supernatant and plated on suitable cell culture dishes for subsequent experiments.

2.3 Human induced pluripotent stem cell modelling

To create a human cell-induced pluripotent stem cell model, the initial phase involved harvesting somatic cells—fibroblasts in this thesis—from patients. The reprogramming of these cells back into a pluripotent state was carried out by the Nottingham Stem Cell Centre.

Subsequent to obtaining the stem cell lines, the cells were cultured in maintenance media for amplification. Following this, they were differentiated into cardiac myocytes and sympathetic neurons for utilization in mechanistic studies and the exploration of therapeutic targets.

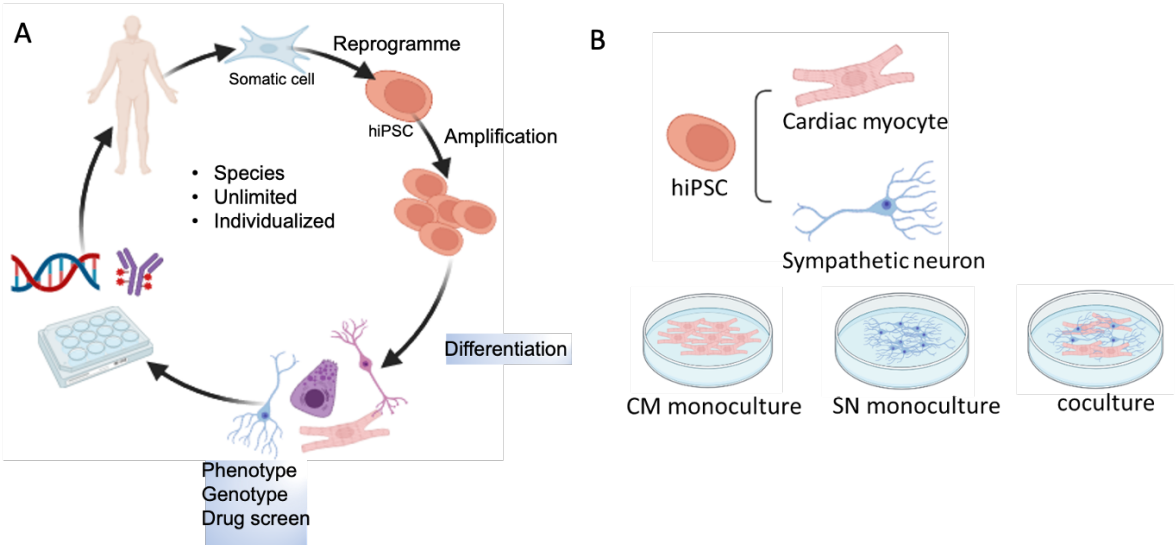


Figure 2.1. A: Schematic diagram of the generation and application of hiPSCs. Somatic cells taken from patients can be reprogrammed to a pluripotent state and differentiated to various cell types *in vitro* to apply physiological context to a human disease. **B:** Overview of study design. To induce cardiac myocytes and sympathetic neurons from hiPSCs, use monoculture, and co-culture to study sympathetically triggered inherited arrhythmia.

First, physiological phenotypes were rigorously tested to validate the differentiation of cell types through the induction protocols. This encompassed various techniques, including single-cell RNA sequencing to capture transcript profiles, flow cytometry to verify tissue-specific protein expression, immunofluorescence staining to visualize cell morphology, and functional experiments such as calcium imaging, electrical mapping, and FRET (Fluorescence Resonance Energy Transfer) to assess their biological responses to extracellular stimuli.

Subsequently, a proof-of-principle model employing normal cells was established to verify that human induced pluripotent stem cell-derived cardiomyocytes (hiPSC-CMs), when exposed to angiotensin II, can effectively replicate cardiac hypertrophy in vitro. Specifically, by subjecting healthy hiPSC-induced cardiac myocytes to 1 μM angiotensin II—a recognized hypertrophic inducer—observable hypertrophic manifestations, including structural remodelling, foetal gene expression, and modification of beta-adrenergic reactions, were identified in these hiPSC-CMs. As a validation model for the hypertrophic effects of angiotensin II, primary Wistar rat myocytes were utilized.

While findings in animal models cannot be directly extrapolated to human disease due to species differences, these primary Wistar rat myocytes are characterized by a high degree of homogeneity and maturity compared to myocytes derived from stem cells. Consequently, they consistently exhibit reliable responses to external stimuli, offering a valuable model for the study of hypertrophic effects.

Lastly, monoculture and co-culture of cardiac myocytes, sympathetic neurons differentiated from CPVT hiSPC were used to determine the role of adrenergic drive in triggering myocytes arrhythmia. Calcium transients were studied in diseased versus healthy hiPSC-CMs and -SNs to uncover the impact of *RYR2* mutation. Nicotinic stimulation on the neuron in neurocardiac co-culture was proved to be able to modify cardiac cAMP level and accelerate myocytes' beating rate.

The first unresolved question centres on identifying therapeutic targets within CPVT neurons capable of reversing the overactivated calcium signalling. Currently, an intervention experiment is underway, focusing on neural cGMP signalling, with sodium nitroprusside serving as a nitric oxide donor.

The second aspect involves exploring functional connections between neurons and myocytes in vitro. This entails investigating whether diseased neurons can instigate arrhythmia in healthy myocytes and conversely, if healthy neurons can mitigate spontaneous discharge in diseased myocytes. These inquiries are being addressed through the implementation of a cross-culture model (Fig.4).

2.3.1 Ethics and cell lines used

Two healthy hiPSC lines, namely SFC854-03-02 and iPS-OX1-19, were employed for cardiac myocyte differentiation in this study. These lines, previously published, were derived from dermal fibroblasts from healthy donors through StemBANCC (SFC854-03-02) or the Oxford Parkinson's Disease Centre (iPS-OX1-19). Participants recruited for this study provided signed informed consent, including the derivation of hiPSC lines from skin biopsies. Ethics approval for control donors was obtained from the National Health Service, Health Research Authority, NRES Committee South Central, Berkshire, UK (REC 10/H0505/71). All experiments adhered to UK guidelines and regulations, as outlined by the Research Ethics Committee (REC).

For the induction of sympathetic neurons, three cell lines—iPS-OX1-19, UKKi007-A, and ReBl-PAT$^{RYR2\text{-}WT}$—were utilized. The UKKi007-A cell line was provided by the European Collection of Authenticated Cell Cultures and ethically approved by the Ethics Committee of the Ruhr-University Bochum, Bad Oeynhausen, Germany (Registration No. 41/2008). The isolation and use of patient fibroblasts for ReBl-PAT$^{RYR2\text{-}WT}$ were approved by the Nottingham Research Ethics Committee (License 09/H0408/74), with sample collections registered under the UK Clinical Research Network, project 8164.

An isogenic pair, CP1 ($CP1^{RYR2\text{-}6737\text{-}T/C}$) and WT ($CP1^{RYR2\text{-}Corr}$), was employed for both cardiac myocytes and sympathetic neuron induction for the study of CPVT. CP1, derived from CPVT patient fibroblasts, carries a heterozygous S2246L mutation in the *RYR2* gene, while WT is a derivative of CP1 with edited correction of the point mutation (6737 T/C to 6737 C). Some experiments in the CPVT study were replicated using another isogenic pair, ReBl-$PAT^{RYR2\text{-}WT}$ and ReBl-$PAT^{RYR2\text{-}13489C/T}$. ReBl-$PAT^{RYR2\text{-}WT}$ is a control cell line reprogrammed from healthy donor fibroblasts, while ReBl-$PAT^{RYR2\text{-}13489C/T}$ is a derivative with an edited mutation on base 13489 (C/T), resulting in a 4497 arginine to cysteine mutation. The isolation and use of patient fibroblasts were approved by the Nottingham Research Ethics Committee (License 09/H0408/74), and sample collections were registered with the UK Clinical Research Network under project 8164.

Chapter five delves into the disease phenotype of CPVT, utilizing a hiPS cell line featuring the RYR2-$S2246L^{+/-}$ mutant (refer to Table 1 for details). The domain architecture was visually represented in Figure 1.11C, adapted from Roston TM et al. 2018[126]. Notably, AA2246 resides within the bridging solenoid region, a segment regarded crucial in regulating the gating of the RyR2 receptor[127,128]. This insight sheds light on the potential significance of AA2246 in influencing the functionality of the RyR2 receptor.

Table 1. RYR2 variant information summary of hiSPC cell lines used in CPVT modelling

Cell line	$CP1^{RYR2\text{-}6737\text{-}T/C}$	$CP1^{RYR2\text{-}Corr}$
Starter or derivative	Starter	Derivative of CP1
Created by	Reprogramming CPVT patient fibroblasts	Edited correction
Disease status	CPVT clinical diagnosis	Predict none
Gene sequence	gctgcagctt t ggtgatggat	gctgcagctt c ggtgatggat
Genotype	6737 T/C (CDS), heterozygous	6737C (CDS), homozygous
Protein change	From serine to leucine at position 2246 (S2246L)	2246S
Protein sequence	SVGLASPAMRGSTPLDVAAA L VMDNNELALALREPDLEKVV	SVGLASPAMRGSTPLDVAAA S VMDNNELALALREPDLEKVV

2.3.2 Maintenance and differentiation of human induce pluripotent cell

hiPSC were amplified in Matrigel-coated (Corning, 356234) cell culture flask in mTeSR medium (STEMCELL Technologies, 85850), then were frozen at $2x10^6$ cells/1ml Crystor (STEMCELL Technologies, 07959) in liquid nitrogen for long term storage. Frozen hiPSCs were thawed and passaged three times for amplification and revitalization before differentiation commenced. To ensure protocol reproducibility, the induction of both cardiomyocytes and sympathetic neurons was replicated over three independent experiments on the SFC854-03-02, $CP1^{RYR2\text{-}6737\text{-}T/C}$, and $CP1^{RYR2\text{-}Corr}$ cell lines.

2.3.2.1 hiPSC-CM differentiation

After thawing, iPSCs underwent three passages before being seeded onto Matrigel-coated 12-well plates, where they were cultured in mTeSR medium until reaching 85-90% confluence. The differentiation process began on day 0, with a medium switch to RPMI (Gibco, 11875093)/B27-insulin (Gibco, A1895601) (RB-) supplemented with 6µM CHIR99021 (TOCRIS, 4423) for a 48-hour incubation period. Subsequently, the medium was changed to RB- on day 2. On day 3, 2.5µM Wnt-C59 (TOCRIS, 5148) was introduced in RB- for another 48 hours. Starting from day 5, cells were nourished with RB- and the medium was refreshed every two days. The purification phase involved changing the medium to RPMI-glucose (Gibco, 11879020)/B27 (Gibco, 17504044) supplemented with 5mM sodium L-lactate (Sigma, 71718) from day 11 to day 14, aiming to eliminate the glucose nutrient supplement. Following purification, hiPSC-CMs were maintained in RPMI/B27 medium (RB+) from day 15 onwards.

For experiments, cells were dissociated using TrypLE enzyme (Gibco, 12604013) and re-seeded on FluoroDishes or coverslips around Day 20. Additionally, a maturation medium (DMEM low glucose (Sigma, D5546) plus 4% oleic acid-BSA (Sigma, O3008), 10µg/ml

insulin (Sigma, I9278), 2mM glutamine, 10% horse serum) could be applied before experiments to enhance myocyte maturation (Fig. 2.2).

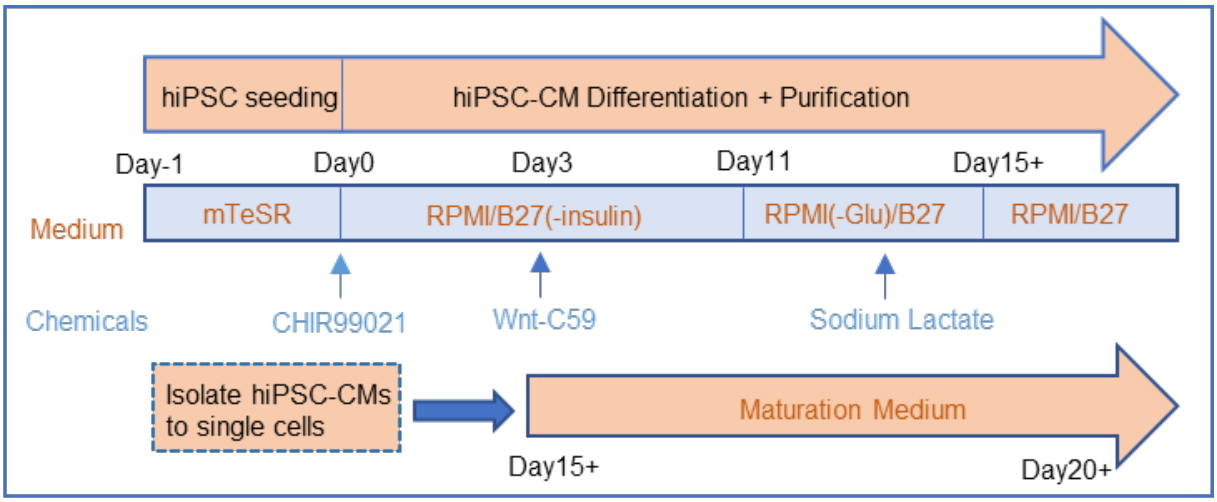


Figure 2.2 Schematic summary of cardiac myocytes induction protocol.

2.3.2.2 hiPSC-SN differentiation

Sympathetic neurons were differentiated from hiPSC according to the protocol proposed by Winbo et al 2020[119]. Briefly, after three passages, hiPSC were seeded on a Matrigel-coated 12-well plate and cultured in mTeSR until 80% confluent. Then a series of chemical compounds were added sequentially (500nM LDN193189 (Sigma, SML0559) day 0-3, 10µM SB431542 (Sigma, S4317) day 0-4, 3µM CHIR99021+10µM DAPT (Sigma, D5942) +0.2µM PD173074 (Sigma, P2499) day 2-7, 60ng/ml Shh C25II (Gibco, PMC8034)+1µM PMP (Sigma, SML0868) day 3- 12, 10ng/ml BMP4 (R&D Systems, 314-BP-010) day 10-14) to culture medium to modified pathways involved in the induction of neuromesodermal progenitors and neural crest cells. Culture medium mTeSR was gradually replaced by N2 medium (Neurobasal plus medium (Gibco, A3582901) supplemented with 2 mM L-glutamine, B-27 Plus (Gibco, A3582801), N2 supplements (Gibco, 11520536), 0.2 mM ascorbic acid (Sigma, A8960), 0.2nM dbcAMP (Sigma, D0260), 10ng/mL NGF (Bio-Techne, 256-GF-100), 10ng/mL BDNF

(R&D Systems, 248-BDB-010), 10ng/ml GDNF (R&D Systems, 212-GD-010)) to promote sympathetic neuron development from day 4 (day 4-5: 75% mTeSR+25% N2 medium; day 6-7: 50% mTeSR+50% N2 medium; day 8-9: 25% mTeSR+75% N2 medium; day 11-12: N2 medium). On day 12, differentiated cells were detached with Accutase (Gibco, A1110501) and re-seeded on a 24-well plate with a seeding density of $1x10^6$ cells/well and cultured in the neuronal medium for 40 days for maturation, after which characterization and co-culture with iPSC-CM can be carried out (Fig 2.3).

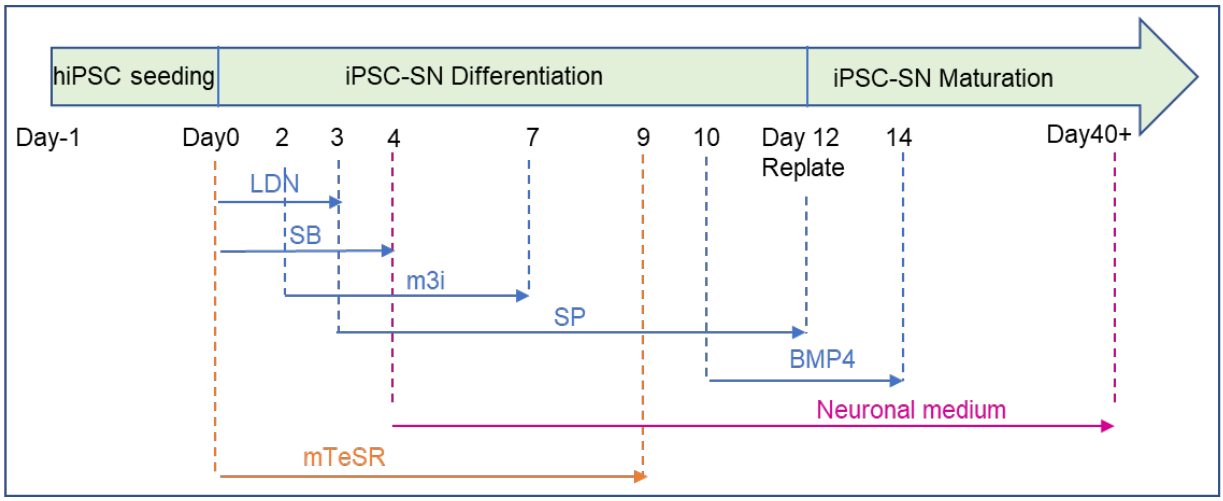


Figure 2.3 Schematic summary of sympathetic neuron induction protocol.

2.3.2.3 Neurocardiac co-culture

Contracting hiPSC-CM over day 20 and hiPSC-SN over day 40 with abundant axon extension were digested on the same day and reseeded together in a Matrigel-coated culture plate for neurocardiac co-culture establishment. TryplE Enzyme was used for hiPSC-CM dissociation by incubating for 7-10 minutes in a 37°C CO_2 incubator. hiPSC-SN were dissociated by 20-40 minutes incubation in 1mg/ml collagenase A (Roche, 10103586001) in Hank's balance salt solution. Detached cells were centrifuged and resuspended in a 1:1 RB+ plus N2 medium, and the seeding density of myocytes to neurons was 1:1. Medium was changed every other day.

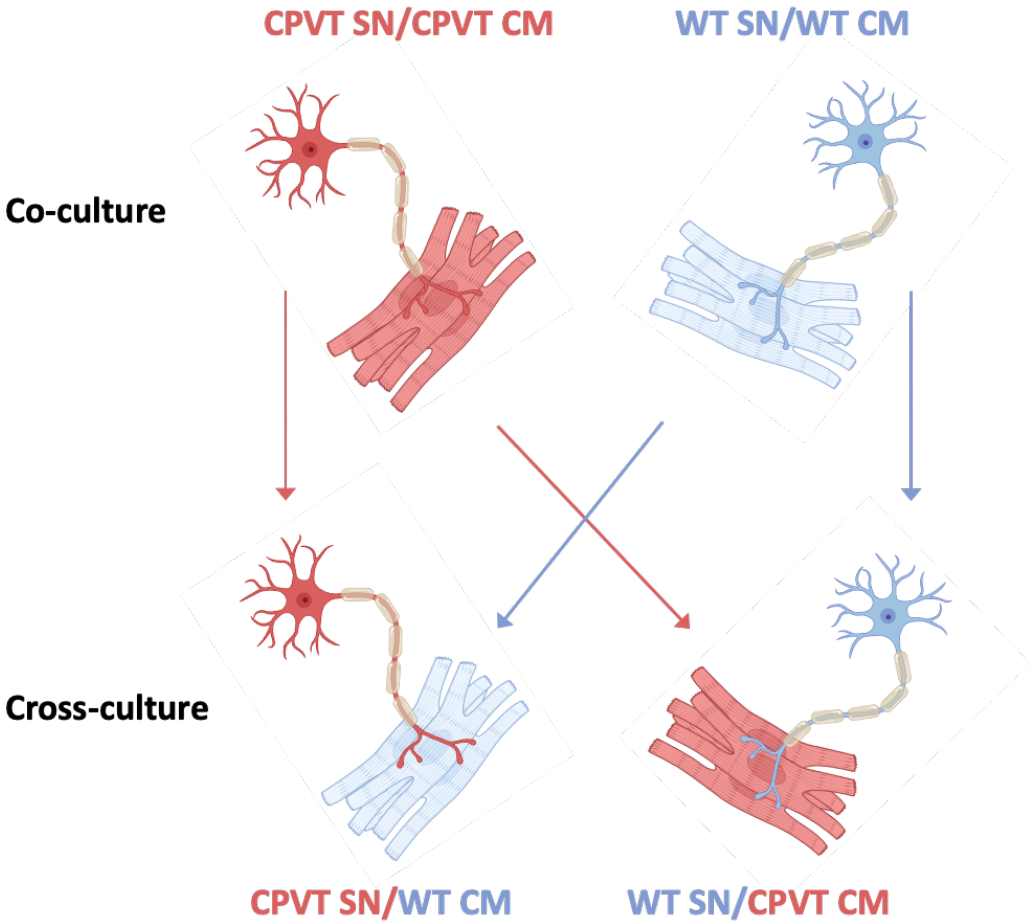


Figure 2.4 Schematic cross-culture establishment. Wild-type (WT) sympathetic neurons were plated on Catecholaminergic Polymorphic Ventricular Tachycardia (CPVT) cardiac myocytes, and CPVT sympathetic neurons were plated on WT cardiac myocytes. The dissociation, replating conditions, and methods were consistent with those used in co-culture. These cultures underwent exposure to the same experimental protocols after at least one week of culture to allow for the establishment of synaptic connections.

2.4 Cell plating for experiments

hiPSC-derived cardiac myocytes, sympathetic neurons, and isolated neonatal rat ventricular myocytes were seeded on 6mm coverslips for Fluorescence Resonance Energy Transfer (FRET) and calcium imaging, on FluoroDish for immunofluorescence, and on microelectrode arrays

for electrical mapping. The specific cell seeding density for each device is detailed in Figure 2.5. The optimization of cell seeding density was performed based on different cell lines and induction batches.

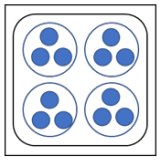
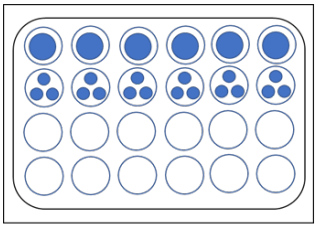
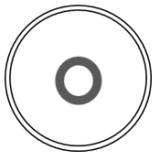
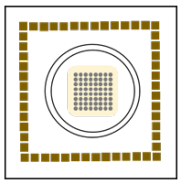
Plating surface	Cell density	Experiment
 6mm coverslip in 4-well plate	250,000 cells per well	FRET or Calcium imaging
 6mm/12mm coverslip in 24-well plate	1,000,000 cells per well	FRET or Calcium imaging
 FluoroDish with 15mm metal ring	50,000 cells in metal ring	Immunofluorescence or FRET
 MEA	500,000 cells on electrode	Electrical mapping

Figure 2.5 Plating conditions of experiments. Cell densities reported are for cardiac myocytes and sympathetic neurons monoculture. In neurocardiac coculture, myocytes and neurons were plated at a 1:1 ratio to reach the total density as listed.

2.5 Immunofluorescence staining

Immunofluorescence (IF) is an immunochemical technique utilizing fluorophore-labeled antibodies to detect and localize various antigens in diverse tissue and cell preparations. IF methods are classified into direct (primary) and indirect (secondary) based on the antibodies employed (Fig. 2.6). In direct IF, the primary antibody directly conjugates to a fluorophore, targeting the epitope. In the indirect method, an unstained primary antibody against the target antigen is detected by a fluorophore-conjugated secondary anti-immunoglobulin antibody. Although more time-consuming, the indirect method is more common and effective. This is because the secondary antibody can be modified to amplify signals, for example, through the use of polyclonal antibodies and biotinylated antibodies (Fig. 2.7). Polyclonal antibodies can recognize multiple epitopes on the primary antibody, while biotinylated antibodies can bind to multiple fluorophores. To prevent the second antibody from cross-reacting with endogenous immunoglobulin in the sample, the primary antibody must be derived from a different species.

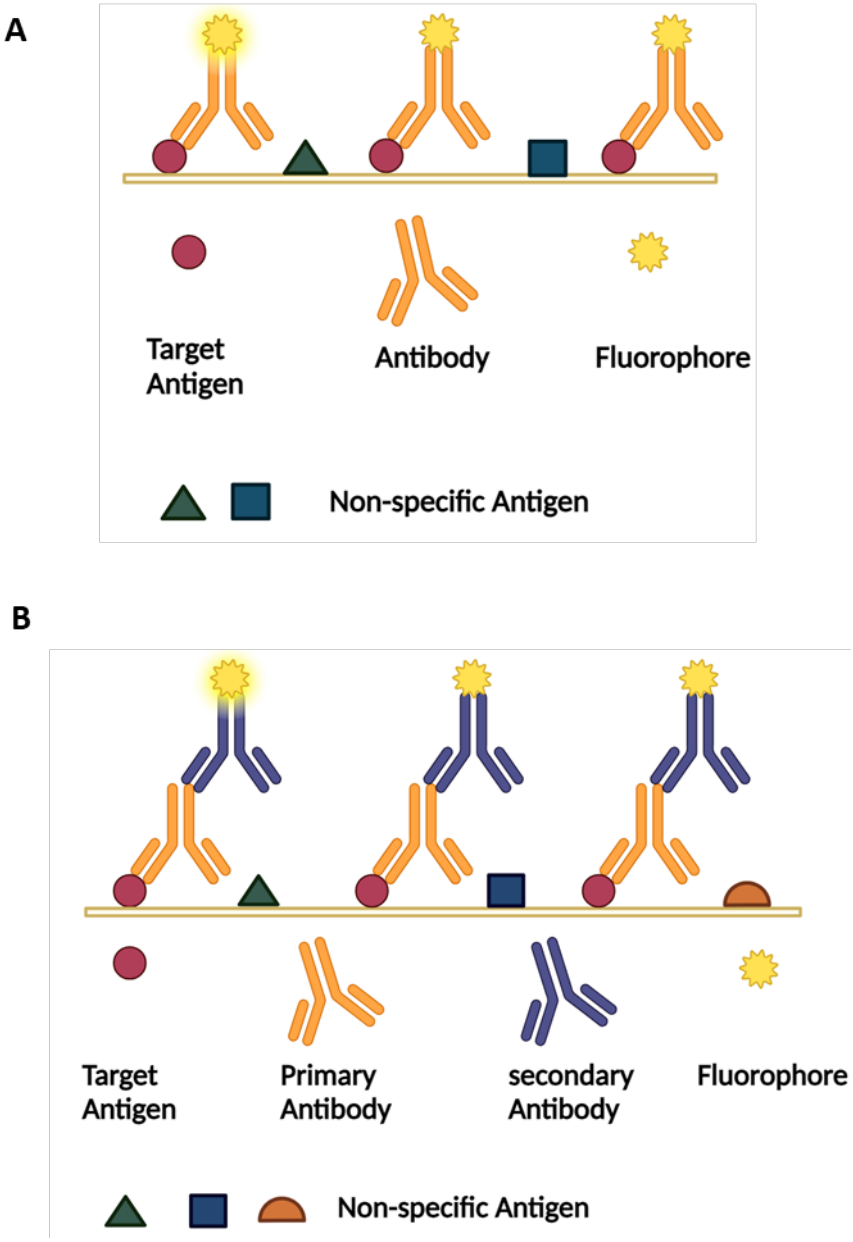


Figure 2.6 Illustration of two methods of immunofluorescence. A. In direct immunofluorescence, an antibody binding to the target antigen is conjugated to a fluorophore. **B.** In indirect immunofluorescence, a primary antibody is designed to detect the target antigen, which is recognized by a secondary antibody with a fluorophore.

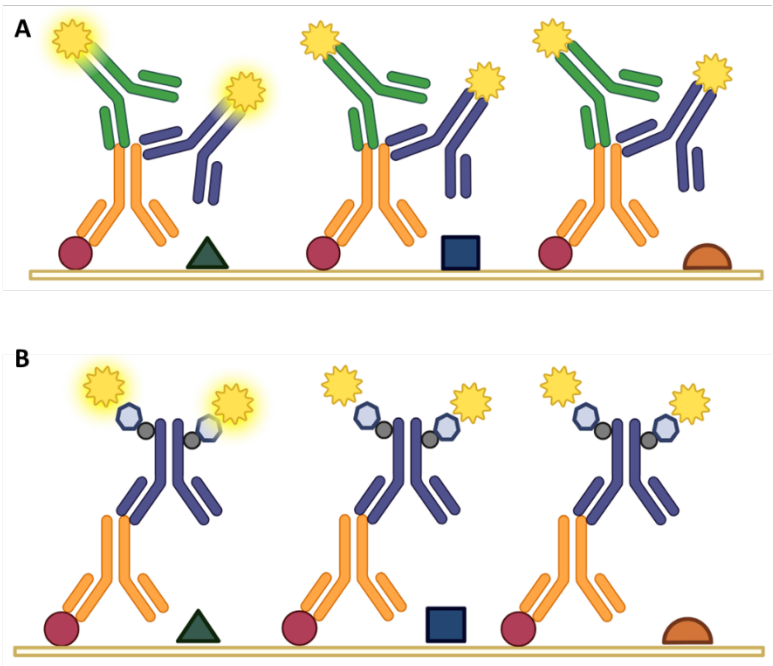


Figure 2.7 Amplification of fluorescence signal in indirect IF. A. Polyclonal secondary antibody amplification. Polyclonal secondary antibodies recognize and bind to different epitopes of the primary antibody, which results in multiple bindings on the primary antibody and amplifies the fluorescent signal as each secondary antibody carries a fluorophore. **B. Biotinylated secondary antibody amplification.** By attaching biotin to a secondary antibody, biotinylation enables the secondary antibody to be tagged with multiple fluorophores through the biotin-streptavidin complex.

In preparation for IF staining, the essential primary step is fixation which preserves morphology and prevents autolysis. The selection of the fixation method is dependent on antigen and cell types aiming to immobilize antigen without disrupting biological architecture and allow antibody permeabilize into staining cells. Formaldehyde is a commonly used chemical fixative which fixes cells by forming intra and intermolecular methylene cross-links[129]. Detergent treatment is required after chemical fixation to permeabilize the cell membrane to allow antibodies to enter. Finally, serum or bovine serum albumin (BSA) is used for blocking the non-specific binding of primary antibodies which cause false-positive results. The serum contains antibodies that bind to non-specific sites in the sample preventing primary

antibodies from reacting with these nontargets. To reduce cross-reactivity between secondary antibody and blocking serum, using matching species is recommended.

2.5.1 Sample preparation

Immunofluorescence was employed to evaluate the anatomical structure of hiPSC-induced cardiac myocytes and sympathetic neurons, validating the expression of tissue-specific proteins and their subcellular location. Cells designated for staining were dissociated using specific enzymes and seeded on FluoroDish at a desirable density for subsequent confocal imaging. Two to five days post-seeding, the cells underwent fixation with 4% formaldehyde at room temperature for 20 minutes, followed by three washes with Tris Buffered Saline (TBS) each lasting five minutes. Subsequently, the cells were permeabilized and blocked in TBS supplemented with 0.5% Triton and 6% donkey serum at room temperature for one hour.

2.5.2 Staining

After permeabilization, cells were incubated with primary antibody (see Table 2) diluted in TBS plus 0.1% triton and 6% donkey serum (blocking buffer) overnight at 4℃. The dish was washed with TBS three times each for five minutes before incubation with secondary antibodies conjugated to Alexa Fluor diluted in blocking buffer at room temperature for two hours in the dark. Cell nuclei were stained by Hoechst (Invitrogen, H3570) at 1:10,000 dilution in TBS for 10 minutes. Finally, the dish was washed three times for five minutes again and embedded in Fluoromount aqueous mounting medium (sigma, F4680) to prevent bleaching. Images were taken by Leica confocal microscope (Leica TCS SP5) and analysed with LAS X software.

Table2 Overview of the immunofluorescent antibodies employed in this thesis			
Antibody	**Catalogue#**	**Dilution**	**Description**
Mouse Anti-α-Actinin	Sigma A7811	1:800	Myocyte specific marker
Rabbit anti-cardiac troponin T	ab45932	1.5µg/ml	Cardiac myocyte specific marker
Mouse anti-cardiac troponin T	ab8295	1µg/ml	Cardiac myocyte specific marker
Mouse anti-tyrosine hydroxylase	Sigma T2928	1:800	Sympathetic neuron marker
Rabbit anti-tyrosine hydroxylase	25859-1-AP	1:200	Sympathetic neuron marker
Rabbit anti-peripherin	ab1530	1:200	Intermediate filament in neurons of the peripheral nervous system
Rabbit anti-synapsin I	ab254349	1:500	Protein regulating neurotransmitter release at synapses
Rabbit anti-PHOX2B	ab183741	1:100	Transcription factor involved in the development of noradrenergic neuron
Alpha-Bungarotoxin Conjugates	B35450	2µg/ml	Bind with nicotinic acetylcholine receptor of neuromuscular junction
Mouse anti-SERCA2 ATPase	MA3919	1:100	Calcium pump located in the sarcoplasmic or endoplasmic reticula
Alexa 488 (anti-mouse or -rabbit)	Invitrogen	1:1000	Secondary fluorescent antibody
Alexa 594 (anti-mouse or -rabbit)	Invitrogen	1:800	Secondary fluorescent antibody
Hoechst 33342	H3570	1:10000	Nucleic acid stain

2.6 Flow cytometry

Flow cytometry is a high-throughput technique designed to measure and detect the physical and chemical properties of cells or particles. In this method, a sample containing a suspension of cells or particles pre-coated with antibodies for specific cell identification flows through the cytometry machine, surrounded by a fast-moving sheath fluid. This sheath fluid channels the cell suspension into a single-file stream due to the higher pressure of the sample flow compared to the sheath fluid, allowing individual cells to be detected by a laser beam.

As the laser strikes each cell, it is deflected around the cell's edges, a phenomenon referred to as light scattering. The scattering of light by each cell is recorded in the forward direction

(forward scatter, FSC) and side direction (side scatter, SSC). FSC is proportional to the cell-surface area or size, while SSC is proportional to the cell's internal complexity and granularity. A combined measurement of FSC and SSC can effectively differentiate cell types within a heterogeneous population.

To determine specific cell marker expression, the immunofluorescence emission wavelength of individual cells, after excitation by various lasers, can also be measured using specific antibodies or dyes (Fig. 2.8). This multifaceted approach provides detailed insights into the characteristics of cells in a given sample.

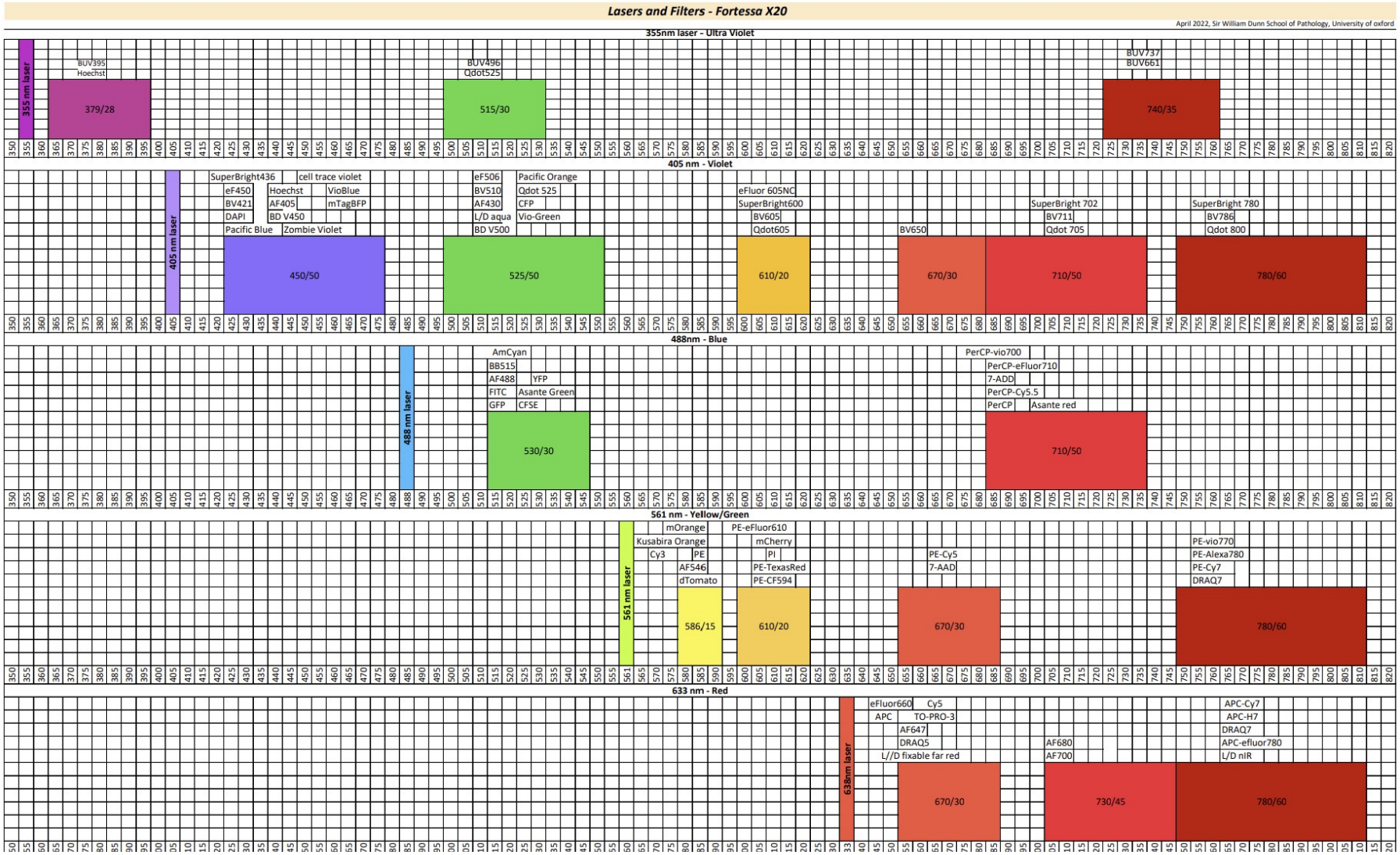


Figure 2.8 Laser and filter of the BD Fortessa X20 flow cytometer. Image credit to Michal Maj, Flow Cytometry Facility, Sir William Dunn School of Pathology, University of Oxford.

2.6.1 Gating

The desired parameters of each cell flowing across the laser beam are recorded as an 'event'. A Photomultiplier tube (PMT) transforms the recorded scattered or emitted photons into a proportional voltage pulse. By analysing FSC, SSC, and fluorescence emission voltage, distinct cell populations can be identified within the heterogeneous mixture. Gating, the process of setting an appropriate threshold between positive and negative voltage, is crucial for population identification.

2.6.1.1 Doublet discrimination

Occasionally, there may be instances where two or more cells passing the laser beam overlap, resulting in a combined voltage peak (Fig. 2.9). To eliminate these joint events that produce inaccurate signals, an examination of the height (-H), width (-W), and area (-A) of Forward Scatter (FSC) or Side Scatter (SSC) should be conducted to discriminate doublets. The height represents the cell's maximal signal, determined by the PMT voltage setting; width signifies the time duration of the signal, correlating with cell size; and area is calculated from height and width for each event as the area under the curve[130].

As depicted in Figure 2.9, theoretically, a doublet formed by the same cell type exhibits increased width and area while maintaining an unchanged height. In singlets, FSC-H is correlated with FSC-A and appears along the diagonal region in the plot (Fig. 2.10). When cells clump together, they exhibit increased area or width relative to height, allowing for effective gating to exclude such events.

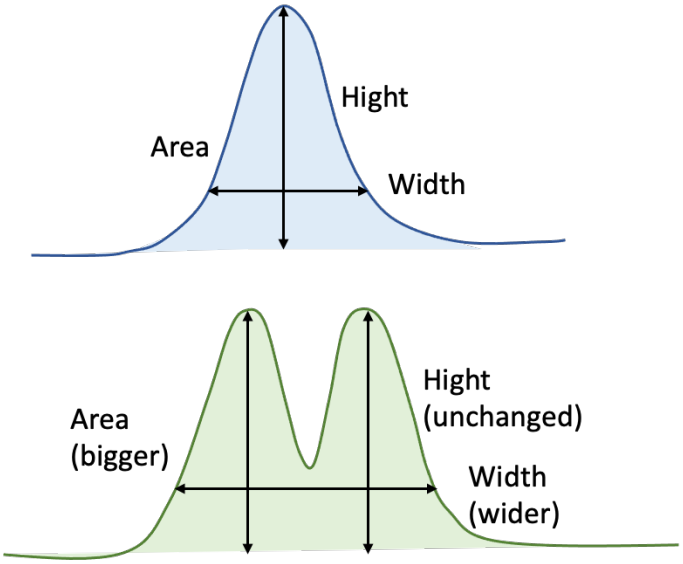


Figure 2.9 The alteration in voltage pulses in a doublet. The voltage pulse of each event comprises three components: pulse height, width, and the integral of height and width, known as area. Pulse height reflects the intensity of fluorescence emitted by the particle, and it remains unchanged when the PMT voltage setting is constant. Pulse width represents the duration of particles passing through the light beam. In the case of a doublet with a larger size, the time of flow increases, resulting in a recorded voltage pulse with a wider width and a larger area.

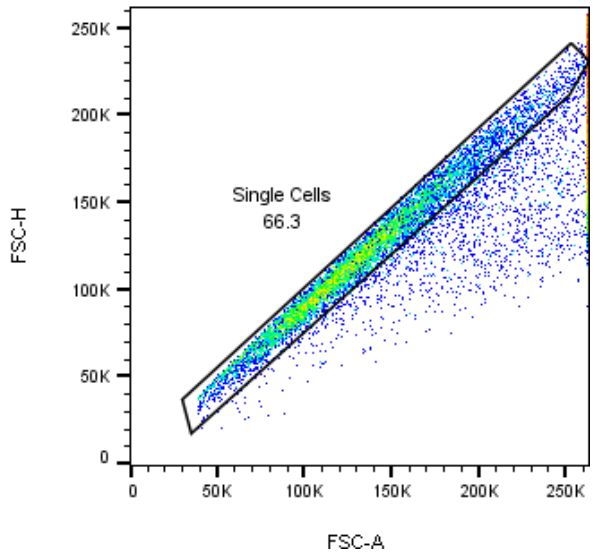


Figure 2.10 Example of single-cell gating. Single cells are selected by plotting the events in the FSC-H versus FSC-A graph and gating the cells around the y=x region. Doublets have increased area at the same height, and thus fall below the diagonal region.

2.6.1.2 Antibody emission

The dispersion of events in a plot can either be continuous or discrete, depending on the composition of cell populations and marker expression. To reduce subjective interpretation when setting the threshold, especially in continuous cases, it's beneficial to create positive and negative control groups based on the antibodies used to aid in calibrating gates for samples. In all scenarios, unstained samples can be used to define negative populations. Furthermore, dead cell samples obtained through microwave treatment, both unstained and stained with LIVE/DEAD, can be employed to refine gating for live-dead staining.

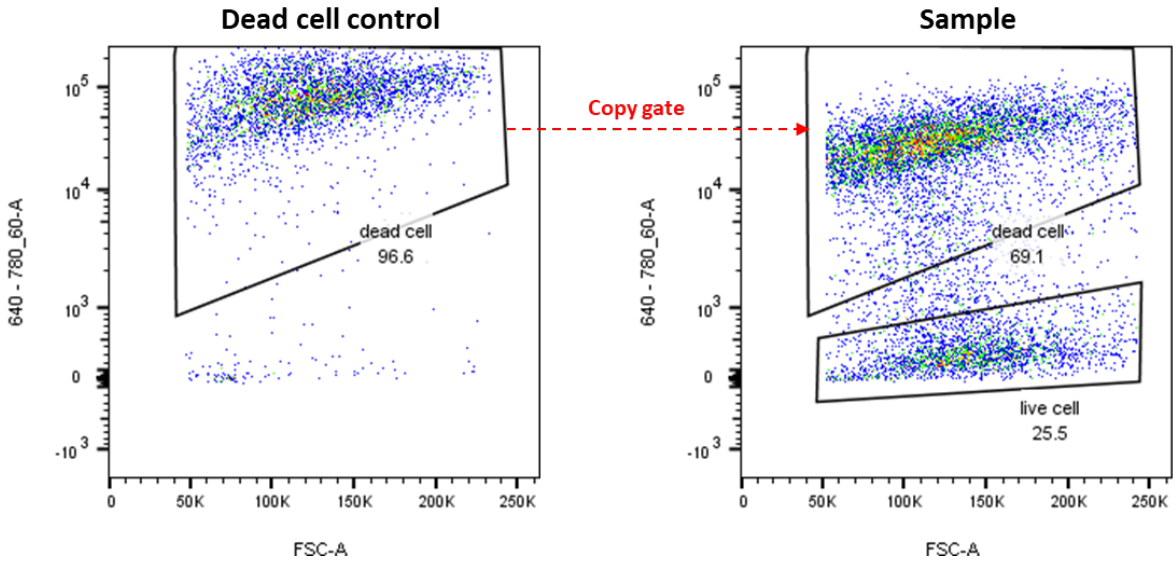


Figure 2.11 Dead cell samples were used as a positive control for live-dead staining. While collecting cell samples for flow cytometry, a portion of cell suspension from the collected sample is microwaved to induce cell death, then is prepared as all the other samples in fixation, blocking and staining. The majority of this dead cell control will display intense fluorescent staining for LIVE/DEAD stains, which enter the dead cells with compromised membranes and react with free amines both in the cell interior and on the cell surface. On the contrary, this dye only reacts with cell surface amine in viable cells. Gating for this dead cell population can be copied to other samples in the same run to help discriminate positive and negative stained populations. It is the same strategy for other fluorophore-conjugated flow antibodies when considering control.

2.6.2 Compensation

In multicolour experiments, despite using lasers at specific excitation wavelengths and filters defining a small range of emission wavelength, fluorophores typically exhibit broad excitation/emission spectra. As a result, specific fluorophores may be excited by different lasers used in the same sample, and the emission light could pass through other filters. This situation leads to readouts that are a combination of signals from multiple channels. To mitigate this issue, selecting antibody conjugates with less overlap in excitation/emission spectra, such as Phycoerythrin (PE, 561-586/15) and Allophycocyanin (APC, 640-670/30) used in this thesis, can help reduce spill-over.

Additionally, a process called 'compensation' is applicable to eliminate this influence. Most analytical software provides automatic compensation with computational algorithms if single-colour control parameters are provided. Compensation beads, which react with individual fluorochrome-conjugated antibodies, are commonly used in single-color compensation controls. By running the compensation beads labelled with only one fluorophore used in experiments through the flow cytometer under the same setting as the samples to be tested, spill-over to every recording channel can be detected. Importing the data into analytic software, such as FlowJo used in this thesis, enables automatic compensation.

2.6.3 Methodology

2.6.3.1 Sample preparation

Differentiated cells were collected in a single-cell suspension and centrifuged. Pellets were resuspended and incubated with Live/Dead stain (ThermoFisher, 65-0865-14). Subsequently, the cells were fixed with 4% formaldehyde, permeabilized, and blocked in a blocking buffer. This was followed by incubation with anti-cTnT (MACS 130-120-403) and anti-ventricular

myosin light chain-2 (MLC2v, MACS 130-119-581) antibodies for hiPSC-CM and anti-TH (Abcam, ab209921) for hiPSC-SN at the required concentrations (Table 2.2). Control groups, including dead cell samples, unstained samples, and compensation beads (Invitrogen 01-2222-42), were prepared.

The cells were then resuspended in FACS buffer (phosphate-buffered saline without calcium and magnesium, Corning, 21-040-CV, 2% fetal bovine serum, Gibco, 16140071, 0.02% NaN3, Sigma, 71289) before being run through the flow cytometer (BD Fortessa X20). Manual calibration was performed before running cell samples through the flow cytometer to detect positive populations. Initially, the unstained sample was used to adjust the FSC (forward scatter) and SSC (side scatter) detectors to position cell dots in a desirable area on the graph for gating. Following that, dead samples, both with and without live/dead stains, and compensation beads incubated with each primary antibody (single stain) were utilized as positive and negative controls to optimize PMT voltage, ensuring the separation of positive fluorescent signals from the background.

2.6.3.2 Data analysis

Results were analysed by FlowJo software. Sample data were plotted on the Graph window in FlowJo. The major cell population of interest was selected with a polygon gate. Forward scatter height (FSC-H) vs forward scatter area (FSC-A) density plot was then used to exclude doublets of this isolated population. The y-axis was then changed to the Live/Dead stain parameter which would turn the plot into two populations, a positively stained dead population with a high fluorescent signal and a negative live population. Polygon gate was used again to isolate the live population. In sympathetic neuron samples, a single parameter histogram was used to identify PE positive (excitation: 640nm, emission: 670nm) population that expresses the sympathetic neuron marker TH. As for double-stained cardiac myocytes, the x-axis and y-axis

were changed to display APC-cTnT and PE-MLC2v respectively to identify the double-positive population.

Table3 Overview of the flow cytometry antibodies employed in this thesis			
Antibody	**Catalogue#**	**Dilution**	**Description**
Anti-cardiac troponin T, APC	MACS 130-120-403	1:50	Cardiac myocyte specific marker
Anti-MLC2v, PE	MACS 130-119-581	1:10	Cardiac myocyte specific marker
Anti-tyrosine hydroxylase, PE	Abcam ab209921	1:2500	Sympathetic neuronal marker

2.7 RT-qPCR

Polymerase chain reaction (PCR) is a Nobel Prize-winning technique developed by Kary Mullis in the 1980s which led to the revolution in molecular biology. PCR relies on the heat-resistant DNA polymerase that can withstand heating and cooling cycles as the denaturation, annealing and extension steps in DNA amplification. Later, by introducing fluorescent probes into the PCR procedure, the amplification of DNA in real-time can be measured, enabling quantitative analysis of the DNA sequence of interest, which was termed real-time PCR or quantitative PCR (qPCR)[131]. In addition, combination of qPCR with reverse transcription, which transcribes RNA into complementary DNA (cDNA), RT-qPCR became a useful tool to detect and quantify RNA. To quantify mRNA expression, the RNA sample is first extracted from cells and then reverse-transcribed into cDNA, which can be quantified with PCR. Primer designed for the target gene is used for the PCR, equipped with a fluorescent probe, which increases in intensity with every replication cycle. The number of cycles taken for the fluorescence intensity to cross a determined threshold is recorded as a Ct value, which gives an index of relative gene expression (Fig. 2.12). Absolute quantification requires a serially diluted standard with known concentration to generate an amplification curve, from which the

Ct values can be used to plot against their log concentrations to produce a standard curve. For relative quantification, it is important to choose a ubiquitously expressed gene as endogenous control that has consistent concentration remaining unchanged under different conditions or across cell lines. Often, genes such as *GAPDH* and *β-actin* are used[132]. Delta Ct method relatively quantifies RNA expression by comparing the Ct value of the target gene to the endogenous control, thus removing the difference in the overall cDNA amount loaded.

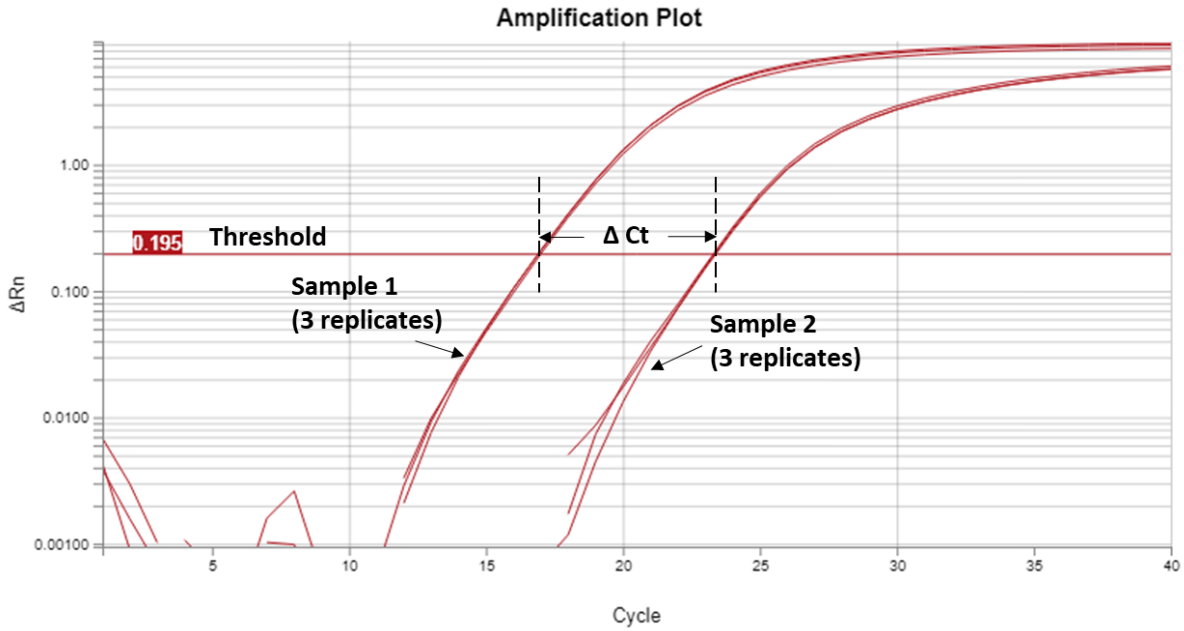


Figure 2.12 Sample amplification plot generated by QuantStudio. The normalized reporter signal (Rn) is determined by dividing the fluorescence intensity of the reporter dye by the fluorescence emission intensity of the passive reference dye, an integral part of the qPCR master mix. Delta Rn is Rn minus baseline fluorescence intensity during the initial cycles (usually 3-15) of PCR. In the Amplification Plot, log(ΔRn) is plotted against the PCR cycle number. The threshold is set by built-in algorithms according to the average standard deviation of Rn during the early PCR cycles. In this plot, each of the two alleles amplified has three replicates that cross the threshold at a close point which reflects the similar amount of expression in the replicates. The average cycle number of sample 1 is 17 and for sample 2 is 23, thus sample 2 expression is lower and require more cycle to reach the threshold.

2.7.1 Methodology

Total RNA was isolated from harvested cell samples using the RNeasy Mini Kit (Qiagen, 74104) following the manufacturer's guidelines. Subsequently, reverse transcription of the extracted RNA was executed using the iScript cDNA Synthesis Kit (Bio-Rad, 1708891). The ensuing real-time quantitative PCR (RT-qPCR) was carried out with a 20µl reaction mixture comprising 2µl cDNA, 7µl RNase-free water, 1µl TaqMan Gene Expression Assay (20X), and 10µl TaqMan Universal PCR Master Mix (Applied Biosystems, 4304437). All employed primers are detailed in Table 4.

Table4 List of TaqMan Gene Expression Assay (20x) used for qRT-PCR

Gene name	Assay ID	Forward primer sequence	Amplicon length
Natriuretic peptide B	Hs00173590_m1	tgctgaggcggcattaagag	82
Natriuretic peptide A	Hs00383230_g1	agaatttgctggaccatttg	105
Myosin heavy chain 6	Hs01101425_m1	tgccctgctggtaatccagt	67
Myosin heavy chain 7	Hs01110632_m1	agggcttgaatgaggagtag	73
Myosin light chain 2	Hs00166405_m1	ttgaccagatgttcgccgcc	98

Amplification took place in the QuantStudio 5, employing the following thermal cycling parameters: an initial 10-minute denaturation at 95°C, followed by 40 cycles of 15 seconds at 95°C and 1 minute at 60°C. Amplification curves were automatically generated by the QuantStudio Design and Analysis software of the real-time PCR system. The comparative ΔCt method was applied for the relative quantification of target gene expression, with GAPDH serving as the endogenous control in all experiments presented in this thesis.

The comparative ΔCt method employed the following equation:

$$\text{Relative gene expression} = 2^{-\Delta Ct}$$

$$\Delta Ct = Ct_{\text{sample}} - Ct_{\text{GADPH}}$$

2.8 Enzyme-linked immunosorbent assay

The enzyme-linked immunosorbent assay (ELISA) is a quantitative analytical method used to measure antibody-antigen reactions by detecting colour changes[133]. It employs enzyme-linked conjugates and substrates to identify and quantify target molecules in biological fluids such as plasma, serum, and cell culture supernatant. In a microplate designed with precoated antibodies targeting specific molecules at the bottom, the formation of an antigen-antibody complex is revealed using enzyme-tagged antibodies.

Following a washing step to remove unbound antibodies and conjugates, an enzyme substrate is added to the medium. This substrate induces a colour change, and the resulting colour, measured as an optical density (O.D) value for absorbance, indicates enzyme activity. The commonly used enzyme is horseradish peroxidase (HRP), which reacts with the 3,3′,5,5′-Tetramethylbenzidine (TMB) substrate, transforming a colourless solution into a blue reaction product. HRP is often supplied as an HRP-streptavidin conjugate, leveraging the robust interaction between streptavidin and biotin. This interaction facilitates the delivery of enzymes to biotin-tagged antibodies recognizing the target molecules.

To halt the HRP-TMB reaction, a stop solution (sulfuric acid) is introduced, changing the colour to yellow and stabilizing it. This allows accurate absorbance measurement by inhibiting peroxidase activity. The colour intensity is directly proportional to the amount of HRP activity, which, in turn, correlates with the quantity of target antigens bound in the sample.

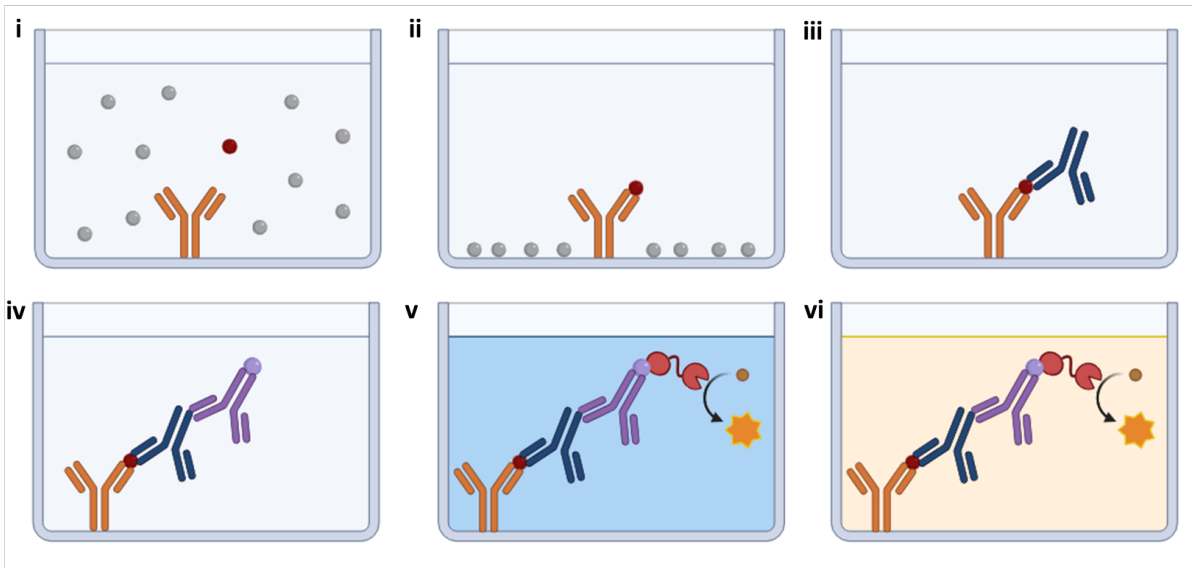


Figure 2.13 Schematic summary of sandwich ELISA steps. i. The sample is added to a precoated microplate; ii. Target antigen binds to specific antibody at the well bottom; iii. Detection antibody binds to antigen; iv. The biotin-labelled antibody binds to the detection antibody; v. HRP-streptavidin conjugate binds to biotin, reacts with TMB substrate and produces a blue colour product; vi. Stop solution terminate the HRP-TMB substrate reaction and change colour to yellow.

2.8.1 Methodology

ELISA kits were employed to quantitatively measure specific protein concentrations in cell culture medium in vitro, following the manufacturer's instructions. Culture media collected from pre-treated cell samples were utilized. Serially titrated standards and samples were added in duplicate to each well of the provided 96-well plate pre-coated with antibodies and incubated at room temperature. Subsequently, the entire plate underwent sequential incubation with biotin and streptavidin-HRP conjugate, with unbound reagents removed at each stage by washing buffer. To quantify HRP activity, TMB substrate was added to each well and incubated in the dark. After a reaction period of 15-30 minutes, a stop solution was introduced, and the optical density (O.D.) for absorbance at 450nm was measured using a microplate reader. A standard

curve was constructed by plotting the mean OD value for each standard on the Y-axis against concentration on the X-axis, as illustrated in Figure 2.14. The concentration of unknown samples was determined by fitting them into the standard curve.

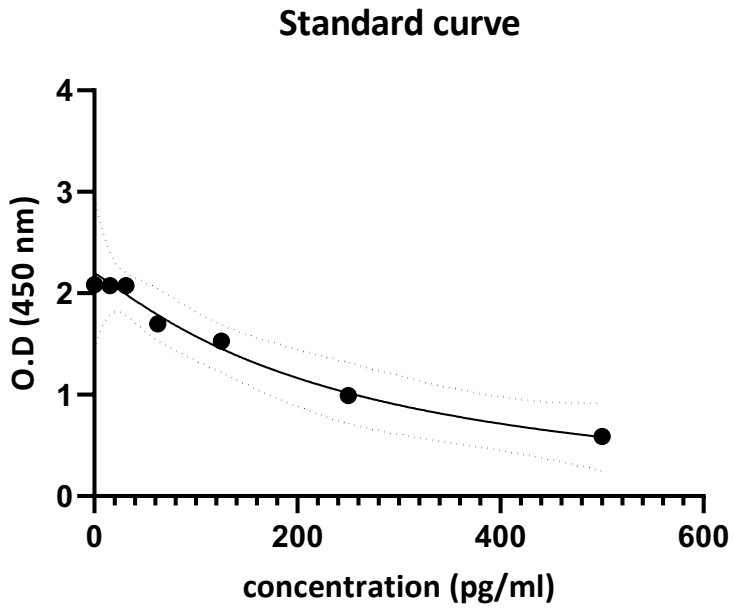


Figure 2.14 Example standard curve. The X-axis is the standard concentration in serial dilution, and the Y-axis is the O.D readout by the microplate reader. By plotting the O.D value of samples into a standard curve generated from the same plate, the target concentration in the sample fluid can be calculated.

2.9 Förster resonance energy transfer (FRET) imaging

The cytosolic cAMP levels, in response to stimulation, were assessed using the Förster resonance energy transfer (FRET) technique. In this approach, living cells were transfected with fluorescent biosensors, and the recorded fluorescence intensities served as a real-time indicator of cAMP levels.

Cyclic nucleotides, including cAMP and cGMP, function as crucial second messengers that mediate extracellular signals and play pivotal roles in numerous signalling pathways, making them a focal point for researchers. The development of fluorescent FRET sensors for cytosolic and subcellular domains, capable of quantitatively detecting changes in cyclic nucleotide levels, has become a powerful tool in studying these molecules.

FRET, or fluorescence resonance energy transfer, involves the energy transfer between donor-acceptor pairs, with fluorophores serving as both the donor and acceptor in the cAMP sensor utilized in this study. The fundamental principle of FRET relies on the overlap of the donor's emission spectra and the acceptor's absorption spectra. This energy transfer is highly dependent on distance, occurring only when the donor-acceptor pair is in close proximity (specifically, less than 10 nm), allowing the emission wavelength from the donor to activate the acceptor.

FRET sensors can target different molecules based on the reactive unit linking the donor and acceptor proteins. When the FRET sensor encounters the target analyte, the interaction induces a structural change in the probe, altering either the distance between the donor and acceptor or the excitation-emission spectra of the fluorophores. This alteration in the fluorescent state of the acceptor is reflected in a change in emission wavelength intensity, providing a measure of the number of target analytes present[134].

2.9.1 cAMP sensors

The cAMP-detecting FRET sensor was initially developed in the early 2000s and has undergone rapid optimization since, enabling more specific measurements in subcellular localization. These sensors utilize the reactive unit known as exchange protein directly activated by cAMP (EPAC), connecting a cyan (CFP) and yellow (YFP) fluorescent protein.

The molecular structure and operational mechanism of the cAMP FRET sensor employed in this study, EPAC-SH187, are depicted in Figure 16. In the absence of cAMP, the two fluorophores remain in close proximity, resulting in maximal fluorescent intensity emitted by YFP as the acceptor. As the environmental cAMP levels increase, the binding of cAMP to EPAC induces a conformational change that separates CFP and YFP, leading to an increase in the FRET ratio. The recorded change in the FRET signal reflects the relative and dynamic alterations in cAMP levels within the cells.

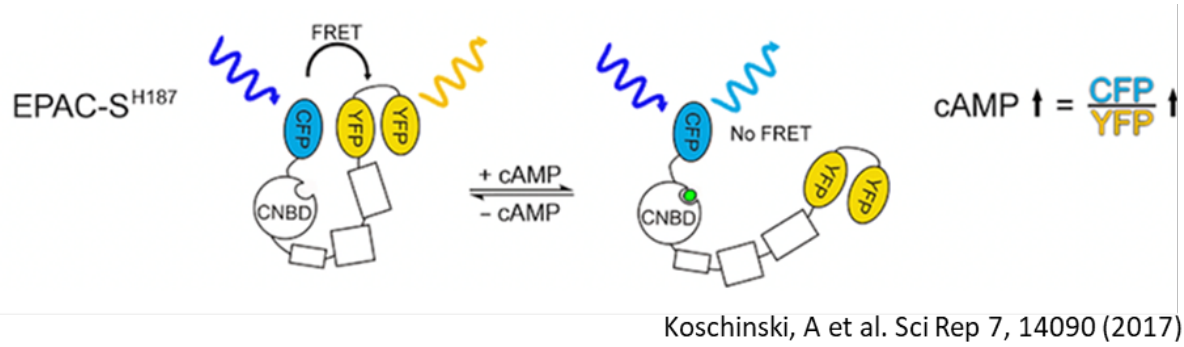


Figure 2.15 The molecular structure and functionality of the EPAC-SH187 sensor. This sensor comprises two fluorescent proteins with overlapping excitation and emission spectra. When the two fluorophores are in close proximity, the emission from a donor can excite the acceptor. The binding of cAMP to the EPAC-S^{H187} sensor induces a protein transformation that separates CFP and YFP. As YFP can no longer receive and be activated by the emission wavelength from CFP, the intensity of YFP decreases, while CFP increases. This change results in an increased FRET ratio. Adapted from Koschinski A, Zaccolo M. Sci Rep. 2017;7(1):14090.

2.9.2 Cell transfection

2.9.2.1 Adenovirus generation

The delivery of EPAC-S^{H187} FRET sensor into neonatal rat ventricular myocyte, hiPSC derived cardiac myocyte and sympathetic neuron were all achieved using adenovirus as the vector with

CMV promotor. The generation and amplification of viral particles are outsourced to Vector Biolabs, US.

2.9.2.2 Viral transfection of FRET sensor

Cells plated on coverslips were transfected with adenoviral vectors encoding the FRET cAMP sensor Epac-S^{H187} by overnight incubation at 37°C, 5% CO2 before FRET measurements. In 4-well plates with 250,000 cells per well, $6x10^6$ particle-forming units (PFUs) were added to neonatal rat myocytes, $8x10^6$ PFUs to iPSC-CM, and $6x10^7$ PFUs to iPSC-SN. Notably, in neurocardiac coculture, a lower-titre adenovirus was used, selectively transfecting cardiac myocytes as neurons exhibit relative resistance to transfection. The viral load for myocytes and co-culture was maintained at 10 times less than that for neurons, ensuring the FRET sensor expression solely in myocytes and preventing neuronal infection. This precaution guaranteed that the recorded FRET signal originated exclusively from pure myocytes. After a 24-hour incubation, cells were washed, and fresh media were applied. Typically, two to three days were required for transfected cells to express the sensors, and the progress of expression was monitored using an LED microscope from day two until bright yellow fluorescence was observed.

2.9.3 FRET measurement

2.9.3.1 Microscope setup

The transfected cells were activated by different chemical agents and images were captured by fluorescent microscope to record emission intensity change. The cells were either perfused or bathed in Tyrode solution to reach a steady state before chemical agents were applied to the cells by diluting them in Tyrode. During the process, images were taken using a Nikon Eclipse Ti2 inverted microscope with a 40x, oil immersion objective, connected to a Cairn Research

Ltd dual OptoLED light source, and a Prisme-BSI photometric camera. Cells were excited every 15 seconds for 100ms; the excitation wavelength was set at 430nm, and emission intensities were recorded at 480nm for CFP and 535nm for YFP, 480/535 nm ratio was automatically calculated over the recording by the MetaFluor software.

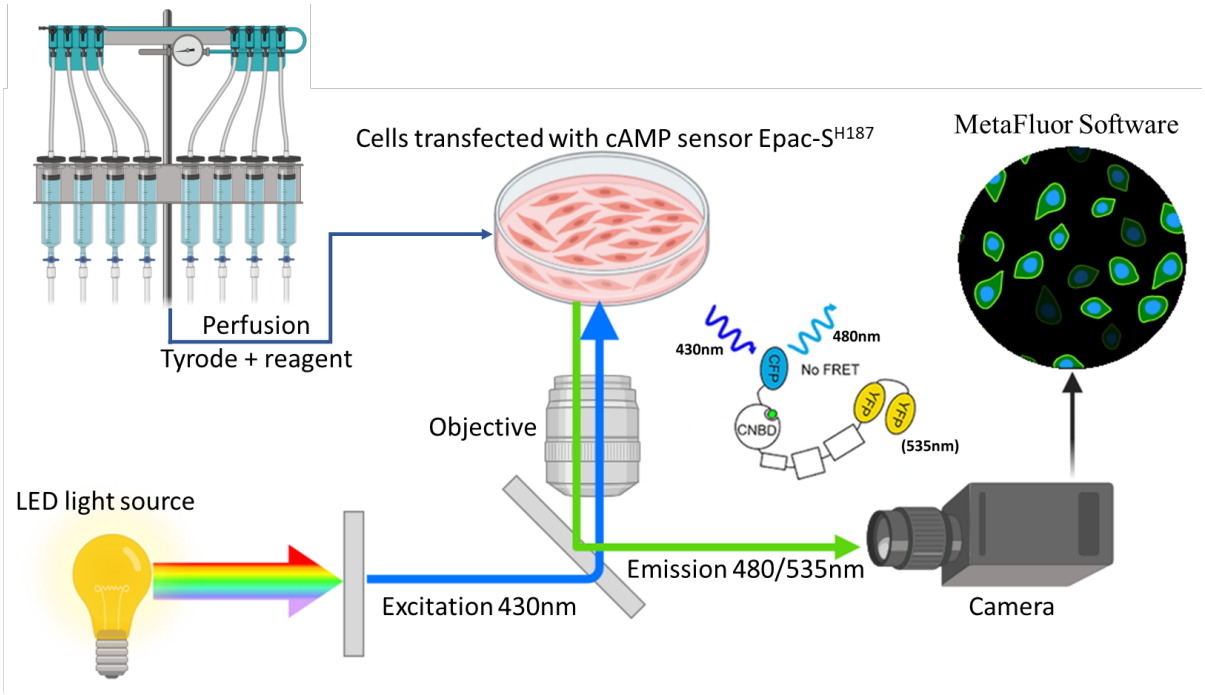


Figure 2.16 The setup of the FRET and calcium imaging system. A coverslip, bearing cells transfected with a FRET sensor or stained with Fura-2-AM, was positioned in the holding chamber integrated with the microscope. The chamber was equipped with a perfusion system enabling controlled exposure of cells to various chemicals. Excitation waves of specific wavelengths from the OptoLED imaging system irradiated the FRET sensor or Fura-2 in cells, and the emitted waves were captured by the photometric camera. Changes in intensities across different emission wavelengths during the experiment were recorded and monitored in the MetaFluor software.

2.9.3.2 FRET data analysis

Background fluorescence was subtracted from the recorded emission intensities, and the raw FRET ratio was calculated as recorded CFP emission intensities over YFP emission intensities for each capturing:

$$Raw\ Ratio = \frac{\text{CFP intensity} - \text{CFP background}}{\text{YFP intensity} - \text{YFP background}}$$

which increases as the cAMP level is elevated. For comparison, the raw ratio was normalized to the average ratio at baseline (R0) and calculated as the mean of four FRET ratios prior to the first drug treatment:

$$FRET\ Ratio = \frac{R}{R_0}$$

The FRET ratio was graphically represented as the response trace for each cell (Fig. 2.17). Peak values following drug stimulation were compared across groups. Cells that did not respond to the combination of IBMX (nonselective PDE inhibitor) and Forskolin (adenylyl cyclase activator)[135], which maximized the cAMP FRET sensor, were excluded from the analysis. These non-responsive cells were considered incompetent for the purposes of the study.

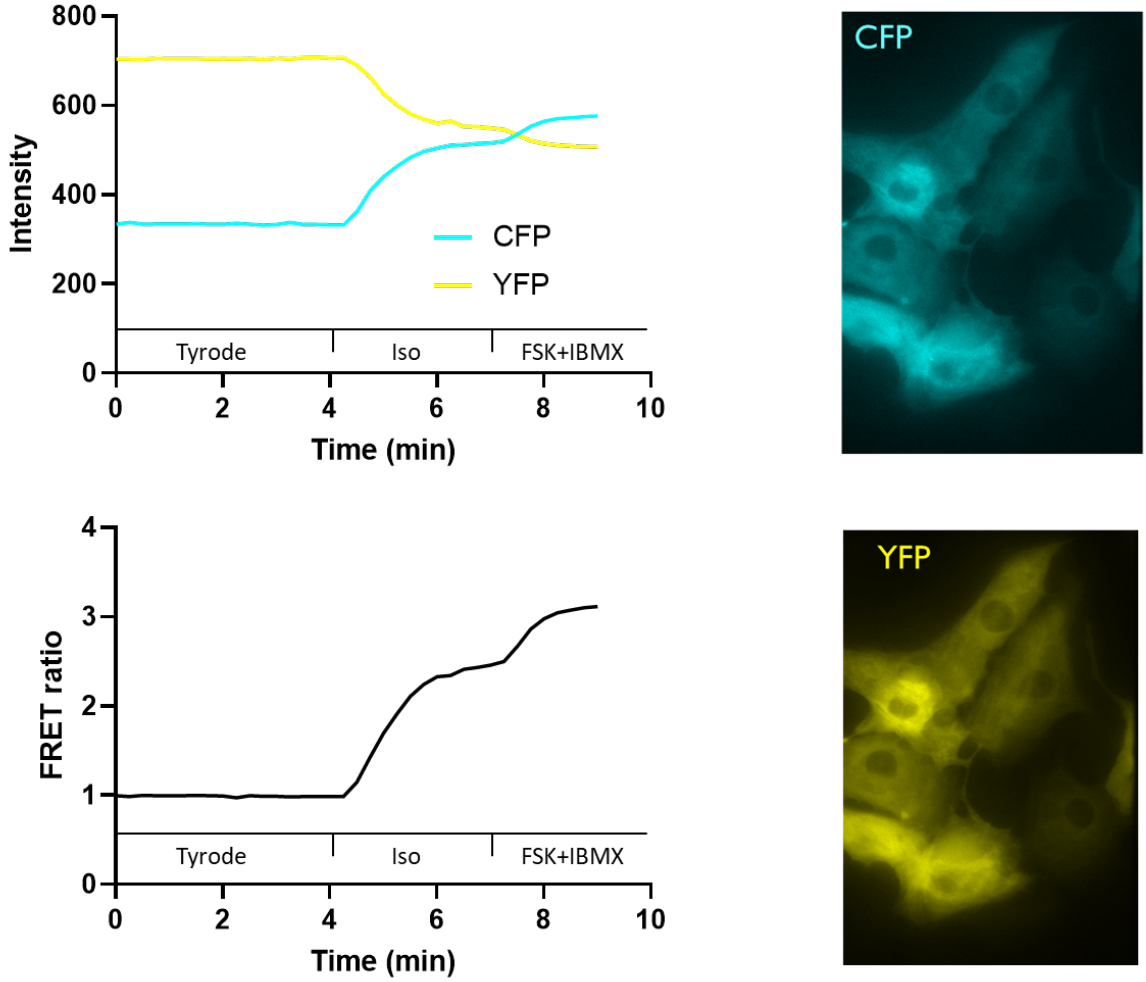


Figure 2.17 Raw trace of EPAC-S^{H187} sensor in iPSC-cardiac myocytes. CFP and YFP intensity and the CFP/YFP ratio reflect the alteration in cAMP level as the sensor shows conformational change. The example trace illustrates the cytosol cAMP level change of a cardiac myocyte derived from a healthy hiSPC line (CP1WT) in response to 10nM isoprenaline applied at four minutes, which increases cAMP through beta-1 receptor (Gs protein-coupled receptor). 25uM FSK (adenylyl cyclase activator) and 100uM IBMX (non-selective PDE inhibitor) are added at the end of the experiment to saturate the cAMP sensor.

2.9.3.3 Experimental protocols and reagents used

Specific protocols for FRET measurements in myocytes, neurons, and co-cultures are detailed in relevant chapters (physiological response in Chapter Three; hypertrophic model in Chapter

Four; CPVT model in Chapter Five). Generally, cells expressing the FRET sensor were perfused or bathed in Tyrode solution (refer to Table 5), and emission intensities were continuously monitored. Data capture commenced once the basal FRET ratio stabilized. A baseline was recorded for two minutes, after which pharmacological reagents diluted in Tyrode solution were applied as necessary for each experiment.

Table 5 Composition of Tyrode's solution used for calcium imaging

Tyrode solution composition	Concentration (mM)
NaCl	135
KCl	4.5
HEPES	20
Glucose	11
$CaCl_2$	2
$MgCl_2$	1

In cardiac myocyte monoculture, stimulation was achieved with isoprenaline, activating beta-adrenergic receptors and inducing cAMP generation. In sympathetic neuron monoculture, nicotine served as the stimulant. The nicotinic acetylcholine receptor (nAChR) expressed on the postganglionic neuron membrane acts as a nonselective cation channel[136], becoming permeable to small monovalent and divalent cations when exposed to agonists. This activation triggers membrane depolarization, playing a role in fast synaptic transmission. Neuronal depolarization, in turn, activates adenylyl cyclases and elevates intracellular calcium concentration ($[Ca^{2+}]_i$), both contributing to an increase in cAMP levels.

In neurocardiac coculture, nicotine was employed to stimulate neurons, leading to the release of noradrenaline into the synaptic cleft. The released noradrenaline then activated the β1 adrenergic receptor on cardiac myocytes, elevating cAMP levels in these cells. To confirm that the responsive elevation of cAMP in cardiac myocytes resulted from sympathetic drive from nicotinic-stimulated neurons, nicotine was used to stimulate cardiac myocyte monoculture as a negative control.

2.10 Calcium imaging

Fura-2-AM, among various fluorescent calcium indicators, is a plasma membrane-permeable molecule that binds to free intracellular calcium ions. Upon intercalation with Ca^{2+}, the excitation-emission spectra of the fluorescent dye are altered, as illustrated in Figure 2.18. Consequently, the ratio of emission wavelength intensity at 340nm to that at 380nm excitation wavelength provides an index of $[Ca^{2+}]$. This ratiometric dye effectively circumvents confounding factors beyond $[Ca^{2+}]$, such as dye concentration and viability, since changes affecting intensity similarly influence both dual wavelengths, maintaining a relatively constant ratio. However, it is worth noting that ratiometric dyes have lower temporal resolution due to the necessity of sequential excitation from two wavelengths. The precise $[Ca^{2+}]$ can be calculated using the following equation:

$$[Ca^{2+}] = \frac{R - R_{min}}{(R_{max} - R) \times Sf \times Kd}$$

where R is the 340/380 ratio at a certain time point, Rmin is the ratio at $[Ca^{2+}]$=0, calibrated with calcium chelator, and Rmax is the ratio when Fura-2 is saturated, calibrated using

ionomycin to expose cytosol to extracellular calcium at mM levels, S*f* is the scaling factor and K*d* is the dissociation constant of Fura-2[137].

It's important to note that in this thesis, relative changes between the average ratio at baseline and the peak ratio after stimulation were compared among different hiPSC lines. Therefore, there was no need for calibration to determine the exact [Ca^{2+}] measurement.

Fura-2 alone contains a charged carboxylate group that reduces the permeability of the cell membrane to the molecule. Thus, in order to allow Fura-2 to cross the membrane and enter the cytosol for intracellular [Ca^{2+}] recording, a charged acetoxymethyl ester derivative was introduced to Fura-2 to form a compound molecule, which is cleaved once inside the cell and effectively trap the dye within the membrane.

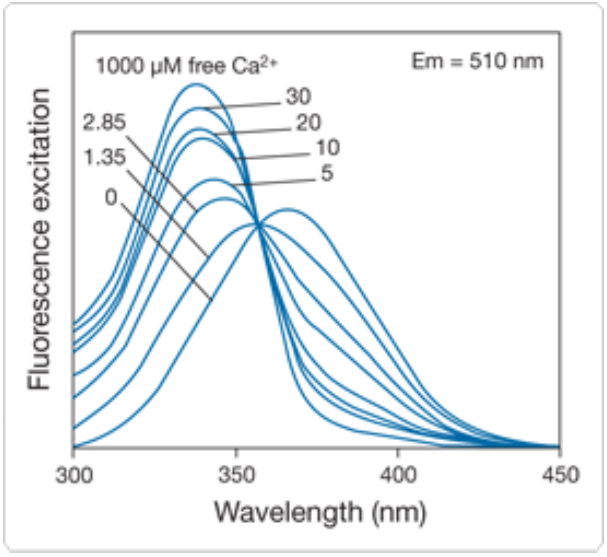


Figure 2.18 Fura2 fluorescence intensity reflecting calcium concentration. Illustration of Fura2 excitation-emission spectrum left-shifted with $[Ca^{2+}]_i$ elevation. (Image credits to ThermoFisher)

2.10.1 Methodology

Intracellular calcium concentration ($[Ca^{2+}]_i$) was assessed in hiPSC-induced cardiac myocytes and sympathetic neurons utilizing the Fura-2-AM live cell calcium indicator. For experiments involving a perfusion system to apply and wash off chemical reagents, cells were re-plated on Matrigel-coated glass coverslips suitable for mounting into the perfusion chamber. In experiments aimed at recording long-lasting or saturation effects where applied reagents did not need to be removed, cells were re-plated on FluoroDish, and reagents were applied by dripping into the bath media using a pipette. The cell plating method is detailed above. Before imaging, cardiac myocytes were loaded with 5 μM Fura-2-AM (Invitrogen, F1221) for 40 minutes at 37 ℃, while sympathetic neurons were loaded for 30 minutes. Subsequently, both cell types were washed with Tyrode solution (refer to Table 5) three times, with each wash lasting five minutes.

Coverslip was loaded on the holding chamber on a Nikon eclipse Ti2 inverted microscope, which connected to the tube from the perfusion system that supply Tyrode solution and dissolved chemicals to the cells. The solution was maintained at 37°C using a temperature controller; the flow rate was set at 2-3 ml per minute. The dish was directly placed on the microscope and drugs were added using a pipette. Images were captured at 340nm and 380nm excitation with a QICLICK digital CCD Photometrics camera connected to an OptoLED fluorescence imaging system housed on the microscope with a 40× oil immersion objective.

Cardiac myocytes were distinguished from fibroblasts on the coverslips based on specific characteristics such as thickness, size, and cell-cell connections. Cardiac myocytes exhibited a bulging and smaller morphology, tending to form connections and grow in clusters. In contrast, fibroblasts were characterized by a flat and larger appearance, dispersing between myocyte clusters. Neurons were identified by their round shape and dendrite outgrowth. Only those cells

that appeared healthy, showing no signs of blebbing or damage, were selected for imaging. This careful selection ensured that the imaged cells were in a suitable and undisturbed condition, allowing for accurate observations.

Images were captured every three seconds at 510 nm emission wavelength when cells were sequentially excited by 340 nm and 380 nm. Background intensity was subtracted from emission intensity for both excitation wavelengths for each image, then calcium concentration was calculated as 340/380 ratio and compared between groups either as peak ratio normalized to baseline ratio for each cell, or as fold change to the normalized baseline ratio for each cell:

$$\Delta[Ca^{2+}] = \frac{R_{peak} - R_0}{R_0}$$

where R_{peak} is the maximum ratio after stimulation, R_0 is baseline ratio calculated as the mean of five consecutive ratio directly prior to addition of the first reagent.

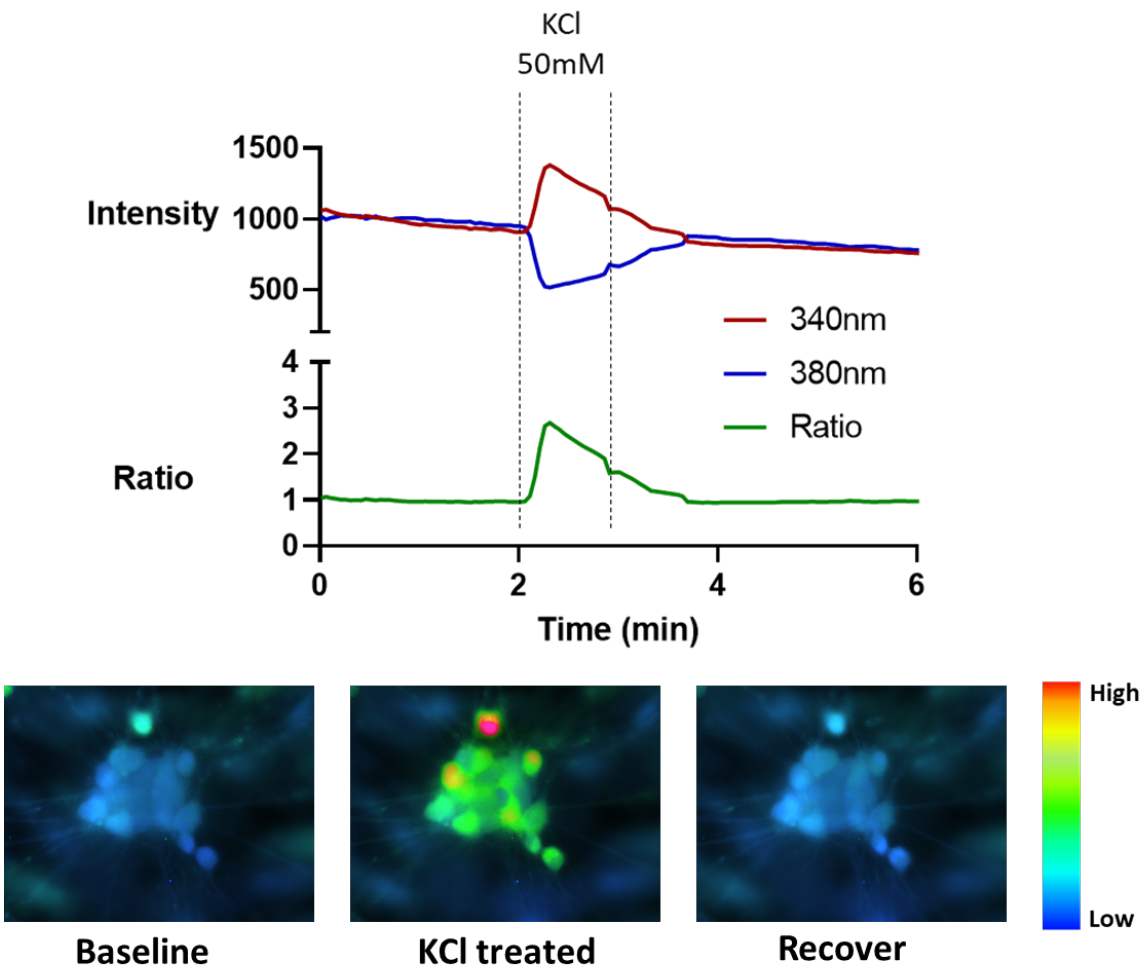


Figure 2.19 Exemplar iPSC derived sympathetic neuron Fura2 Ca^{2+} imaging trace. The emission intensities of Fura-2, excited at 340 nm and 380 nm, undergo changes when neurons are stimulated with 50 mM potassium chloride. The evoked transient increase in intracellular calcium concentration ([Ca2+]i) leads to the chelation of Fura-2, altering its excitation-emission spectra. This results in an increase in the intensity of 340 nm illuminated light and a reduction in the intensity of 380 nm illuminated light, consequently elevating the 340/380 ratio. It is important to note that gradual dye leakage and photo-bleaching may cause a decline in both 340 and 380 nm-induced emission intensities. However, as a ratiometric dye, this does not significantly impact the ratio that reflects the change in calcium ions. The 340/380 ratio images of the neurons, from which the recording was taken, exhibited a low value at baseline and wash-off, and an increased value when treated with KCl.

2.11 Electrical mapping

Microelectrode array (MEA), together with optical mapping, are electrophysiological mapping techniques that have been developed in the past few decades for the study of neurons and muscle cells that create and transduce ion currents through their membrane when excited. It was in 1972 that Thomas et al.[138] published the first paper on using a microelectrode array for the recording of the electrical properties of cultured cells. MEA makes an extracellular recording of electrical signals at multiple sites of a small area preparation of freshly sliced tissues or cultured cells. The preparation of the sample on the electrode can be maintained and recorded over the developmental process and therefore makes MEA a good technique to study the plasticity of electrical interactions among the cultured cells or tissues. Microelectrodes as the critical component for electrical signal collection, which used to be low in number and simple in arrangement for each array, have been developed to be more flexible in size, distance and shape to cover the preparation of tissues or cells that provide higher spatial and temporal resolution.

MEA mapping can be used to record spontaneous depolarization generated electrical signals, as well as stimulation-triggered action potential when connected to a stimulator that can exert an electrical stimulus on cells surrounding the selected electrode. The amplitude and shape of the recorded signal are dependent on the number of cells and the contact between cells and electrodes when sampling properties (e.g. sampling rate) and signal processing (e.g. system gain and bandwidth) are settled.

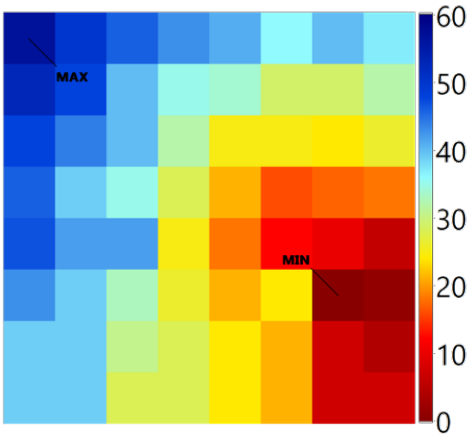
2.11.1 Methodology

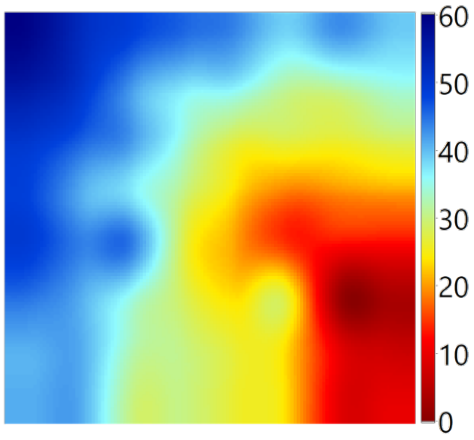
Microelectrode array (MappingLab EGMA064200700) was pre-coated sequentially with 0.1% polyethyleneimine and Matrigel. Mature hiPSC-CMs were digested by TryPLE with seven minutes of incubation at 37°C, 5% CO_2. Detached myocytes were then collected and centrifuged at 600g, four min, and resuspended in RB+ medium at a concentration of $5X10^6$/ml. Myocytes were replated on a microelectrode array by adding 40 µl of cell suspension covering the electrode area. Medium (RB+ supplemented with 10µM Rock inhibitor) was slowly topped up to 1ml after two hours of incubation that allowed cell attachment. Myocytes were recovered on the electrode array for 3-5 days after digestion, and the RB+ medium was changed every other day. Experiments were conducted when cardiac myocytes regained spontaneous contraction. Microelectrode with attached cardiac myocytes were installed onto the electrical mapping system (MappingLab Cat.16-1036CS) that records the electrical field signals of cardiac myocytes simultaneously from 64 channels.

2.11.2 Data analysis

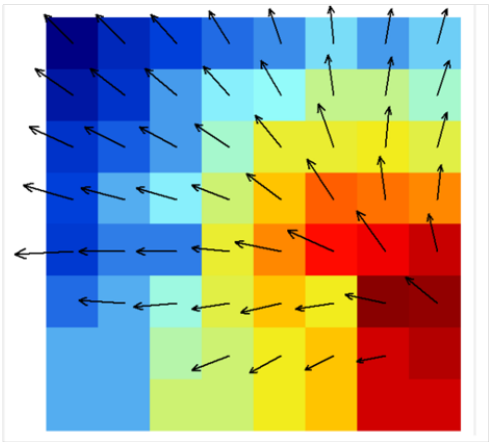
Conduction velocity and filed potential were analysed using activation map (Fig. 2.20) and potential map (Fig. 2.21) with EMap Scope 5 software. Field potential duration (FPD, from the beginning of QRS complex to the peak of T wave), width of QRS complex, RR interval, heart rate, heart rhythm and ectopic beat were measured and calculated at baseline and at the application of different chemical compounds.

A





B



Statistics

SpeedItem	SpeedValue(mm/ms)
Average	0.061947
Std	0.007904
Variance	0.000062
Median	0.061836
Max	0.088212
Min	0.045552
Coefficient of Variability	0.127589

Figure 2.20 A. Example of activation map (left panel) and contour map (right panel). Each square on the map corresponds to an electrode, and the colour of the square indicates cell activation in timely order. The colour gradient on the activation map depicts the direction in which the activation is spreading. The MIN channel represents the location of the initial depolarization, while the MAX channel is the site of the most recent activation. **B. Example of conduction map.** The arrows on the map indicate the direction of propagation, and their size reflects the speed of propagation. The statistics table shows the conduction velocity, which is calculated using a built-in function based on time and distance (mm/ms).

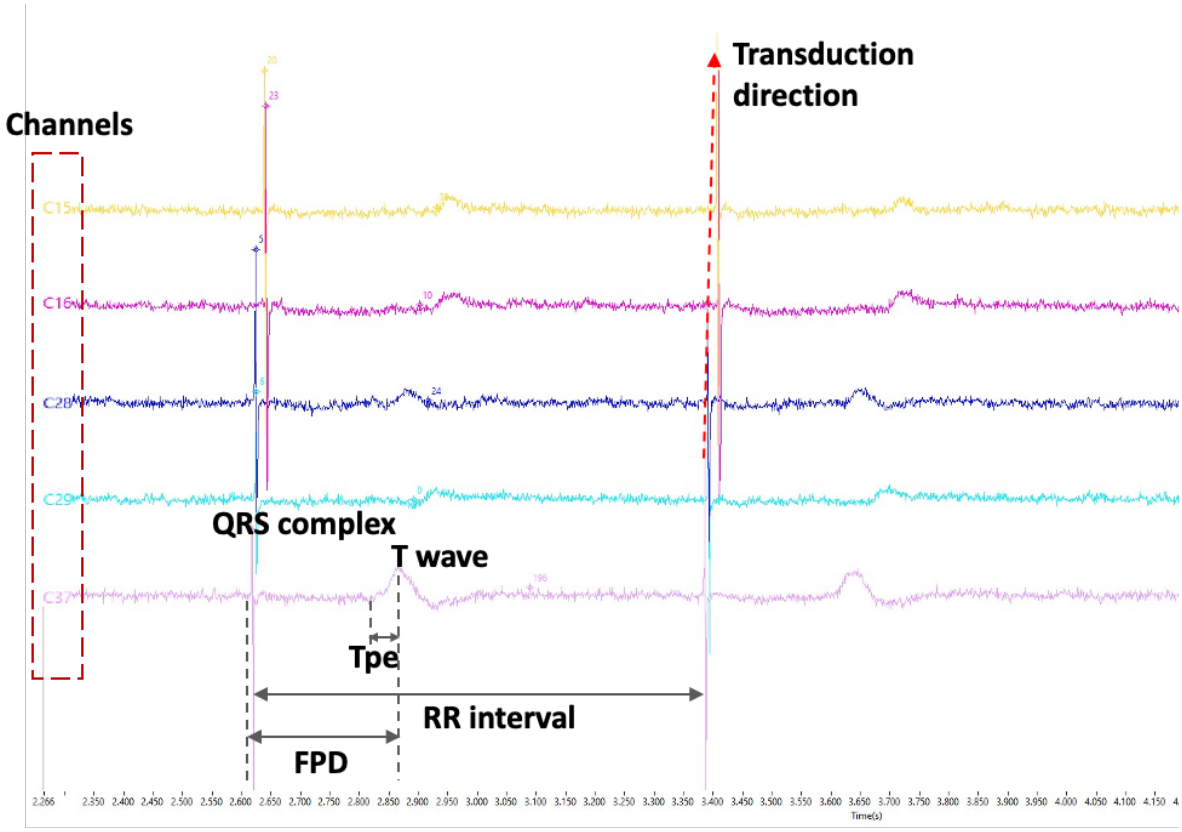


Figure 2.21. Sample potential map of iPSC derived cardiac myocytes recorded using electrical mapping system. Each color represent signal recorded from a single channel as indicated on the left side. The parameters measured in this thesis are depicted on channel 37 (pink), encompassing two waves - the QRS complex and T wave - and three intervals: field potential duration (FPD, from the beginning of the QRS complex to the peak of the T wave), RR interval, and Tpe (from the beginning to the peak of the T wave). The duration of the QRS complex and T wave reflects depolarization and repolarization velocity, while FPD represents the summation of action potentials from all single cells within the recording area of this electrode, and the RR interval reflects the beating rate. A time-lapse of the beginning of the QRS complex among different channels is observed, reflecting the transduction of electrical signals propagating from early depolarized cells to others. By analyzing the duration of propagation between channels, conduction direction and velocity can be calculated.

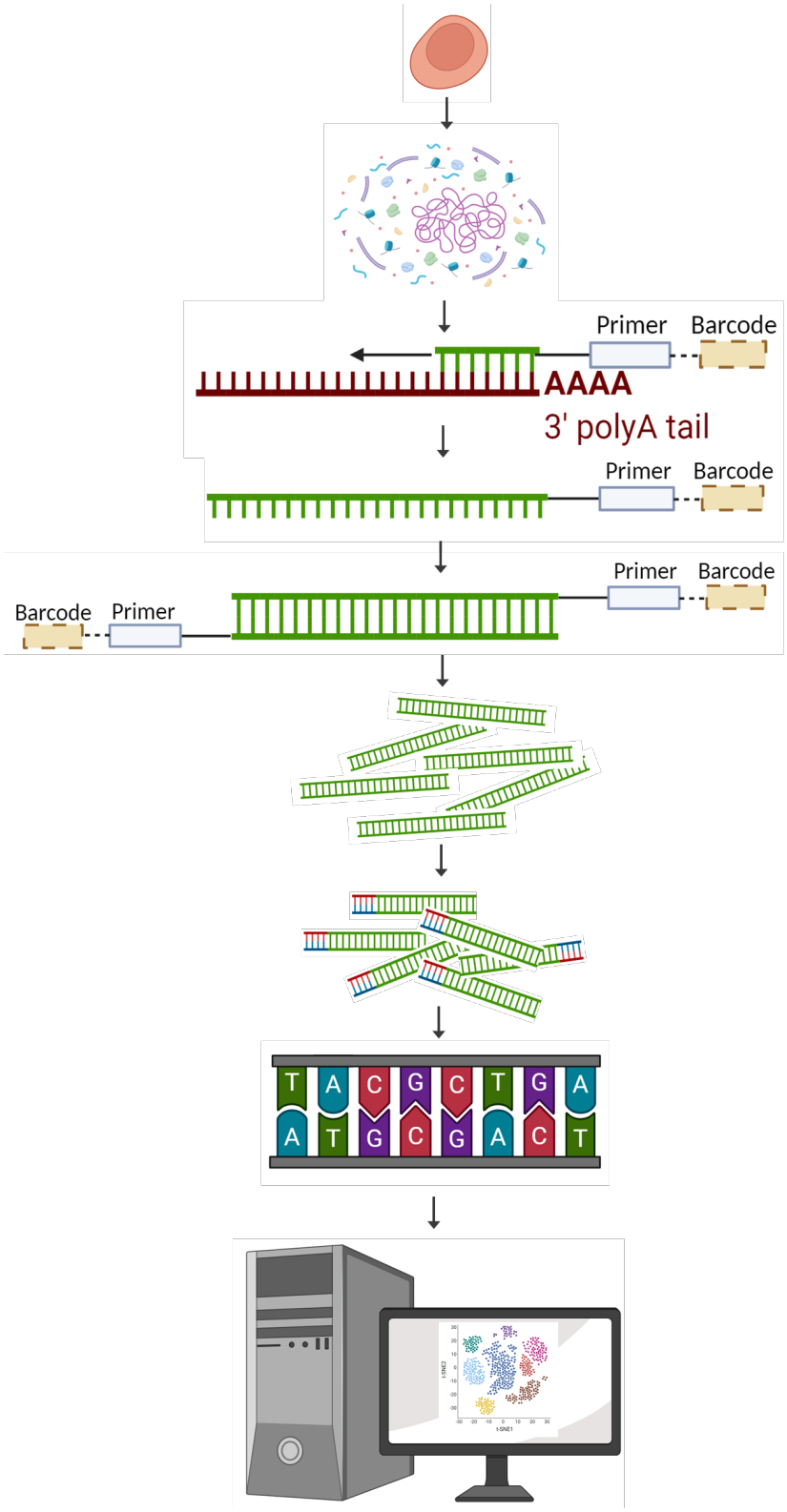
2.12 Single RNA sequencing

In recent decades, RNA sequencing (RNAseq) has undergone rapid development and refinement in both methodology and data analysis[139]. Early-stage, low-throughput methods for

gene expression evaluation, such as Northern blots and PCR, paved the way for advancements in this field. The first genome-wide quantification of gene expression, known as transcriptomics, was achieved with hybridization-based microarrays in 1995[140]. Although these microarrays are relatively high-throughput and cost-effective, they come with drawbacks, including a requirement for prior knowledge of the genome sequence and susceptibility to high cross-hybridization background artefacts.

To overcome these technical limitations, sequence-based methods that directly determine transcript sequences were introduced. The revolutionary Next-Generation Sequencing (NGS) [141,142], commonly referred to as RNA sequencing, emerged as a transformative method for high-throughput RNA analysis. This approach involves sequencing cDNA from homogenized tissue, providing a vast amount of information for biomedical discoveries. Initially, NGS delivers bulk information, representing the average gene expression in a large population of cells.

To delve into cellular heterogeneity and assess differences between individual cells, the first single-cell RNA sequencing (scRNAseq) protocol was published in 2009[143]. This ground-breaking method allowed for the study of the biological properties of individual cells at the genomic level, enabling a deeper understanding of the intricacies within heterogeneous cell populations.



① **Single cell isolation**

② **Cell lysis**

③ **Reverse transcription**

④ **cDNA amplification**

⑤ **Library preparation**

⑥ **Sequencing**

⑦ **Data analysis**

Figure 2.22 schematic summary of a general methodological pipeline of single-cell RNA sequencing. Basic steps in conducting scRNA-seq include: 1) single cell isolation; 2) lysis of collected single cells; 3) reverse transcription of RNA in cell lysis particles to cDNA; 4) amplification of cDNA; 5) sequencing library preparation; 6) sequencing run; 7) data analysis with computational techniques.

Since the inception of the first scRNAseq study, numerous advancements in reagents and platforms have been developed and made commercially available to researchers. While there may be variations, all protocols generally adhere to key methodological principles (Fig. 2.23).

The initial and crucial step in scRNAseq involves the effective and precise isolation of a single cell for subsequent processing. In the case of in vitro cell culture, cells are dissociated using an appropriate enzyme, followed by resuspension in a preserving solution and single-cell sorting. Among various emerging techniques for single-cell and single-nuclei isolation, the most commonly used methods include fluorescence-activated cell sorting (FACS) and microfluidics-based techniques (Fig. 2.23)[144]. In FACS, cells are labelled with antibodies targeting specific cell markers, which can be identified by fluorescent detectors. In droplet-based microfluidics, cells in suspension are encapsulated into microdroplets with a sequencing bead linked to a unique barcode primer sequence. This primer sequence is then hybridized to the RNA of the cell after lysis. Manual sorting with a capillary glass pipette is another practical procedure, particularly for very few or fragile cells.

Following isolation, cells are lysed based on the chosen isolation methods. Reverse transcription from selected RNA in cell lysis to complementary DNA (cDNA) and cDNA amplification are then performed using a designed primer sequence. Some primers may contain adapter sequences and unique molecular identifiers (UMIs) as required in protocols. The amplified cDNA is further fragmented and tagged with an index barcode using library preparation techniques, after which the samples are ready for sequencing. Experimental design

and sample properties are essential considerations when deciding on the scRNAseq protocol and platform.

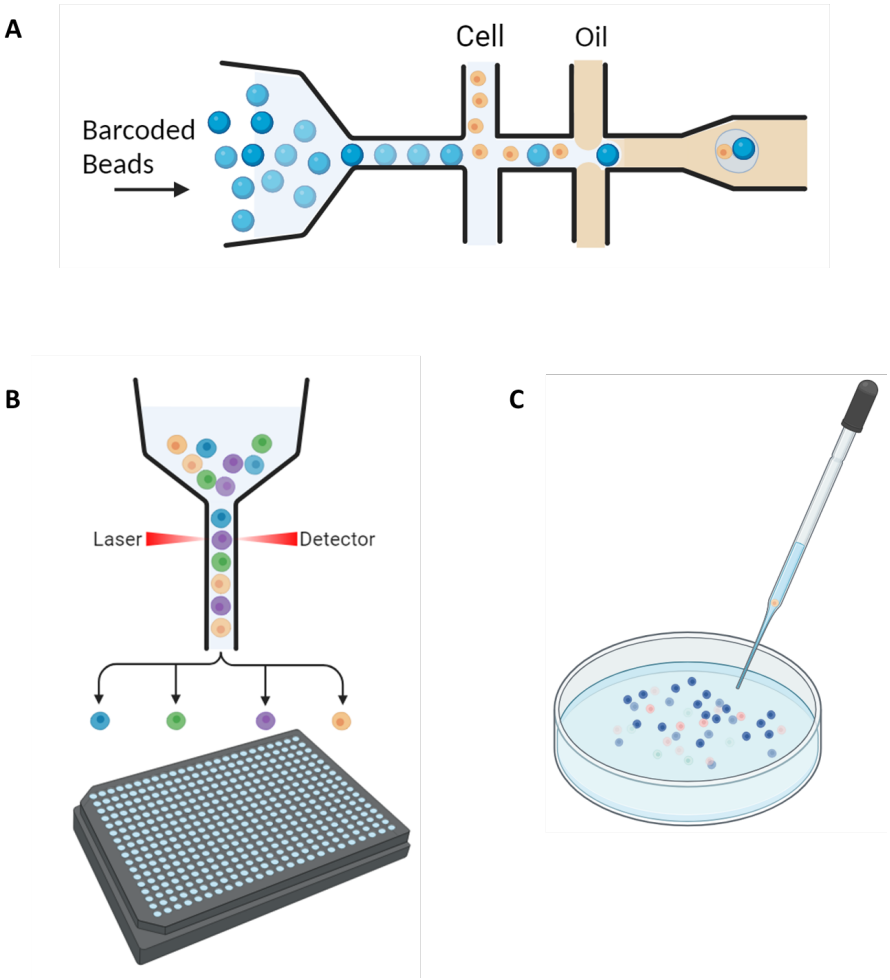


Figure 2.23 Commonly used single-cell isolation methods. A. Microfluidics single-cell genomic. A single cell is loaded with a barcode bead containing a unique barcode sequence in a microdroplet. **B**. Fluorescence-activated cell sorting. Fluorescence antibodies labelled cells are sorted by staining pattern into the plate. **C**. Micropipetting. Single cells are manually aspirated with a capillary glass pipette under a microscope.

The analysis of scRNAseq data also follows a general pipeline, including quality control (QC), aligning reads to the transcriptome, quantifying the number of reads mapping to each gene and other assessments such as testing for differential expression between samples and detecting

allele-specific expression. Although there are some public tools and algorithms for QC and data interpretation, no consensus and gold-standard statistical methods have been reached. Thus, the involvement of computational biologists and expertise in RNAseq data analysis is always required to adjust algorithm details and parameters and address unique computational challenges during data interpretation for scRNAseq studies.

2.13 Statistical analysis

Before conducting the t-test and the ANOVA test, all data underwent an assessment for normal distribution. In cases where the data did not exhibit normal distribution, non-parametric tests, such as the Mann-Whitney test for t-tests and the Kruskal-Wallis test for ANOVA, were employed. All data were presented as mean ± SEM. Significance levels were denoted as *p<0.05, **p<0.01, ***p<0.001, ****p<0.0001. Data analysis and plotting were performed using GraphPad Prism, while figures were created using PowerPoint and Biorender.

Chapter 3：Phenotyping human induced pluripotent stem cell derived cardiac myocytes and sympathetic neuron

3.1 Introduction

3.1.1 General introduction of the hiPS cell evolution

Stem cell science gained momentum when James Thomson in 1998[89] grew the first embryonic stem cells in a dish. This set the platform for Christine Mummery in 2001[145] to use stem cells to create beating heart cells outside the body. However, it was the reprogramming of fibroblasts back to their pluripotent state in 2006 by Takahashi and Yamanaka that resulted in human induced pluripotent stem cell (hiPSC) technology transforming biology and providing an opportunity to study human disease *in-vitro*[87,88]. In heart physiology, the induction of cardiomyocytes from hiPSC was rapidly realized by applying the standard embryoid bodies-based protocol for embryonic stem cells[146,147] which was optimized overtime by more precise control of the embryonic development signal[94,97,148,149]. To date, the speed to generate hiPSC has been enhanced and genetic stability improved using novel modified synthetic mRNA transfection methods[150,151].

While primary cells from patients with genetic-based arrhythmias are largely unavailable, hiPSC has emerged as a tool to model inherited cardiac syndromes[102,152–154]. Human iPSC-induced cardiomyocytes were first applied in a mechanistic study of LQTS in 2010[102], where patients derived cells were capable of recapitulating the electrical phenotype of the disease. Given the power of the sympathetic nervous system to trigger arrhythmia in patients with cardiac channelopathies[9,155], attention has recently focused on developing neuronal-cardiac co-

culture systems either with animal cells or stem cells in order to facilitate the study of neurocardiac interactions[116,119,120,156–159].

This has been met with some success. Oh et al.[116] were the first to report evidence for functional coupling where noradrenaline-secreting sympathetic neurons in co-culture were capable of driving heart rate in neonatal cardiac myocytes when stimulated pharmacologically or optogenetically. Similarly, others[119,120] showed selective induction of healthy human sympathetic neurons could enable precise control of cardiac myocyte beating. Development of a diseased cardiac-neural co-culture system has not been firmly established, although Winbo et al.[121] recently reported that sympathetic-derived neurons in monoculture from an LQT1 patient (*KCNQ1* loss-of-function variants) showed increased excitability and neurotransmission. Whether a hiPSC cardiac-neural co-culture system can also replicate and mimic cardiac-neural responses seen in other mammalian systems remains to be established.

In this chapter, I adapted current protocols of cardiac myocytes and sympathetic neuronal differentiation from hiPSC and conducted physiological phenotyping of these cells to confirm cell type and cell function. Cardiac myocyte induction protocol was trialled and optimized with 2 cell lines, SFC854-03-02 and iPS-OX1-19; iPS-OX1-19, UKKi007-A, and ReBl-PAT$^{RYR2\text{-}WT}$ were used for sympathetic neuron induction protocol evaluation. After phenotyping, the hiPSC derived cardiac myocytes was testified as applicable in disease modelling by modelling cardiac hypertrophy in vitro. I also developed hiPSC-SN in mono-culture and co-culture with hiPSC-CM and assessed the utility of this culture to respond to physiological stimuli.

3.1.2 Understanding cardiac hypertrophy

Cardiovascular diseases remain the leading cause of mortality, with cardiac hypertrophy emerging as a primary risk factor predisposing individuals to cardiac arrhythmias and heart failure[160]. This hypertrophic condition serves as an adaptive response to heightened ventricular wall stress or increased ventricular volume. The classification of cardiac hypertrophy spans physiological and pathological categories, distinguished by the preservation or impairment of heart function, respectively. These categories differ in underlying molecular mechanisms, cardiac phenotype, and prognosis[161].

Physiological cardiac hypertrophy manifests in response to postnatal growth[162], athletic training[163], and pregnancy[164]. In these cases, the compensatory hypertrophic response serves to maintain normal cardiac function. Conversely, pathological cardiac hypertrophy is induced by common factors such as hypertension, valvular disease, and genetic cardiomyopathy, leading to maladaptive changes in the heart structure and function[165].

Both physiological and pathological hypertrophy present as an increase in cardiac mass and enlargement of individual cardiomyocytes either in length or width. The growth of myocytes is accompanied by angiogenesis and increased mitochondria infiltration under physiological conditions to support the survival of cells and maintenance of contractile function[166]. The enlargement of cells is usually reversible except in postnatal hypertrophy if stimuli are removed[167]. Conversely, a heart with pathological hypertrophy progresses to heart failure with the replacement of normal heart tissue by fibrosis and cell death. Although increasing evidence suggests the potential of partial reversal of the hypertrophy with heart failure therapies[167].

Various signalling pathways have been implicated in the development of cardiac hypertrophy. The distinction between physiological and pathological hypertrophy is suggested to hinge on the nature of the initial stimuli[161]. Despite this, there are shared signalling pathways, such as

Akt signalling, bridging both physiological and pathological cardiac hypertrophy. This shared involvement adds to the intricacy of mechanistic studies in this field[168].

3.1.3 Cardiac myocytes are non-generative cells

Cardiomyocytes represent one of the initial cell types to terminate differentiation during embryonic development. Postnatally, instead of proliferating, these cells augment in size to meet increased demands[162]. This augmentation occurs through either lateral growth, involving the addition of sarcomeres in parallel, or longitudinal growth, where sarcomeres are added in series. In response to pressure overload, the heart undergoes concentric hypertrophy, while volume overload induces eccentric hypertrophy[169].

Adult cardiac myocytes exhibit limited regenerative capacity, and their turnover rates are minimal. Under normal conditions, the estimated turnover of cardiomyocytes ranges from 0.5% to 2% per year, with a slightly higher turnover observed in the presence of injury[170]. Consequently, in cases of heart muscle tissue damage, fibrotic tissue replacement serves as a reparative mechanism, given the permanent nature of cardiac myocytes.

3.1.4 Induced pluripotent stem cells emerging as a powerful tool

Cardiac hypertrophy plays a pivotal role in cardiac remodelling and contributes significantly to cardiac events. Therefore, gaining a comprehensive understanding of the underlying molecular mechanisms is imperative for advancing our knowledge of cardiac pathophysiology. Due to the non-regenerative nature of primary cardiac myocytes, hiPSC-derived cardiac myocytes emerge as a valuable tool for in vitro mechanistic investigations of cardiac hypertrophy at the molecular level. This approach allows for controlled experimentation and detailed molecular analyses, facilitating the elucidation of key pathways and factors involved

in hypertrophic processes. The utilization of hiPSC-derived cardiac myocytes addresses the limitations associated with primary cells, providing a versatile and reproducible platform for advancing our insights into cardiac hypertrophy and, consequently, contributing to the development of targeted therapeutic strategies.

This chapter presents a cardiac hypertrophic model that was established using healthy hiPSC-CMs in a dish. Pathological myocyte hypertrophy was induced by angiotensin II (AngII), an established hypertrophic agent commonly used for animal models[171]. Derived myocytes were also capable of recapitulating pathological hypertrophy when challenged with angiotensin II.

3.2 Methods

3.2.1 Flow cytometry

Cardiac myocyte-specific structural protein antibodies, anti-cTnT and anti-MLC2v, and sympathetic neuron key enzyme antibody, anti-TH were applied in flow cytometry to verify the induced cell type from hiPSCs. Both cardiac myocytes and sympathetic neurons were collected from two different cell lines. The preparation of cell samples and the rundown of flow were illustrated in Chapter 2. Briefly, induced hiPSC-CMs (over day 20) or hiPSC-SNs (over day 40) were collected and permeabilized in blocking buffer before staining with respective antibodies, then resuspended in FACS buffer for running in flow machine. Data collected were analyzed in FlowJo as illustrated in Chapter 2 to report the percentage of cells that expressed tissue-specific markers.

3.2.2 Immunofluorescence

Induced cardiomyocytes and sympathetic neurons from hiPSC were dissociated and seeded on FluoroDish at desirable density for subsequent confocal imaging. When contraction resumed in hiPSC-cardiac myocytes or axons in hiPSC-sympathetic neurons regenerated, these cells were fixed with 4% formaldehyde, permeabilized and blocked in TBS plus 0.5% triton and 6% donkey serum. hiPSC-cardiac myocytes were then incubated in TBS with primary antibodies, anti-α-actinin (Sigma, A7811) and anti-cTnT (Abcam, ab45932), overnight at 4℃. As for hiSPC-sympathetic neurons, anti-PHOX2B (ab183741), anti-TH (Sigma, T2928), and anti-peripherin (Sigma, AB1530) were used. Then secondary antibodies conjugated to Alexa Fluor 488 (Invitrogen A28175) and 594 (Invitrogen A-11012) were applied at room temperature for two hours. Cell nuclei were stained by Hoechst (Invitrogen, H3570) for 10 minutes. Images were taken by Leica confocal microscope (Leica TCS SP5) and analysed with LAS X and ImageJ software.

Sarcomere length was determined using LAS X, and the measurement of cell size and nuclear size for day 20 and day 40 hiPSC-CMs was conducted using ImageJ. (Fig. 3.1) The sarcomere length of each cardiac myocyte was calculated as the average length of three randomly selected sarcomeres in that cell. A free selection tool was used to manually outline cells in merged immunofluorescent images. The Hoechst-stained layer was used for the measurement of nuclear surface area. The plug-in threshold algorithm automatically identified the high-fluorescent area as nuclei, which could be selected with the wand tool and added to the ROI manager. The pixel size of the selected area was automatically measured using the plug-in function in FlowJo ROI Manager and was converted to physical size with scale.

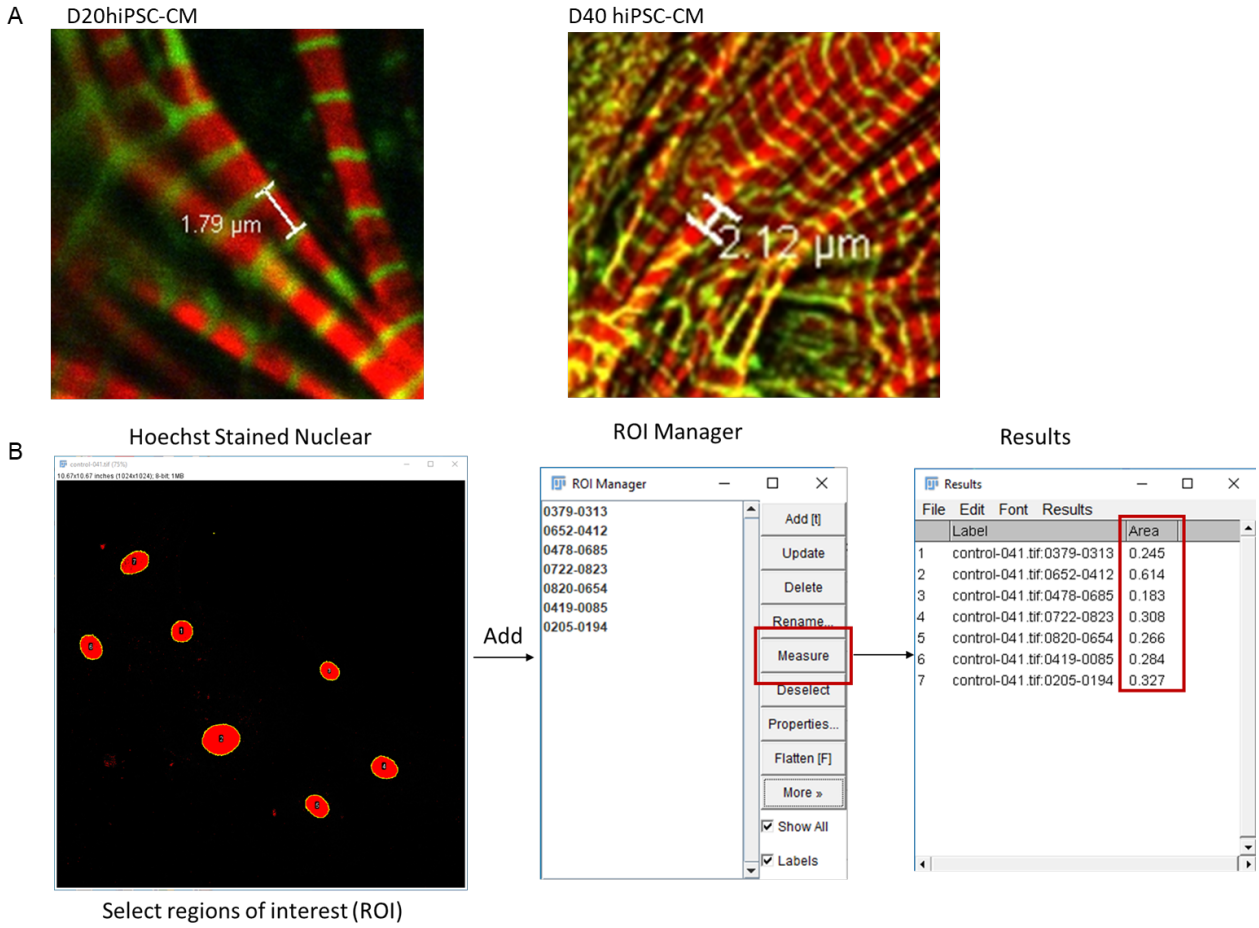


Figure 3.1 Examples of sarcomere length, nuclear surface area, and cell surface area measurement. A. Sarcomere length was measured as the distance between two α-actinin stained lines that link actin filaments at the Z-line. B. Example of surface area measurement using ImageJ selection tools and ROI manager. For nuclear measurement, image thresholding was applied in the Hoechst-stained layer which partition the nuclear area from the background, whereas the whole cell edge was manually selected. Selected regions were added to the ROI manager which automatically quantify the pixel area of each region.

3.2.3 qRT-PCR

Total RNA from day 19 and day 41 hiPSC-CMs were extracted using a RNeasy mini kit (Qiagen,74104) according to the manufacturer's instructions. Extracted RNA was transcripted to cDNA using the iScript cDNA synthesis kit (Bio-Rad, 1708891). Following RT-qPCR was conducted with TaqMan Gene Expression Assay(20X). To evaluate the maturation of cardiac

myocytes, ventricular myosin light chain-2 (MYL2, Hs00166405_m1) and myosin heavy chain α isoform (MYH6, Hs01101425_m1) gene expression was tested. Thermal cycling parameters are as follows: 10 min at 95°C, followed by 40 cycles of 15s at 95°C and one min at 60°C.

3.2.4 Electrical mapping

To assess the adrenergic response in hiPSC-induced cardiac myocytes, the cells were reseeded on a microelectrode array to record their electrical signals. Recordings were conducted in both the standard culture medium as a control and in the culture medium supplemented with 1μM isoprenaline. One million cardiac myocytes were reseeded on each 64-channel electrode (EGMA064200700) and maintained for 3 to 5 days to allow spontaneous contraction to recover after digestion. Then field electrical signal was recorded for 10 seconds at baseline and after applying isoprenaline using the EMapRecord software. The protocol is as follows: 1. Install electrode array onto mapping system, allow several minutes for the electrical signal to stabilize; 2. Record 10s baseline electrical signal; 3. Apply 100μl of 10μM isoprenaline to 900μl culture medium in the electrode well, immediately record 10s electrical signal; 4. Record another 10s of electrical signal one min after adding isoprenaline. The recorded data file was analysed using EMapScope.

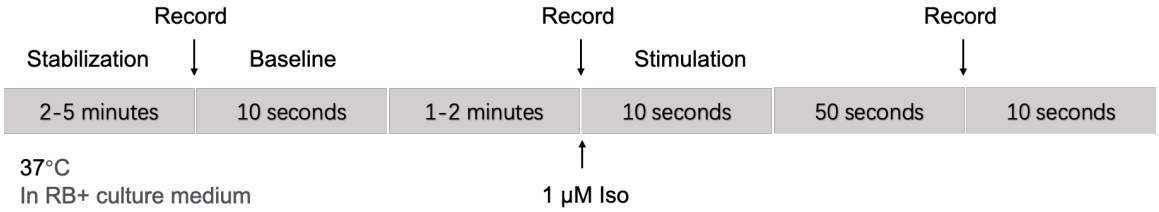


Figure 3.2 Electrical mapping protocol summary. Cardiac electrical signal at baseline, immediate isoprenaline response, and plateau isoprenaline response were recorded for 10 seconds each.

3.2.5 Calcium imaging

Day 40 hiPSC-SNs were dissociated and replated on FluoroDish. After three to five days for axon regeneration, these cells were employed in calcium imaging using Fura2-AM (5 μM, loaded for 30min at 37 ℃) as an intracellular calcium indicator. Throughout imaging, cells were bathed in Tyrode solution at 36.5℃, with the supplement of angiotensin II (100nM, 200nM) at two minutes and 50 mM KCl at five minutes. Images were captured at 340nm and 380nm excitation wavelength at 1s intervals. Intensity ratio represented cytosolic calcium level was recorded, based on which the peak responses to angiotensin and potassium were calculated.

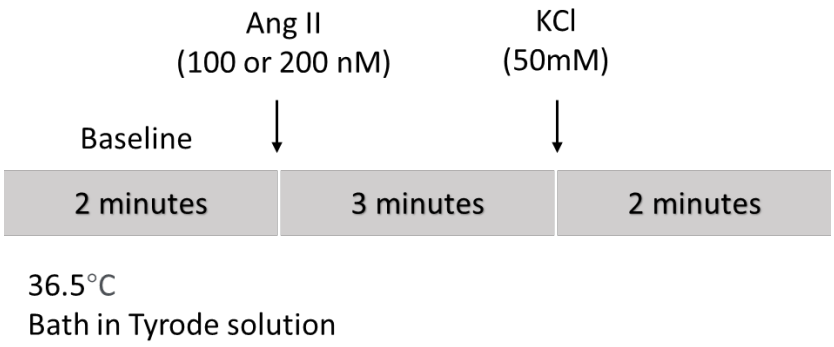


Figure 3.3 Calcium imaging protocol summary. Fura2-preloaded hiPSC-SNs were bathed in Tyrode solution, and angiotensin II and KCl were supplemented to Tyrode at 2min and 5min. Emission wavelength intensity was continuously captured at 1s interval during the process.

3.2.6 Förster resonance energy transfer

Cardiomyocytes were transfected with adenoviral vectors encoding the Förster resonance energy transfer (FRET) cAMP sensor Epac-SH187 by incubation overnight at 37°C, 5% CO_2 before the FRET measurements. Cytosolic cAMP response to different stimuli in the transfected cells was recorded as cyan fluorescent protein (CFP)/yellow fluorescent protein (YFP) emission intensity change. Cells were bathed in Tyrode solution (135mM NaCl (Sigma,

S7653), 4.5 mM KCl (Sigma, P9541), 20 mM HEPES (Sigma, H3375), 11mM glucose (Sigma, G7021), 1mM MgCl2 (SERVA, 39772.02), 2 mM CaCl2 (BioVision, B1010), titrated with NaOH to pH 7.4) to reach a stable baseline before isoprenaline (Sigma, I6504), IBMX (non-selective phosphodiesterase inhibitor; 3-isobutyl-1-methylxanthine, Sigma, I5879) and forskolin (FSK, adenylyl cyclase agonist; Cayman Chemical, 11018) were applied. Images were taken using a Nikon Eclipse Ti2 inverted microscope with a 40× oil immersion objective, connected to a Cairn Research dual OptoLED light source, and a Prime BSI photometric camera. The excitation wavelength was set at 430 nm, and emission was measured at 480 and 535 nm for CFP and YFP, respectively. Background fluorescence was subtracted from the recorded emission intensities, and the FRET ratio was calculated as CFP over YFP and normalized to the average FRET ratio at baseline for comparison.

3.2.7 Enzyme-linked immunosorbent assay

Supernatants were collected from day 64 hiPSC-SNs seeded at one million cells per well in a 24-well plate. Enzyme-linked immunosorbent assay using Norepinephrine ELISA Kit (ab287789) was performed according to the manufacturer's protocol. Briefly, samples and standards were added to the provided 96-well plate in duplicate. Biotin, streptavidin-HRP conjugate, and TMB substrate were added to the plate and incubated, then washed off in sequence. After incubation, the optical density of absorbance was read at 450nm.

3.2.8 In vitro cardiomyocyte hypertrophy induction

To develop myocyte hypertrophy, healthy hiPSC-CMs (SFC854 and OX1-19) and Wistar neonatal rat ventricular myocytes were incubated in respective culture media supplemented with 100nM, 1uM angiotensin II (MedChem Express, HY-13948A) for 48 hours.

Morphological and functional alterations of AngII-induced hypertrophy were compared between human and rat models. Although species difference hinders the translation of findings in an animal model to human disease, diverse features of cardiac hypertrophy are conserved in rat cardiac myocytes and can be recapitulated in vitro[172]. Even human induced pluripotent stem cells outweigh rat ventricular myocytes in many aspects, they also display heterogeneity in epigenetic profiles and cellular behaviours in differentiation[154], while primary rat myocytes are relatively homogenous. Therefore, incorporating both animal and human iPSC models was aimed to demonstrate the conservation of hypertrophic phenotypes and the applicability of hiPSC-CMs in disease modelling.

3.2.9 Cell size and nuclear size measurement

Mature hiPSC-CMs and isolated Wistar neonatal rat ventricular myocytes were dissociated into single cells plated on confocal dish, and exposed to angiotensin II for 48 hours to induce hypertrophy. Primary antibodies anti-cardiac troponin T (anti-cTnT, ab45932, rabbit) and anti-α-actinin (Sigma A7811, mouse) were used in this section to visualize the morphological alteration in myocyte sarcomere structure and cell size. Secondary antibodies applied were Goat anti-Mouse IgG-Alexa Fluor 488 (Invitrogen A28175) and Goat anti-Rabbit IgG-Alexa Fluor 594 (Invitrogen A-11012). Cell nuclei were stained by Hoechst (Invitrogen, H3570). Images were taken by Leica confocal microscope (Leica TCS SP5) and analysed with LAS X software.

Confocal immunofluorescence images captured from both control and hypertrophic myocytes, stained with anti-cTnT and anti-α-actinin, were subjected to analysis using ImageJ software. Cell boundaries were delineated manually using the polygon selections tool, aligning with cytoskeleton staining. The nuclear area was automatically identified utilizing the Wand (Tracing) Tool, following the application of a threshold to the Hoechst-stained image layer for

pixel selection within the nuclear region. The chosen area was integrated into the ROI manager, facilitating the automatic measurement of pixel size. This pixel size was subsequently converted to physical dimensions in micrometres, guided by the provided image scale.

3.2.10 Myocytes hypertrophic marker gene expression

Total RNA from control and hypertrophic hiPSC-CM were extracted using RNeasy mini kit and reverse transcription to cDNA was performed using the iScript cDNA synthesis kit. Following RT-qPCR was conducted with the following primers: *NPPB* Hs00173590_m1; *NPPA* Hs00383230_g1; *MYH6* Hs01101425_m1; *MYH7* Hs01110632_m1, which are established cardiac myocytes hypertrophy marker gene. Amplification curves were generated automatically by the real-time PCR systems QuantStudio5. Relative quantification compared target gene expression between control and hypertrophic groups using the comparative ΔCT method. *GAPDH* was used as an internal control.

3.2.11 proBNP secretion

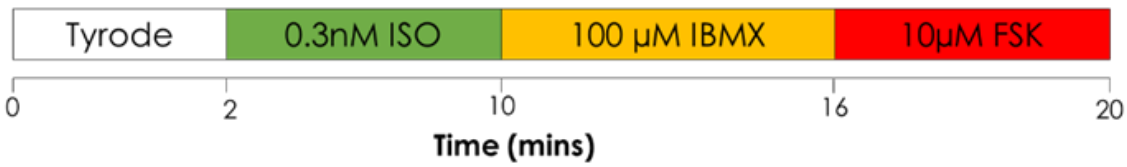
Pro-brain natriuretic peptide (pro-BNP) is a cardiac hormone secreted by ventricle myocytes under mechanical stress, which is cleaved by a protease to an inactive N-terminal pro-BNP (NT-proBNP) and releases an active C-terminal BNP[173]. BNP and NT-proBNP are both biomarkers of cardiac hypertrophy[174]. The pro-BNP concentration in hiPSC-derived cardiomyocyte culture media was measured using the Human proBNP/NPPB ELISA kit (Invitrogen, EHPRONPPB) according to the manufacturer's instructions. Cell culture media were collected from hypertrophic and control groups. Collected samples were transferred to the supplied pro-BNP antibody coated 96-well in duplicate, followed by adding biotin, streptavidin-HRP, TMB substrate, and stop solution sequentially. Absorbance at 450nm was measured by a spectrophotometer (Thermo Multiskan GO).

3.2.12 Cytosolic cAMP measurement

In both neonatal rat models and hiPSC-CM models, cardiomyocytes were transfected with adenoviral vectors encoding the FRET cAMP sensor Epac-S^{H187} through overnight incubation at 37℃ with 5% CO2 before conducting FRET measurements. The cytosolic cAMP response to various stimuli in the transfected cells was documented as changes in CFP/YFP emission intensity. The excitation wavelength was set at 430nm, with emission measurements at 480nm and 535nm for CFP and YFP, respectively. Recorded emission intensities had background fluorescence subtracted, and the FRET ratio was calculated as CFP over YFP, subsequently normalized to the average FRET ratio at baseline for comparative analysis.

3.2.12.1 FRET protocol

Cells were perfused continuously in Tyrode solution for 2 minutes at 2-3ml/min to reach a stable baseline before pharmacological agents: isoprenaline (0.3 nM), IBMX (100 µM, nonselective phosphodiesterase inhibitor) and Forskolin (10 µM, FSK, adenylyl cyclase agonist) diluted in Tyrode solution subsequently applied at 2 minutes, 10 minutes and 16 minutes, as shown below:



3.3 Results

3.3.1 Cardiac myocyte and sympathetic neuron induction from hiPSCs

Detailed induction procedures of cardiac myocytes and sympathetic neurons from hiPSC are illustrated in chapter two. Cardiomyocyte differentiation was adapted from a well-established small molecule modulated differentiating approach[94,175,176]. There have been several published methods reporting sympathetic neuronal differentiation from hiPSC[117,119,177,178]. Here we adapted the method reported by Winbo et al 2020[119]. The morphology of hiPSCs, induced cardiac myocytes, and sympathetic neurons under the microscope are shown in Figure 3.4. However, the ultrastructure of synapses can only be visualized using an electron microscope[179].Thus, anti-synapsin antibody was applied to validate synapse formation (Fig. 3.5 B). Synapsin, a neuron-specific phosphoprotein, plays a pivotal role in synaptogenesis, vesicle docking, and release[180].

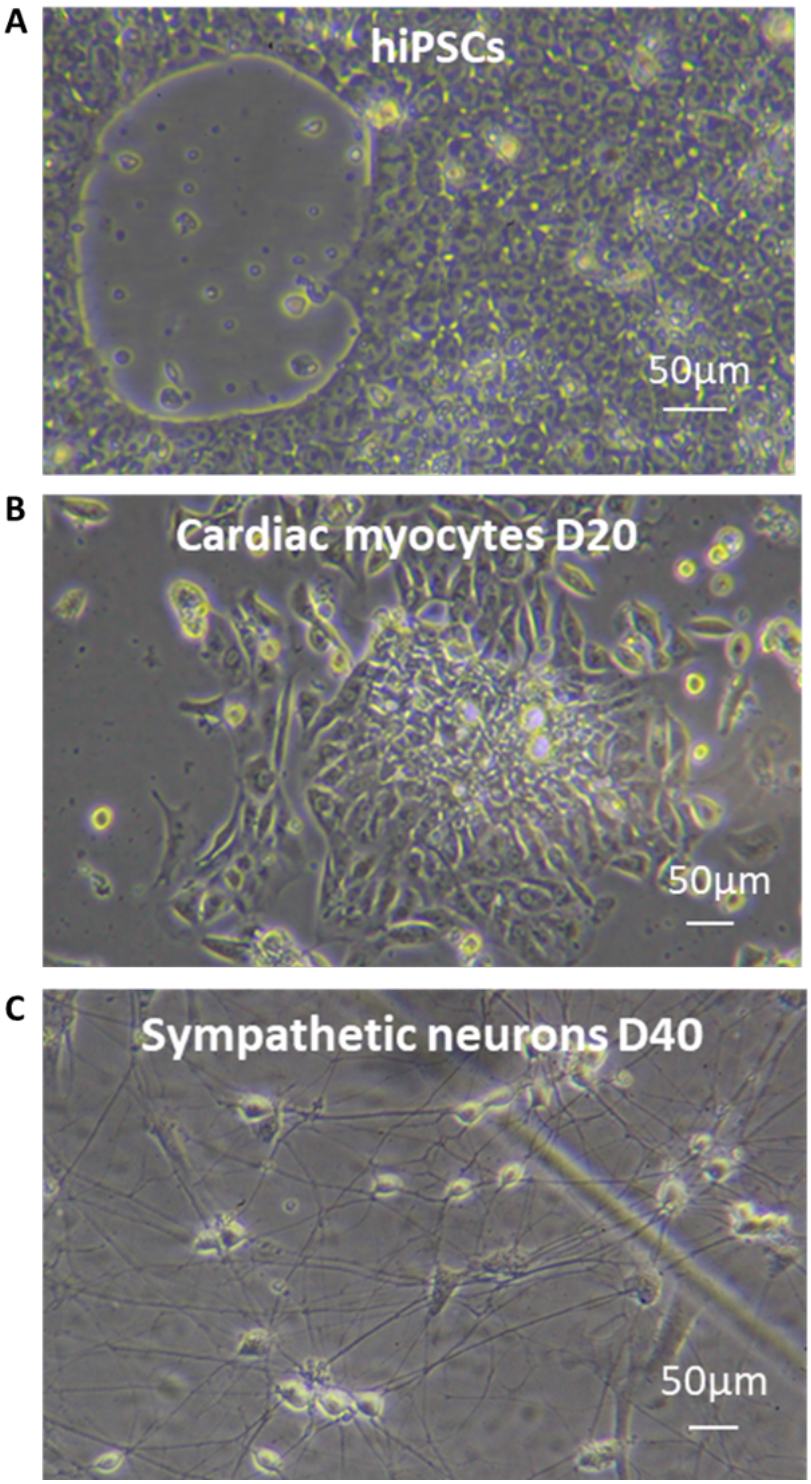


Figure 3.4 Typical brightfield images of hiPSC, hiPSC-CMs, hiPSC-SNs and co-culture. **A.** Thawed healthy hiPSCs (SFC854) plated on Matrigel coated 6-well plate for two days. Single hiPSC appears as a round cell with a prominent nuclear-to-cytoplasm ratio. HiPSCs collectively form relatively round colonies characterized by smooth borders. **B.** Image captured on the second day after reseeding of 20 days hiPSC-derived cardiac myocytes dissociated and reseeded as monolayer. Dissociated single myocytes exhibit an elongated, cylinder-shaped morphology with a centrally located large round nucleus. **C.** 40 days sympathetic neurons replated on coverslips for 3 days. During the maturation phase, sympathetic neurons display dendritic outgrowth, resembling shiny beads on a string.

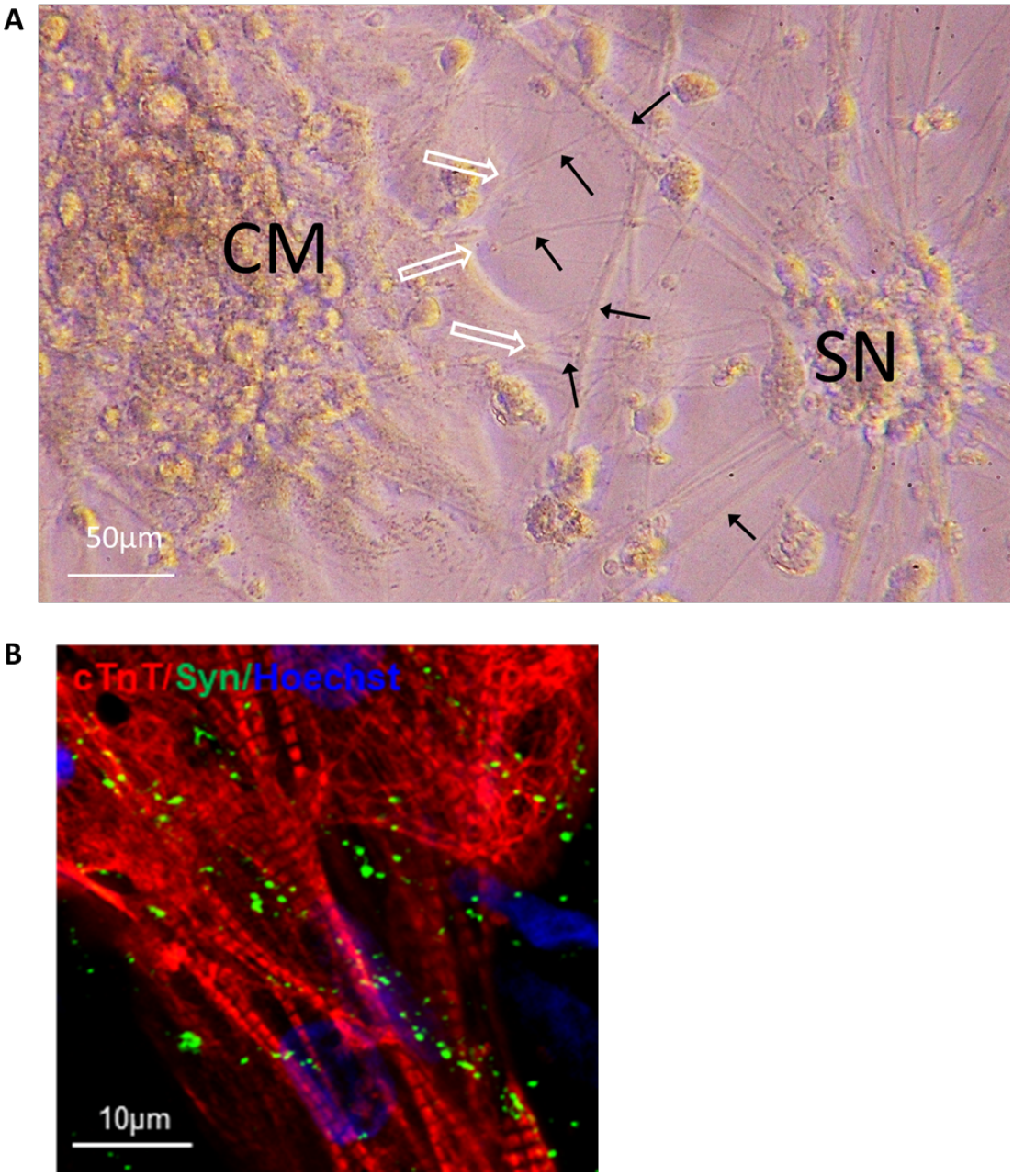


Figure 3.5 Typical brightfield image of hiPSC derived neurocardiac co-culture. A. In the neurocardiac coculture (day 9), axons (black arrow) extend to connect with beating myocyte clusters, being the substrate for synapses formation at the sites of contact (white arrow). **B.** A representative IF figure of day 7 neurocardiac coculture (20 days myocytes and 40 days neuron), stained with anti-synapsin and anti-cTnT. The presence of dot-stained synapsin overlapping with cardiac troponin T evidenced the synaptogenesis around cardiomyocytes. 58.49 ± 8.462% nucleated cells were striated myocytes evidenced by positive staining with anti-cTnT, among which 92.21 ± 4.945% were innervated by neuron (IF images n=6, nucleated cells n=216).

Flow cytometry was used to validate the induction efficiency of hiPSC-CM and hiPSC-SN. Day 20 hiPSC-CM was stained by anti-cTnT and anti-MLC2v. According to positive and negative signals set by compensation beads, and compared to the non-stained control, 80% of hiPSC-CM induced from SFC854-03-02 hiPSC expressed both cardiac-specific proteins (Fig. 5). Day 42 hiPSC-SN (derived from UKKi007-A) was stained by anti-TH with 84.3% of hiPSC-SN showing positive for TH expression compared to the non-stained control sample (Fig. 3.6).

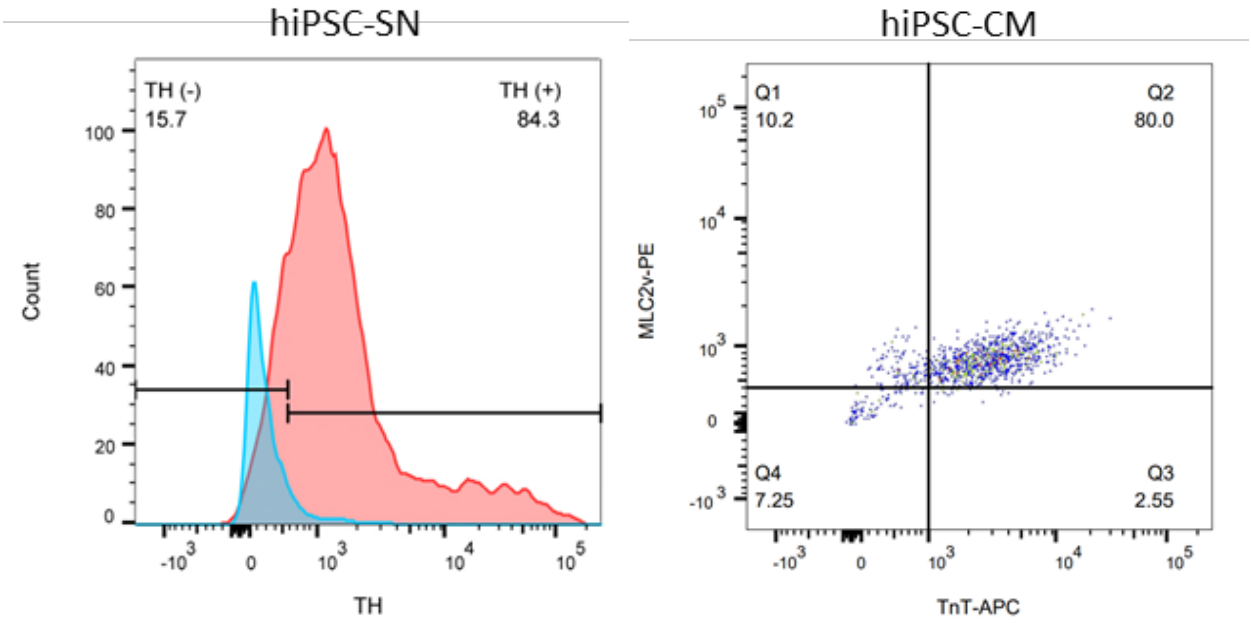


Figure 3.6 Flow cytometric results from day 20 cardiac myocytes and day 50 sympathetic neurons. In the dot plot graph (left), the right upper quadrant showed a positive population for MLC2v and cTnT in hiPSC-CM (from SFC854-03-02) being 80%. In the histogram (right), the blue curve represented blank control and the red curve represented hiPSC-SN (from UKKi007-A) stained with TH. Compared to negative control, 84.3% of hiPSC-SN expressed TH.

3.3.2 Morphological phenotype of hiPSC, hiPSC-CM and hiPSC-SN

Cell morphology was further delineated through immunofluorescence staining, employing anti-cTnT and anti-α-actinin for hiPSC-CM staining. cTnT, a component of the troponin complex, extends along the longitudinal sarcomere, covering the actin thin filament, while α-actinin crosslinks the thin filaments and serves as a binding point for thick filaments along the Z-disc. Co-staining of cTnT and α-actinin in hiPSC-CMs revealed colocalization, delineating the structure of adjoining sarcomeres (Fig. 3.7). This provides compelling evidence supporting the cellular identity as cardiac myocytes.

For hiPSC-SN staining, anti-TH and anti-peripherin were utilized. Peripherin, a filamentous protein associated with neurite elongation, labeled the axon of hiPSC-SNs, while cell bodies were predominantly marked by TH, confirming the sympathetic neuron nature of the cells (Fig. 3.8).

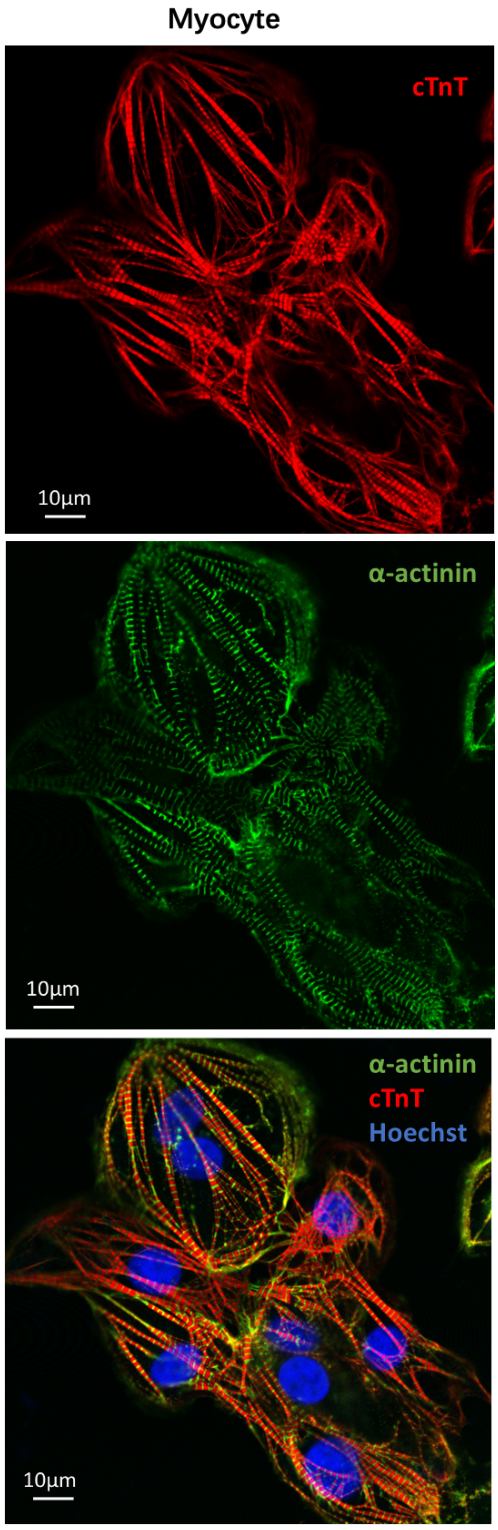


Figure 3.7 Structural characterization of day 20 cardiac myocytes by immunofluorescence staining. cTnT: cardiac troponin T; The alignment of cTnT and α-actinin depicted the structure of sarcomere within cardiac myocytes. Of the 87 nucleated cells (confocal image n=6), 84 (96.6%) stained double positive, among which 75 displayed well-organized sarcomeres while 9 showed some fragmentations.

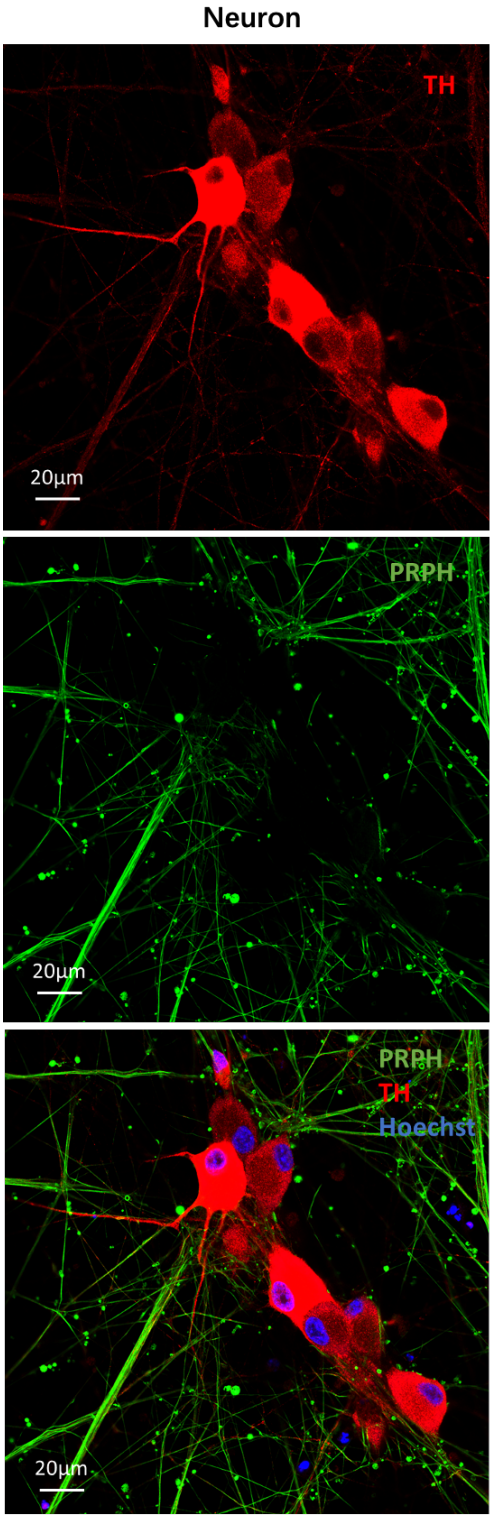


Figure 3.8 Structural characterization of day 42 sympathetic neurons by immunofluorescence staining. TH: tyrosine hydroxylase, an enzyme that catalyses the conversion of L-tyrosine to L-3,4-dihydroxyphenylalanine, which is the rate-limit step in catecholamine synthesis; PRPH: peripherin, a peripheral neuron-specific intermediate filament protein. Anti-TH stained neuron cell body and axon, peripherin staining outlined the axon extension and formation of varicosities. 18 out of 28 (64.29%) nucleated cells (confocal image n=2) are double positive for TH and Peripherin.

Maturation medium for cardiac myocytes with low glucose and high fatty acid supplements as well as prolonged culture duration from 20 days to 40 days significantly enlarged the surface area of hiPSC-CMs and its nuclear. Sarcomere length also extended from 1.593±0.018 (n=22) to 1.877±0.028 (n=19) which is close to normal adult cardiac myocytes[181] (Fig. 3.9). Expression of the *MYH6* gene declined while *MYL2* increased in the maturated day 40 cardiac myocytes. *MYH6* encodes cardiac myosin heavy chain α which is abundantly expressed in both atria and ventricles in the foetus, and switched to β isoform in the ventricle, predominantly expressed only in atrial after birth. *MYL2* on the contrary encodes an adult isoform of myosin light chain and was found to elevate in the day 41 hiPSC-CMs.

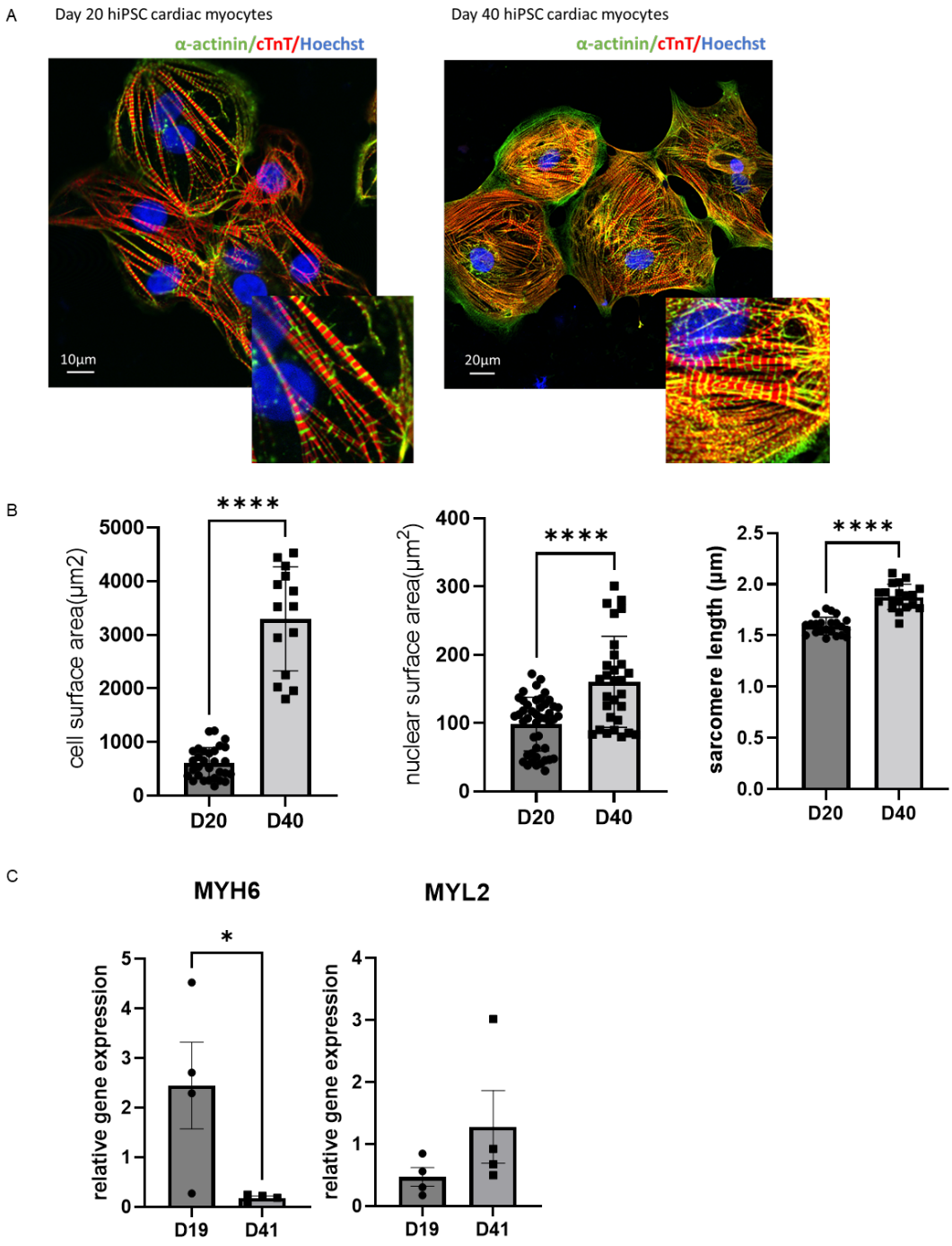


Figure 3.9 Maturation medium and prolonged culture induce structural maturation of hiPSC-CMs. A. confocal image of day 20 and day 40 cardiac myocytes stained by anti-α-actinin and anti-cardiac troponin T (cTnT). hiPSC-CMs of both ages had well-structured sarcomere, but myofibrils in day 40 cardiac myocytes were more densely packed. B. Cell size, nuclear size, and sarcomere length were significantly increased in maturated hiPSC-CMs. Cell size 606.3 ± 53.02 μm^2 (n=30) to 3300 ± 258.7 μm^2 (n=14); nuclear size increased from 98.46 ± 5.879 μm^2 (n=45) to 160.5 ±12.39 μm^2 (n=29); sarcomere length increased from 1.593 ± 0.018 μm (n=22) to 1.877 ± 0.028 μm (n=19), $p<0.05$; C. Expression of the *MYH6* gene declined (2.452 ± 0.8731, n=4 vs 0.1824 ± 0.0386, n=4, $p<0.05$) while *MYL2* increased (0.4727 ± 0.1493, n=4 vs 1.280 ± 0.5867, n=4, $p>0.05$) by maturation.

PHOX2B was expressed in hiPSC-SNs at the early induction stage. It is a transcription factor involved in the differentiation of noradrenergic neuron populations that is constitutively expressed in sympathoadrenal lineage neural crest cells derived from neuroblastoma. TH and peripherin expression were detected on day 20 and day 42. Peripherin is a neural filament protein expressed in the peripheral nervous system that forms a structural network.

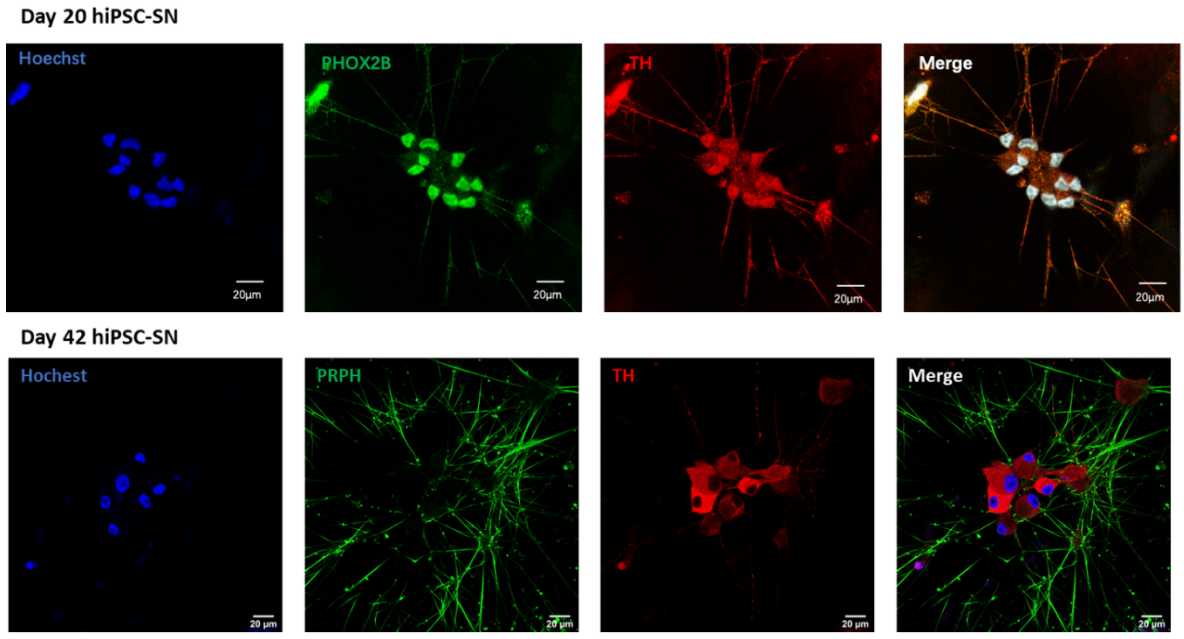


Figure 3.10 Sympathetic neurons immunofluorescence staining. Day 20 hiPSC-SNs stained positive for PHOX2B in the nucleus and TH in cytoplasm. The PHOX2B expression in the nucleus was assessed using ImageJ Coloc2. Pearson's correlation coefficient of 0.85 was obtained, which indicated a strong positive correlation between Hoechst and PHOX2B signals. Day 42 hiPSC-SNs which expressed TH also had abundant axons stained by anti-peripherin. The percentage of double-positive stained cells was 64%.

3.3.3 Functional phenotype of hiSPC-CM and hiPSC-SN

3.3.3.1 Electrical mapping of hiPSC-CM

The membrane action potential is a crucial characteristic of cardiac myocytes, and electrical mapping serves as a method to assess the field potential (FP) of a cell layer on the electrode area, reflecting the summation of action potentials across these cells. The recorded signal

typically comprises a QRS wave during stimulation when cells depolarize and a T wave as repolarization occurs (Fig. 3.11A). In hiPSC-induced cardiac myocytes exhibiting spontaneous contractions, a baseline recording revealed normal QRS and T waves. Upon the introduction of 1 μM isoprenaline, a notable shortening of field potential duration and an increase in heart rate were observed (Fig. 3.11B), while the conduction velocity remained at the same level (Fig. 3.11C). The RR interval was shortened by isoprenaline from 0.968±0.055s to 0.501±0.011s (n=7), and field potential duration from 0.323±0.013s to 0.191±0.010s (n=6), corrected FPD from 1.758±0.111s to 1.164±0.033s (n=6), $p<0.01$.

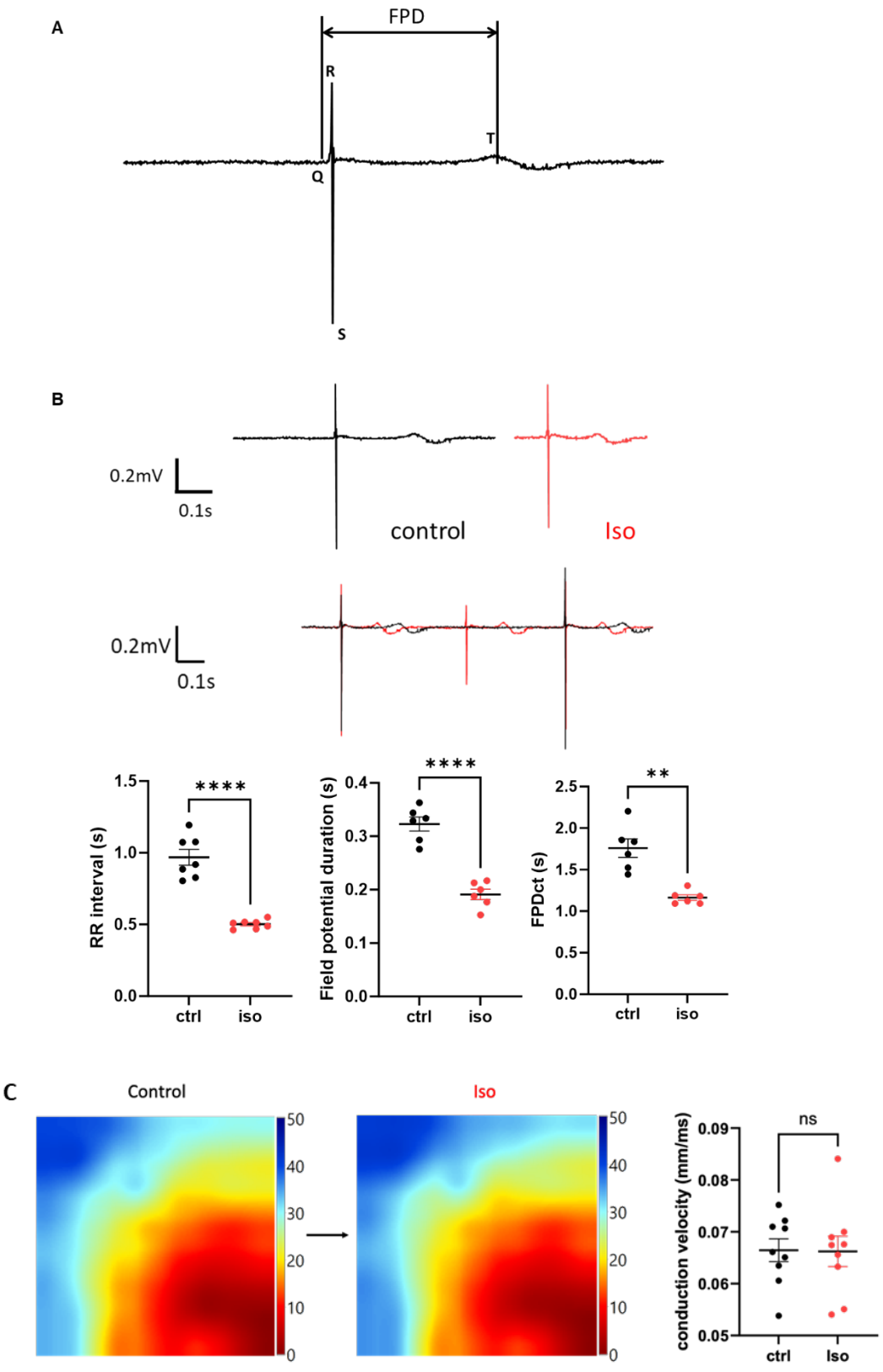

A
FPD
R
T
Q
S
B
0.2mV
0.1s
control
Iso
0.2mV
0.1s
RR interval (s)
****
ctrl
iso
Field potential duration (s)
****
ctrl
iso
FPDct (s)
**
ctrl
iso
C
Control
Iso
50
40
30
20
10
0
conduction velocity (mm/ms)
ns
ctrl
Iso

Figure 3.11 Isoprenaline responsiveness in hiPSC-CMs. **A**. Sample MEA recorded electrical signal from hiPSC-CM showed QRS complex and T wave representing depolarization and repolarization respectively. **B**. Application of 1 μM Isoprenaline to hiPSC-CMs (Day 31, replated on MEA two days) remarkably shortened field potential duration and RR interval, indicating beta-adrenergic responsiveness in hiPSC-induced cardiac myocytes. The RR interval was shortened by isoprenaline from 0.968±0.055s to 0.501±0.011s (n=7), and field potential duration from 0.323±0.013s to 0.191±0.010s (n=6), corrected FPD from 1.758±0.111s to 1.164±0.033s (n=6), $p<0.01$. **C. Example activation maps at baseline and 1 μM isoprenaline stimulation**. The activation site located at the right lower corner at both phases. The propagation direction of activation and the conduction velocity were not changed by isoprenaline. The conduction velocity at baseline was 0.0665±0.0022 mm/ms, and 0.0662±0.0029 mm/ms with 2 minutes incubation with isoprenaline (n=9, $p>0.05$). The increased beating rate indicated the automaticity of myocytes was activated by isoprenaline. Thus, field potential duration recorded at each channel displayed shortened waves beats to beats. However, the propagation of the electrical activities among myocyte clusters, which dominated by cellular gap junctions, remained unchanged. This was displayed in the 64-channel conduction map that showed the propagation of electrical signal from the activation channel to the surrounding channels at one beat.

3.3.3.2 hiPSC-SN calcium transient measurement

$[Ca^{2+}]_i$ was measured in hiPSC-SN derived from a healthy cell line ReBl-PATRYR2-WT using calcium-sensitive fluorescent ratiometric dye Fura2-AM. hiPSC-SN were bathed in Tyrode solution to reach a steady basal Ca^{2+} level, then stimulated by angiotensin II (100 nM or 200 nM) followed by 50 mM KCl $[Ca^{2+}]_i$ showed significant elevation from baseline level during the application of AngII (Fig 10, $p<0.05$) given the well-established presence of AT1 receptors on the neuron. Depolarization of neurons with 50 mM KCl also induced an abrupt $[Ca^{2+}]_i$ increase from 1.09±0.01 to 1.38±0.05, $p<0.0001$ (in 100 nM AngII), 1.03±0.01 to 1.44±0.04, $p<0.0001$ (in 200 nM AngII) (Fig. 3.12). These results are consistent with the behaviour of neurons to receptor and voltage activation in the regulation of $[Ca^{2+}]_i$.

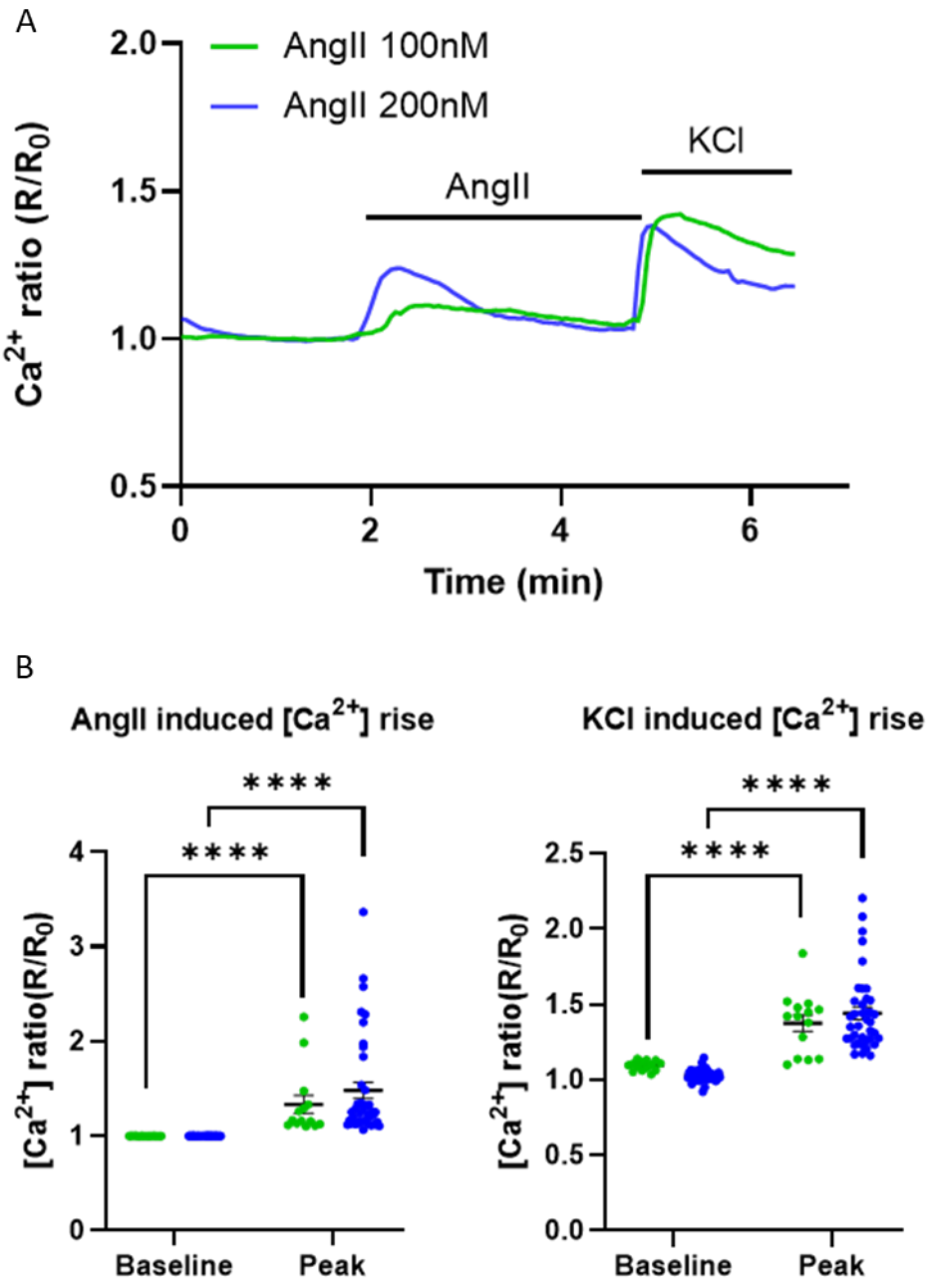


Figure 3.12 Intracellular calcium transient of healthy hiPSC derived sympathetic neuron monoculture (ReBl-PAT$^{RYR2\text{-}WT}$). A. $[Ca^{2+}]_i$ level increased significantly at the application of 100 nM or 200 nM angiotensin II (AngII) and 50 mM KCl. **B.** Exposure to AngII caused significant $[Ca^{2+}]_i$ elevation from 1.00 ± 0.0002 to 1.33 ± 0.09, $p < 0.0001$ (100 nM), and 1.00 ± 0.0004 to 1.48± 0.09, $p < 0.0001$ (200 nM). Further stimulation of neurons with 50 mM KCl also induced an abrupt $[Ca^{2+}]_i$ increase from 1.09 ± 0.01 to 1.38 ± 0.05, $p < 0.0001$ (in 100 nM AngII), and 1.03 ± 0.01 to 1.44 ± 0.04, $p < 0.0001$ (in 200 nM AngII).

3.3.3.3 Noradrenaline release

The capability of hiSPC-SNs in noradrenaline secretion was confirmed by ELISA. The result showed that neuronal culture medium of one million sympathetic neurons derived from a healthy human induced pluripotent cell line ($CP1^{RYR2\text{-}Corr}$) collected after 24-hour incubation contained 32.57 ± 4.31 pg/ml (n=4) noradrenaline interpolated from the standard curve.

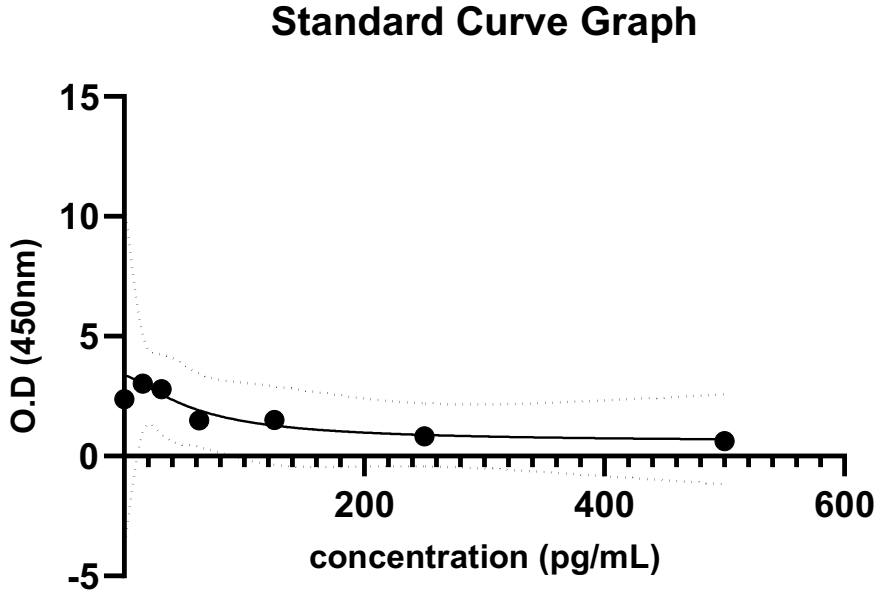


Figure 3.13 Standard curve plotted with reconstituted norepinephrine standard supplied in the kit. The curve was generated by plotting the mean optical density (OD) value for each standard on the y-axis against its concentration on the x-axis.

3.3.4 Cardiac hypertrophy modelling using hiPSC-cardiac myocyte

3.3.4.1 Anatomical alteration in hypertrophic hiPSC-CM

The myofibril structure of hypertrophic cardiac myocytes was distorted as represented by discrete immunofluorescence staining of α-actinin and cTnT (Fig. 3.14A). Myofilament rearrangement is an indicator of stress-induced pathological hypertrophy. To assess cell enlargement, cell size, and nuclear size were measured by immunostaining. Imaging fields for

control and AngII-treated myocytes were randomly selected, and all cells and nuclei with clear and complete borders in the view were involved in surface area measurements to avoid selection bias. Cell surface area significantly increased from 606.3±53.02 μm2 (control) to 1096±79.89 μm2 (AngII 100 nM) and 964.7±161.0 μm2 (AngII 1 μM), $p<0.01$. Nuclear significantly enlarged from 98.46±5.879 μm2 (control) to 135.6±5.63 μm2 (AngII 100 nM) and 135.9±11.0 μm2 (AngII 1 μM), $p<0.01$. This is consistent with activated biosynthesis in the nucleus and enhanced protein synthesis in the cytosol (Fig. 3.14B).

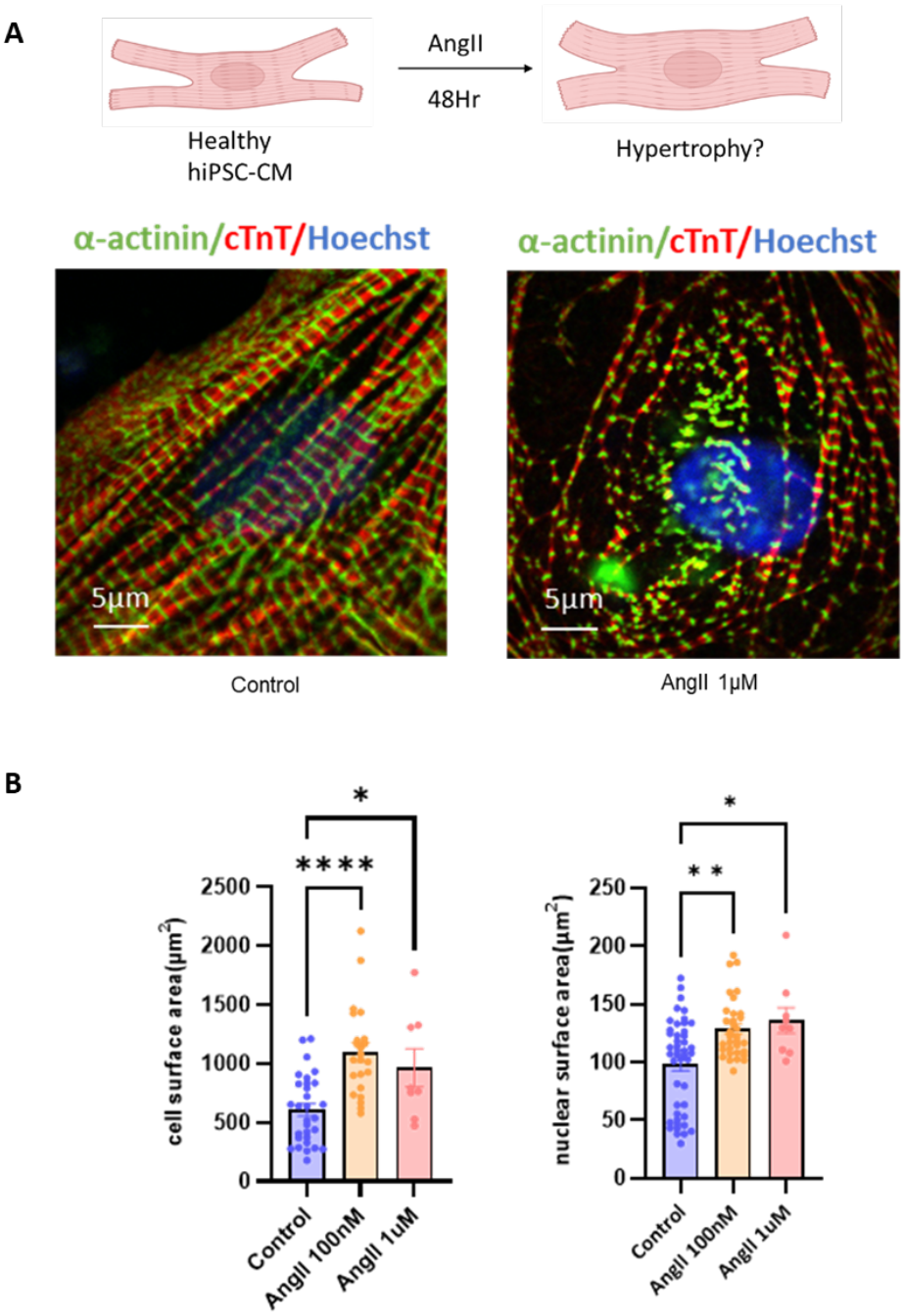


Figure 3.14 A.**Sarcomere distortion with angiotensin II treatment**. The cartoon illustrated the induction of cardiac hypertrophy by exposing healthy hiPSC-CMs to AngII for 48 hours. Immunofluorescence staining of α-actinin and cTnT in hiPSC-CMs displayed disruption of cardiac structural protein with 1 μM AngII incubation. Sarcomeres became fragmented and were not organized into parallel myofilament bundles. **B. AngII-induced hiPSC derived cardiac myocyte enlargement**. Cell and nucleus surface area were obtained using the immunofluorescence staining. Treated with AngII resulted in a significant increase in cell size (left) and nuclear size (right) in the induced cardiac myocytes model. Cell size: 606.3±53.02 μm2 (control, n=30) vs 1096±79.89 μm2 (AngII 100nM, n=23) vs 964.7±161.0 μm2 (AngII 1μM, n=8), $p<0.01$. Nuclear size: 98.46±5.879 μm2 (control, n=45) vs 135.6±5.63 μm2 (AngII 100nM, n=36) vs 135.9±11.0 μm2 (AngII 1μM, n=9), $p<0.01$.

3.3.4.2 Overexpression of foetal gene in hypertrophic hiPSC-CM

Reactivation of foetal genes is well-documented in hypertrophic cardiac myocytes during the process of cardiac remodelling. To explore this phenomenon, qPCR was conducted to assess the RNA expression of B-type natriuretic peptide (*NPPB*), a representative foetal gene, in hiPSC-CMs. The transcription of *BNP* in myocytes treated with 1 μM angiotensin II was significantly elevated ($p<0.01$) compared to the untreated control group. Notably, coincubation with the angiotensin II receptor blocker losartan (20 μM) attenuated the observed increase in *BNP* expression (Fig. 3.15A). Furthermore, the measurement of pro-BNP secretion levels, using an ELISA kit, exhibited a dose-dependent increase in the cell culture medium of hypertrophic hiPSC-CMs (Fig. 3.15A). The reactivation of *BNP* expression was corroborated by iPS-OX1-19 hiPSC-differentiated cardiomyocytes, along with another crucial cardiac hypertrophic marker, *MYH7* (Fig. 3.15B).

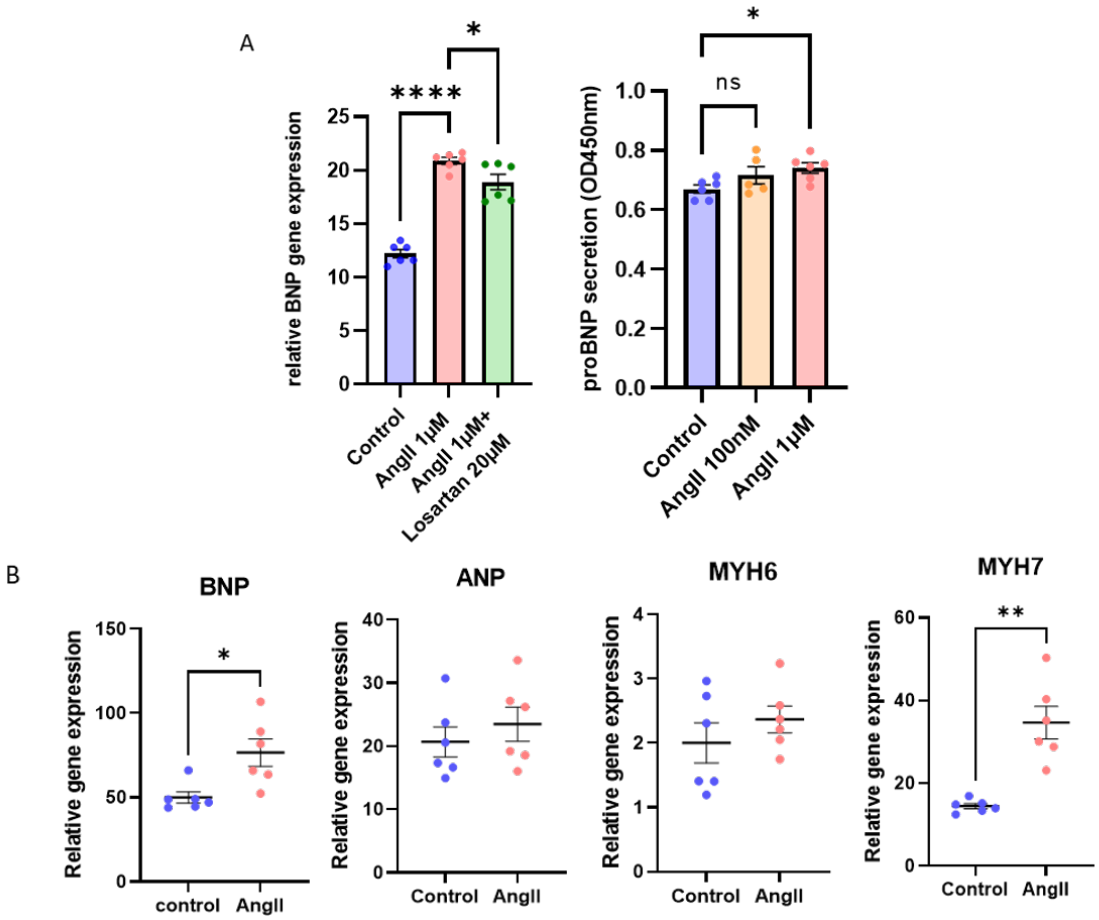


Figure 3.15 Increased fetal gene expression in hypertrophic hiPSC derived cardiac myocytes. **A**. *BNP* mRNA expression significantly increased in 1 μM AngII treated myocytes. Pre-treated myocytes with angiotensin II receptor blocker Losartan were able to antagonize *BNP* enhancement (left). Control: 12.20±0.38, n=6, AngII: 20.87±0.33, n=6, p<0.01; AngII+Lorsatan: 18.90±0.72, n=6, p<0.05. Quantitative ELISA in cell culture supernatant revealed a tendency to increase proBNP secretion in hypertrophic groups (right). Control: 0.67±0.01, n=6; AngII 100nM: 0.72±0.03, n=5, p=0.22; AngII 1μM: 0.74±0.02, n=6, p<0.05. **B**. RT-qPCT repeated with iPS-OX1-19 hiPAC-CMs confirmed a significant increase of *BNP* and *MYH7*, and an increased tendency of *ANP* and *MYH6*. *BNP*: control 49.91±3.33, n=6 vs AngII 76.56±8.11, n=6, p<0.05; *ANP*: control 20.68±2.39, n=6 vs AngII 23.48±2.72, n=6, p=0.46; *MYH6* control 2.00±0.31, n=6 vs AngII 2.37±0.21, n=6, p=0.35; *MYH7* control 14.47±0.63, n=6 vs AngII 34.65±3.94, n=6, p<0.01.

3.3.4.3 Beta adrenergic hyperresponsiveness in hypertrophic hiPSC-CM

Elevated cAMP levels during beta-adrenergic stimulation are commonly associated with hypertrophied myocytes. In this study, hiPSC-CMs loaded with the cAMP FRET-sensor Epac-S^{H187} were sequentially stimulated by 0.3 nM isoprenaline, 100 nM IBMX, and 10 μM FSK. The cytosolic cAMP generation during beta receptor activation was significantly higher in angiotensin II (1 μM) treated iPSC-CM (1.377±0.02, n=28 vs 1.607±0.05, n=39, $p<0.001$) (Fig. 3.16 Top). The nonselective PDE inhibitor IBMX further increased cytosolic cAMP levels. To demonstrate the dynamic operating range of the sensor, 10 μM FSK was added to saturate cytosolic cAMP at the end of the experiments. Both cAMP elevations were more prominent in hypertrophic myocytes. Similarly, the FRET response of hiPSC-CM closely resembled the cAMP response of hypertrophied neonatal rat ventricular cardiomyocytes when stimulated with isoprenaline (Fig. 3.16 Bottom), indicating a conserved phenotypic response across model systems.

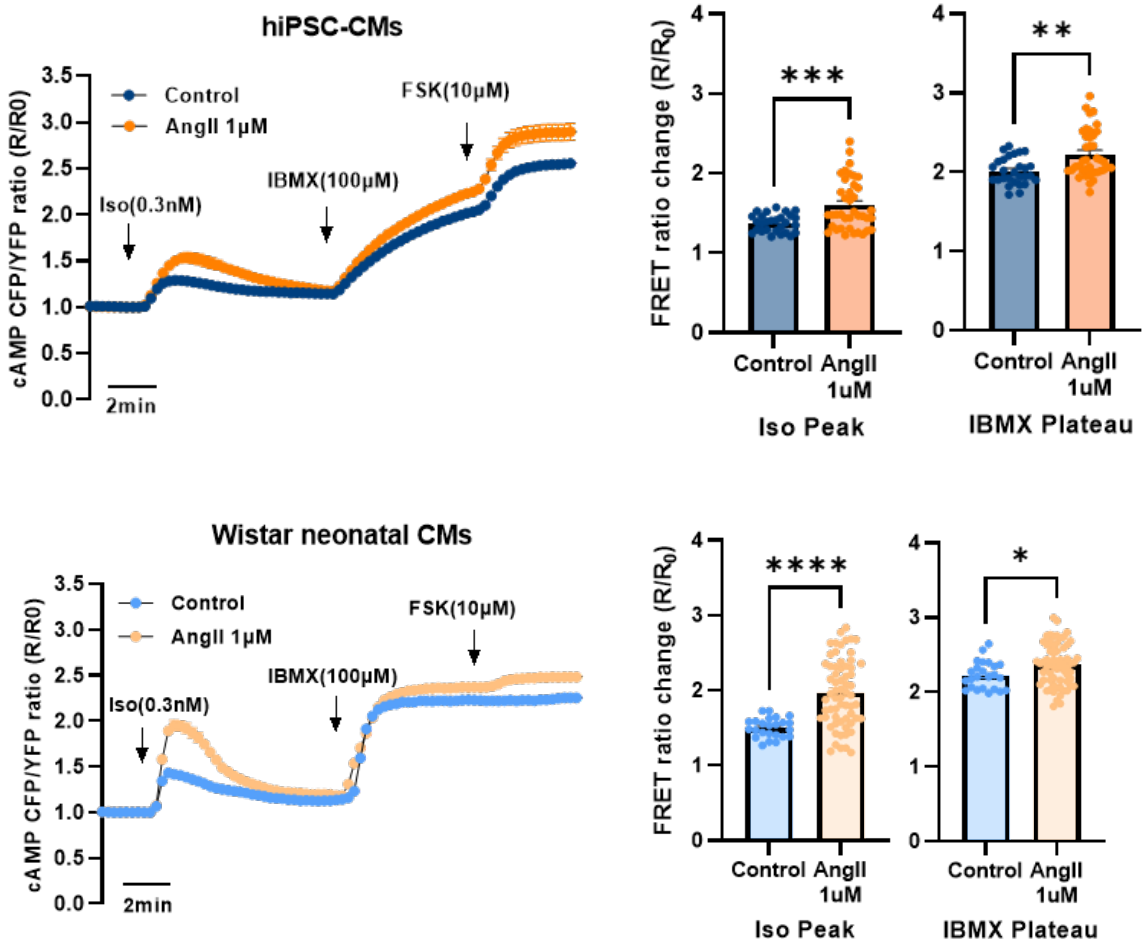
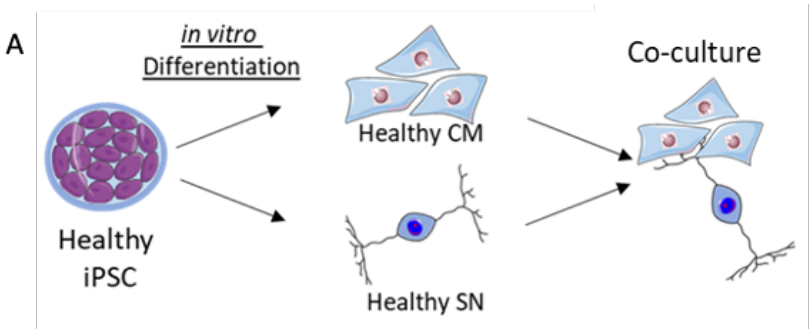


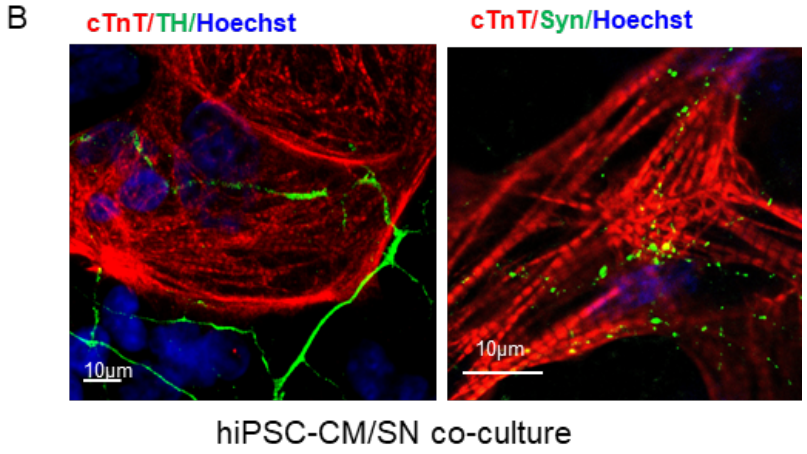
Figure 3.16. Grouped data showing dynamic increases in cAMP in response to Isoproterenol, IBMX, and Forskolin in hiPSC-CM (Top panel) and Wistar neonatal cardiomyocyte (Bottom panel) models. 1 μM Angiotensin II treated group caused beta-adrenergic hyperresponsive and increased maximal cAMP level in both models. In the hiPSC model, isoprenaline-stimulated cAMP increased from 1.377±0.02 (n=28) to 1.607±0.05 (n=39) in the hypertrophic group, $p<0.001$; IBMX boosted cAMP level was also significantly higher in AngII treated hiPSC-CMs (2.228±0.5, n=39) than control (2.013±0.03, n=28), $p<0.01$. The tendency of cAMP elevation was similar in the Wistar rat model. Isoprenaline triggered cAMP: control 1.50±0.03, n=24 vs AngII 1.97±0.06, n=64, $p<0.0001$. IBMX induced cAMP: control 2.226±0.04, n=24 vs AngII 2.37±0.04, n=64, $p<0.05$.

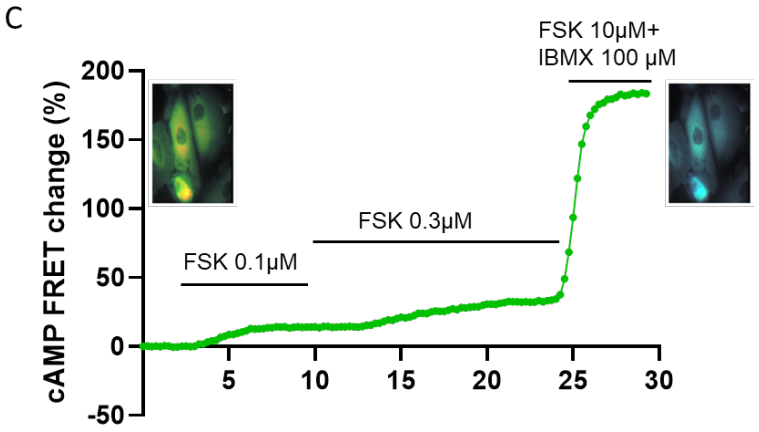
3.3.5 Neurocardiac coculture establishment

To assess the viability of myocytes and neurons derived from hiPSC as a reliable in vitro model for neurocardiac disease studies, mature hiPSC-CMs (SFC854) and hiPSC-SNs (CP1RYR2-Corr) were co-cultured to establish neurocardiac connectivity (Fig. 3.17A). Upon re-plate, hiPSC-SNs extended axons towards hiPSC-CMs, forming varicosities in close proximity to the myocytes, indicating the establishment of a neurocardiac junction. Staining with cTnT and TH confirmed the co-existence and connection of cardiac myocytes and sympathetic neurons in the co-culture. Additionally, anti-synapsin staining revealed varicosity formation around cardiac myocytes. Cardiac myocytes aggregated to form clusters, with sympathetic neurons dispersing around these myocyte clusters. Axons extended to establish connections with both myocytes and other neurons (Fig. 3.17B), mirroring patterns observed in earlier reports[117].

Subsequently, I recorded cAMP FRET changes in hiPSC-CM in monoculture and co-culture with hiPSC-SN condition in response to two concentrations of Forskolin (FSK) to verify the functional neurocardiac connection (Fig. 3.17D). Original traces showed increased cAMP generation in hiPSC-CM in response to FSK. Cytosolic cAMP at baseline showed no significant difference between hiPSC-CM in monoculture and co-culture. However, when stimulated by FSK (0.1 μM and 0.3 μM), the increase of cAMP was significantly higher in myocytes co-cultured with hiPSC-SN (n=9) than monocultured myocytes alone (n=19) (FSK 0.1 μM: 24.73±3.49% vs 9.30±0.53%, $p<0.0001$; FSK 0.3 μM: 38.87±1.71% vs 21.33±1.26%, $p<0.0001$). The exaggerated cAMP response of the myocyte in the co-culture (compared to myocyte monoculture) is probably a combination of FSK-activated myocyte cAMP, and the likely FSK-activated cAMP in neurons enhancing transmission to further increase cAMP in myocytes via beta receptor activation of the second messenger pathway.


A
in vitro
Differentiation
Healthy
iPSC
Healthy CM
Healthy SN
Co-culture


B
cTnT/TH/Hoechst
cTnT/Syn/Hoechst
10μm
10μm
hiPSC-CM/SN co-culture


C
FSK 10μM+
IBMX 100 μM
FSK 0.3μM
FSK 0.1μM
cAMP FRET change (%)
200
150
100
50
0
-50
5
10
15
20
25
30

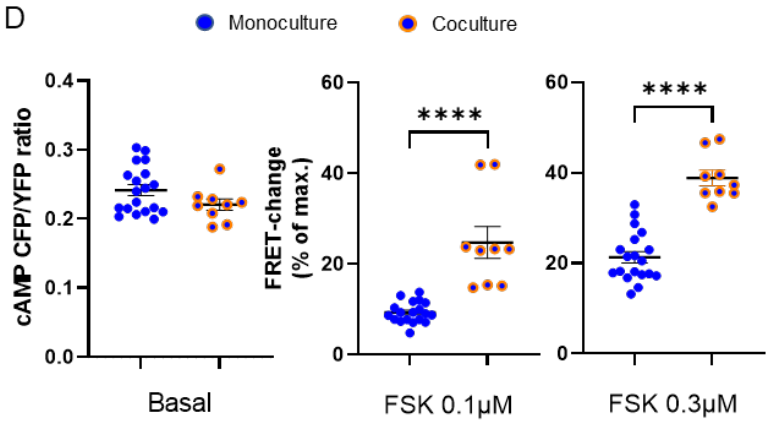

D
Monoculture
Coculture
cAMP CFP/YFP ratio
0.4
0.3
0.2
0.1
0.0
FRET-change
(% of max.)
60
40
20
0
****
****
Basal
FSK 0.1μM
FSK 0.3μM

Figure 3.17 The phenotype of hiPSC derived neuro cardiac monoculture. A: Cartoon showing cardiac myocytes and sympathetic neurons differentiated from a healthy hiPSC line and co-cultured together. B: hiPSC-derived neurocardiac co-culture fixed and stained with cTnT (CM) and TH (SN) (left), cTnT (CM) and Syn (SN) (right). The overlay showed sympathetic neurons dispersed around cardiac myocyte clusters and extended axons towards myocytes, and dot staining of anti-synapsin showed varicosities. C: Representative original FRET trace showing dynamics of cytosolic cAMP changes in response to adenylyl cyclase activator Forskolin (FSK, 0.1 and 0.3 μM) in healthy 20-day iPSC-CM. Saturation of the sensor was achieved by using FSK (10 μM) and IBMX (100 μM). E: Comparison of myocytes cytosolic cAMP changes between iPSC-CM monoculture and co-culture with iPSC-SN. Baseline cAMP level showed no significant difference between monoculture and co-culture, while co-culture with SN activated myocytes' response to FSK with a significantly higher increase of cytosolic cAMP. Baseline: 0.24±0.01% (n=19) vs 0.22±0.01% (n=9), P=0.11; FSK 0.1 μM: 9.30±0.53% (n=19) vs 24.73±3.49% (n=9), p<0.0001; FSK 0.3 μM: 21.33±1.26% (n=19) vs 38.87±1.71% (n=9), p<0.0001

3.4 Discussion

Here, I present a differentiation protocol for the induction of sympathetic neurons and for the generation of cardiac myocytes from two human iPSC cell lines. Both myocytes and neurons expressed cell-type-specific structural proteins and membrane receptors that underpin specific physiological functions in response to stimuli. Following calcium and cAMP phenotyping of monoculture hiPSC-SN and hiPSC-CM, I established hiPSC neurocardiac co-cultures and demonstrated anatomical and functional connectivity.

3.4.1 hiPSC cardiac myocyte differentiation and characterization

In the past decades, many protocols have been established for the differentiation of cardiac myocytes from hiPSC[94,97,175,182]. In this study, I adapted widely used defined RPMI/B27 medium monolayer small molecule guided differentiation protocol.[149] The Wnt signalling pathway has been shown to have a biphasic effect in directing cardiogenesis. Early exposure to the GSK3 inhibitor CHIR99021 promotes the induction of mesoderm progenitor cells.

Moreover, the following inhibition of canonical Wnt signalling by Wnt-C95, results in further differentiation to cardiac fate[94]. Indeed, the concentration of these small molecules influences the induction proficiency across different cell lines[94]. Here I used 6 μM CHIR99021 for 48 hours (Day 0-2), 2.5 μM Wnt-C95 for 48 hours (Day 3-5), and yielded ca. 80% cTnT and MLC2v double-positive cardiac myocytes from two hiPSC lines. In addition, I found that hiPSC confluency to commence cardiomyocyte differentiation is critical in optimizing cell yield. A high confluency at 90% in a 12-well plate was optimal in generating cardiomyocytes with spontaneous contraction from Day 7-9 following induction. I also observed that derived myocytes were best purified by shifting the nutritional supply from glucose to fatty acid using glucose-free RPMI medium supplemented with 5 mM sodium lactate from Days 11-14. This helped minimize non-cardiac cell proliferation over cardiac myocyte maturation, since other cell types required glucose for differentiation and are intolerant to lactate metabolism as reported by Gasper et al 2014[183]. Therefore, I conducted experiments at around day 20 to avoid over-expansion of other cell types. For longer cell maintenance, the medium could be changed to a low glucose maturation medium supplemented with fatty acids to minimize non-cardiac cell enhancement[184]. Also, cell size and expression of adult myosin light chain isoform were remarkably increased by the maturation medium.

Electrophysiological property is critical in hiPSC-CMs phenotyping since the normal function of the heart relies heavily on an effective excitation-contraction coupling. Hence, I characterized the action potential of hiPSC-CMs using electrical mapping. The recorded electrical signal from hiSPC with spontaneous contraction showed that the resting heart rate of these cells ranged from 50-90 beats/min. After isoprenaline treatment, FPD and RR were both shortened significantly, indicating that the hiPSC-CM expressed beta-adrenergic receptors and were responsive to stimulation.

3.4.2 hiPSC sympathetic neuron differentiation and characterization

Coupling of sympathetic neurons to cardiac myocytes is an emerging field to study the role of neuronal-myocyte signaling systems in a dish[158,185], although there are only a few studies that have investigated this coupling using human iPSC cell models[116,119,120]. I differentiated sympathetic neurons from hiPSC based on the published technique by Winbo et al 2020[119]. Since no standardized sympathetic neuronal induction protocol is available to date, our data serve as another validation of this feeder-free, chemical-directed induction process. I found that hiPSC-SN showed typical round cell bodies with extensive axonal outgrowth (Figs. 3.4 and 3.8). Staining of tyrosine hydroxylase and peripherin confirmed these neuron-like cells as catecholaminergic in nature, underscoring them as being sympathetic neurons. ELISA detected noradrenalin secretion in the neuronal culture medium. Their functional electrophysiological properties, including resting membrane potential and action potential kinetics, have been described previously[119].

I further phenotyped these cells and tested their $[Ca^{2+}]_i$ in response to cell stimulation, since Ca^{2+} is a crucial messenger that underpins synaptic plasticity[186] and neurotransmission[187]. Using live cell calcium imaging, I observed that $[Ca^{2+}]_i$ could be enhanced in response to angiotensin II and high extracellular potassium. Angiotensin II acts through AT1 receptors, which activates phospholipase C that cleaves phospholipid phosphatidylinositol 4,5-bisphosphate (PIP2) into diacylglycerol (DAG) and inositol 1,4,5-trisphosphate (IP3). IP3 then diffuses in the cytosol and binds to IP3 receptors on the endoplasmic reticulum that in turn releases stored Ca^{2+} into the cytosol[188]. High potassium induced depolarization activates plasma membrane voltage-gated calcium channels, which allows extracellular Ca^{2+} influx to activate downstream signaling pathways involved in exocytosis of classical transmitters[189]. In particular, Winbo et al. 2021 demonstrated the utility of this neuronal monoculture system

when sympathetic neurons derived from a LQT1 lineage had increased excitability and transmission, suggesting that a component of the disease phenotype may also reside in the neuron[121]. When taken together with Winbo, our observations are consistent with the notion that our hiPSC-derived neurons are sympathetic in nature and can respond to classical physiological stimuli.

In both cardiac myocyte and sympathetic neuron differentiation, batch-to-batch inconsistency is still a great hindrance to the application of cells. Monitoring the homogeneity of hiPSCs is a critical factor in achieving a higher induction efficiency as it represents the pluripotency that these hiPSCs possess. Therefore, it is important to be gentle while passaging hiPSCs to avoid physical stimulation that could induce unwanted differentiation. Also, adjustment of seeding density based on the proliferation rate of each batch of cell and different cell lines, and regular dissociation and reseeding are all useful to keep the stem cells thriving.

3.4.3 hiPSC-CM recapitulate cardiac hypertrophy *in vitro*

In this chapter, I characterized the pathophysiological function of hiPSC-CMc exposed to a hypertrophic agent. These cells hypertrophied following treatment with angiotensin II incubation in 100 nM, or 1 μM angiotensin II for 48 hours. Significant observed significant increases in cell size and nuclear enlargement with sarcomere disarray was observed. In addition, expression of the fetal gene *BNP* and gene *MYH7*, which are established markers of cardiac hypertrophy, were also elevated. When stimulated by isoproterenol, cAMP levels were significantly enhanced in hypertrophic hiPSC-CM, which indicates remodelling of beta receptor coupled cAMP signalling. This adrenergic hyper-responsiveness was also

recapitulated in neonatal Wistar rat ventricular myocytes, thus supporting the idea that the signalling pathway is conserved across mammalian systems.

Pressure and volume overload, along with inherited mutations, are prevalent causes of pathological cardiac hypertrophy[165]. Such hypertrophy can lead to various adverse outcomes, ranging from heart failure to cardiac arrest, imposing a substantial burden on affected individuals as the condition progresses. Consequently, the identification of key molecular regulators for targeting cardiac hypertrophy holds significant clinical importance. Despite considerable progress in understanding the mechanisms underlying cardiac hypertrophy, numerous interconnected correlations remain to be fully elucidated.

As research continues to unveil additional pathways responsible for inducing hypertrophic changes in cells, such as PI3K-AKT1 and RAS-RAF-MEK-MAPK in physiological hypertrophy, as well as PLC-PIP2-IP3 and cAMP-PKA in pathological hypertrophy[161], it becomes imperative to identify common targets involved under different circumstances. This pursuit not only holds therapeutic promise but also raises questions about the existence of specific pathological hypertrophic targets within these multiple integrated signalling pathways. Further exploration in this direction could offer valuable insights into determining the prognosis of hypertrophy.

However, human cardiac myocytes are terminally differentiated cells where there is a limited supply for in vitro studies. The development of human iPS cells and cardiac myocyte induction protocol provide a promising platform as a human disease model. For in vitro modelling, isoproterenol, adrenaline, or noradrenaline mimic neurohormonal activation during pressure and stress overload. Agonists for angiotensin II type I receptors and endothelin-1 receptors are all effective inducers for cardiac hypertrophy.

The central focus of this chapter revolves around the validation of a hypertrophic model using human induced pluripotent stem cells (hiPSCs) in comparison to a more homogenous animal model, specifically rat ventricular myocytes. In vitro exposure to angiotensin II induced hypertrophic responses in both hiPSC and animal models, manifesting as cell enlargement, expansion of nuclear size, overexpression of active genes during early cardiac development, and heightened responsiveness of the second messenger cAMP in hiPSC-derived cardiac myocytes (hiPSC-CMs).

Morphological changes indicative of cardiac hypertrophy, such as fragmented myofilaments and a substantial twofold increase in cell size ($p<0.01$), were consistently observed in angiotensin II-treated hiPSC-CMs, aligning with common hypertrophic features. Elevated expression of hypertrophic marker genes, including *BNP*, *ANP*, *MYH6*, and *MYH7*, as well as increased proBNP protein secretion, further underscored the hypertrophic phenotype. Comparative functional analysis with rat ventricular myocytes revealed the conservation of beta-adrenergic hyperresponsiveness, characterized by an augmented cAMP generation in response to isoprenaline treatment, in both models.

In essence, the exposure of cultured hiPSC-CMs to stressors like angiotensin II successfully mimics the activation of downstream signaling pathways triggered by stress or pressure overload in the heart. The recapitulation of hypertrophic phenotypes in hiPSC-CMs positions this model as a valuable tool for molecular studies aimed at discovering therapeutic targets in the context of hypertrophy.

3.4.4 Neural-cardiac signalling in co-culture

Several groups have successfully coupled healthy iPSC sympathetic neurons and cardiac myocytes and shown the power of the neuron to drive cardiac excitability[116,119,120]. I further

demonstrate the utility of the hiPSC neurocardiac co-culture system with additional validating signals. First, both neurons and myocytes were able to survive and thrive in co-culture. Secondly, immunostaining confirmed the formation of neuronal varicosities adjacent to myocyte clusters, which is the anatomical basis for functional connectivity (Fig. 3.5). Physiologically, the increased cytosolic cAMP response to adenylyl cyclase activation was found to be enhanced in myocytes co-cultured with neurons compared to myocyte monocultures alone, suggesting greater cAMP dependent facilitated neurotransmission. The augmented enzyme function could also be a result of myocyte maturation when co-culturing with neurons[159,190], where recent studies suggest secreted neurotrophic factors enhance the synaptic efficacy of the co-culture[185,191,192]. However, our co-culture responded in a dynamic fashion to activation of cAMP with forskolin, resulting in a larger FRET signal in co-cultured myocytes compared to myocytes in monoculture. Here, forskolin application to the co-culture could give rise to increased neurotransmission that would act on cardiac myocytes as an extra stimulus to raise myocyte cAMP.

In conclusion, I have recapitulated various anatomical and physiological characteristics of human cells by hiPSC-CM and hiPSC-SN. Whether these cell types have the full transcriptomic atlas of actual human cells remains to be established. Nevertheless, the hiPSC monoculture and co-culture preparations behave in a manner that mimics key physiological responses seen in other mammalian cell types and therefore may provide a framework for target discovery and a mechanistic understanding of human pathophysiological states.

3.5 Limitations

Although the induction protocols for cardiac myocytes and sympathetic neurons are robust, variations in yield and purification could be seen in different batches and cell lines. Increasing

the number to involve more cell lines and differentiation batches from each cell line would be useful to improve the reliability of the conclusion. Also, further efforts should be made to improve the reproducibility of induction protocols. Strategies include adjusting the concentration of small molecules used in the differentiation according to the responses of different cell lines and exploring and targeting more precise or critical signaling pathways that determine the direction of cell differentiation.

Cardiac hypertrophy is a compensation response of the heart to increased workload, while monolayer hiPSC-CM culture lacks the three-dimensional organization to mimic the structural changes within heart chambers and to recapitulate the effect of hypertension or mechanical stretch as an increased force on the heart. Cell culture in a dish can only be used to investigate molecular signalling by modifying relative pathways with gene transfer or chemical substances. Furthermore, the heterogeneity of hiSPC-CM could obscure the exact responsible target for the disease phenotypes as other cell types besides working cardiac myocytes might also play a role in triggering hypertrophic change. For example, fibroblasts were among the implicated components that mediate cardiac hypertrophy[193] and may also contribute to the initiation of hypertrophic changes, further complicating the interpretation of experimental outcomes.

CHAPTER 4: Catecholaminergic polymorphic ventricular tachycardia disease modelling using hiPSC-derived cardiac myocytes and sympathetic neuron

4.1 Background

4.1.1 Catecholaminergic polymorphic ventricular tachycardia: a disease of the sarcoplasmic reticulum calcium release channel

CPVT is an important cause of sudden cardiac death among the young[194]. Although it has a relatively low prevalence of 1 in 5,000 to 10,000, the mortality rate is 30-50% in untreated patients by age 40 years[195]. Patients with CPVT usually have normal heart structure and normal resting electrocardiogram, which mask early diagnosis and hinder proper management to prevent the onset of disease. Pathogenesis of CPVT was reported to be associated with dysregulated intracellular calcium signalling in cardiac cells[152,196]. 60%-75% of CPVT patients were found to have a hereditary disease with mutations affecting the function of several proteins that assemble to regulate the calcium release channel on the sarcoplasmic reticulum membrane (Fig 4.1B), among which a *RYR2* gain-of-function mutation accounts for over 70% of the phenotype (CPVT1).

4.1.2 Exercise and activation of the sympathetic nervous system facilitates the onset of CPVT

CPVT patients are usually asymptomatic until increased sympathetic tone such as exercise or emotional stress triggers the lethal arrhythmia[197]. Increased sympathetic tone phosphorylates RyR2 receptors to facilitate the opening of the channel through adrenergic signalling, which

exacerbates calcium efflux and predisposes to delayed afterdepolarizations. Targeting sympathetic activity using beta-blockers is the current first line of treatment for CPVT patients, with resistant cases progressing to more radical cardiac stellectomy[155]. Although both interventions are not without significant off-target side effects (e.g. fatigue and Horner's syndrome respectively). My thesis has asked two questions. Firstly, is CPVT also a disease of the sympathetic nervous system? Secondly, are cardiac sympathetic neurons a viable target for gene therapy to turn down the gain of neurotransmission in CPVT?

4.1.3 Disease in a dish: Human cell modelling of CPVT

Primary cells from patients with genetic-based arrhythmias are largely unavailable because of invasive patient tissue sampling and the non-regenerative nature of somatic cells. Human induced pluripotent stem cell (hiPSC) technology is a useful platform for the study of human genetic diseases especially those involving the interaction of two or more cell types, as it offers the chance to generate unlimited amounts and multiple types of somatic cells carrying the same genetic information[87,88].

Therefore, the objective of this chapter was to identify cellular neurocardiac arrhythmia mechanisms that underpin life-threatening cardiac events in CPVT using a hiPSC-derived co-culture model. My first step was to generate hiPSC-CMs and hiPSC-SNs and conduct physiological phenotyping of these differentiated cells for validation. Secondly, I established monocultures and co-cultures from a patient with a CPVT genotype (with isogenic pairing) to generate a model of triggered arrhythmia for the study of neurocardiac interaction. (Fig. 4.1)

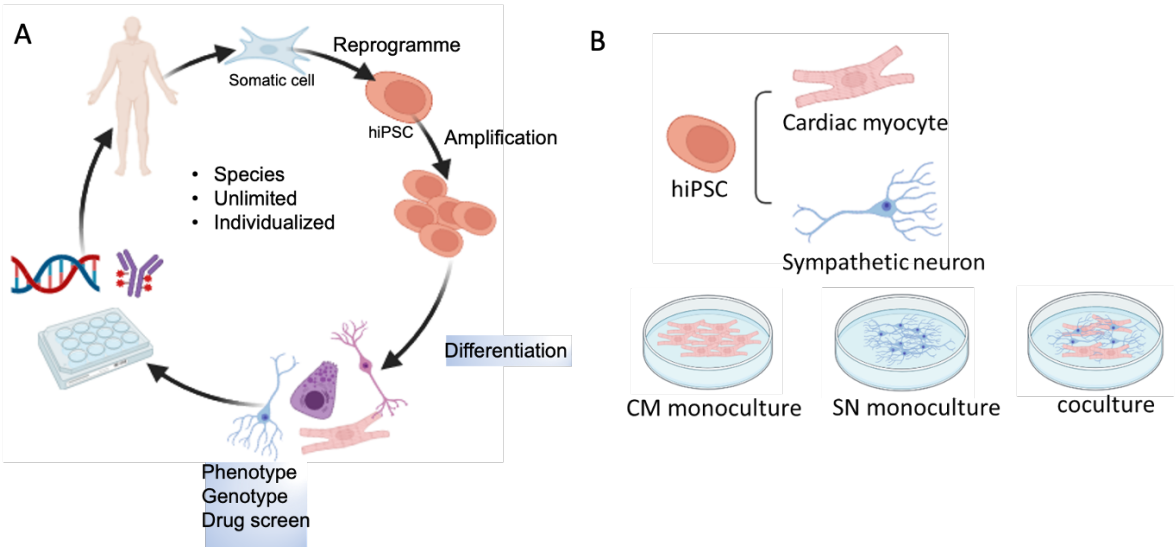


Figure 4.1 A: Schematic diagram of the generation and application of hiPSCs. Somatic cells taken from patients can be reprogrammed to a pluripotent state, and differentiated to various cell types in vitro to apply physiological context to a human disease. **B:** Overview of study design. To induce cardiac myocytes and sympathetic neurons from hiPSCs, use monoculture, and co-culture to study sympathetically triggered inherited arrhythmia.

4.2 Methods

4.2.1 Flow cytometry

The established protocols, as verified in chapter three, were systematically employed for the induction of cardiac myocytes and sympathetic neurons in two isogenic pairs of hiPS cell lines: CP1 (CP1$^{RYR2\text{-}6737\text{-}T/C}$) vs WT (CP1$^{RYR2\text{-}Corr}$), and ReBl-PAT$^{RYR2\text{-}WT}$ vs ReBl-PAT$^{RYR2\text{-}13489C/T}$. To validate the differentiated cell types, flow cytometry, utilizing cell type-specific antibodies,

was implemented. In brief, cells underwent fixation and permeabilization before being subjected to staining with flow antibodies. For hiPSC-CMs, anti-cTnT and anti-MLC2v antibodies were utilized, while anti-TH antibodies were employed for hiPSC-SNs. Subsequently, the flow cytometer detected the fluorescence of the stained population in the prepared cell samples. The outcomes of double-stained hiPSC-CMs were represented as a density plot featuring a quad gate demarcating positive and negative populations. Conversely, single-stained hiPSC-SNs data were depicted as a histogram with a ranged gate indicating the negative control region and a bisector gate separating the positive and negative populations.

4.2.2 Immunofluorescence imaging

Cell morphologies were compared between wild-type and CPVT hiPSC-CMs and hiPSC-SNs using immunofluorescence staining. D20 cardiac myocytes and D40 sympathetic neurons were replated on glass bottom FluoroDish and cultured for 3 to 5 more days before fixing with 4% formaldehyde. After permeabilized and blocked in TBS plus 0.5% triton and 6% donkey serum, hiPSC-CMs were stained with anti-cTnT and anti-α-actinin to visualize sarcomere, with anti-RyR2 and anti-α-actinin to confirm expression of RyR2 receptor on cardiac myocytes and with anti-RyR2 and anti-SERCA2 to explore the subcellular localization of RyR2 receptor. hiPSC-SNs were double-stained with anti-TH and anti-PRPH to validate cell type, with anti-nAChR or anti-RyR2 and anti-TH to confirm expression of nicotinic acetylcholine receptor and RyR2 receptor on sympathetic neurons, with anti-RyR2 and anti-SERCA2 to explore the subcellular localization of RyR2 receptor in neurons. Images were taken by Leica confocal microscope (Leica TCS SP5) and analysed with LAS X and ImageJ software.

The measurement of sarcomere length involved utilizing the cTnT and α-actinin double-stained image, with the distance between two Z lines marked by the anti-α-actinin antibody. Within each cell, three sarcomeres were randomly chosen, and the average of their respective lengths

was computed to determine the sarcomere length. Meanwhile, the axonal diameter was determined by assessing the thickness of peripherin-stained neurofilaments. Comparative analysis of sarcomere length and axonal diameter was conducted between disease and healthy cell lines.

4.2.3 Calcium imaging

Intracellular calcium concentration ($[Ca^{2+}]_i$) was assessed in hiPSC-induced cardiac myocytes and sympathetic neurons using the Fura2-AM live cell calcium indicator. Chemical reagents were dissolved in Tyrode solution and delivered to the cells through a perfusion system. In the cardiac myocyte monoculture, calcium discharge in response to 0.3nM, 1nM isoprenaline, 50 mM KCl, and 10 mM caffeine was recorded. Calcium transients in hiPSC-SNs was triggered by 50mM KCl, 100μM nicotine, and 10mM caffeine. In the neurocardiac coculture, 50 mM KCl was administered, and cytosolic calcium concentration in hiPSC-SNs was quantified. The region of interest (ROI) for fluorescence intensity capture was selected based on microscopic features. Image acquisition was performed at 340nm and 380nm excitation using a QICLICK digital CCD Photometrics camera connected to an OptoLED fluorescence imaging system, which was housed on a Nikon eclipse Ti2 inverted microscope equipped with a 40× oil immersion objective.

4.2.4 Förster resonance energy transfer

As an important upstream signalling molecule in regulating calcium, cytosolic cAMP was measured using the FRET cAMP sensor Epac-S^{H187}. The FRET sensor working mechanism was introduced in chapter two. cAMP generation was induced using 10nM isoprenaline for hiPSC-CM, nicotine for hiPSC-SN (50μM) and neurocardiac coculture (10μM) and saturated using 25μM Foskolin plus 100μM IBMX. Nicotine was used to activate neurons in the

coculture, but the output signal was recorded from cardiac myocytes to reflect incoming stimulation from activated neurons. Approximately 10 times more adenoviral load was required to infect hiPSC-SN compared to hiPSC-CM, thus a low titer of adenoviral vector can transfect the FRET sensor into cardiac myocytes in the neurocardiac coculture without infecting sympathetic neurons. Cells were prepared as a monolayer on coverslips; viral volume was adjusted by cell amount and incubated overnight. After transfection, cells were allowed to replicate and express the FRET sensor for two to three days. During the experiment, coverslips were transferred to the holding chamber on the microscope and perfused by Tyrode solution and stimulating reagents. Images were captured in one frame per 15 seconds by fluorescent microscope to record CFP (480nm) and YFP (535nm) emission intensity change. The FRET ratio (CFP/YFP) was normalized to the saturation level.

4.2.5 Electrical mapping

The investigation involved the characterization and comparative analysis of cardiac action potentials across genotypes (WT versus CPVT) and diverse culture methods (monoculture versus co-culture) utilizing a microelectrode array. Post differentiation, cardiac myocytes were either replated on microelectrodes to form syncytium monolayers or co-seeded with sympathetic neurons to establish synapses. Electrical mapping procedures were conducted upon the recovery of cardiac spontaneous contractions. In the monoculture setup, baseline and 1μM Isoprenaline-stimulated field potentials were recorded. Conversely, the coculture system was subjected to stimulation by 100μM nicotine to replicate the accelerated heart rate induced by activated sympathetic neurons. EMapRecord 5 acquisition software was employed for the recording of electrical signals, and subsequent analysis was conducted using EMapScope 5. Parameters assessed encompassed field potential duration (FPD, corrected through the

equation: FPDct = FPD/RR^1/2), RR interval, the width of the QRS complex (depolarization duration), and the width of the T wave (repolarization duration) (Fig. 4.2).

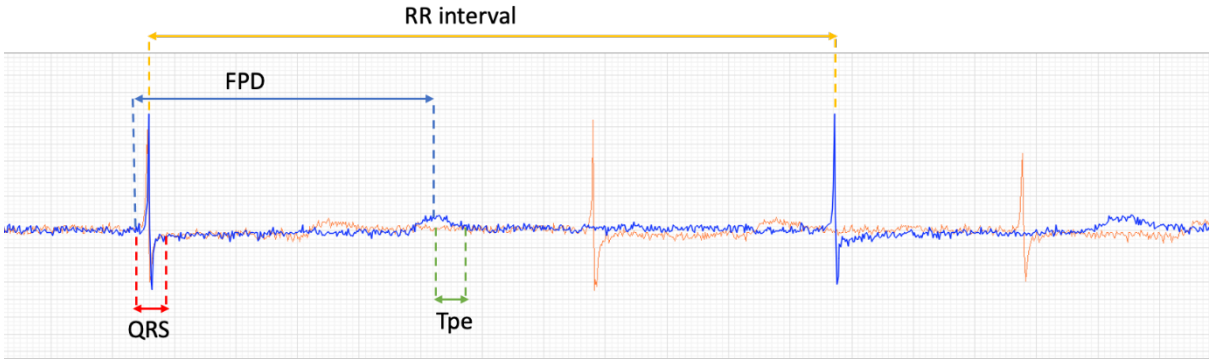


Figure 4.2 Electrical mapping interpretation. Sample data illustrated the field potential of hiPSC-derived cardiac myocytes at baseline (blue trace) and after 1 µM isoprenaline treatment (orange trace). Measurement was demonstrated using the blue trace. RR interval is the distance between two R waves. Field potential duration (FPD) is measured from the beginning of the QRS complex to the peak of the T wave. Tpe is measured as the distance from the peak to the end of the T wave.

4.2.6 Noradrenaline release assay

WT and CP1 hiPSC-SNs were replated on a 24-well plate at 1 million per well on day 12 and fed until day 40. To collect supernatant for ELISA, cells were treated with 1 ml plain neuronal media or neuronal medium supplemented with 100 µM nicotine for 1 hour. Collected samples were added in duplicate to 96-well plated supplied in the NA-release ELISA kit (ab287789) and incubated with biotin, streptavidin-HRP conjugate, and TMB substrate sequentially. Then optical density for absorbance was measured at 450nm and noradrenaline concentration in supernatant was calculated from the standard curve.

4.3 Results

4.3.1 Differentiation efficiency of cardiac myocytes and sympathetic neurons

The differentiation efficiency of cardiac myocytes and sympathetic neurons from CPVT and control cell lines were testified using flow cytometry. Results showed that more than 80% of differentiated myocytes were double positive for cTnT and MLC2v, which suggested these cells to be ventricular cardiac myocytes (Figure 4.3.A). However, ReBI-PAT$^{RYR2\text{-}WT}$ induction efficiency was only 70.8%, which was relatively low compared to other cell lines (Figure 4.3.B). There was the batch-to-batch difference in stem cell response to induction reagents which remained to be clarified and improved. TH positive neurons accounted for 75-97% of differentiated cells among the four cell lines using compensation beads as control (Figure 4.4).

The batch-to-batch inconsistency of stem cell differentiation is still a notable obstacle in generalizing hiPSC application in laboratory experiments. To improve the reliability of comparison between disease and healthy cell lines, cells from different cell lines used in the same experiments were always differentiated at the same time with the same batch of chemicals and media. Preservation of pluripotency of hiPSCs was a critical factor in attaining optimal differentiation when all the cells are homogenous and respond to factors directing embryonic development in a physiological way. Using cell lines of lower passage number, gentle process during passage, and regular renewal of chemicals are all practical ways to maintain hiPSC pluripotency, although decisive factors remain unclear.

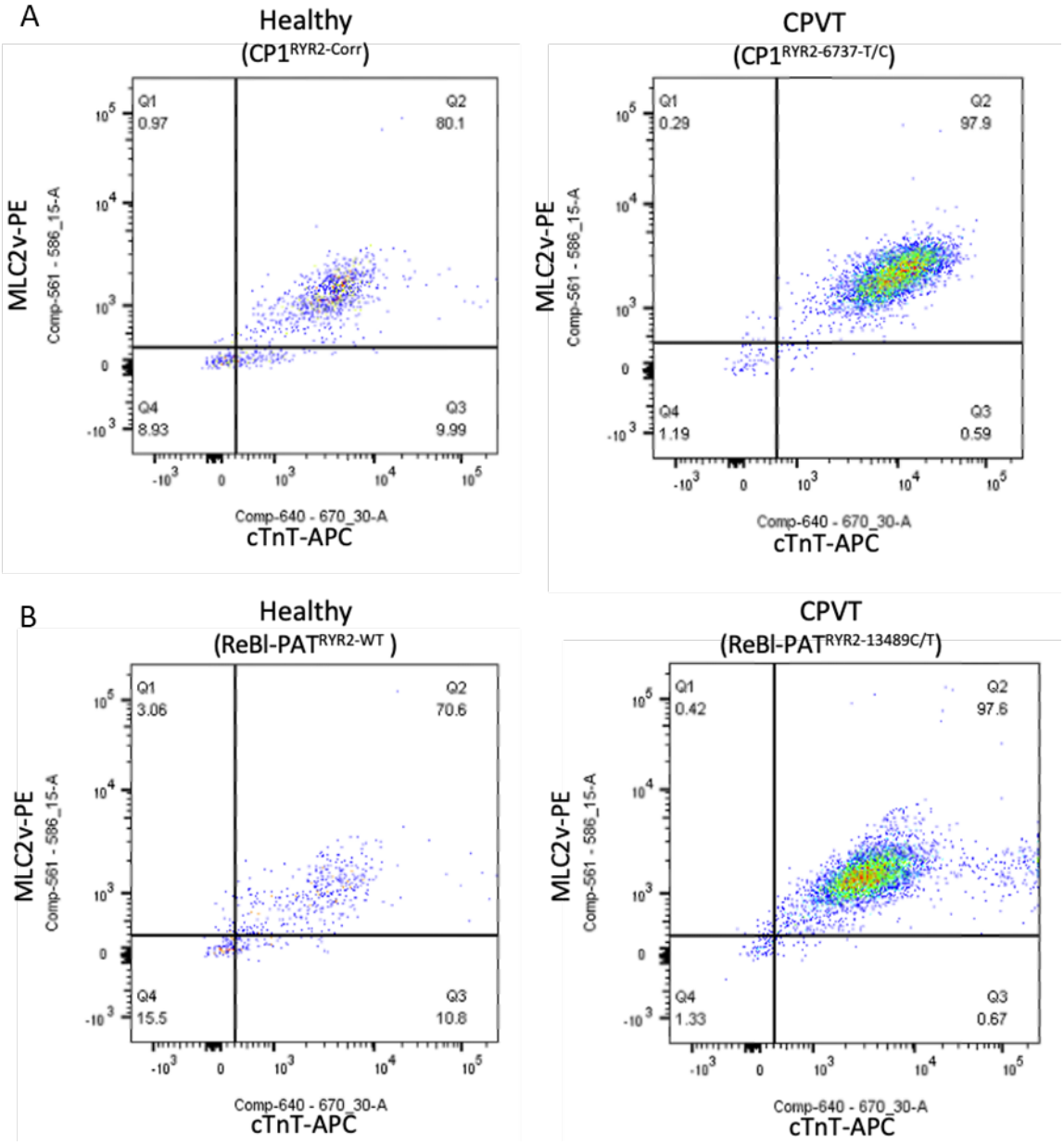


Figure 4.3 Flow cytometry of hiPSC cardiac myocytes. The expression of cell type-specific markers in cardiac myocytes was examined within the context of CPVT versus Control genotypes. A two-parameter density plot was employed to visualize the stained population in hiPSC-CM samples derived from two CPVT cell lines, CP1$^{RYR2\text{-}6737\text{-}T/C}$ in comparison to isogenic control cell line CP1$^{RYR2\text{-}Corr}$ (**A**), and ReBI-PAT$^{RYR2\text{-}13489C/T}$ in comparison to isogenic control cell lines ReBI-PAT$^{RYR2\text{-}WT}$ (**B**). The right-upper quadrant (Q2) of the density plot specifically delineated the MLC2v and cTnT double-positive populations.

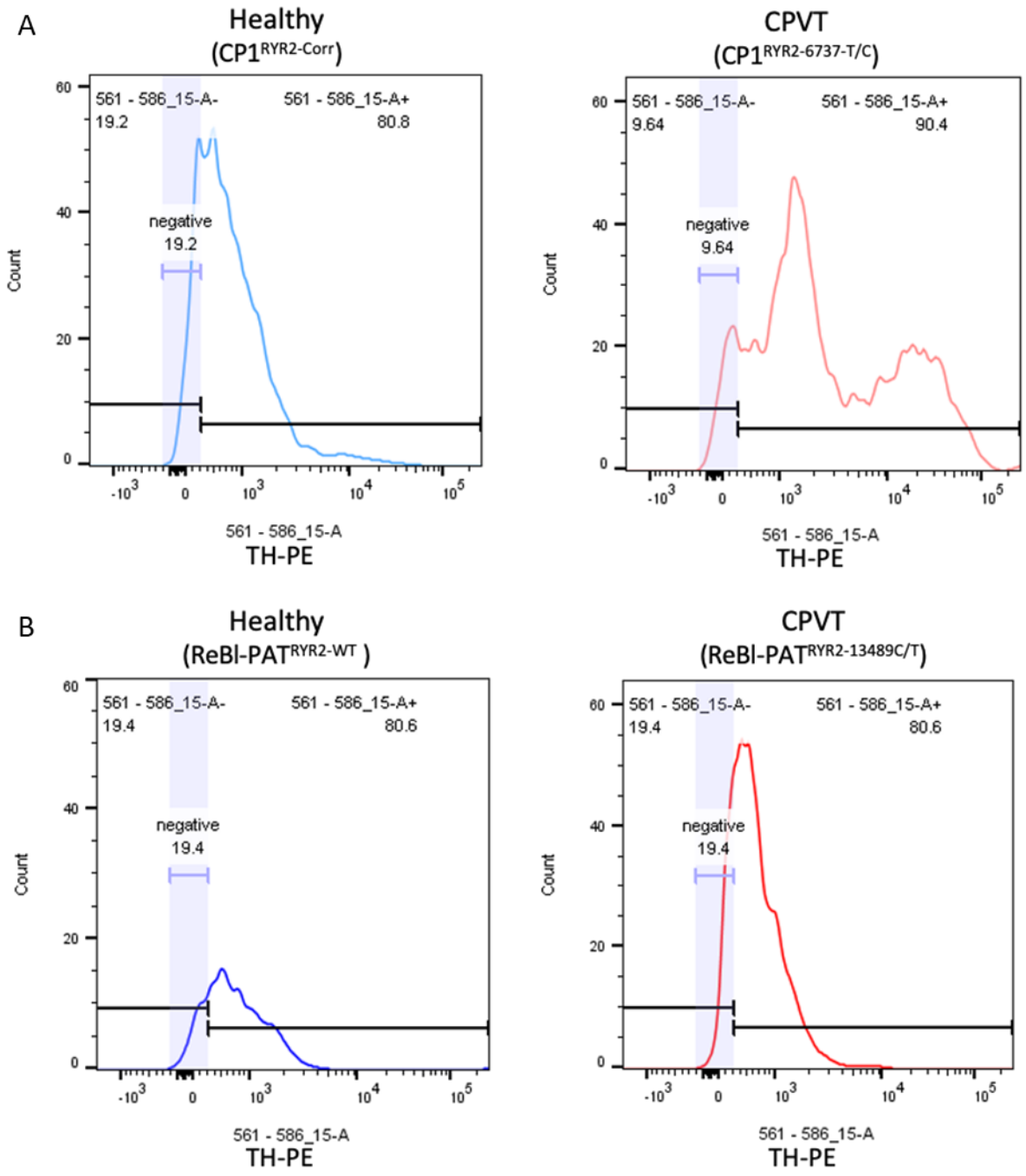


Figure 4.4 Flow cytometry of hiPSC sympathetic neurons. The expression of cell type-specific markers in sympathetic neurons was examined within the context of CPVT versus Control genotypes. Neurons were derived from two CPVT cell lines, CP1$^{RYR2\text{-}6737\text{-}T/C}$ in comparison to isogenic control cell line CP1$^{RYR2\text{-}Corr}$ (**A**), and ReBI-PAT$^{RYR2\text{-}13489C/T}$ in comparison to isogenic control cell lines ReBI-PAT$^{RYR2\text{-}WT}$ (**B**). A single-parameter histogram was utilized to identify cells expressing tyrosine hydroxylase. The positioning of the cursor, guided by compensation beads, facilitated the establishment of gates for discerning positive and negative stained populations.

4.3.2 Morphological phenotyping of hiPSC-CM and hiPSC-SN between genotypes

Sarcomere organization and RyR2 receptor expression were meticulously compared between WT and CPVT cardiac myocytes (Fig.4.5), while the distribution of neurofilaments, nicotinic acetylcholine receptors, and RyR2 receptor expression was analysed in WT and CPVT sympathetic neurons (Fig. 4.6). At the resolution limit of the confocal microscope, no discernible differences were observed in the expression and assembly of these critical functional and structural proteins within myocytes and neurons across genotypes. To quantitatively assess anatomical features, representative parameters such as sarcomere length for cardiac myocytes and axonal diameter for sympathetic neurons were measured (Fig. 4.7). Remarkably, no significant disparities were identified in these measurements. The average sarcomere length for both genotypes was approximately 2 μm, as determined from cTnT and α-actinin-stained day 50+ hiPSC-CMs. This measurement aligns with the reported sarcomere length (distance between adjacent z-discs) in adult human cardiac myocytes from previous studies, ranging from 1.75 μm to 2.3 μm[198]. The axon diameter, measured as the width of peripherin-stained filaments, was 0.592±0.018μm (n=68) in WT hiPSC-SNs and 0.581±0.018μm (n=51) in CPVT hiPSC-SNs (refer to Fig. 4.7). It is noteworthy that there exists a wide range of axon diameters among mammalian neurons in the peripheral nervous system, spanning from 0.1 μm to 20 μm, contingent upon factors such as location, function, and myelination[199]. The unmyelinated nature of axons in sympathetic neurons derived from hiPSCs in vitro, along with constraints on radial growth within the culture plate, contributed to the approximate uniformity in cross-sectional diameter along the length of neurofilaments within a scan.

Myocyte

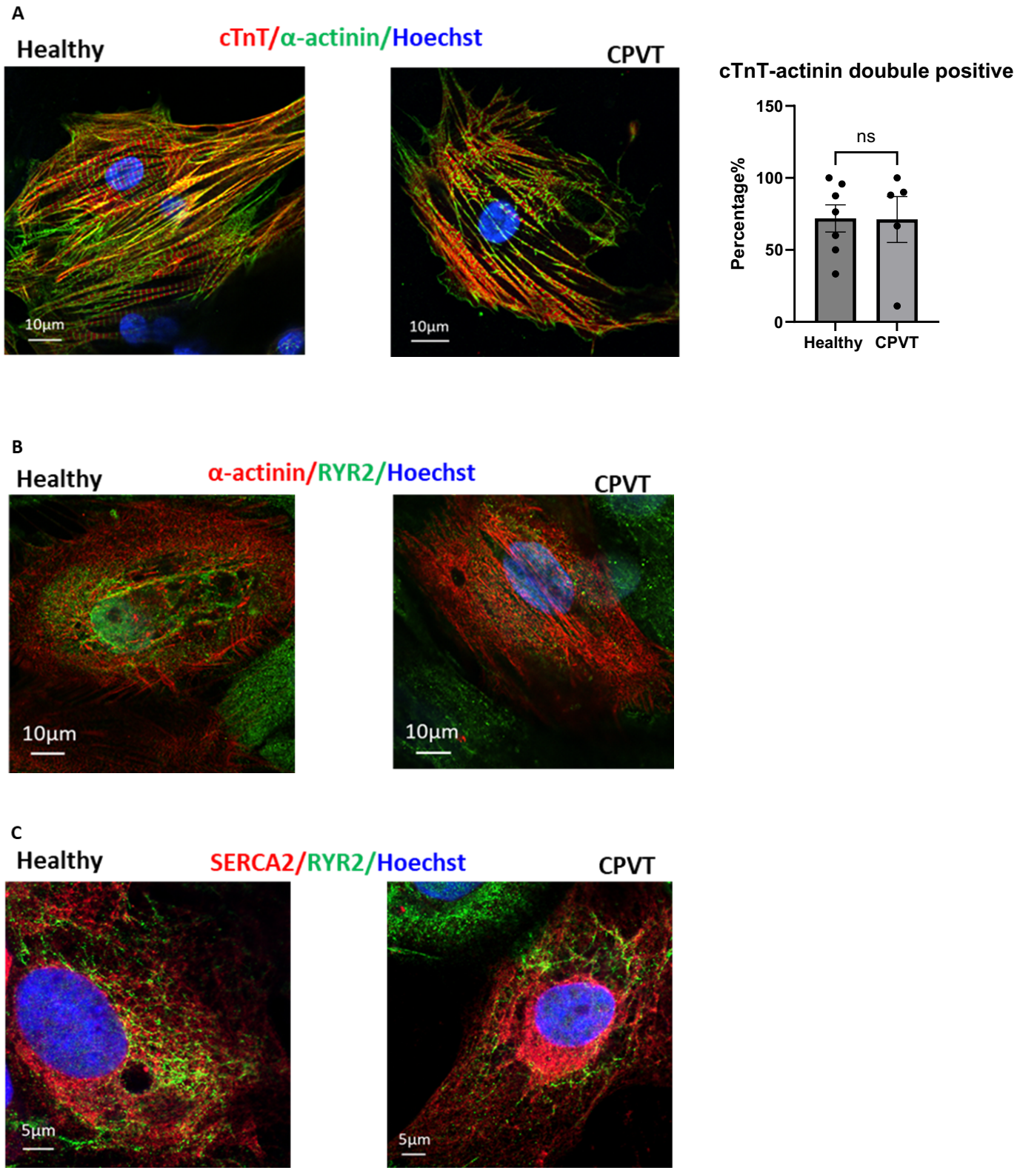
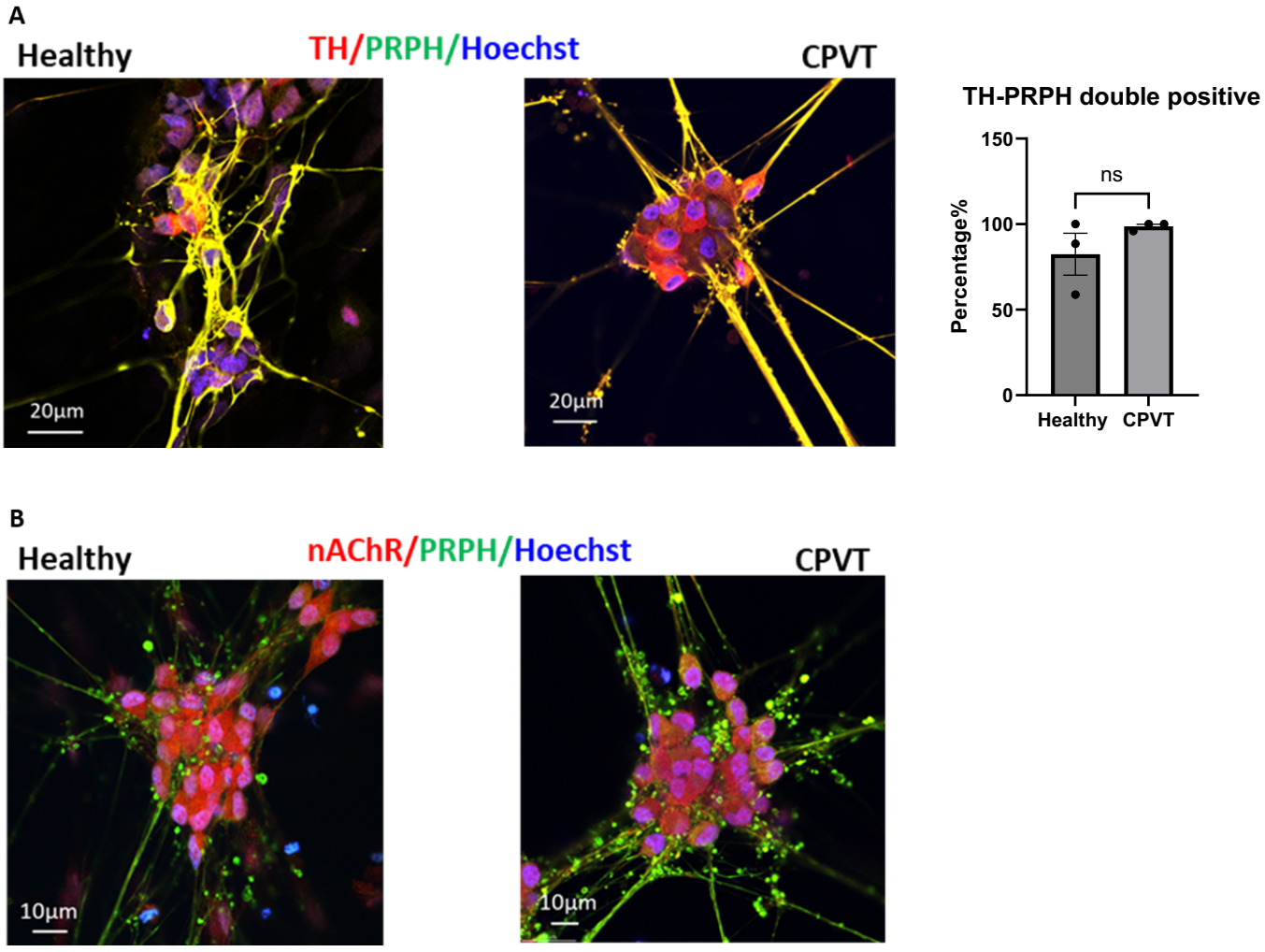

A
Healthy
cTnT/α-actinin/Hoechst
CPVT
10μm
10μm
cTnT-actinin doubule positive
150
100
50
0
Percentage%
ns
Healthy
CPVT
B
Healthy
α-actinin/RYR2/Hoechst
CPVT
10μm
10μm
C
Healthy
SERCA2/RYR2/Hoechst
CPVT
5μm
5μm

Figure 4.5 Cell type-specific marker expression in cardiac myocytes. A. cTnT and α-actinin staining showed the well-organized myofibrils and contractile unit sarcomere. Percentage of double-stained myocytes was 71.88±9.431% (n=7) in healthy cell line and 71.16±15.96% (n=5) in CPVT cell line, unpaired t test, p>0.05. RyR2 is expressed in α-actinin positive cells in the cytoplasm (**B**), colocalized with SERCA2 which outlines the sarcoplasmic reticulum as a continuous linear-shaped structure spread out from the nucleus (**C**). The colocalization between SERCA2 and RYR2 was quantitatively assessed using Manders' overlap coefficient obtained by ImageJ. In healthy myocytes, tM1 (fraction of green signal overlapping with red) was 0.836 and tM2 (fraction of red signal overlapping with green) 0.763; in CPVT myocytes, tM1 was 0.877 and tM2 was 0.869. Both cell lines had tM1 and tM2 above 0.75, indicating substantial colocalization of RyR2 with SERCA2.

Neuron



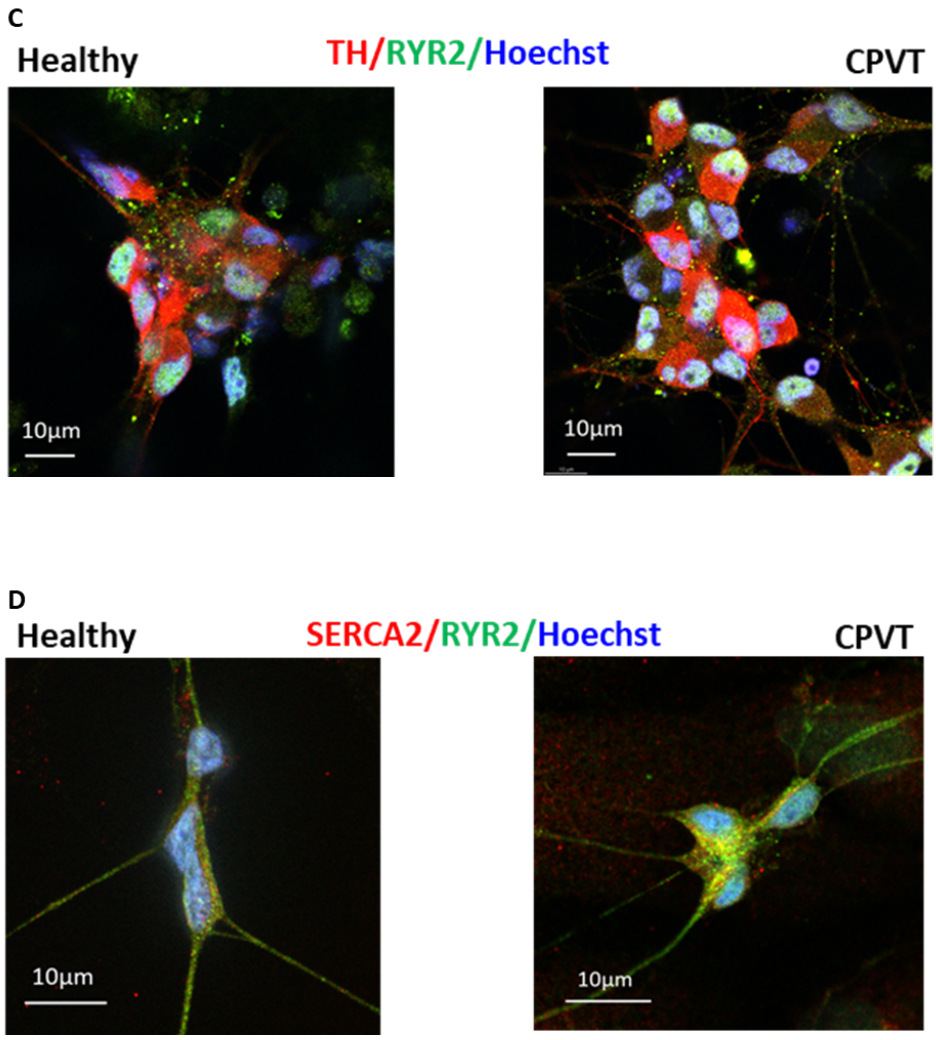


Figure 4.6 Cell type-specific marker expression in sympathetic neurons (CPVT vs Control). Double stained with TH and peripherin validated the cells as dopaminergic neurons in the peripheral nervous system. Percentage of double-stained cell was 82.46±12.27% (n=3) in healthy cell line and 98.65±1.351% (n=3) in CPVT cell line, Mann-Whitney test, p>0.05. (**A**)These cells also expressed nicotinic acetylcholine receptors (**B**) and RyR2 receptors (**C**) on the cell body. However, as sympathetic neuron has a large nucleus-to-cytoplasm ratio, the structure of the endoplasmic reticulum stained with SERCA2 was not well viewed under a 40X confocal microscope (**D**). Although the ultrastructure of ER was not clearly displayed due to the resolution limitation, Manders' correlation coefficient indicated moderate colocalization between RyR2 and SERCA (Healthy tM1:0.846, tM2:0.889; CPVT tM1: 0.714, tM2:0.787).

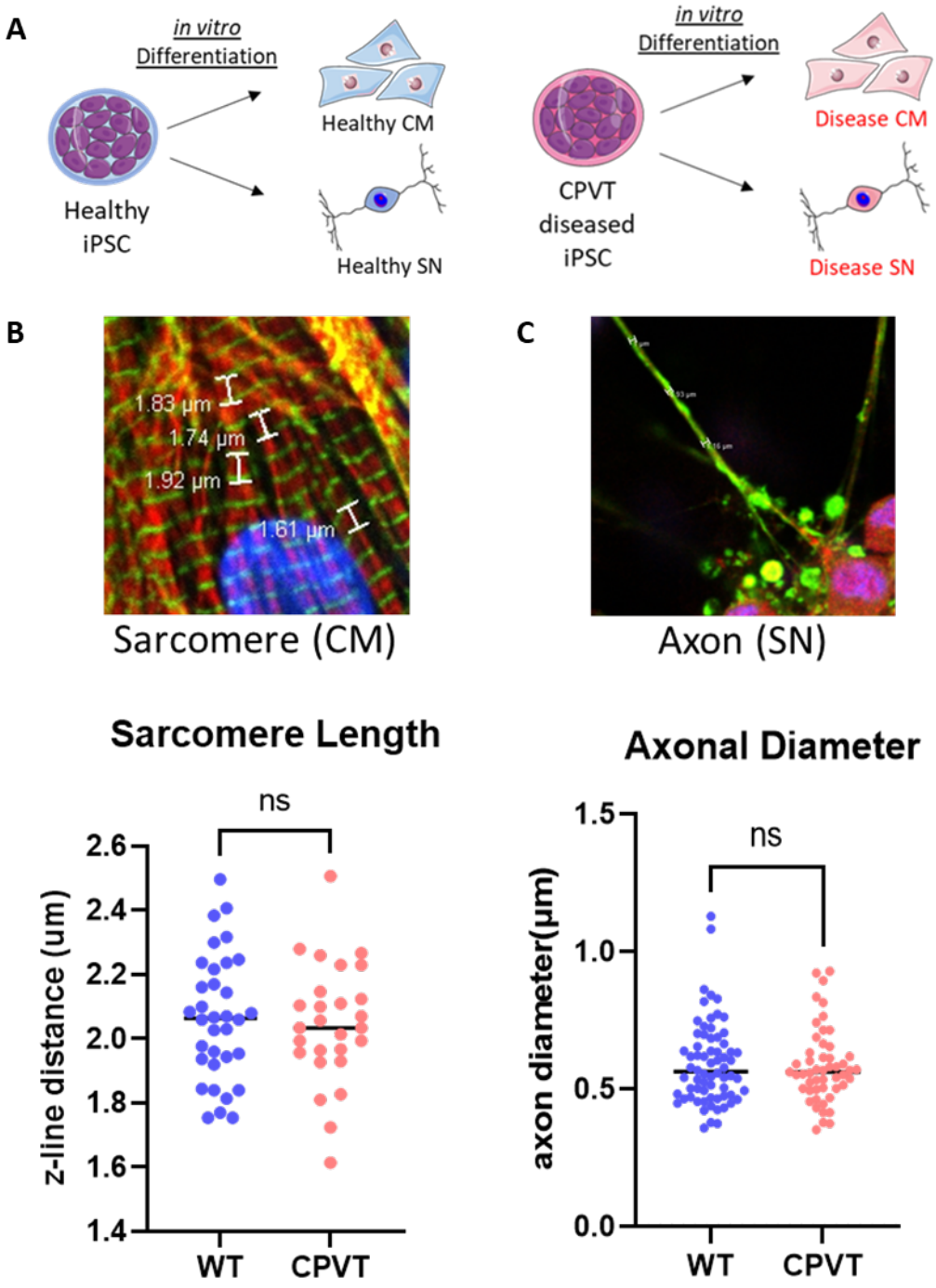


Figure 4.7 Structural comparison in CM and SN. A. Diagram of myocytes and neurons induction from healthy and diseased hiPSCs. Sarcomere length and axon diameter were measured and compared between cell lines using the immunofluorescence confocal images. **B.** In hiPSC-CM stained with cTnT (red) and α-actinin (green), sarcomere length equals the distance between 2 consecutive α-actinin stained lines, which was 2.065±0.033µm (n=34) of WT hiPSC-CMs and 2.047±0.036µm (n=27) of CPVT hiPSC-CMs ($p>0.05$). **C.** The axonal diameter was measured on peripherin-stained hiPSC-SNs. No significant difference was detected between the WT neurons (0.592±0.018 µm, n=68) and CPVT neurons (0.581±0.018 µm, n=51), $p>0.05$.

The underlying mechanism of CPVT is the dysregulation of calcium release from SR/ER through the altered RyR2 receptor. Thus, calcium imaging was the first functional characterization being conducted using these hiPSC-derived CPVT models.

4.3.3 CPVT calcium dysregulation

4.3.3.1 CPVT myocytes showed arrhythmic spontaneous calcium discharge when stimulated

Do CPVT hiPSC-derived cardiac myocytes present calcium dysregulation of RyR2 defect as previous studies reported? Calcium imaging using Fura-2 as a Ca^{2+} indicator was used to study intracellular calcium transients in hiPSC-CMs. Application of either isoprenaline (β-adrenergic stimulation), a high concentration of potassium (membrane depolarization), or caffeine (RyR2 receptor activator) induced Ca^{2+} elevation in healthy and CPVT myocytes, with the diseased myocytes presenting higher responses and more spontaneous calcium transients after stimulation (Fig. 4.8). This extra calcium leak would predispose to afterdepolarizations in CPVT.

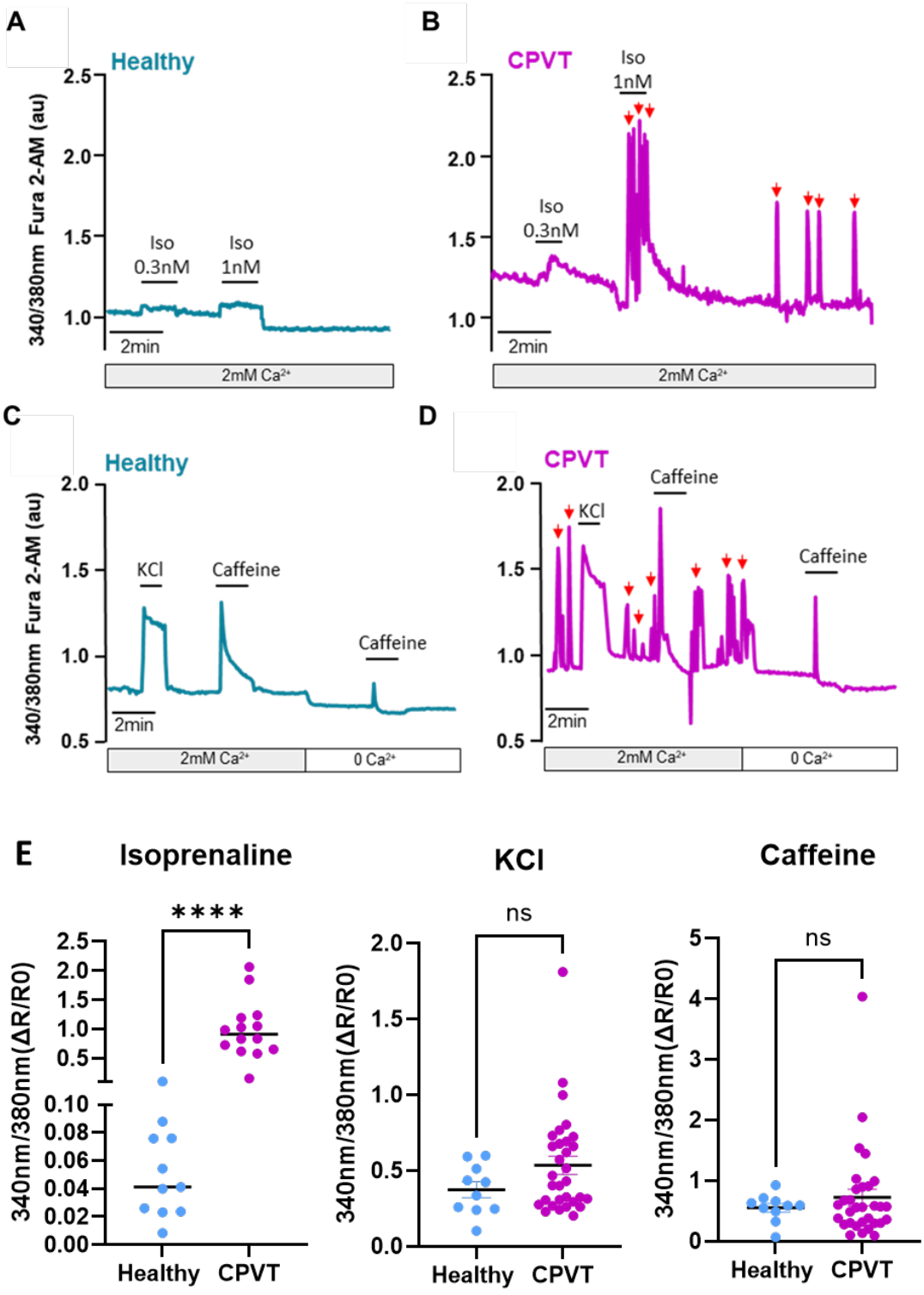

A
Healthy
340/380nm Fura 2-AM (au)
Iso 0.3nM
Iso 1nM
2min
2mM Ca2+
B
CPVT
Iso 1nM
Iso 0.3nM
2min
2mM Ca2+
C
Healthy
KCl
Caffeine
Caffeine
2min
2mM Ca2+
0 Ca2+
D
CPVT
KCl
Caffeine
Caffeine
2min
2mM Ca2+
0 Ca2+
E
Isoprenaline
KCl
Caffeine
****
ns
ns
340nm/380nm(ΔR/R0)
Healthy
CPVT

Figure 4.8 Representative raw data trace showing fluorescence ratio of Fura-2 AM to assess the dynamic changes of intracellular calcium handling response to β-adrenergic stimulation (0.3 and 1nM Isoproterenol; **A, B**), 50mM KCl (**C, D**) and 10mM caffeine (in 2mM calcium or 0 calcium solution; **C, D**) in hiPSC-CM derived from healthy (**left**) and CPVT patient (**right**) iPSC. CPVT hiPSC-CM expressed a high response to the stimulations when compared with the healthy line and showed spontaneous discharge before or after stimulations. Red arrows indicate spontaneous discharge. Isoprenaline-triggered calcium increase was significantly higher in CPVT myocytes (0.99±0.13, n=14) compared to healthy myocytes (0.05±0.01, n=11), $p<0.05$. Although calcium elevation in response to KCl and caffeine was not significant in CPVT myocytes, irregular calcium discharge was detected in 24 out of 31 (77.4%) diseased myocytes, whereas only 1 out of 10 (10%) healthy myocytes presented spontaneous calcium discharge.

Does this calcium phenotype also present in the CPVT neuron?

4.3.3.2 Calcium imaging revealed abnormal calcium transients in CPVT neurons

Calcium imaging was next conducted on hiPSC-SN to test the hypothesis that a CPVT phenotype also resides in the sympathetic neuron. Sympathetic neurons derived from the CPVT cell line have markedly enhanced responsive intracellular Ca^{2+} transients compared to their isogenic controls following membrane depolarization with 50mM KCl (Fig. 4.9A) or following acetylcholine receptor stimulation with nicotine (Fig. 4.9B) or following RyR2 receptor stimulation with caffeine (Fig. 4.9C). These results indicate that impairment also resides in the neuron itself and open up the possibility that the neuron may be a viable site for therapeutic modulation.

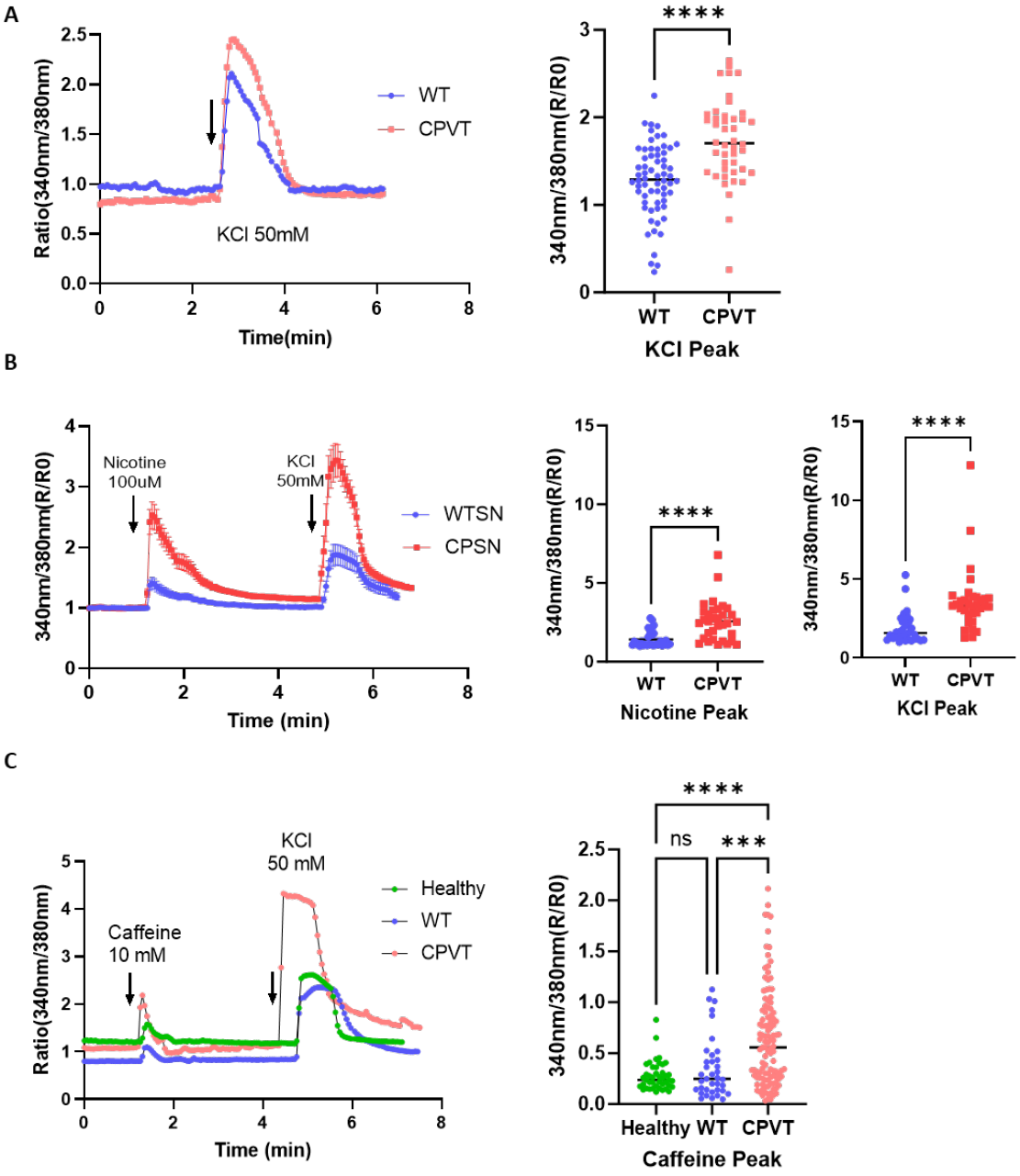


Figure 4.9 Representative Ca^{2+} dynamics trace in hiPSC-SN monoculture in response to 50mM potassium chloride (KCl, **A**), WTSN 1.280 ± 0.052, n=64; CPSN 1.732 ± 0.072, n=44; 100µM nicotine (**B**), WTSN 1.423 ± 0.093, n=31; CPSN 2.571 ± 0.217, n=33; and 10 mM caffeine (**C**) in CPVT group (red) vs isogenic healthy group (blue) and a non-isogenic healthy group (green), Healthy 0.276 ± 0.215, n=43; WTSN 0.351 ± 0.049, n=37; CPSN 0.650 ± 0.045, n=113. Intracellular calcium level was significantly higher in response to all these stimulations in the diseased CPVT groups, $p<0.01$.

4.3.4 Noradrenaline released from CPVT and control neurons

Calcium functions as a critical second messenger in mediating the release of neurotransmitters from synaptic vesicles. Given the observed augmentation in calcium transients in CPVT neurons, an anticipated consequence was the heightened release of noradrenaline (NA) in the diseased group. Supernatants from hiPSC-SNs were collected both at baseline and after nicotine stimulation for the quantification of NA concentration. In WT neurons, the baseline NA concentration in the supernatant was 108.3 pg/ml, escalating to 149.0 pg/ml post-stimulation. In contrast, the baseline and stimulated NA concentrations in CPVT neuron supernatant were both increased compared to WT, measuring 151.7 pg/ml and 171.3 pg/ml, respectively (Fig. 4.10). Both baseline and stimulated noradrenaline secretion showed a trend of increase in the CPVT cell lines. The lack of significance could be due to a small sample size, which reduced the power of this test. Despite the lack of statistical significance, the observed elevated release could still be important in suggesting a potential pathological effect in the diseased line.

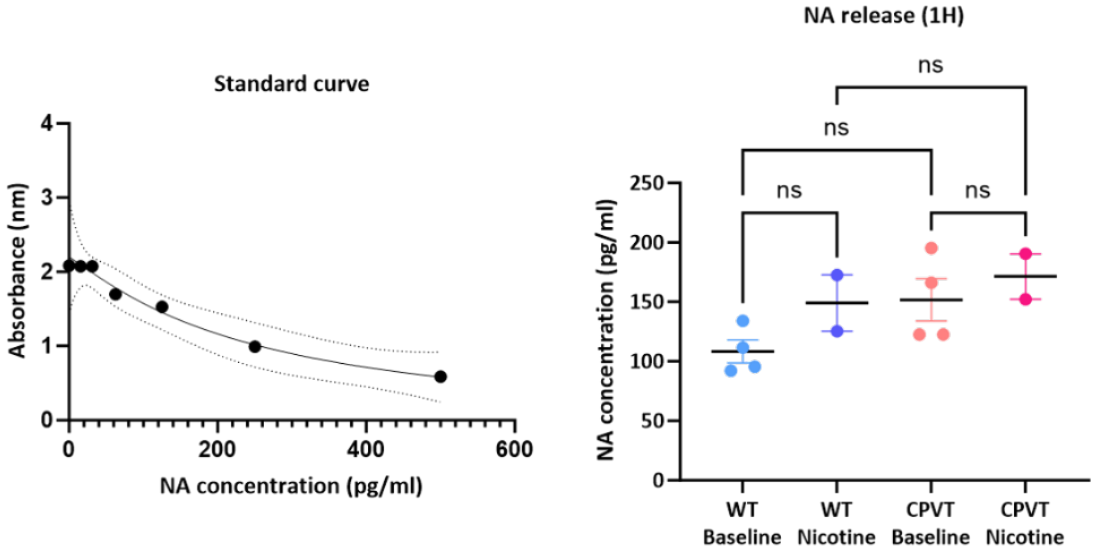


Figure 4.10 Noradrenaline release from WT hiPSC-SNs vs CPVT hiPSC-SNs. Noradrenaline concentrations in supernatants from sympathetic neuron cultures, incubated for 1 hour with and without nicotine (100 μM) stimulation, were assessed using an ELISA kit. Both baseline and nicotine-stimulated noradrenaline release were found to be higher in CPVT neurons, although not reaching statistical significance ($p>0.05$). Notably, hiPSC-SNs demonstrated responsiveness to nicotine stimulation, resulting in an elevation of noradrenaline secretion in both WT and CPVT cell lines. Noradrenaline concentrations at baseline: WT 108.3±9.597 pg/ml (n=4) vs CPVT 151.7±17.79 pg/ml (n=4), at nicotine stimulation: WT 149.0±23.65 pg/ml (n=2) vs CPVT 171.3±19.17 pg/ml (n=2).

4.3.5 Cyclic nucleotides signalling

4.3.5.1 cAMP signalling was suppressed in CPVT cardiac myocytes and sympathetic neurons

PKA phosphorylation is one of the various post-translational modifications of RyR2 receptors that control the release of Ca^{2+} from intracellular stores. Using a cytosol cAMP FRET sensor, I evaluated the activity of this upstream messenger in hiPSC-CMs and hiPSC-SNs. In response to 10nM isoprenaline, cAMP in healthy cardiac myocytes increased to 40.42±3.03%, n=17, which was significantly higher than CPVT myocytes (8.456±2.666%, n=15) (Fig. 4.11A). In neurocardiac coculture, however, 10 μM nicotine stimulation triggered a similar level of cAMP elevation in WT and CPVT myocytes (Fig. 4.11C). As a negative control, the application of 10 μM and 100μM nicotine on cardiac myocytes monoculture induced no elevation of cAMP (Fig. 4.11A). Hence, the elevation of cAMP in myocytes within the co-culture setting was prompted by neurotransmitters released from nicotine-activated neurons. Neurotransmission might be hyperactivated in the CPVT group even in the setting of a suppressed cAMP signal, leading to the increase in cAMP levels in CPVT myocytes to a state comparable to that of healthy myocytes. Similar to myocyte monoculture, CPVT hiPSC-SNs demonstrated a less responsive

reaction to nicotinic stimulation, as indicated by a subdued increase in cAMP levels compared to healthy hiPSC-SNs (40.47±6.131%, n=14 vs 22.03±3.999%, n=14) (Fig. 4.11B).

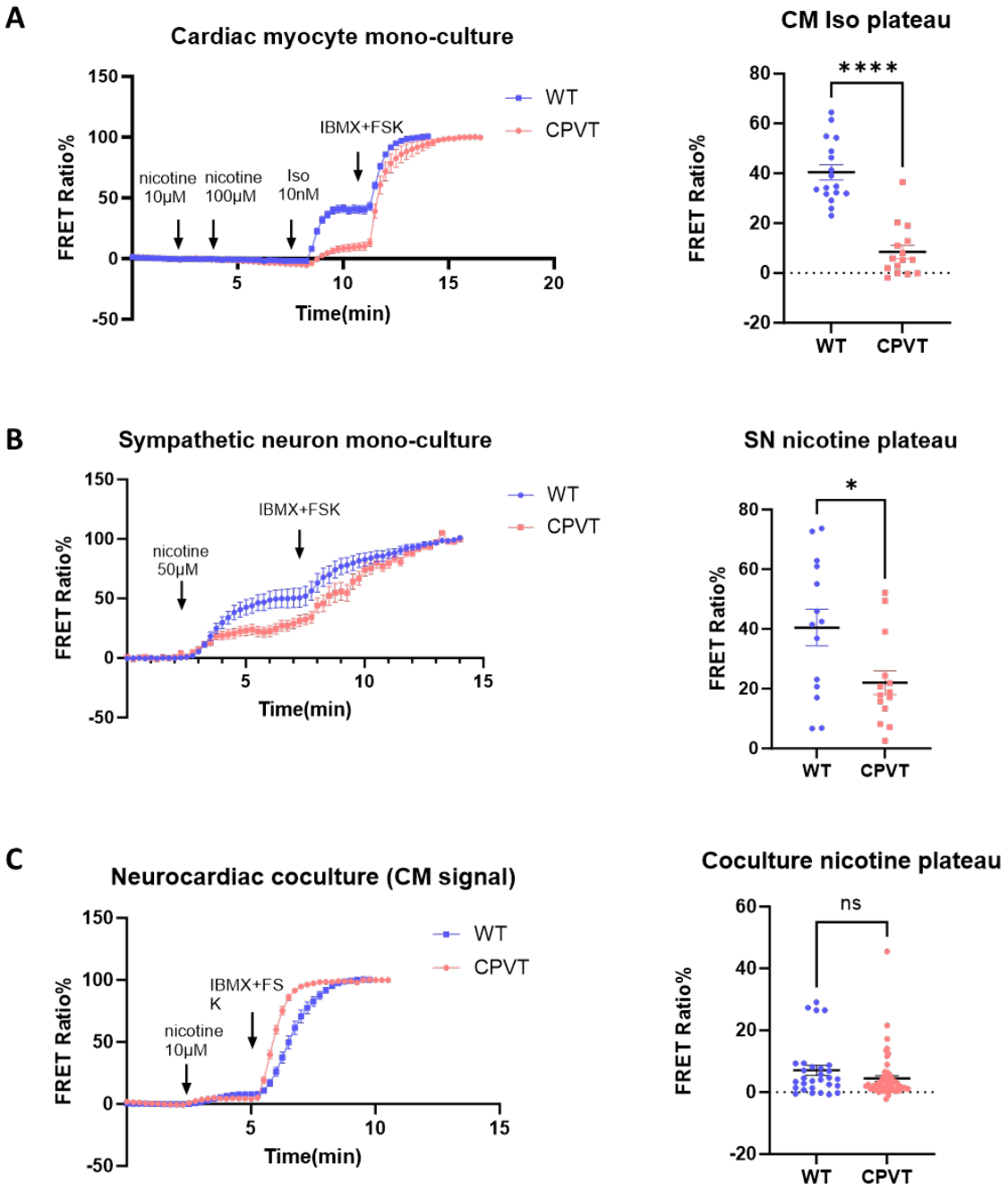


Figure 4.11 Intracellular cAMP response in cardiac myocytes (A), sympathetic neurons (B) and cardiac myocytes cocultured with sympathetic neurons (C). Nicotine stimulation elevated cAMP in sympathetic neurons which was more significant in the healthy group (40.47±6.131%, n=14 vs 22.03±3.999%, n=14, $p<0.05$), while cardiac myocytes alone were irresponsive to nicotine stimulation. Similarly, cAMP elevation in healthy cardiac myocytes in response to isoprenaline activation was significantly higher than CPVT myocytes (40.42±3.03%, n=17 vs 8.456±2.666%, n=15, $p<0.001$). In neurocardiac coculture (WT: both the neurons and myocytes from the healthy line, CPVT: both the neurons and the myocytes from CPVT line), the application of nicotine resulted in a cAMP increase in myocytes (7.098±1.633%, n=29 vs 4.404±0.9503%, n=57, $p>0.05$). The difference between healthy and diseased groups was insignificant in coculture.

4.3.5.2 Neuronal calcium was not altered by cGMP supplement

The functionality of cAMP-PKA in activating neuronal calcium channels is finetuned by cGMP through PDE activity modulation. Also, cGMP-PKG signalling antagonize the effect of PKA phosphorylation as discussed in Chapter One. Thus, whether cGMP level is suppressed in CPVT neurons, which could also result in an overactivated calcium signalling, is worth studying. The effect of cGMP was studied by measuring the alteration of the amplitude of calcium transient after cGMP supplement. Each cell was stimulated by 50mM KCl twice in sequence with the first stimulation in Tyrode perfusion and the second after six-minute perfusion in 100μM 8-bromo-cGMP. A negative control group that did not receive 8-bromo-cGMP was used (Fig 4.12A). The calcium rise declined at the second KCl stimulation. However, there was no significant difference between the 8-bromo-cGMP group and the negative control group within a genotype (Fig 4.12B). Thus, the reduction was resulted from unknown variables, such as time or repeated stimulation, instead of the 8-bromo-cGMP perfusion.

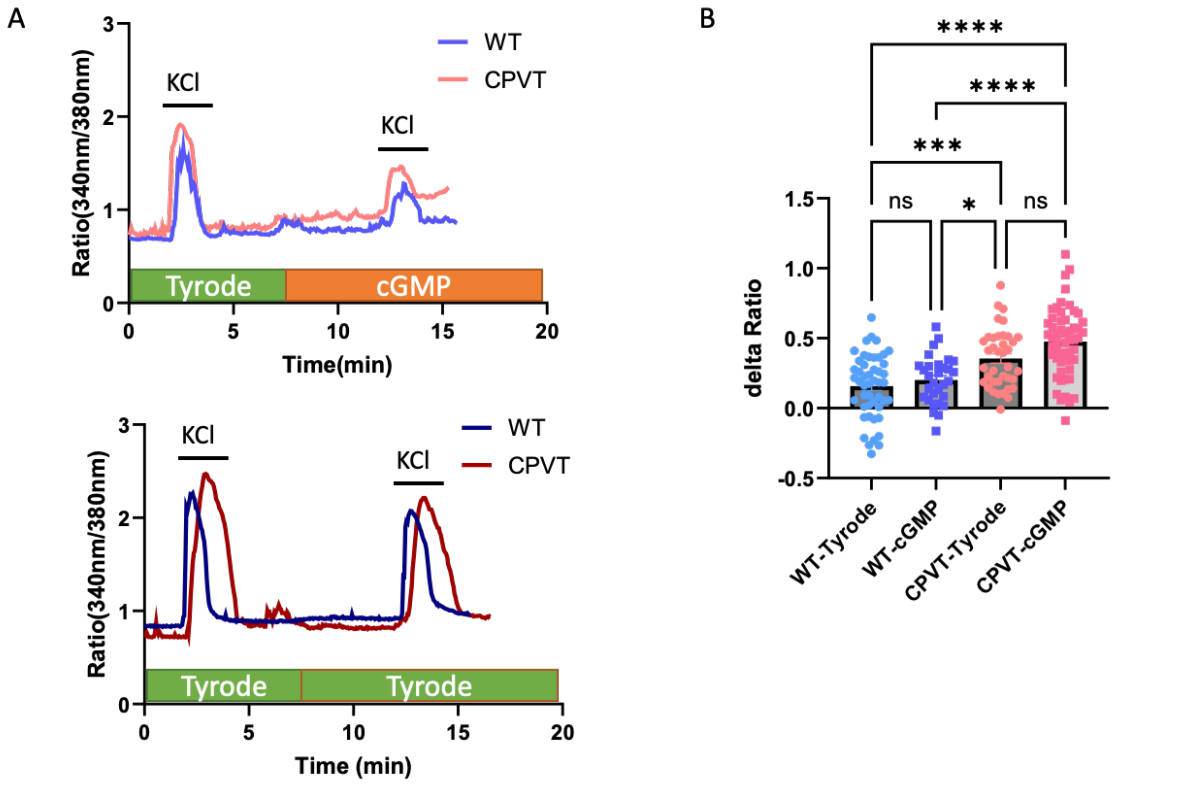


Figure 4.12 The effect of 8-bromo-cGMP on neuronal calcium transient. A. The representative traces of calcium level change in healthy and CPVT neurons in response to 50mM KCl stimulation in the perfusion of Tyrode solution versus 8-bromo-cGMP. **B.** The decrement in amplitude between the first and second calcium rise was calculated as the delta Ratio (Peak1 minus Peak2). WT neuron: 0.158±0.033 (control, n=48) vs 0.202±0.031 (cGMP, n=30), p>0.05; CPVT neurons: 0.355±0.034 (control, n=38) vs 0.476±0.034 (cGMP, n=54). Results showed a depression of the second calcium peak, and this reduction in calcium level was significantly larger in CPVT neurons.

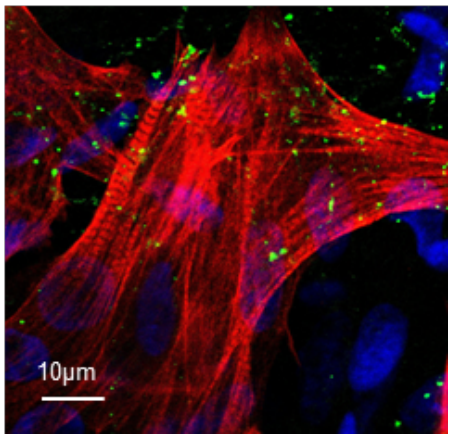
Since sympathetic neurons had an impact on cAMP generation in cardiac myocytes, how calcium the transient was regulated by the neurocardiac coculture was also explored.

4.3.6 Neurocardiac coculture

4.3.6.1 Visualization of neurocardiac coculture with immunofluorescence stain

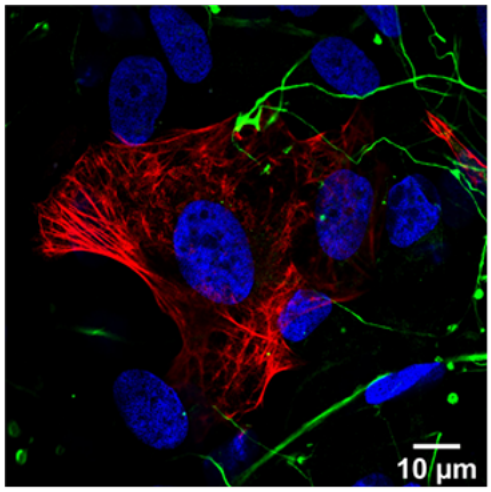
Cell type-specific protein staining in neurocardiac co-culture confirmed the cell type of cardiac myocytes (α-actinin and cTnT) and sympathetic neurons (TH and PRPH) when reseeded together. The dot-stained synaptic vesicles adjacent to cardiac myocytes showed the formation of synapses (Fig. 4.13).

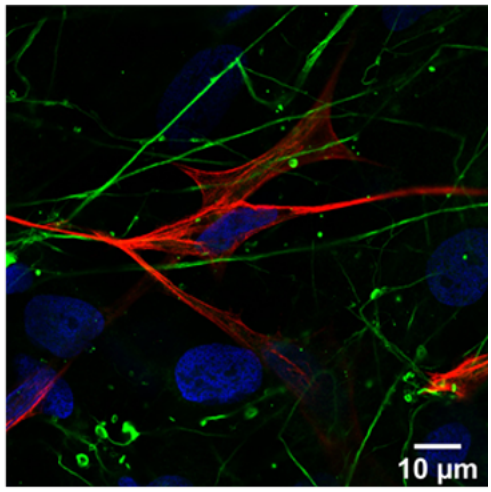
A cTnT/Syn/Hoechst



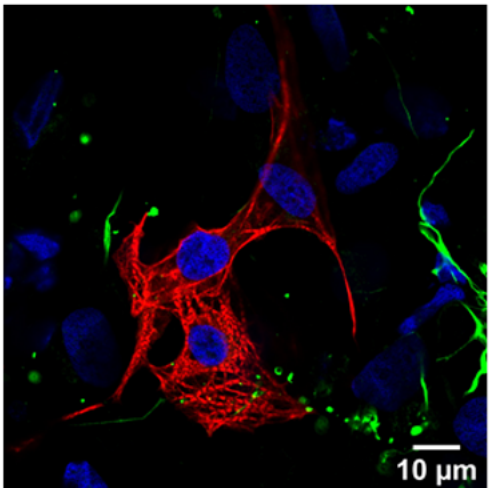
B cTnT/PRPH/Hoechst

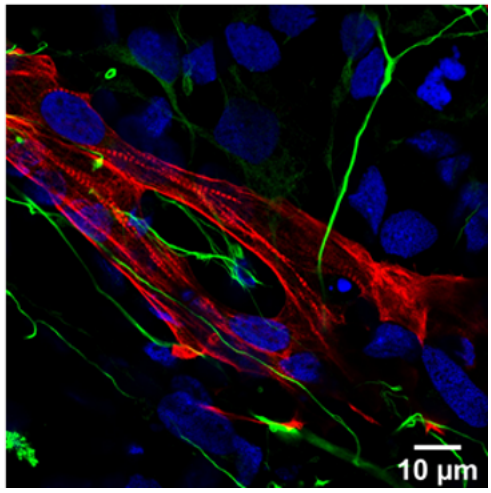
CP1$^{RYR2\text{-}Corr}$ CP1$^{RYR2\text{-}6737\text{-}T/C}$





ReBl-PAT$^{RYR2\text{-}WT}$ ReBl-PAT$^{RYR2\text{-}13489C/T}$





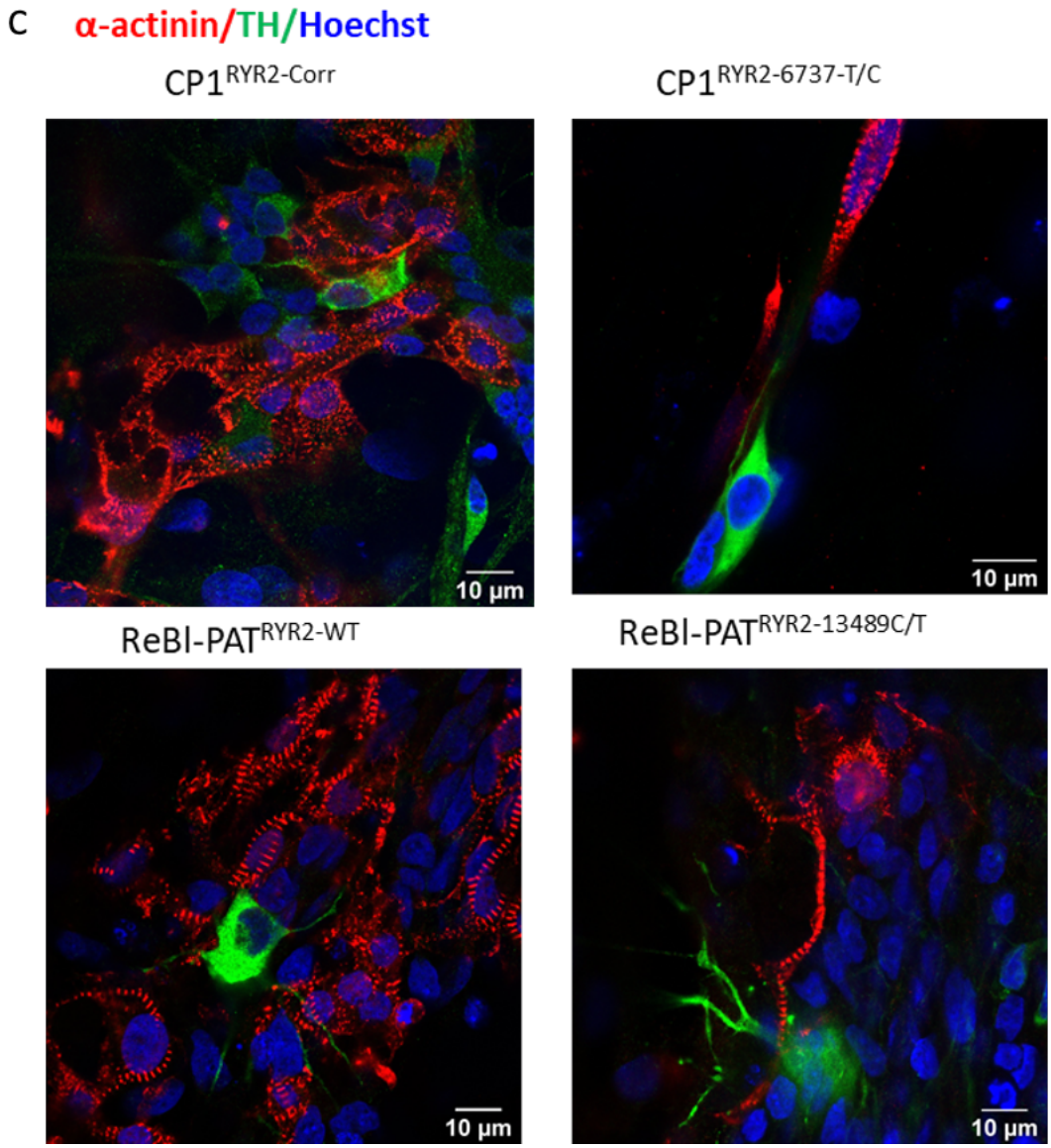


Figure 4.13 Immunofluorescence showing co-localization of cardiac and neuronal cell markers in coculture. Cardiac myocytes and sympathetic neurons cocultured in a dish were differentiated from the same hiPSC line, including 2 control lines ($CP1^{RYR2\text{-}Corr}$ and $ReBI\text{-}PAT^{RYR2\text{-}WT}$) and 2 CPVT lines ($CP1^{RYR2\text{-}6737\text{-}T/C}$ and $ReBI\text{-}PAT^{RYR2\text{-}13489C/T}$). The formation of varicosities was depicted by anti-synapsin I antibody as the dot-stained vesicles (**A**). The overlay of cTnT with peripherin (**B**), and α-actinin with TH (**C**) provided a general impression of the interspersion of neurons and its outgrowth among cardiac myocytes.

4.3.6.2 Cardiac feedback regulation on neuronal calcium signalling was not detected

To ascertain potential distinctions in the impact of healthy and CPVT myocytes on sympathetic neurons, two cross-culture setups were established (Fig. 4.14). Cardiac myocytes and sympathetic neurons, derived from either CPVT or healthy hiPSCs, were co-seeded on 6mm coverslips and cultured for one week. Fura-2 intensity signals were then recorded from neurons within the coculture system, whether in the presence of CPVT myocytes or healthy myocytes. High potassium was introduced to the neurocardiac coculture, leading to depolarization of the plasma membrane in both myocytes and neurons. Fura-2 fluorescence intensity, measured from sympathetic neurons, revealed that CPVT neurons exhibited a higher amplitude of calcium transients, irrespective of whether they were in coculture or cross-culture. Interestingly, within the same genotype, the amplitude of neuronal calcium spikes remained unaffected by myocytes originating from different cell lines (Fig. 4.15).

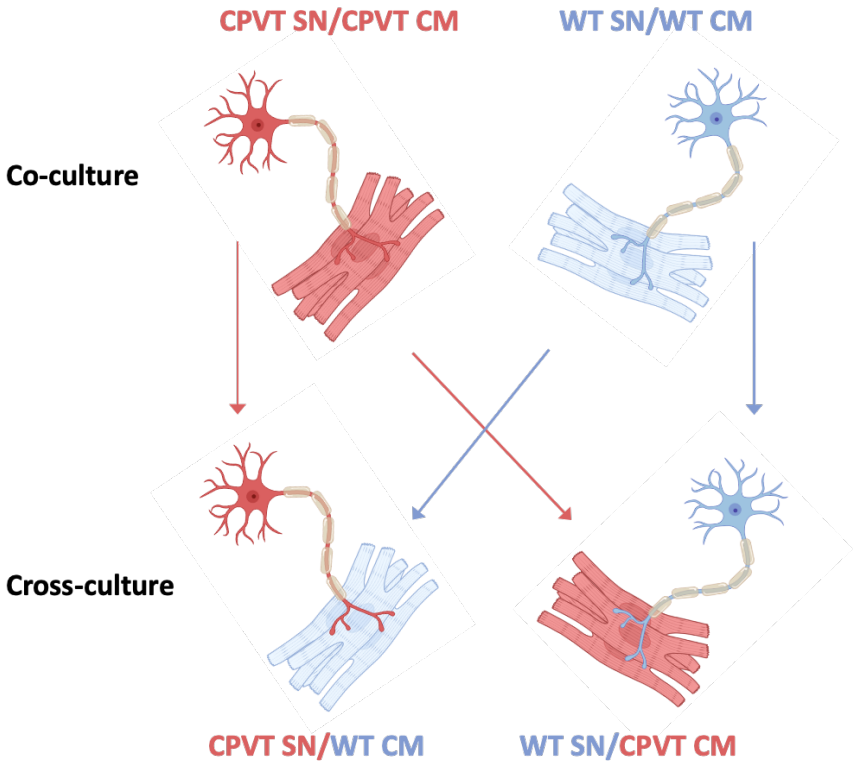


Figure 4.14 Diagram illustrating co-culture and cross-culture.

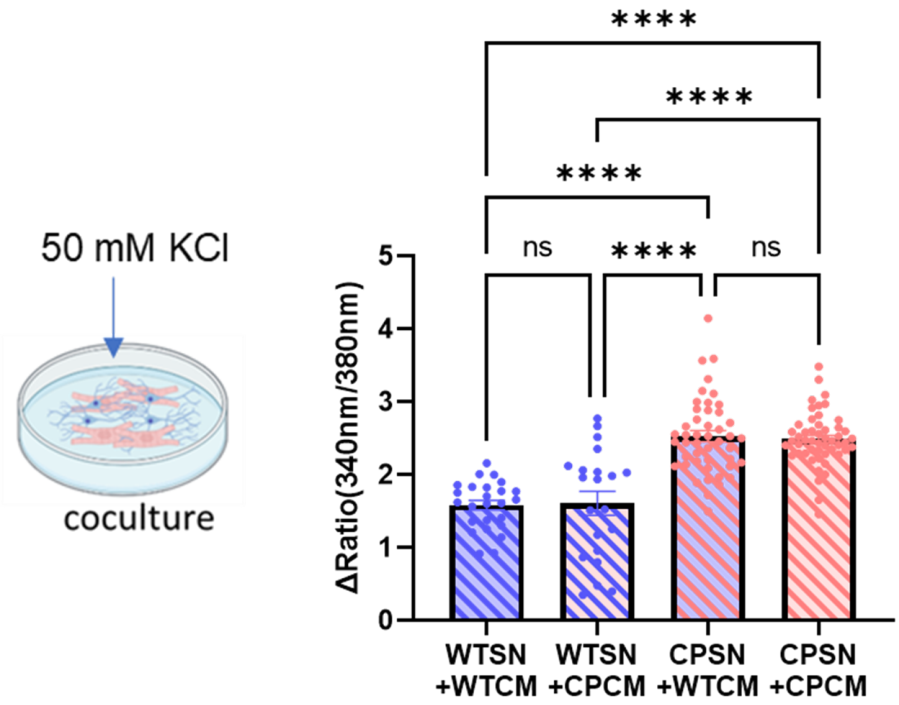


Figure 4.15 Co-culture versus cross-culture effects on calcium spikes in hiPSC-SN. Upon stimulation with high potassium (50mM), the calcium release in neurons was significantly higher in CPVT-afflicted neurons (CPSN) compared to their isogenic healthy counterparts. Whether cocultured with healthy myocytes (WTCM) or CPVT myocytes (CPCM), the intracellular calcium concentration in neurons showed no significant alterations (WTSN+WTCM 1.583 ± 0.066, n=25; WTSN+CPCM 1.610 ± 0.164, n=21; CPSN+WTCM 2.529 ± 0.077, n=46; CPSN+CPCM 2.490 ± 0.050, n=51).

4.3.7 Electrical mapping

4.3.7.1 Cardiac action potential phenotype

The ECG trace stands as a pivotal diagnostic tool in clinical assessments of CPVT, emphasizing the significance of electrical physiology characterization in disease modelling. The utilization of Microelectrode Array (MEA) emerges as a convenient yet powerful approach for investigating cell electrical properties, capturing the cardiac action potential as an extracellular field potential. As illustrated in Figure 4.16, representative brightfield images of hiPSC-CMs

seeded on the MEA plate demonstrate the experimental setup. Each plate comprises 64 channels designed to record electrical signals from the electrode's local area.

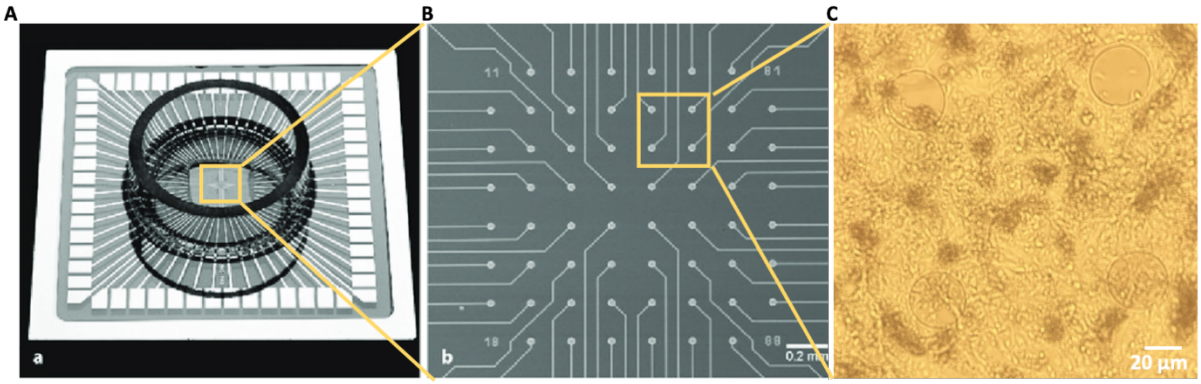


Figure 4.16 Sample brightfield images of hiPSC culture on MEA plate. (A) featured the microelectrode array which is produced with a layer of conducting material connecting the electrode grid (**B**) at the centre to the amplifiers. Microelectrodes record the electrical activity of myocytes growing in a monolayer on the electrode surface (**C**). Figure adapted from Egert U, Meyer T. Heart on a Chip — Extracellular Multielectrode Recordings from Cardiac Myocytes in Vitro. Springer; 2005:432-453.

4.3.7.2 Baseline comparison between healthy and CPVT myocytes

Field potentials were recorded from Day 37 hiPSC-derived cardiac myocytes of both WT and CPVT origins, as depicted in Figure 4.17. At baseline, 47% (8 out of 17) of CPVT hiPSC-CMs demonstrated arrhythmic properties in the spontaneous beating, including tachycardia and re-entry phenomena. Among the regular beating myocytes, no statistically significant differences were discerned between WT and CPVT myocytes in key parameters such as heart rate (RR interval), depolarization duration (QRS), and repolarization dispersion (Tpe, peak-to-end duration of the T wave), but CPVT myocytes presented a shortened corrected FPD. (Fig 4.18).

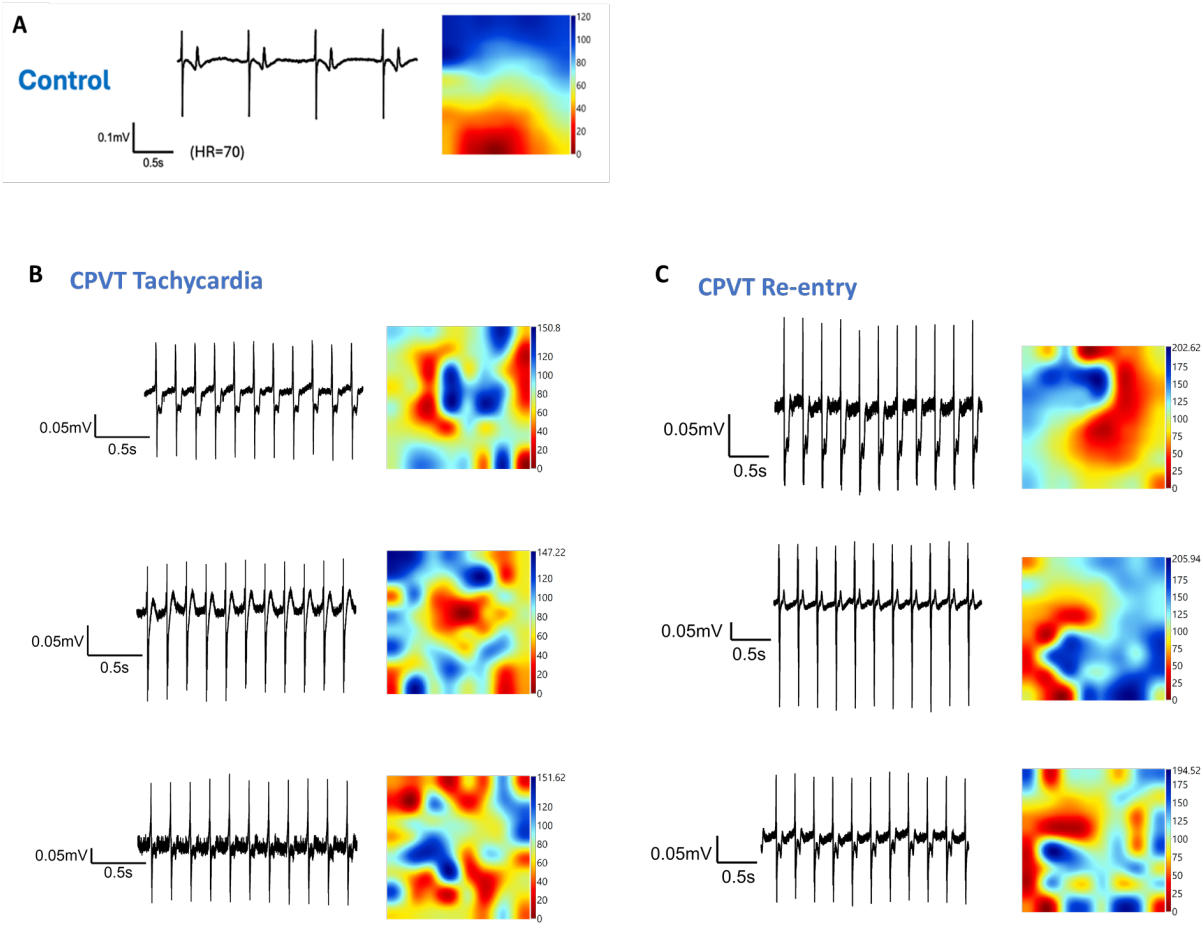
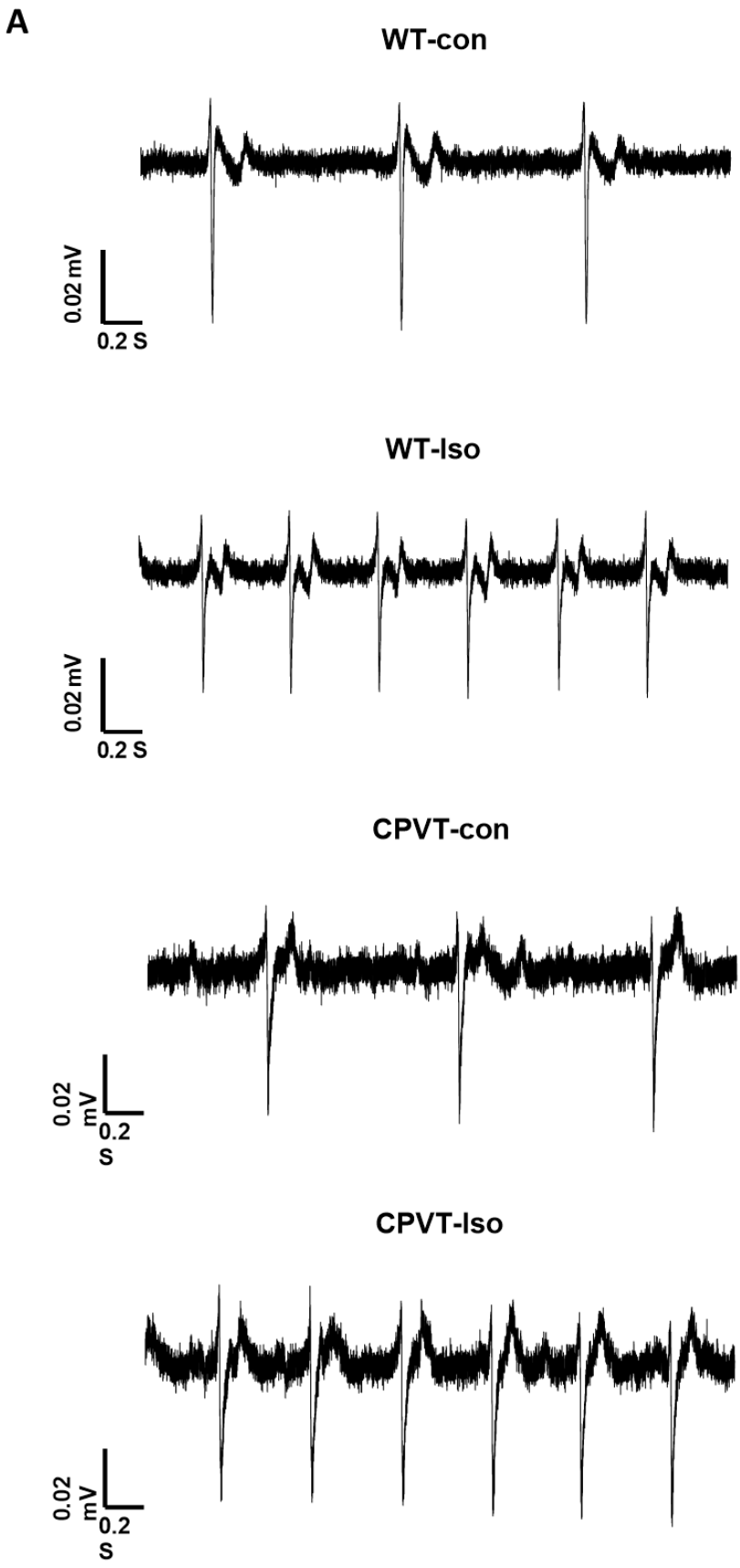


Figure 4.17 Example baseline field potential waveforms and activation maps of CPVT and healthy cardiac myocytes. A: control. **B**: CPVT with tachycardia. **C**: CPVT with the re-entry phenomenon. None of the healthy myocytes presented arrhythmia during baseline recording (n=8), whereas 8 out of 17 (47%) CPVT myocytes displayed arrhythmic features such as tachycardia and re-entry. The activation site and propagation direction tend to vary with beats in the plates that presented arrhythmic features.

4.3.7.3 Isoprenaline effects on the cardiac action potential between control and CPVT

To simulate sympathetic activation on the heart, a critical trigger for the onset of CPVT, isoprenaline was applied to the regular-beating healthy and CPVT hiPSC-CMs. This induced a remarkable increase in heart rate for both cell lines, although it's worth noting that no arrhythmias were triggered by the application of 1μM isoprenaline or incremental isoprenaline (increase from 100nM to 5 μM) in the CPVT-afflicted myocytes (Fig. 4.19).


A
WT-con
0.02 mV
0.2 S
WT-Iso
0.02 mV
0.2 S
CPVT-con
0.02 mV
0.2 S
CPVT-Iso
0.02 mV
0.2 S

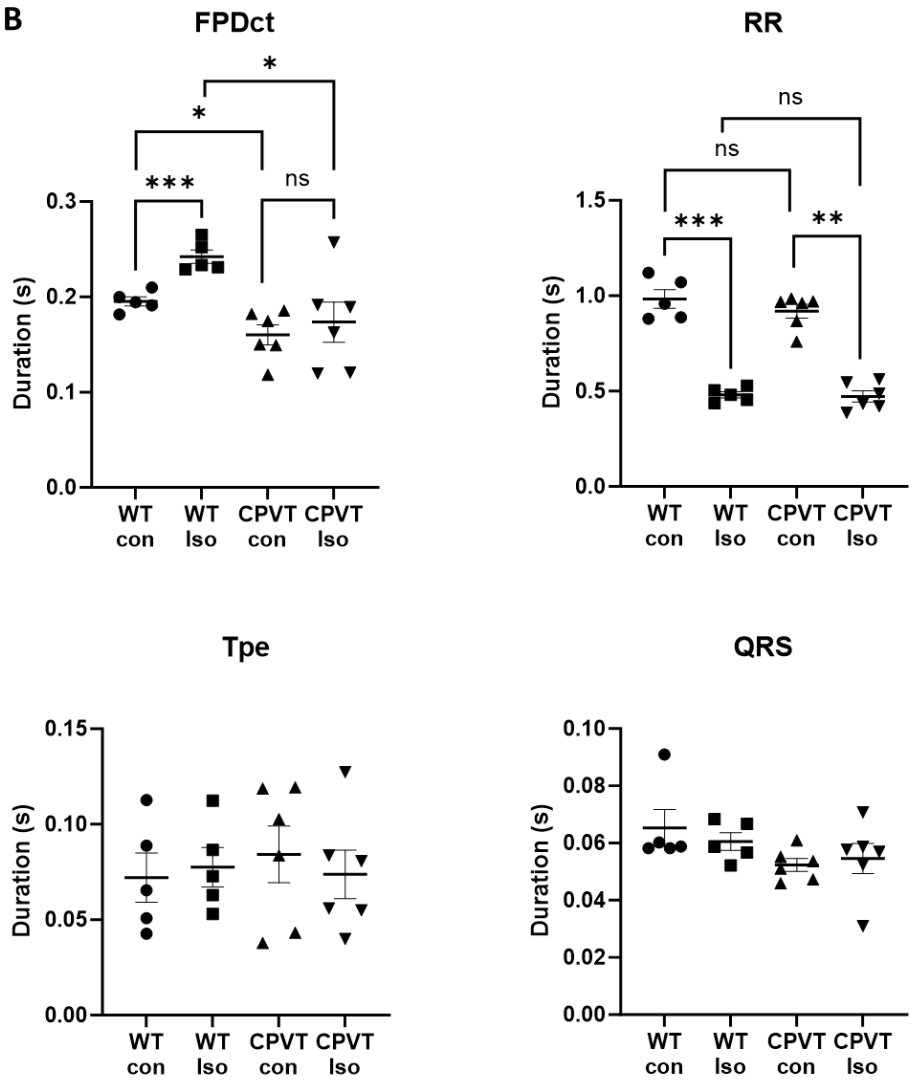


Figure 4.18 Electrical mapping of CPVT and healthy cardiac myocytes. **A.** Representative electric signals at baseline (-con) and after 1 μM isoprenaline stimulation (-Iso). **B.** Corrected field potential duration (FPDct) was shorter in CPVT cardiac myocytes at baseline and Iso stimulation compared to healthy myocytes. FDPct at baseline was 0.195±0.005s (WT, n=5) vs 0.160±0.010s (CPVT, n=6), $p<0.05$; after isoprenaline activation was 0.242±0.007s (WT, n=5) vs 0.174±0.021s (CPVT, n=6). RR interval, Tpe, and QRS showed no significant genotype difference either at baseline (WT vs CPVT: RR 0.983±0.049s, vs 0.919±0.036, Tpe 0.072±0.013s vs 0.084±0.015s, QRS 0.065±0.006s vs 0.052±0.002s, $p<0.05$) or after isoprenaline stimulation (WT vs CPVT: RR 0.481±0.016s, vs 0.472±0.029, Tpe 0.077±0.010s vs 0.074±0.013s, QRS 0.061±0.003s vs 0.054±0.005s, $p<0.05$). Isoprenaline shortened the RR interval in both cell lines.

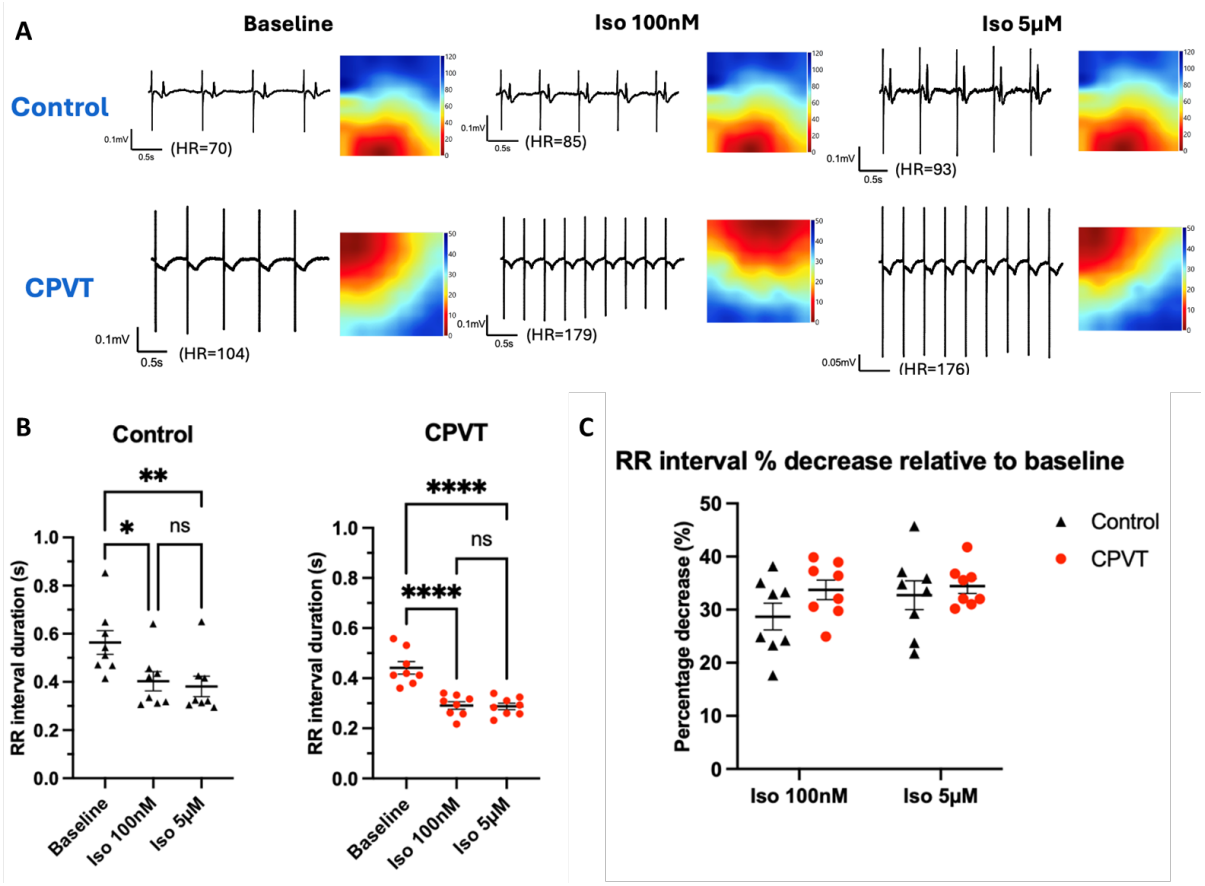


Figure 4.19 A. Representative field potential waveforms and activation maps of CPVT and healthy cardiac myocytes at isoprenaline stimulation. **B**. RR interval showed significant reduction in both control and CPVT myocytes after 100nM isoprenaline stimulation. Increase dosage of isoprenaline did not further increase beating rate. Control (n=8): baseline: 0.56±0.05s, Iso 100nM 0.40±0.04s, Iso 5μM 0.38±0.04s; CPVT (n=8): baseline: 0.44±0.02s, Iso 100nM 0.29±0.02s, Iso 5μM 0.29±0.01s. **C**. Percentage decrease in RR interval induced by isoprenaline presented no difference between control and CPVT myocytes.

4.3.7.2 Neuro-cardiac functional connection

To assess the functional connection established between hiPSC-SNs and hiPSC-CMs, the neurocardiac coculture was subjected to nicotine stimulation. In comparison to monoculture conditions, where the heart rate showed a slight increase with 100 μM nicotine and a significant increase with 1 μM isoprenaline as figure 4.20A showed, nicotine stimulation notably accelerated the heart rate in the neurocardiac co-culture (Figure 4.20B). This observation

suggests that neurons in the co-culture were functionally activated, converting adrenergic neurotransmitters through the synaptic cleft to myocytes and thereby modifying the heart rate. Moreover, the baseline heart rate of cardiac myocytes co-cultured with CPVT sympathetic neurons was faster than those co-cultured with healthy neurons, indicating higher baseline neurotransmission from diseased neurons. However, it was also observed that RR shortened more in myocytes co-cultured with healthy neurons compared to those co-cultured with diseased neurons, ultimately leading to a similar RR duration in both setups suggesting some compensation (Fig 4.20C).

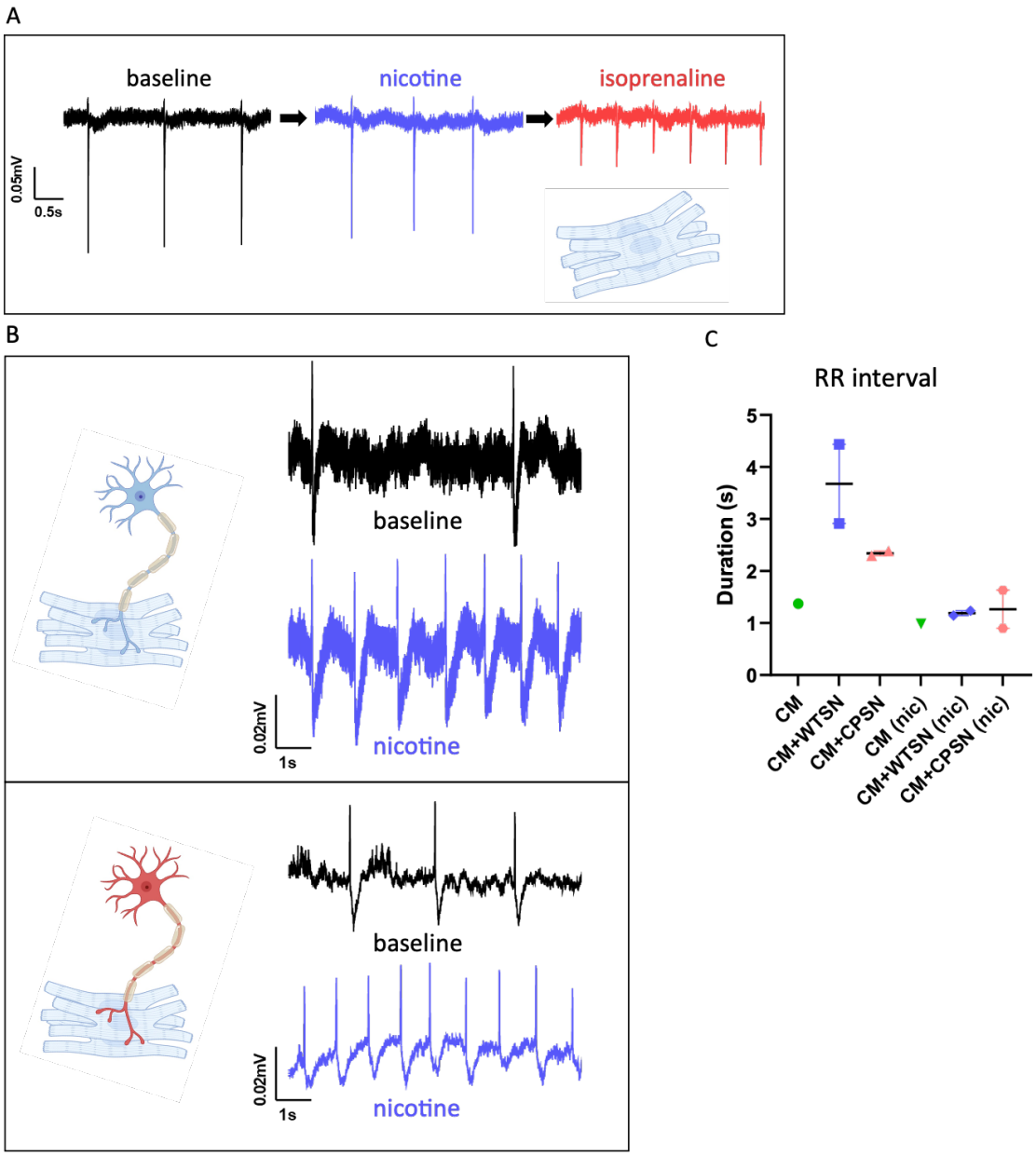


Figure 4.20 A. Representative raw data trace showing electrical activity in cardiac myocytes in monoculture. **B.** Representative field potential trace of cardiac myocytes coculture with healthy sympathetic neurons and CPVT sympathetic neurons. **C. RR interval was shortened in co-culture and cross-culture when stimulated with nicotine.**. Healthy myocytes monoculture: baseline 1.373s vs nicotine 0.987s (n=1); myocyte co-cultured with WT sympathetic neuron: baseline 3.676±0.761s vs nicotine 1.919±0.045s (n=2); myocyte co-cultured with CPVT neuron: baseline 2.338±0.046 s vs nicotine 1.263±0.367 s (n=2), $p>0.05$.

4.4 Discussion

This chapter presented a primary novel finding that sympathetic neurons derived from catecholaminergic polymorphic ventricular tachycardia hiPSCs are hyperactivated, which manifested as an enhanced calcium signal and a trend for higher noradrenaline secretion.

The critical role of autonomic innervation in cardiovascular diseases, such as hypertension and cardiac channelopathy, has been well-documented. Likewise, in the context of CPVT, frequent triggers such as exercise and emotional stress often precede the onset of arrhythmia. Surprisingly, the dysregulation of sympathetic activity has not received substantial attention in the exploration of underlying mechanisms. In contrast, there has been intensive scrutiny of RyR2 receptor instability in cardiac myocytes as a focal point in understanding the CPVT mechanism causing arrhythmia. The question of whether sympathetic neurons are hyperexcitable in CPVT remains unresolved.

To answer this question, disease models were generated using a CPVT hiPS cell line carrying *RYR2* mutation and its isogenic mutation-corrected counterpart. Cardiac myocyte and sympathetic neuron differentiation were replicated on these stem cell lines. The validation of cell-type-specific protein expression in cardiac myocytes and sympathetic neurons derived from hiPSCs was conducted through rigorous methods including flow cytometry, immunofluorescence staining, and single-cell RNA sequencing. While structural abnormalities were indistinguishable under the light microscope between healthy and CPVT cell lines, heightened calcium signals were discerned in the diseased cardiac myocytes and sympathetic neurons.

The characterization of calcium signalling revealed a higher frequency of spontaneous calcium sparks and an augmented calcium transient post-stimulation in CPVT hiPSC-CMs, aligning with previous publications. Under the conditions where extracellular [Ca^{2+}] was maintained in

2mM to mimic physiological states and without additional interventions affecting calcium influx or efflux channels, both direct and indirect activation of ryanodine receptors resulted in a higher amplitude of calcium discharge in CPVT cardiac myocytes. This was observed with the application of 50mM KCl, which depolarizes the plasma membrane and opens LTCC, isoprenaline, which activates Gs protein and phosphorylates RyR2 and phospholamban, or caffeine, which directly activates RyR2.

CPVT, as a severe arrhythmic disease, stems from aberrant calcium handling. The triggered activity arises from a diastolic calcium leak from the sarcoplasmic reticulum through the RyR2 receptor, which exhibits a higher open probability (Po) due to hereditary changes. The open probability of the RyR2 receptor is sensitive to both luminal and cytosolic [Ca^{2+}]. The cytosolic-side calcium gating of RyR2, termed calcium-induced-calcium-release (CICR), is biphasically dependent on calcium concentration, being activatory at low concentrations (1-10μM) and inhibitory at high concentrations (> 10μM)[200]. Increased luminal Ca^{2+} significantly raises the Po of RyR2 channels, although the exact mechanism remains controversial[201]. Most studies on CPVT calcium leak propose a decreased threshold of ER [Ca^{2+}] as the primary cause, while some indicate that certain *RYR2* mutations increase cytosolic calcium sensitivity[202].

Calcium transients were also enhanced in CPVT sympathetic neurons in response to membrane depolarization (KCl or nicotine) and RyR2 stimulation (Caffeine) as discovered in cardiac myocytes, which to the best of my knowledge has not yet been reported. The elevated intracellular calcium induced hypersecretion of the sympathetic neurotransmitter noradrenaline, which indicated that in CPVT, sympathetic input to the cardiac myocytes was higher. This was evidenced by electrical mapping of neurocardiac coculture, in which myocyte beating rates were faster when co-cultured with CPVT sympathetic neurons. Although it is a cardiac arrhythmic disease, the first-line treatment for CPVT is a beta blocker to suppress sympathetic

adrenergic stimulation. However, beta blockers are only effective in up to 50% of CPVT patients[203]. Left cardiac sympathetic denervation (LCSD) or implantable cardioverter defibrillator (ICD) are surgical interventions for some refractory patients. However, unlike other inherited arrhythmic syndrome, CPVT is considered the only disease that the ICD may increase the risk of onset since inappropriate ICD discharge and the patient's emotional stress to the discharge could become triggers of arrhythmia[204]. Given the adverse effects of current effective management for CPVT, the discovery of other pharmacological therapies targeting sympathetic neurons would be beneficial. Thus, I further investigated the underlying mechanisms that could give rise to the hyperexcitable calcium signal in CPVT hiPSC-SNs.

Enhanced calcium signalling can result directly from the dysfunction of release (gain-of-function) or reuptake (loss-of-function) calcium channels such as RyR2 in the case of CPVT, or aberrant regulation of these channels including second messengers and membrane potential. Early work by our group has listed cAMP/cGMP crosstalk[205] and M current[49] as potential regulators of calcium signalling. However, upstream cAMP signalling was found to be suppressed in CPVT cardiac myocytes and sympathetic neurons. To induce cAMP generation, I used isoprenaline and nicotine to stimulate cardiac myocytes and sympathetic neurons respectively. Isoprenaline is a nonselective beta-adrenergic receptor agonist, which binds to the Gs protein-coupled receptor and activates transmembrane adenylyl cyclase (tmAC)[206], upregulating cAMP level. cAMP further activates PKA which then phosphorylates RyR2 at serine-2031 and -2809 enhancing the channel's response to luminal calcium and increasing open probability[207]. Nicotinic receptor is a nonselective cation channel which leads to membrane depolarization when activated. Membrane depolarization activates membrane potential-sensitive ACs that increase cAMP production[208]. Besides, calcium entering through nicotinic receptors also acts on soluble adenylyl cyclase (sAC) to generate more cAMP[209,210]. Suppressed cAMP level detected in CPVT hiPSC derived myocytes and neurons opposed this

second messenger as the origin of dysregulated calcium in CPVT. Instead of being overactive, the cAMP was downregulated in diseased cell lines, (control sympathetic neuron 40.47±6.131%, n=14 vs CPVT sympathetic neuron 22.03±3.999%, n=14, $p<0.05$) which might be explained by negative feedback control of the elevated baseline cytosolic [Ca^{2+}] resulting from RyR2 leakage. It is also worth noting that the change of the subcellular compartmentalized cAMP level could be opposite to the whole cell level, enabling PKA activation at the RyR2 region. Interestingly, when measuring the whole-cell cAMP level of cardiac myocytes in neurocardiac co-culture, the same nicotinic treatment increased cAMP in CPVT myocytes to the same level as in healthy myocytes. As isoprenaline triggered higher cAMP response in healthy cardiac myocytes, (40.42±3.03%, n=17 vs 8.456±2.666%, n=15, $p<0.001$), the elevation of cAMP in CPVT myocytes suggested that myocytes in the co-culture received enhanced synaptic transmission from CPVT neurons. This also supported the finding that CPVT sympathetic neurons were hyperexcitable. Additionally, cytokines from cardiac myocytes and sympathetic neurons might have modified each other as a co-culture effect and augmented cAMP response in cardiac myocytes[158].

I also utilized the microelectrode array to conduct action potential characterization of hiPSC-derived cardiac myocytes. In clinical settings, the typical ECG of a CPVT patient appears normal at rest, but under stress, it can manifest ventricular premature beats (resulting from delayed after depolarizations in the case of CPVT) leading to bidirectional ventricular tachycardia and polymorphic ventricular tachycardia[211]. Pasquale et al., in their work, identified delayed after depolarization at rest and after 1 μM Isoprenaline stimulation in CPVT hiPSC-CMs using whole-cell patch-clamp techniques[212]. In the microelectrode array recording I conducted, the application of 1 μM isoprenaline induced significant heart rate acceleration in both WT and CPVT hiPSC-CMs without triggering delayed after depolarization in the diseased line. This suggests that both cell lines exhibited an adrenergic-responsive behaviours. However,

for monolayer cardiac myocyte culture, a higher concentration of isoprenaline may be required to elicit propagating arrhythmic electrical activity compared to single-cell patch-clamp experiments, where there is greater electrotonicity in the network of myocytes preventing arrhythmia compared to the single cell experiments[213].

4.5 Future direction

Present findings suggest that besides the well-studied cardiac myocyte defect in CPVT, sympathetic neurons derived from hiPSC carrying an *RYR2* mutation also displayed dysregulation in intracellular calcium signalling. It would be of therapeutic benefit to further clarify the involved cellular pathway to ascertain a target site for therapeutic intervention.

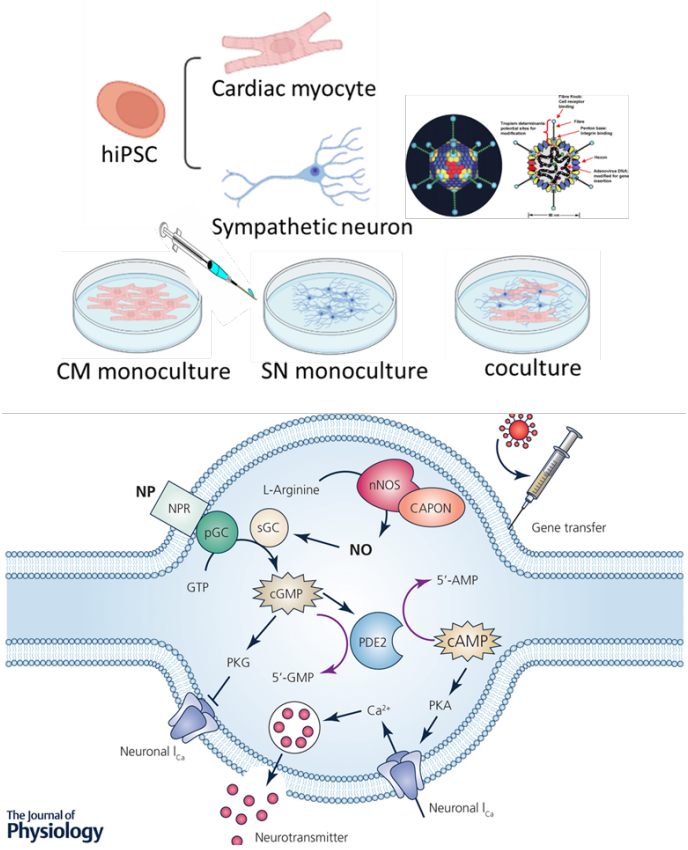


Figure 4.21 Gene therapeutic targets in neurons with site-specific vectors for NOS1-AP (CAPON) to decrease noradrenergic transmission and post-synaptic excitability in patients with LQT1. Is this pathway linked to abnormal transmission in human CPVT? Can we recapitulate cardiac afterdepolarisations caused by sympathetic activation in a model of human iPSC differentiated myocytes and neurons from patients with CVPT, and target key proteins to rescue the electrophysiological phenotype?

Previous work from our group has identified that impairment of cyclic nucleotide signalling, coupled with abnormal regulation of phosphodiesterase (PDEs), is linked to enhanced intracellular calcium transients ($[Ca^{2+}]_i$) and exocytosis in rat sympathetic neurons[205]. NOS1AP is of specific neurocardiac interest as it also regulates neurotransmission and postsynaptic excitability in cardiac sympathetic neurons, where neuronal NOS1AP loss-of-function is associated with sympathetic hyperactivity and increased arrhythmia risk[214] (Fig 4.21), especially in patients with LQT syndrome. In the hiPSC CPVT model, although whole cell cAMP was suppressed in myocytes and neurons, studies should further investigate subcellular compartmentalized cAMP in the vicinity of RyR2 receptor with RyR2 targeted FRET sensors[215] and PKA phosphorylation activity with AKAR4 fluorescent biosensor. On the cGMP side, enhancing the NO/cGMP pathway with supplementary 8-bromo-cGMP to the CPVT sympathetic neurons appeared to not affect the calcium rise triggered by KCl in a pilot study (Fig. 4.12), where six minutes of perfusion with 8-bromo-cGMP caused no significant change in peak $[Ca^{2+}]_i$. A cGMP FRET sensor Ad-CMV-cGi500 could be used to confirm that 8-bromo-cGMP perfusion increases the cellular cGMP level. Also, a direct study of the cGMP level in CPVT versus healthy sympathetic neurons could be conducted using this FRET sensor with sodium nitroprusside stimulation.

Enhanced membrane firing is another factor contributing to calcium hyperactivity. M current as a noninactivating potassium channel maintains the resting membrane potential and raises the threshold for firing an action potential[49]. Reduced M current density therefore increases the excitability of neurons. Davis et al reported functionally downregulated M current in SHR stellate ganglia neurons, which displayed aberrant electrical activity[49]. Pharmacological activation of M current reduced the firing rate in SHR neurons while M current inhibition recapitulated diseased phenotype in Wistar neurons. Manipulation of M current with KCNQ

inhibitor XE-991 and activator retigabine on CPVT calcium signalling would be a fruitful avenue to investigate.

Chapter 5: Target discovery to attenuate neurotransmission in catecholaminergic polymorphic ventricular tachycardia neurons

5.1 Introduction

5.1.1 Rationale for target discovery

Dysautonomia, particularly sympathetic hyperactivity, plays an important role in triggering ectopic beats in catecholaminergic polymorphic ventricular tachycardia (CPVT). The current effective management of CPVT arrhythmic attack involves beta-adrenergic blockers to minimize sympathetic function[216]. I proposed a hypothesis suggesting that CPVT sympathetic neurons carry certain abnormalities leading to enhanced adrenergic neurotransmission. Identifying potential pathogenic molecules in sympathetic neurons of CPVT patients would be clinically beneficial, as prolonged use of beta blockers coincides with many off-target effects such as bradycardia, hypotension, fatigue, and dizziness[217].

Although RyR2 is mainly expressed in cardiac tissue, it is also the predominant subtype in the nervous system[218]. Therefore, a gain-of-function mutation related to CPVT could also give rise to abnormal calcium discharge in sympathetic neurons that promote noradrenaline release[218]. However, besides *RYR2* mutation, which would be difficult to correct by directly targeting the receptor conformational change, modulation of calcium-associated signalling pathways (as discussed in chapter one) might provide a tractable therapeutic opportunity.

5.1.2 Application of RNA sequencing in target discovery

RNA sequencing (RNAseq) is a genomic approach to assess gene expression in cells that enables a thorough molecular understanding of cell physio-pathological behaviours. Genomic profiling provides a blueprint for understanding cellular biological processes. Moreover, it is important to accurately phenotype of hiPSCs if they are to be used with confidence in modelling human diseases.

Next-generation sequencing (NGS) enables high throughput RNA analysis through the sequencing of cDNA from homogenized tissue. The vast amount of information generated has revolutionized the road map for biomedical discoveries[141,142]. It provides bulk information as an average of gene expression in a large population of cells. To assess the difference between single cells, the first single-cell RNA sequencing (scRNAseq)[143] protocol was published in 2009 and allowed the study of the biological properties of the individual cell at the genomic level.

RNAseq not only quantifies transcript levels but also facilitates the discovery of novel variants, alternative splicing, allele-specific expression, and gene fusion[219]. In diseased states, dysregulations in transcriptomes give an insight into the potential mishandling pathways that could be involved in the aetiology of disease.

In this chapter, scRNAseq was applied on cardiac myocytes and sympathetic neurons derived from WT and CPVT human-induced pluripotent stem cells. The aim was to provide a transcriptome of these cells to facilitate the discovery of novel therapeutic targets in diseased neurons by comparing gene expression between wildtype versus CPVT cell lines.

5.2 Methods

5.2.1 Sample preparation

Two batches of hiPSC-CMs and hiPSC-SNs in monoculture and co-culture were prepared for sequencing. Differentiation and co-culture protocols were described in the method chapter. Sample details were illustrated in Table 1. Two isogenic pairs, $CP1^{RYR2\text{-}6737\text{-}T/C}$(disease) vs $CP1^{RYR2\text{-}Corr}$ (control), and $ReBl\text{-}PAT^{RYR2\text{-}13489C/T}$ (disease) vs $ReBl\text{-}PAT^{RYR2\text{-}WT}$ (control) were used in the first batch induction. On the day of sample collection for this batch, cardiac myocytes were 61 days old, sympathetic neurons were 88 days old, and neurocardiac co-culture was on day 19. Cardiac myocytes were digested by seven-minutes incubation of TryplE enzyme (Gibco, 12604013), and Accutase (Gibco, A1110501) was used for sympathetic neurons and co-culture with 40 minutes to one-hour incubation by checking morphological change under a microscope. For the second batch, myocytes and neurons were derived from $CP1^{RYR2\text{-}6737\text{-}T/C}$ and $CP1^{RYR2\text{-}Corr}$ hiPSCs. Cardiac myocytes were on day 41 (WT) and day 39 (CPVT), sympathetic neurons were on day 63 (WT) and day 66 (CPVT), and co-culture was on day 11 when collected. In this batch, hiPSC-SN and co-culture were dissociated by 20-40 minutes of incubation in 1mg/ml collagenase A (Roche, 10103586001) in Hank's balanced salt solution.

Table 1. Summary of scRNAseq sample details					
Sample id	Genotype	Phenotype	Diagnosis	Target cell type	Cell age at collection
P_011_A11	CP1$^{RYR2\text{-}Corr}$	Control	Edited correction	Cardiac myocyte	Day 41
P_011_D11	CP1$^{RYR2\text{-}6737\text{-}T/C}$	CPVT	CPVT clinical diagnosis	Cardiac myocyte	Day 39
P_011_A10	CP1$^{RYR2\text{-}6737\text{-}T/C}$	CPVT	CPVT clinical diagnosis	Sympathetic neuron	Day 88
P_011_C10	CP1$^{RYR2\text{-}Corr}$	Control	Edited correction	Sympathetic neuron	Day 88
P_011_E10	ReBl-PAT$^{RYR2\text{-}WT}$	Control	No clinical symptom	Sympathetic neuron	Day 88
P_011_G10	ReBl-PAT$^{RYR2\text{-}13489C/T}$	CPVT	Edited mutation	Sympathetic neuron	Day 88
P_011_B11	CP1$^{RYR2\text{-}Corr}$	Control	Edited correction	Sympathetic neuron	Day 63
P_011_E11	CP1$^{RYR2\text{-}6737\text{-}T/C}$	CPVT	CPVT clinical diagnosis	Sympathetic neuron	Day 66
P_011_B10	CP1$^{RYR2\text{-}6737\text{-}T/C}$	CPVT	CPVT clinical diagnosis	Co-culture	Day 19 (Day 61+ Day 88)
P_011_D10	CP1$^{RYR2\text{-}Corr}$	Control	Edited correction	Co-culture	Day 19 (Day 61+ Day 88)
P_011_F10	ReBl-PAT$^{RYR2\text{-}WT}$	Control	No clinical symptom	Co-culture	Day 19 (Day 61+ Day 88)
P_011_H10	ReBl-PAT$^{RYR2\text{-}13489C/T}$	CPVT	Edited mutation	Co-culture	Day 19 (Day 61+ Day 88)
P_011_C11	CP1$^{RYR2\text{-}Corr}$	Control	Edited correction	Co-culture	Day 11 (Day 41+ Day 63)
P_011_F11	CP1$^{RYR2\text{-}6737\text{-}T/C}$	CPVT	CPVT clinical diagnosis	Co-culture	Day 11 (Day 39+ Day 66)
QC drop out	CP1$^{RYR2\text{-}6737\text{-}T/C}$	CPVT	CPVT clinical diagnosis	Cardiac myocyte	Day 61
QC drop out	CP1$^{RYR2\text{-}Corr}$	Control	Edited correction	Cardiac myocyte	Day 61
QC drop out	ReBl-PAT$^{RYR2\text{-}WT}$	Control	No clinical symptom	Cardiac myocyte	Day 61
QC drop out	ReBl-PAT$^{RYR2\text{-}13489C/T}$	CPVT	Edited mutation	Cardiac myocyte	Day 61

5.2.2 Dead cell removal

After dissociation, dead cells were removed using the MACS Dead Cell Removal Kit (130-090-101) to improve sample quality. Cell suspensions were centrifuged at 300rcf for 5min and resuspended in 100µl Dead Cell Removal Microbeads for 15 minutes incubation at room temperature. After incubation, cell suspensions were diluted with 500µl Binding Buffer and applied to a pre-rinsed MS column, which retained magnetic labeled cell debris, dead cells, and dying cells after cell suspension passed through. The column was further rinsed with 2ml Binding Buffer. Live cells collected in effluent were centrifuged at 300rcf for 5min and resuspended in 1ml PBS plus 0.04% BSA (AM2616) and transferred to a 2ml tube for two more washes with centrifugation and resuspension under the same condition.

5.2.3 Single cell RNA sequencing and data analysis

Single-cell suspension was delivered on ice for sequencing by Novo Nordisk. Raw sequencing data from two batches were combined and analysed by computational biologists from Novo Nordisk. QC filtering, transcripts quantification, and differential gene expression assessment under different culture conditions and between healthy and disease genotypes were conducted. Uniform Manifold Approximation and Projection (UMAP) was used to visualize the transcript profiles and cell clustering.

5.3 Results

5.3.1 Key marker gene expression identified cardiac myocytes and sympathetic neurons

After processing, 80,896 cells with good quality control were sequenced. scRNAseq revealed multiple cell clusters with different transcriptomes in the combination samples comprised of cardiac myocyte monoculture, sympathetic neuron monoculture, and neuro-cardiac co-culture (Fig. 5.1A). These clusters aligned to three major cell types, namely neurons, cardiac myocytes, and fibroblasts, indicated by high-expressed well-known cell markers as illustrated in figure 5.1B.

MAP2 is a marker of neuron differentiation[220,221]; it encodes for neuron-specific cytoskeletal protein which plays a role in determining and stabilizing dendritic shape[222]. *ACTC1* encodes cardiac α-actin, which forms the thin filament with tropomyosin and troponin as a major constituent of the contractile apparatus[223]. *COL3A* encodes the alpha 1 chain of type III collagen which is extensively expressed in most connective tissues[224,225]. *TOP2A* is an indicator

of labile cells under active division as DNA topoisomerase II which is encoded by *TOP2A* and is involved in replication and transcription[226].

Cell populations were further classified according to top-ranked expressed genes within each cluster (Fig. 5.1C). Cardiac myocytes and sympathetic neurons were both confirmed by exclusively enriched marker genes expressed in the cluster, namely *GAL*, *VIP*, and *NOS1* in sympathetic neurons, and *ACTC1* and *MYL4* in cardiac myocytes. Galanin encoded by the *GAL* gene is a small neuropeptide with various functions in the central and peripheral nervous system. NOS1 (neuronal nitric oxide synthase) located in the sympathetic stellate ganglionic neurons is an important regulator of cardiac autonomic function through NO/cGMP signalling pathway[227]. Vasoactive intestinal peptide (VIP) is also a neuropeptide that functions as a neuromodulator and neurotransmitter, regulating muscle contraction, vasodilation, and exocrine function. It is reported to be an important modulator of cell survival, growth, and differentiation during sympathetic nervous system development[228]. High expression of *MAP2*, *STMN2* (Stathmin 2), and *DCX* (Doublecortin) were also detected in the sympathetic neuronal cluster. Both *STMN2* and *DCX* are microtubular proteins with stathmin 2 regulating axonal growth[229] and doublecortin regulating neuronal migration[230]. Besides *ACTC1*, *MYL4* (Myosin light chain 4), which is enriched in embryonic cardiac muscle and adult atria, was also abundantly expressed in the cardiac muscle cluster. Other neuronal clusters identified in the samples were neural progenitor cells under development, which mainly express *DCX* as a neuronal marker, and neural glial cells, with *GFAP* as the key marker. *GFAP* (Glial fibrillary acidic protein) is uniquely expressed in glial cells, including astrocytes in the central nervous system[231], Schwann cells in the peripheral nervous system, and enteric glial cells[232].

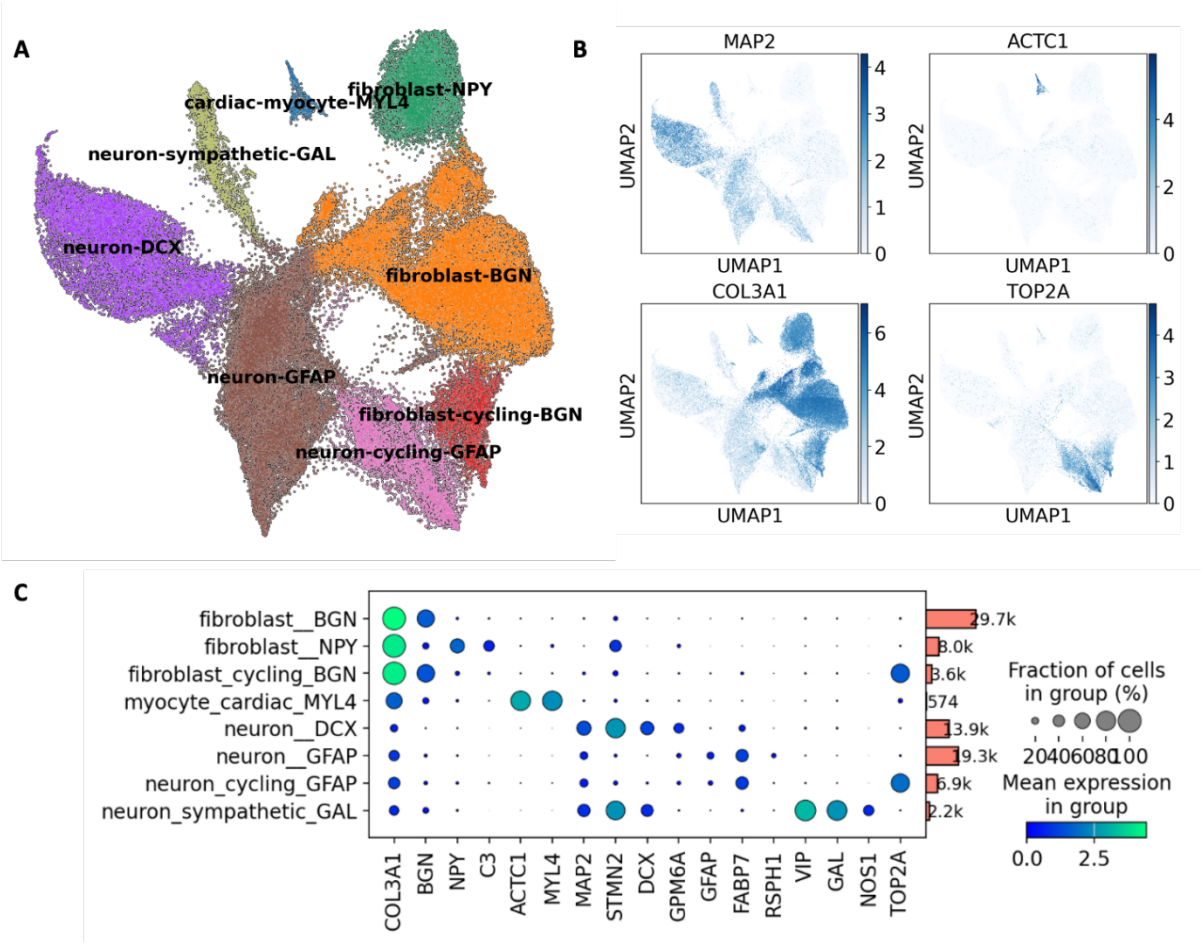


Figure 5.1 Cell populations in hiPSC-derived CPVT models. A. UMAP visualization of cell clusters generated from the combination of gene profile of hiPSC-derived cardiac myocytes, sympathetic neurons, and neurocardiac co-culture samples. **B.** The expression of *MAP2* (Microtubule-associated protein 2), *ACTC1*(Actin alpha cardiac muscle 1), and *COL3A1* (Collagen type III alpha 1 chain) revealed three major cell types of the differentiation as neuron, myocyte, and fibroblast respectively. *TOP2A* encoding for DNA topoisomerase II involved in transcription expressed highly in a labile cell population. **C.** Key marker genes used for subpopulation identification. *GAL*, *VIP*, and *NOS1* were primarily expressed in sympathetic neurons; *ACTC1* and *MYL4* were primarily expressed in cardiac myocytes.

5.3.2 Dysregulated gene expression in the sympathetic neuron due to genotype

Differential gene expression analysis between genotypes on the sympathetic neuron cluster discovered seven upregulated and five downregulated genes in the CPVT cell line (Fig. 5.2). *SERPINA3* was the one with the false discovery rate (FDR)<0.05, which was significantly decreased in CPVT neurons. *SERPINA3* encodes a member of the serpin family of proteins functioning to inhibit serine proteinase with comprehensive pathophysiological implications involving neuronal and cardiovascular pathogeneses, inflammatory and oncogenic processes, and kidney diseases[233].

Among other potential target transcripts, some were indicative of sympathetic hyperactivity, including *MOXD1* and *PHOX2A*, which are involved in noradrenaline biosynthesis and were expressed at higher levels in CPVT sympathetic neurons. *MOXD1* (DBH-like monooxygenase protein 1) is involved in the dopamine catabolic process, and *PHOX2A* is a transcription regulator protein that regulates the expression of tyrosine hydroxylase and dopamine beta-hydroxylase in sympathetic neurons[234–236]. Taken together these transcripts support the hypothesis that neurons were sympathetic by nature.

Apart from direct sympathetic-related functions, some of these genes are involved in other neuronal actions. *TM4SF4*, *SPOCK1* and *CD44* are involved in cell-cell interaction and reported to play a role during neuronal differentiation[237–239]. *TM4SF4* encodes a cell surface protein implicated in signal transduction in regulating cell differentiation and was found to be reduced in *PHOX2A* knock-out mice thus interfering with neuronal development[240]. But most studies implicate *TM4SF4* in cancer progression[241,242]. *SPOCK1* encodes a proteoglycan testican-1 that may play a role in cell-cell, cell-matrix interaction. It is found actively expressed during neuron migration and axonal growth at the onset of neurogenesis[243] and promotes blood-brain-barrier development[244]. *CD44* encodes a cell surface glycoprotein involved in cell

adhesion and migration. It is reported to be a modulator of synaptic plasticity, which affects the morphology and excitatory transmission of dendrites in hippocampal neurons; possibly through altering Cdc42 activity[245]. Increasing evidence suggests that CD44 plays a role in molecular interaction and signal transduction in various types of glial and neuronal cells[239]. This transcript was decreased in CPVT neurons. Besides cell surface protein encoding transcripts, *CRABP2* and *TTR* encode carrier proteins that are implicated in the regulation of neuron cell growth. CRABP2 (cellular retinoic acid binding protein 2) is a cytosol-to-nuclear shuttling protein for retinoic acid, which was reported to be upregulated in a differentiated neuron probably because RA signalling plays an important role in cell growth[246]. TTR (transthyretin) is a carrier protein that transports thyroid hormone and retinol in plasma and cerebrospinal fluid. It is reported to be involved in axonal growth and neural regeneration.[247] Dysregulated *TTR* was found in Alzheimer's disease[248], cardiac sympathetic denervation[249], and other neural degenerative diseases due to amyloidosis. Here, *TTR* was decreased in CPVT neurons. *TNFSF13B* encodes a cytokine expressed in B cell lineage cells and acts as a potent B cell activator[250]. Besides being a well-developed proinflammatory factor (increased in CPVT neurons), recent studies also provided some clues that TNFSF13B could support neural cell survival[251]. *MEG3* (Maternally expressed 3) is a long non-coding RNA with undetermined functions overexpressed in the pituitary and cerebellum. *MEG3* was decreased in CPVT neurons. It has been proposed to mediate neuronal apoptosis during ischemia,[252] oxidative stress[253] and can regulate synaptic plasticity[254].

The remaining transcripts are not overtly associated with neuronal disorders. *MIA* (Melanoma inhibitory activity) is an oncogene elevated in melanoma[255] regulating cell migration and invasion through cell-matrix adhesion. *PMEPA1* encodes a transmembrane protein induced by androgen and transforming growth factor beta. It antagonizes TGF-beta signalling thus possibly controlling cell proliferation, differentiation, and apoptosis. *PMEPA1* could be a

candidate tumour suppressor gene or oncogene probably due to the distinct functions of its different isoforms[256–259].

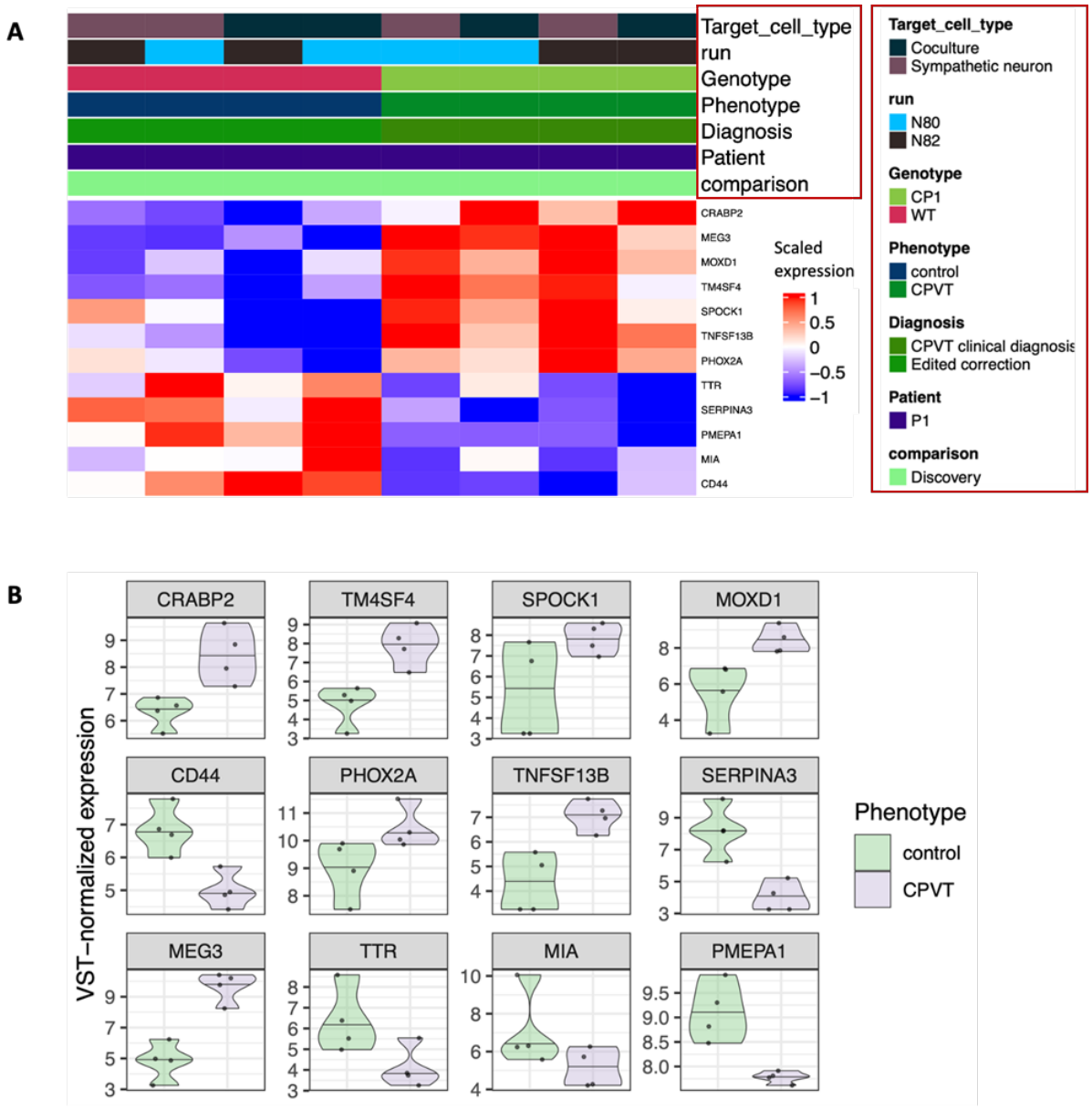


Figure 5.2 Lists of dysregulated genes in sympathetic neurons due to genotype (FDR<0.2). A. 12 differentially expressed genes were identified in eight sympathetic neuron samples. Patient P1 refers to the isogenic hiPSC pair ($CP1^{RYR2\text{-}6737\text{-}T/C}$ and $CP1^{RYR2\text{-}Corr}$) taken from the same patient, which was assigned to the discovery group. **B.** Normalized expression level of these dysregulated genes in control versus CPVT sympathetic neurons. Expression of *CRABP2*, *TM4SF4*, *SPOCK1*, *MOXD1*, *PHOX2A*, *TNFSF13B*, *MEG3* were elevated while *CD44*, *SERPINA3*, *TTR*, *MIA* and *PMEPA1* were reduced in CPVT hiPSC derived sympathetic neurons.

Gene Set Enrichment Analysis (GSEA) was applied to RNA-seq data comparing CPVT versus control samples. The analysis revealed some positive and negative enrichment based on cellular component in the CPVT hiPSC derived cardiac myocytes and sympathetic neuron (Fig.5.3).

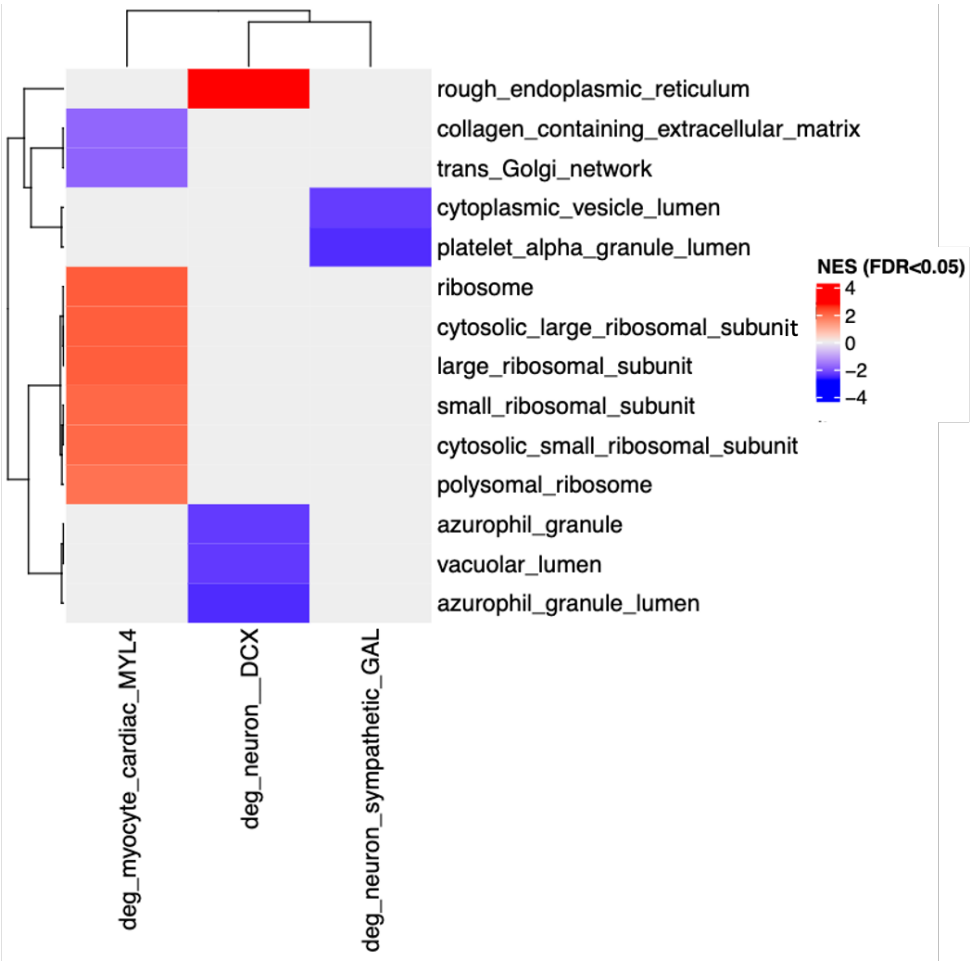


Figure 5.3 The analysis revealed significant enrichment in gene sets involved in the ribosome subunits in the CPVT cardiac myocytes (FDR<0.05), implying that the diseased myocytes are prepared for increased protein synthesis. This can be associated with processes such as cell growth, proliferation or response to certain stimuli. Significant downregulation of genes associated with 'collagen containing extracellular matrix' and 'trans Golgi network' were detected in CPVT myocyte samples, which suggested a reduction in extracellular matrix synthesis or remodelling and impairment in protein sorting and trafficking. In CPVT sympathetic neuron, 'cytoplasmic vesicle lumen' and 'platelet alpha granule lumen' were significantly decreased. The former one suggested that gene encoding proteins localized to the cytoplasmic vesicle were decreased, potentially indicating impairment in vesicle-mediated processes such as protein transport, secretion and signalling.

5.4 Discussion

Here I report novel transcriptome profiles of hiPSC induced cardiac myocytes and sympathetic neurons in catecholaminergic polymorphic ventricular tachycardia disease and discovered several potential candidate therapeutic targets in CPVT sympathetic neurons.

Transcriptome profiling has been presented in hiPSC-derived cardiac myocytes of cardiac differentiation[260–264], maturation[265–268], and cell type heterogeneity[269]. This has provided a comprehensive insight into the genetic basis of hiPSC-derived cardiac myocyte and served as a foundation for its application in disease modelling. Besides uncovering the differentiation process at cardiac lineage from pluripotent stem cells, pathological remodelling[270] and some hereditary cardiac diseases[271,272] were also studied using RNA sequencing. There are no reports on the transcriptomic profile of hiPS cells from CPVT patients.

Single-cell transcriptome analysis has been performed on various subtypes of iPSC-derived neurons and glia of the central nervous system (CNS) as well as the peripheral nervous system (PNS) to a lesser extent[273]. Similar to those of hiPSC-CM, scRNAseq studies have been conducted in hiPSC-SNs for many purposes. These include profiling neuronal cell markers expression across differentiation[274–282], interpreting molecular functional constituents[283,284] and revealing disease mechanisms for therapeutic target discovery.[285,286]

hiPSC-derived cortical glutamatergic neurons in Alzheimer's disease and midbrain dopaminergic neurons in Parkinson's disease are commonly studied cell types with differential expression analysis to identify biological subtypes, molecular mechanisms, or therapeutic targets of the disease. Transcriptomic studies of other hereditary neurodegenerative diseases such as Huntington's[287], amyotrophic lateral sclerosis[288], and Friedreich ataxia[289] were also conducted on affected cell types including motor neurons, sensory neurons, astrocyte, oligodendrocyte, and microglia, or cerebral/PNS organoid derived from hiPSC. However, no

data has been reported from hiPSC-derived sympathetic neurons either healthy or in CPVT. There are only a few attempts on sympathetic neuron induction from hiPSC to date, which makes it far less thorough than differentiating neurons of central nervous systems. This partially explains the lack of transcriptome profiling of this population of cells. In addition, CPVT is regarded as a cardiac disease with inherited calcium mishandling in myocytes, whereas there has been less focus on the intrinsic traits of neurons, even though current therapy targets adrenergic activity as the trigger of arrhythmia[9].

Here, I describe the transcriptome profile of healthy and CPVT hiPSC-derived cardiac myocytes and sympathetic neurons in monoculture and co-culture. Pooled data identified eight clusters, which mapped to three major cell types as cardiac myocytes, neuronal cells, and fibroblasts. We couldn't detect a high level of *MYH7*, *MYL2*, *TNNI3*, or *TNNT2* expression in the cardiac myocytes as commonly used cell markers in late-stage cardiac myocytes[260,265], possibly because our cardiac myocytes were still in the early stage of development and the sample size was modest while the cardiac cluster comprised only a low proportion of the total cell count. Although not listed in the top upregulated genes over cardiac induction from hiPSC, *ACTC1* and *MYL4* identified in CPVT and WT hiPSC-derived cardiac myocytes are well-established cardiac myocyte markers for cell type validation[267,290]. As for sympathetic neurons, a dataset of gene expression in hiPSC neuropeptides is presented. *GAL*, *VIP*, and *NOS1* were significantly enriched in the sympathetic cluster with high expression of peripheral neurofilament protein-encoding genes *STMN2* and *DCX*, which gives us confidence that these cells were sympathetic neurons in nature.

Our study also shed light on the candidate genes that could contribute to the diseased phenotypes of CPVT neurons. *MOXD1* and *PHOX2A* were upregulated in diseased sympathetic neurons and could be responsible for enhanced adrenergic activity in CPVT.

Except for *MOXD1* and *PHOX2A*, most of the other identified dysregulated genes assume unspecific roles in autonomic physiological processes. Some of these transcripts have already been linked to neuronal dysfunction, most of which were neural dysgenesis related. Since these transcripts are closely involved in cell proliferation and differentiation, differential expression across genotypes may indicate that developmental state could be affected in diseased neurons. However, determining whether CPVT neuron maturation was impeded remains inconclusive, since there were both up- and down-regulation of these transcripts.

SERPINA3 was significantly suppressed in CPVT sympathetic neurons. α-1-antichymotrypsin, encoded by *SERPINA3* functions to inhibit serine protease, which degrades many proteins to modulate their activity and process cellular information[291,292]. The regulatory mechanism of *SERPINA3* expression remained largely unknown[293]. The expression profile and function of *SERPINA3* have been studied sporadically in amyloidosis, cancer, and inflammatory disease [294–296]. Diverse molecular pathways are involved in different diseases, depending on the site of dysregulated α-1-antichymotrypsin and the involved proteins that are not properly degraded. In the brain, Alzheimer's disease and prion disease are the most studied diseases associated with *SERPINA3* overexpression[297]. SerpinA3 is produced by glial cells surrounding the amyloidosis region and forms part of the β-amyloid deposit. Its role in prion disease is less understood with some hypotheses related to chromatin condensation and misfolded protein accumulation[298]. Recent work also suggests that SerpinA3 promotes the proliferation of several glial and neural progenitor cells during embryonic development through the downstream target gene *Glo1*[299]. However, increased levels of SerpinA3 in the cerebrospinal fluid could also be a marker of cognitive dysfunction during AD progression[300]. Overall, the balance between α-1-antichymotrypsin and protease activity seems to play an important role in anti-inflammatory, antioxidant, antiangiogenetic, antitumorigenic, and antifibrotic[301]. How *SERPINA3* downregulation affects sympathetic neuronal activity requires additional experimental

investigations to test whether it is related to oxidative stress pathways that are known to upregulate sympathetic transmission[302,303].

5.5 Limitations

scRNAseq also revealed cell type heterogeneity in both cardiac myocyte and sympathetic neuron induction. It was reported that differentiation efficiency is defined as the proportion of target cell types varied across hiPSC lines and the reasons are still obscure[281]. The source of variance has been hypothesized to be related to iPSC heterogeneity, iPSC passage number, and experiment practices such as media volume changes, differentiation starting date, somatic genetic changes or epigenetic changes arising from cellular reprogramming[304,305]. Thus, it is worth the effort to control variates during reprogramming and differentiation and use isogenic cell lines while preparing cells for differential gene expression analysis to minimize confounding factors.

Chapter 6: Concluding Discussion

6.1 The main findings of this thesis are:

1. Feeder-free small molecule-induced differentiation protocols of hiPSCs to cardiac myocytes and sympathetic neurons were validated on six and four cell lines respectively for their reproducibility and efficiency.

2. Anatomical and functional connections were established between hiPSC cardiac myocytes and sympathetic neurons in a co-culture system that enabled measurement of noradrenaline from activated sympathetic neurons to regulate cardiac second messengers and beating rate.

3. Application of angiotensin II induces cell size enlargement, foetal gene overexpression, and beta-adrenergic hyperresponsiveness in hiPSC-derived cardiac myocytes *in vitro*, suggesting the predictive ability of hiPSC-CM to recapitulate the human phenotype associated with hypertrophy in disease modelling.

4. CPVT hiPSC-CMs showed a higher frequency of spontaneous calcium discharge during Fura-2 calcium imaging, which is consistent with the gain-of-function mutation of *RYR2*. CPVT hiPSC-SNs also displayed an elevated amplitude of calcium spikes in response to plasma membrane depolarization suggesting that CPVT is also a disease of the cardiac sympathetic nervous system.

5. *SERPINA3* was found downregulated in CPVT hiPSC-derived sympathetic neurons following single-cell RNA sequencing. This transcript might be a candidate therapeutic target given its role in cellular oxidative stress.

6.2 Cardiac myocyte and sympathetic neuron induction from hiPSC

I present a differentiation protocol for the induction of sympathetic neurons and for the generation of cardiac myocytes from human iPS cell lines. Flow cytometry and immunofluorescence confirmed cardiac troponin T, α-actinin, MLC2v expression in derived cardiac myocytes, and TH, PRPH, and nAChR expression in derived sympathetic neurons. By comparing the sarcomere length, maturation medium with low glucose and high fatty acid supplement along with prolonged culture duration from 20 days to 40 days significantly lengthened the sarcomere to resemble adult human cardiac myocytes. Further patch clamp experiments to study the electrophysiologic properties would be required for a better phenotypic profile of hiPSC-CM maturation.

Besides morphology, I also reported field potential characteristics of hiPSC-CMs and calcium transient in hiPSC-SNs as markers of physiological function. Although not as precise as a single ion channel measurement using patch clamp, electrical mapping with a microelectrode array provided a convenient route to depict the depolarization and repolarization of the cardiac membrane potential of the monolayer culture. In hiPSC-CMs, responsiveness to isoprenaline was recorded as a significantly shortened RR interval and field potential duration from baseline. As a crucial messenger that underpins synaptic plasticity and neurotransmission, hiPSC-SNs $[Ca^{2+}]_i$ responded to Angiotensin II stimulation, which opens IP3R on the ER membrane to release stored calcium to facilitate exocytosis of the transmitter.

It is noteworthy that many factors affect the reproducibility of differentiation from human induced pluripotent stem cells and the reasons are still under investigation. My experience pointed out that the passage number of hiPSCs, confluency at the beginning of differentiation, and fresh reagents are important contributing factors to the differentiation outcome.

I established a human-induced pluripotent stem cell-derived co-culture system of cardiac myocytes with sympathetic neurons for the first time. Immunofluorescence showed the dot-stained synaptic vesicles adjacent to the cardiac myocyte cluster in the coculture that laid the anatomical foundation for interaction. By stimulating the co-culture with nicotine, which activates acetylcholine receptors on neurons, heart rate and cardiac cytosolic cAMP level in myocytes were increased by neurotransmitters from sympathetic neurons. It is interesting to note that the neural-responsive calcium transient amplitude was dampened by co-culturing with cardiac myocytes. Moreover, heart rate was decelerated in the co-culture. This indicates that in the co-culture, myocytes and neurons may act on each other as a stabilizer that either increases the threshold of activation or diminishes the extent of response. Publications have shown that co-culture with other cell types promotes the maturation of in vitro cell culture possibly through paracrine cytokine that mimics the in vivo state[116,306]. Based on this, the stabilized physiological function identified in co-cultured hiPSC-CM and hiPSC-SN might be explained by a more mature status just as membrane potential becomes further depolarized with cell growth. The exact underlying mechanism is not fully understood and requires further studies.

6.3 Application of hiPSC in disease modelling: pathological cardiac hypertrophy

hiPSC could be a powerful tool in the field of disease modelling, pharmaceutical screening, and regenerative medicine. Merits of hiPSC include cellular self-renewal, patient-specific regarding contextualization, and overcoming species disparity and ethical issues. However, current works with hiPSC still have limitations such as inconsistent phenotypes, heterogeneous differentiation outcomes, immature phenotypes, and potential tumorigenicity[307]. While refinements including quality control using early markers of pluripotency and successful

differentiation, purification kits, and maturation methods are being published, there is however, no gold standard validation of hiPSC.

I applied hiPSC-CM developed with the up-to-date small-molecule differentiation protocol in pathogenic cardiac hypertrophy modelling to assess its ability to recapitulate the hypertrophic response. Exposure of day 20 plus hiPSC-CM to angiotensin II for 48 hours triggered sarcomere distortion, significant cell, and nuclear enlargement, *BNP* and *MYH7* overexpression, increased proBNP secretion, and beta-adrenergic hyperresponsive. These remodelling characteristics of anatomical structure, gene expression, and second messenger signalling are in accordance with pathogenic hypertrophy. This gives us confidence that a hiPSC-derived disease model may be efficacious in understanding molecular mechanisms of disease as an adjunct to target discovery for the identification of new therapies.

6.4 CPVT disease modelling with hiPSC-CM and hiPSC-SN

Catecholaminergic polymorphic ventricular tachycardia is one of the inherited arrhythmia syndromes induced by hypersympathetic nerve activity with a high morbidity rate but without definitive treatment. It is elucidated that calcium leakage from the RyR2 receptor on the SR membrane with gain-of-function mutation during diastole triggers delay after depolarization through increased activity of the sodium-calcium exchanger[308]. Based on previous work done by our group, sympathetic hyperactivity seems to play a critical role in driving the adrenergic phenotype in a series of cardiovascular diseases, including hypertension and long QT syndrome. Thus, I hypothesized that CPVT as an adrenergic-triggered arrhythmia probably has a disease component residing in the sympathetic neuron. I used a hiPSC line that was reprogrammed from fibroblast taken from a clinically diagnosed patient carrying RYR2-S2246L$^{+/-}$ mutation and used gene editing technology to correct the mutant gene to create the isogenic control line.

6.4.1 Cardiac myocytes calcium leakage

In CPVT hiPSC-CM, spontaneous calcium discharge was found at a higher frequency compared to isogenic control. Calcium transient amplitude was also higher in the diseased cardiac cytosol after isoprenaline and caffeine stimulation. Further experiments aimed at precise recording of ER calcium change with ER calcium indicator or with 0 mM calcium extracellular solution plus Thapsigargin to block calcium influx and reuptake would be helpful to firmly establish RYR2 receptor dysregulation.

6.4.2 Hyperactive calcium discharge in CPVT sympathetic neuron

Calcium imaging with Fura-2/AM was conducted on hiPSC-SN to answer whether sympathetic neurons with the same genetic mutation also present calcium hyperactivity. Membrane depolarization, RyR2 receptor agonist, and acetylcholine receptor agonist triggered whole calcium increases that were significantly higher in CPVT sympathetic neurons. Likewise, the identified calcium hyperresponsiveness resulted from a combination of calcium influx through voltage-gated ion channels, release from internal stores, efflux by ATPase or exchanger, and reuptake by SERCA or mitochondria uniporter[309]. I have not investigated at the subcellular level yet, but I did attempt to study an important regulation signalling pathway involving cAMP-PKA that modifies many of these calcium channels. It was surprising to observe that the cytosolic free cAMP elevation in CPVT neurons and myocytes was less significant than in healthy ones. This result hinted that cAMP-PKA phosphorylation may not be the origin of increased calcium. On the contrary, being an upstream modulator, cAMP was suppressed by negative feedback control from elevated free calcium in the cytosol. However, since CPVT is adrenergic triggered and cAMP is the main second messenger mediated by adrenergic receptor activation, isoprenaline-induced cAMP elevation should play a role in reaching the threshold

to open the unstable RyR2 receptor in CPVT. In addition, cAMP signalling has been reported to be subcellular compartmentalized, and PDE subtypes regulate local cAMP at different sites[310], therefore, there could be a local cAMP increase even if total cellular cAMP level decreases. RyR2 receptor targeted cAMP FRET sensor is now available to have a more accurate measurement at nanodomain.

I also measured the calcium response to high K^+ in neurons co-cultured with cardiac myocytes. Cardiac myocyte growth with neurons did not exert an influence on the neuronal calcium response in terms of the calcium transient amplitude. CPVT neurons still reacted more actively to external stimulation in co-culture. Co-cultured with healthy or CPVT cardiac myocytes did not make a difference in the extent of calcium elevation in sympathetic neurons.

6.5 Transcript profile of cardiac myocyte and sympathetic neuron differentiation from CPVT vs WT hiPSC

Single-cell RNA sequencing was conducted for the first time from CPVT and WT hiPSC-derived cardiac myocytes and sympathetic neurons. The transcriptome profile identified 8 clusters as: cardiac myocytes, sympathetic neurons, astrocytes, progenitor neuronal cells, unknown neural cells, and fibroblasts. *ACTC1* and *MYL4* were identified in hiPSC-derived cardiac myocytes. *GAL*, *VIP*, and *NOS1* were significantly enriched in the sympathetic cluster with high expression of peripheral neurofilament protein-encoding genes *STMN2* and *DCX*.

6.5.1 *SERPINA3* gene expression downregulated in CPVT hiPSC-SN

Differential analysis between genotypes filtered out *SERPINA3* as the significantly downregulated gene in CPVT hiPSC sympathetic neurons. It encodes one member of the serine protease inhibitor family, α-1-antichymotrypsin, which functions to reduce protein degradation. Interestingly, upregulated *SEPINA3* was found in astroglia cells surrounding amyloid beta aggregate in Alzheimer's disease[311]. It has also been found to be involved in inflammatory disease and cancer[293], and may be related to an imbalance between α-1-antichymotrypsin and protease activity. The improperly degraded protein may also result in deficient cell types and contribute to the phenotypes of the disease itself. An imbalance in serpin-protease homeostasis leads to pathophysiological phenotypes. Mutations in *SERPINA3* result in deficiency or complete loss of serpin expression. This leads to an excess in target protease activity and thus a disruption of the downstream pathway, especially pathways involving oxidative stress, cellular proliferation, and apoptosis[233]. Many serpinopathies are related to intracellular accumulation caused by the improper folding of the proteins. Whether CPVT is a serpinopathy remains to be determined, but to date, my data suggests this may be the case. Future studies need to be directed at testing the veracity of the *SERPINA3* hypothesis.

In conclusion, I have recapitulated various anatomical and physiological characteristics of human cells by hiPSC-CM and hiPSC-SN and also provided the transcriptomic atlas of these cell types and identified a key transcript that may underpin the neural phenotype in CPVT. The hiPSC monoculture and co-culture preparations behave in a manner that mimics key physiological responses seen in other mammalian cell types and therefore may provide a framework for target discovery and a mechanistic understanding of human pathophysiological states.

References

1. Waxenbaum JA, Reddy V, Varacallo M. Anatomy, Autonomic Nervous System. In: *StatPearls*. StatPearls Publishing; 2023. Accessed December 21, 2023. http://www.ncbi.nlm.nih.gov/books/NBK539845/

2. Tindle J, Tadi P. Neuroanatomy, Parasympathetic Nervous System. In: *StatPearls*. StatPearls Publishing; 2023. Accessed December 21, 2023. http://www.ncbi.nlm.nih.gov/books/NBK553141/

3. Bylund DB. Adrenergic Receptors. In: Lennarz WJ, Lane MD, eds. *Encyclopedia of Biological Chemistry (Second Edition)*. Academic Press; 2013:57-60. doi:10.1016/B978-0-12-378630-2.00334-0

4. Kuhar MJ, Couceyro PR, Lambert PD. α- and β-Adrenergic Receptors. In: *Basic Neurochemistry: Molecular, Cellular and Medical Aspects. 6th Edition*. Lippincott-Raven; 1999. Accessed February 6, 2024. https://www.ncbi.nlm.nih.gov/books/NBK28138/

5. Chaudhary PK, Kim S. An Insight into GPCR and G-Proteins as Cancer Drivers. *Cells*. 2021;10(12):3288. doi:10.3390/cells10123288

6. Sassone-Corsi P. The Cyclic AMP Pathway. *Cold Spring Harb Perspect Biol*. 2012;4(12):a011148. doi:10.1101/cshperspect.a011148

7. Kashou AH, Basit H, Chhabra L. Physiology, Sinoatrial Node. In: *StatPearls*. StatPearls Publishing; 2023. Accessed December 21, 2023. http://www.ncbi.nlm.nih.gov/books/NBK459238/

8. Coote JH, Chauhan RA. The sympathetic innervation of the heart: Important new insights. *Auton Neurosci*. 2016;199:17-23. doi:10.1016/j.autneu.2016.08.014

9. Winbo A, Paterson DJ. The Brain-Heart Connection in Sympathetically Triggered Inherited Arrhythmia Syndromes. *Heart Lung Circ*. 2020;29(4):529-537. doi:10.1016/j.hlc.2019.11.002

10. Rajendran PS, Challis RC, Fowlkes CC, et al. Identification of peripheral neural circuits that regulate heart rate using optogenetic and viral vector strategies. *Nat Commun*. 2019;10(1):1944. doi:10.1038/s41467-019-09770-1

11. Ishikawa Y, Homcy CJ. The adenylyl cyclases as integrators of transmembrane signal transduction. *Circ Res*. 1997;80(3):297-304. doi:10.1161/01.res.80.3.297

12. Y Z, We W, X Z, et al. Cardiomyocyte PKA Ablation Enhances Basal Contractility While Eliminates Cardiac β-Adrenergic Response Without Adverse Effects on the Heart. *Circulation research*. 2019;124(12). doi:10.1161/CIRCRESAHA.118.313417

13. Zhang R, Zhao J, Mandveno A, Potter JD. Cardiac troponin I phosphorylation increases the rate of cardiac muscle relaxation. *Circ Res*. 1995;76(6):1028-1035. doi:10.1161/01.res.76.6.1028

14. McNamara JW, Singh RR, Sadayappan S. Cardiac myosin binding protein-C phosphorylation regulates the super-relaxed state of myosin. *Proc Natl Acad Sci U S A*. 2019;116(24):11731-11736. doi:10.1073/pnas.1821660116

15. Liu Y, Chen J, Fontes SK, Bautista EN, Cheng Z. Physiological and pathological roles of protein kinase A in the heart. *Cardiovasc Res*. 2022;118(2):386-398. doi:10.1093/cvr/cvab008

16. Gordan R, Gwathmey JK, Xie LH. Autonomic and endocrine control of cardiovascular function. *World J Cardiol*. 2015;7(4):204-214. doi:10.4330/wjc.v7.i4.204

17. Barrett MS, Bauer TC, Li MH, et al. Ischemia-reperfusion myocardial infarction induces remodeling of left cardiac-projecting stellate ganglia neurons. *Am J Physiol Heart Circ Physiol*. 2024;326(1):H166-H179. doi:10.1152/ajpheart.00582.2023

18. Durães Campos I, Pinto V, Sousa N, Pereira VH. A brain within the heart: A review on the intracardiac nervous system. *J Mol Cell Cardiol*. 2018;119:1-9. doi:10.1016/j.yjmcc.2018.04.005

19. Gomez JF, Cardona K, Romero L, Ferrero JM, Trenor B. Electrophysiological and structural remodeling in heart failure modulate arrhythmogenesis. 1D simulation study. *PLoS One*. 2014;9(9):e106602. doi:10.1371/journal.pone.0106602

20. Franciosi S, Perry FKG, Roston TM, Armstrong KR, Claydon VE, Sanatani S. The role of the autonomic nervous system in arrhythmias and sudden cardiac death. *Auton Neurosci*. 2017;205:1-11. doi:10.1016/j.autneu.2017.03.005

21. Gardner RT, Ripplinger CM, Myles RC, Habecker BA. Molecular Mechanisms of Sympathetic Remodeling and Arrhythmias. *Circ Arrhythm Electrophysiol*. 2016;9(2):e001359. doi:10.1161/CIRCEP.115.001359

22. Sridharan A, Bradfield JS, Shivkumar K, Ajijola OA. Autonomic nervous system and arrhythmias in structural heart disease. *Auton Neurosci*. 2022;243:103037. doi:10.1016/j.autneu.2022.103037

23. Fukuda K, Kanazawa H, Aizawa Y, Ardell JL, Shivkumar K. Cardiac innervation and sudden cardiac death. *Circ Res*. 2015;116(12):2005-2019. doi:10.1161/CIRCRESAHA.116.304679

24. Weiss JN, Garfinkel A, Karagueuzian HS, Chen PS, Qu Z. Early afterdepolarizations and cardiac arrhythmias. *Heart Rhythm*. 2010;7(12):1891-1899. doi:10.1016/j.hrthm.2010.09.017

25. Rizzo S, Basso C, Troost D, et al. T-cell-mediated inflammatory activity in the stellate ganglia of patients with ion-channel disease and severe ventricular arrhythmias. *Circ Arrhythm Electrophysiol*. 2014;7(2):224-229. doi:10.1161/CIRCEP.113.001184

26. Crotti L, Monti MC, Insolia R, et al. NOS1AP is a genetic modifier of the long-QT syndrome. *Circulation*. 2009;120(17):1657-1663. doi:10.1161/CIRCULATIONAHA.109.879643

27. Herring N, Paterson DJ. Nitric oxide-cGMP pathway facilitates acetylcholine release and bradycardia during vagal nerve stimulation in the guinea-pig in vitro. *J Physiol*. 2001;535(Pt 2):507-518. doi:10.1111/j.1469-7793.2001.00507.x

28. Gees M, Colsoul B, Nilius B. The role of transient receptor potential cation channels in Ca2+ signaling. *Cold Spring Harb Perspect Biol*. 2010;2(10):a003962. doi:10.1101/cshperspect.a003962

29. Shuttleworth TJ. Arachidonic acid, ARC channels, and Orai proteins. *Cell Calcium*. 2009;45(6):602-610. doi:10.1016/j.ceca.2009.02.001

30. Del Prete D, Checler F, Chami M. Ryanodine receptors: physiological function and deregulation in Alzheimer disease. *Mol Neurodegener*. 2014;9:21. doi:10.1186/1750-1326-9-21

31. Hiess F, Yao J, Song Z, et al. Subcellular localization of hippocampal ryanodine receptor 2 and its role in neuronal excitability and memory. *Commun Biol*. 2022;5(1):183. doi:10.1038/s42003-022-03124-2

32. Cooper D, Dimri M. Biochemistry, Calcium Channels. In: *StatPearls*. StatPearls Publishing; 2023. Accessed December 21, 2023. http://www.ncbi.nlm.nih.gov/books/NBK562198/

33. Brini M, Calì T, Ottolini D, Carafoli E. Neuronal calcium signaling: function and dysfunction. *Cell Mol Life Sci*. 2014;71(15):2787-2814. doi:10.1007/s00018-013-1550-7

34. Catterall WA. Voltage-gated calcium channels. *Cold Spring Harb Perspect Biol*. 2011;3(8):a003947. doi:10.1101/cshperspect.a003947

35. Su SC, Seo J, Pan JQ, et al. Regulation of N-type voltage-gated calcium channels and presynaptic function by cyclin-dependent kinase 5. *Neuron*. 2012;75(4):675-687. doi:10.1016/j.neuron.2012.06.023

36. Blazon M, LaCarubba B, Bunda A, et al. N-type calcium channels control GABAergic transmission in brain areas related to fear and anxiety. *OBM Neurobiol*. 2021;5(1). doi:10.21926/obm.neurobiol.2101083

37. Yang L, Liu G, Zakharov SI, Bellinger AM, Mongillo M, Marx SO. Protein kinase G phosphorylates Cav1.2 alpha1c and beta2 subunits. *Circ Res*. 2007;101(5):465-474. doi:10.1161/CIRCRESAHA.107.156976

38. Sassone-Corsi P. The cyclic AMP pathway. *Cold Spring Harb Perspect Biol*. 2012;4(12):a011148. doi:10.1101/cshperspect.a011148

39. Tanwar M, Khera L, Haokip N, Kaul R, Naorem A, Kateriya S. Modulation of cyclic nucleotide-mediated cellular signaling and gene expression using photoactivated adenylyl cyclase as an optogenetic tool. *Sci Rep*. 2017;7(1):12048. doi:10.1038/s41598-017-12162-4

40. Hofmann F, Bernhard D, Lukowski R, Weinmeister P. cGMP regulated protein kinases (cGK). *Handb Exp Pharmacol*. 2009;(191):137-162. doi:10.1007/978-3-540-68964-5_8

41. Francis SH, Corbin JD. Cyclic nucleotide-dependent protein kinases: intracellular receptors for cAMP and cGMP action. *Crit Rev Clin Lab Sci*. 1999;36(4):275-328. doi:10.1080/10408369991239213

42. Burnette JO, White RE. PGI2 opens potassium channels in retinal pericytes by cyclic AMP-stimulated, cross-activation of PKG. *Exp Eye Res*. 2006;83(6):1359-1365. doi:10.1016/j.exer.2006.07.011

43. Willipinski-Stapelfeldt B, Lübberstedt J, Stelter S, Vogt K, Mukhopadhyay AK, Müller D. Comparative analysis between cyclic GMP and cyclic AMP signalling in human sperm. *Mol Hum Reprod*. 2004;10(7):543-552. doi:10.1093/molehr/gah065

44. Hartwig C, Bähre H, Wolter S, Beckert U, Kaever V, Seifert R. cAMP, cGMP, cCMP and cUMP concentrations across the tree of life: High cCMP and cUMP levels in astrocytes. *Neurosci Lett*. 2014;579:183-187. doi:10.1016/j.neulet.2014.07.019

45. Calamera G, Moltzau LR, Levy FO, Andressen KW. Phosphodiesterases and Compartmentation of cAMP and cGMP Signaling in Regulation of Cardiac Contractility in Normal and Failing Hearts. *Int J Mol Sci*. 2022;23(4):2145. doi:10.3390/ijms23042145

46. Zaccolo M, Movsesian MA. cAMP and cGMP signaling cross-talk: role of phosphodiesterases and implications for cardiac pathophysiology. *Circ Res*. 2007;100(11):1569-1578. doi:10.1161/CIRCRESAHA.106.144501

47. Isidori AM, Cornacchione M, Barbagallo F, et al. Inhibition of type 5 phosphodiesterase counteracts β2-adrenergic signalling in beating cardiomyocytes. *Cardiovasc Res*. 2015;106(3):408-420. doi:10.1093/cvr/cvv123

48. Sadek MS, Cachorro E, El-Armouche A, Kämmerer S. Therapeutic Implications for PDE2 and cGMP/cAMP Mediated Crosstalk in Cardiovascular Diseases. *Int J Mol Sci*. 2020;21(20):7462. doi:10.3390/ijms21207462

49. Davis H, Herring N, Paterson DJ. Downregulation of M Current Is Coupled to Membrane Excitability in Sympathetic Neurons Before the Onset of Hypertension. *Hypertension*. 2020;76(6):1915-1923. doi:10.1161/HYPERTENSIONAHA.120.15922

50. Wladyka CL, Kunze DL. KCNQ/M-currents contribute to the resting membrane potential in rat visceral sensory neurons. *J Physiol*. 2006;575(Pt 1):175-189. doi:10.1113/jphysiol.2006.113308

51. Berg T. Kv7(KCNQ)-K+-Channels Influence Total Peripheral Resistance in Female but Not Male Rats, and Hamper Catecholamine Release in Hypertensive Rats of Both Sexes. *Front Physiol*. 2018;9:117. doi:10.3389/fphys.2018.00117

52. Ackerman MJ, Clapham DE. chapter 18 - Excitability and Conduction. In: Chien KR, ed. *Molecular Basis of Cardiovascular Disease (Second Edition)*. W.B. Saunders; 2004:311-335. doi:10.1016/B978-0-7216-9428-3.50023-8

53. Bers DM. Cardiac sarcoplasmic reticulum calcium leak: basis and roles in cardiac dysfunction. *Annu Rev Physiol*. 2014;76:107-127. doi:10.1146/annurev-physiol-020911-153308

54. Hoang-Trong TM, Ullah A, Jafri MS. Calcium Sparks in the Heart: Dynamics and Regulation. *Res Rep Biol*. 2015;6:203-214. doi:10.2147/RRB.S61495

55. Behere SP, Weindling SN. Inherited arrhythmias: The cardiac channelopathies. *Ann Pediatr Cardiol*. 2015;8(3):210-220. doi:10.4103/0974-2069.164695

56. Arzamendi D, Benito B, Tizon-Marcos H, et al. Increase in sudden death from coronary artery disease in young adults. *Am Heart J*. 2011;161(3):574-580. doi:10.1016/j.ahj.2010.10.040

57. Myerburg RJ, Junttila MJ. Sudden cardiac death caused by coronary heart disease. *Circulation*. 2012;125(8):1043-1052. doi:10.1161/CIRCULATIONAHA.111.023846

58. Boczek NJ, Tester DJ, Ackerman MJ. The molecular autopsy: an indispensable step following sudden cardiac death in the young? *Herzschrittmacherther Elektrophysiol*. 2012;23(3):167-173. doi:10.1007/s00399-012-0222-x

59. Schwartz PJ, Stramba-Badiale M, Crotti L, et al. Prevalence of the congenital long-QT syndrome. *Circulation*. 2009;120(18):1761-1767. doi:10.1161/CIRCULATIONAHA.109.863209

60. Yee LA, Han HC, Davies B, et al. Sex Differences and Utility of Treadmill Testing in Long-QT Syndrome. *J Am Heart Assoc*. 2022;11(18):e025108. doi:10.1161/JAHA.121.025108

61. Schwartz PJ, Crotti L, Insolia R. Long-QT syndrome: from genetics to management. *Circ Arrhythm Electrophysiol*. 2012;5(4):868-877. doi:10.1161/CIRCEP.111.962019

62. van der Horst J, Greenwood IA, Jepps TA. Cyclic AMP-Dependent Regulation of Kv7 Voltage-Gated Potassium Channels. *Front Physiol*. 2020;11:727. doi:10.3389/fphys.2020.00727

63. Wang Q, Shen J, Splawski I, et al. SCN5A mutations associated with an inherited cardiac arrhythmia, long QT syndrome. *Cell*. 1995;80(5):805-811. doi:10.1016/0092-8674(95)90359-3

64. Tranebjærg L, Samson RA, Green GE. Jervell and Lange-Nielsen Syndrome. In: Adam MP, Feldman J, Mirzaa GM, et al., eds. *GeneReviews®*. University of Washington, Seattle; 1993. Accessed December 21, 2023. http://www.ncbi.nlm.nih.gov/books/NBK1405/

65. Dusi V, Pugliese L, De Ferrari GM, et al. Left Cardiac Sympathetic Denervation for Long QT Syndrome: 50 Years' Experience Provides Guidance for Management. *JACC: Clinical Electrophysiology*. 2022;8(3):281-294. doi:10.1016/j.jacep.2021.09.002

66. Ajijola OA, Lellouche N, Bourke T, et al. Bilateral Cardiac Sympathetic Denervation for the Management of Electrical Storm. *Journal of the American College of Cardiology*. 2012;59(1):91-92. doi:10.1016/j.jacc.2011.09.043

67. Wleklinski MJ, Kannankeril PJ, Knollmann BC. Molecular and tissue mechanisms of catecholaminergic polymorphic ventricular tachycardia. *J Physiol*. 2020;598(14):2817-2834. doi:10.1113/JP276757

68. Richardson SJ, Thekkedam CG, Casarotto MG, Beard NA, Dulhunty AF. FKBP12 binds to the cardiac ryanodine receptor with negative cooperativity: implications for heart muscle physiology in health and disease. *Philosophical Transactions of the Royal Society B: Biological Sciences*. 2023;378(1879):20220169. doi:10.1098/rstb.2022.0169

69. Wehrens XHT. The molecular basis of catecholaminergic polymorphic ventricular tachycardia: what are the different hypotheses regarding mechanisms? *Heart Rhythm*. 2007;4(6):794-797. doi:10.1016/j.hrthm.2006.12.016

70. Ng K, Titus EW, Lieve KV, et al. An International Multicenter Evaluation of Inheritance Patterns, Arrhythmic Risks, and Underlying Mechanisms of CASQ2-Catecholaminergic Polymorphic Ventricular Tachycardia. *Circulation*. 2020;142(10):932-947. doi:10.1161/CIRCULATIONAHA.120.045723

71. Terentyev D, Nori A, Santoro M, et al. Abnormal interactions of calsequestrin with the ryanodine receptor calcium release channel complex linked to exercise-induced sudden cardiac death. *Circ Res*. 2006;98(9):1151-1158. doi:10.1161/01.RES.0000220647.93982.08

72. Gong D, Chi X, Wei J, et al. Modulation of cardiac ryanodine receptor 2 by calmodulin. *Nature*. 2019;572(7769):347-351. doi:10.1038/s41586-019-1377-y

73. Bhuiyan ZA, Hamdan MA, Shamsi ETA, et al. A novel early onset lethal form of catecholaminergic polymorphic ventricular tachycardia maps to chromosome 7p14-p22. *J Cardiovasc Electrophysiol*. 2007;18(10):1060-1066. doi:10.1111/j.1540-8167.2007.00913.x

74. Webster G, Aburawi EH, Chaix MA, et al. Life-threatening arrhythmias with autosomal recessive TECRL variants. *Europace*. 2021;23(5):781-788. doi:10.1093/europace/euaa376

75. Liu N, Ruan Y, Priori SG. Catecholaminergic polymorphic ventricular tachycardia. *Prog Cardiovasc Dis*. 2008;51(1):23-30. doi:10.1016/j.pcad.2007.10.005

76. Bannister ML, Thomas NL, Sikkel MB, et al. The mechanism of flecainide action in CPVT does not involve a direct effect on RyR2. *Circ Res*. 2015;116(8):1324-1335. doi:10.1161/CIRCRESAHA.116.305347

77. Antzelevitch C, Brugada P, Brugada J, Brugada R, Towbin JA, Nademanee K. Brugada syndrome: 1992-2002: a historical perspective. *J Am Coll Cardiol*. 2003;41(10):1665-1671. doi:10.1016/s0735-1097(03)00310-3

78. Probst V, Wilde AAM, Barc J, et al. SCN5A mutations and the role of genetic background in the pathophysiology of Brugada syndrome. *Circ Cardiovasc Genet*. 2009;2(6):552-557. doi:10.1161/CIRCGENETICS.109.853374

79. Mizusawa Y, Wilde AAM. Brugada syndrome. *Circ Arrhythm Electrophysiol*. 2012;5(3):606-616. doi:10.1161/CIRCEP.111.964577

80. Li Y, Lang S, Akin I, Zhou X, El-Battrawy I. Brugada Syndrome: Different Experimental Models and the Role of Human Cardiomyocytes From Induced Pluripotent Stem Cells. *J Am Heart Assoc*. 2022;11(7):e024410. doi:10.1161/JAHA.121.024410

81. Vaseghi M, Gima J, Kanaan C, et al. Cardiac sympathetic denervation in patients with refractory ventricular arrhythmias or electrical storm: intermediate and long-term follow-up. *Heart Rhythm*. 2014;11(3):360-366. doi:10.1016/j.hrthm.2013.11.028

82. Vaseghi M, Barwad P, Malavassi Corrales FJ, et al. Cardiac Sympathetic Denervation for Refractory Ventricular Arrhythmias. *J Am Coll Cardiol*. 2017;69(25):3070-3080. doi:10.1016/j.jacc.2017.04.035

83. Gurdon JB. The developmental capacity of nuclei taken from intestinal epithelium cells of feeding tadpoles. *J Embryol Exp Morphol*. 1962;10:622-640.

84. Wilmut I, Schnieke AE, McWhir J, Kind AJ, Campbell KH. Viable offspring derived from fetal and adult mammalian cells. *Nature*. 1997;385(6619):810-813. doi:10.1038/385810a0

85. Davis RL, Weintraub H, Lassar AB. Expression of a single transfected cDNA converts fibroblasts to myoblasts. *Cell*. 1987;51(6):987-1000. doi:10.1016/0092-8674(87)90585-x

86. Yamanaka S. Induced pluripotent stem cells: past, present, and future. *Cell Stem Cell*. 2012;10(6):678-684. doi:10.1016/j.stem.2012.05.005

87. Takahashi K, Yamanaka S. Induction of pluripotent stem cells from mouse embryonic and adult fibroblast cultures by defined factors. *Cell*. 2006;126(4):663-676. doi:10.1016/j.cell.2006.07.024

88. Karagiannis P, Takahashi K, Saito M, et al. Induced Pluripotent Stem Cells and Their Use in Human Models of Disease and Development. *Physiol Rev*. 2019;99(1):79-114. doi:10.1152/physrev.00039.2017

89. Thomson JA, Itskovitz-Eldor J, Shapiro SS, et al. Embryonic stem cell lines derived from human blastocysts. *Science*. 1998;282(5391):1145-1147. doi:10.1126/science.282.5391.1145

90. Kehat I, Kenyagin-Karsenti D, Snir M, et al. Human embryonic stem cells can differentiate into myocytes with structural and functional properties of cardiomyocytes. *J Clin Invest*. 2001;108(3):407-414. doi:10.1172/JCI12131

91. Schulz TC, Noggle SA, Palmarini GM, et al. Differentiation of human embryonic stem cells to dopaminergic neurons in serum-free suspension culture. *Stem Cells*. 2004;22(7):1218-1238. doi:10.1634/stemcells.2004-0114

92. Burridge PW, Anderson D, Priddle H, et al. Improved human embryonic stem cell embryoid body homogeneity and cardiomyocyte differentiation from a novel V-96 plate aggregation system highlights interline variability. *Stem Cells*. 2007;25(4):929-938. doi:10.1634/stemcells.2006-0598

93. Batalov I, Feinberg AW. Differentiation of Cardiomyocytes from Human Pluripotent Stem Cells Using Monolayer Culture. *Biomark Insights*. 2015;10(Suppl 1):71-76. doi:10.4137/BMI.S20050

94. Lian X, Zhang J, Azarin SM, et al. Directed cardiomyocyte differentiation from human pluripotent stem cells by modulating Wnt/β-catenin signaling under fully defined conditions. *Nat Protoc*. 2013;8(1):162-175. doi:10.1038/nprot.2012.150

95. Lyra-Leite DM, Gutiérrez-Gutiérrez Ó, Wang M, Zhou Y, Cyganek L, Burridge PW. A review of protocols for human iPSC culture, cardiac differentiation, subtype-specification, maturation, and direct reprogramming. *STAR Protoc*. 2022;3(3):101560. doi:10.1016/j.xpro.2022.101560

96. Paige SL, Osugi T, Afanasiev OK, Pabon L, Reinecke H, Murry CE. Endogenous Wnt/beta-catenin signaling is required for cardiac differentiation in human embryonic stem cells. *PLoS One*. 2010;5(6):e11134. doi:10.1371/journal.pone.0011134

97. Burridge PW, Matsa E, Shukla P, et al. Chemically defined generation of human cardiomyocytes. *Nat Methods*. 2014;11(8):855-860. doi:10.1038/nmeth.2999

98. Zhang M, Schulte JS, Heinick A, et al. Universal cardiac induction of human pluripotent stem cells in two and three-dimensional formats: implications for in vitro maturation. *Stem Cells*. 2015;33(5):1456-1469. doi:10.1002/stem.1964

99. Lin Y, Zou J. Differentiation of Cardiomyocytes from Human Pluripotent Stem Cells in Fully Chemically Defined Conditions. *STAR Protoc*. 2020;1(1):100015. doi:10.1016/j.xpro.2020.100015

100. Tan Y, Han P, Gu Q, et al. Generation of clinical-grade functional cardiomyocytes from human embryonic stem cells in chemically defined conditions. *J Tissue Eng Regen Med*. 2018;12(1):153-163. doi:10.1002/term.2381

101. Cho S, Discher DE, Leong KW, Vunjak-Novakovic G, Wu JC. Challenges and opportunities for the next generation of cardiovascular tissue engineering. *Nat Methods*. 2022;19(9):1064-1071. doi:10.1038/s41592-022-01591-3

102. Moretti A, Bellin M, Welling A, et al. Patient-specific induced pluripotent stem-cell models for long-QT syndrome. *N Engl J Med*. 2010;363(15):1397-1409. doi:10.1056/NEJMoa0908679

103. Matsa E, Rajamohan D, Dick E, et al. Drug evaluation in cardiomyocytes derived from human induced pluripotent stem cells carrying a long QT syndrome type 2 mutation. *Eur Heart J*. 2011;32(8):952-962. doi:10.1093/eurheartj/ehr073

104. Itzhaki I, Maizels L, Huber I, et al. Modelling the long QT syndrome with induced pluripotent stem cells. *Nature*. 2011;471(7337):225-229. doi:10.1038/nature09747

105. Pierre M, Djemai M, Poulin H, Chahine M. NaV1.5 knockout in iPSCs: a novel approach to study NaV1.5 variants in a human cardiomyocyte environment. *Sci Rep*. 2021;11(1):17168. doi:10.1038/s41598-021-96474-6

106. Ben Jehuda R, Barad L. Patient Specific Induced Pluripotent Stem Cell-Derived Cardiomyocytes for Drug Development and Screening In Catecholaminergic Polymorphic Ventricular Tachycardia. *J Atr Fibrillation*. 2016;9(2):1423. doi:10.4022/jafib.1423

107. Pölönen RP, Swan H, Aalto-Setälä K. Mutation-specific differences in arrhythmias and drug responses in CPVT patients: simultaneous patch clamp and video imaging of iPSC derived cardiomyocytes. *Mol Biol Rep*. 2020;47(2):1067-1077. doi:10.1007/s11033-019-05201-y

108. Arslanova A, Shafaattalab S, Ye K, et al. Using hiPSC-CMs to Examine Mechanisms of Catecholaminergic Polymorphic Ventricular Tachycardia. *Curr Protoc*. 2021;1(12):e320. doi:10.1002/cpz1.320

109. Davis RP, Casini S, van den Berg CW, et al. Cardiomyocytes derived from pluripotent stem cells recapitulate electrophysiological characteristics of an overlap syndrome of cardiac sodium channel disease. *Circulation*. 2012;125(25):3079-3091. doi:10.1161/CIRCULATIONAHA.111.066092

110. Li W, Stauske M, Luo X, et al. Disease Phenotypes and Mechanisms of iPSC-Derived Cardiomyocytes From Brugada Syndrome Patients With a Loss-of-Function SCN5A Mutation. *Front Cell Dev Biol*. 2020;8:592893. doi:10.3389/fcell.2020.592893

111. Liang P, Sallam K, Wu H, et al. Patient-Specific and Genome-Edited Induced Pluripotent Stem Cell-Derived Cardiomyocytes Elucidate Single-Cell Phenotype of Brugada Syndrome. *J Am Coll Cardiol*. 2016;68(19):2086-2096. doi:10.1016/j.jacc.2016.07.779

112. Ma D, Liu Z, Loh LJ, et al. Identification of an INa-dependent and Ito-mediated proarrhythmic mechanism in cardiomyocytes derived from pluripotent stem cells of a Brugada syndrome patient. *Sci Rep*. 2018;8(1):11246. doi:10.1038/s41598-018-29574-5

113. Lewis-Israeli YR, Wasserman AH, Gabalski MA, et al. Self-assembling human heart organoids for the modeling of cardiac development and congenital heart disease. *Nat Commun*. 2021;12(1):5142. doi:10.1038/s41467-021-25329-5

114. Sieber-Blum M. Growth factor synergism and antagonism in early neural crest development. *Biochem Cell Biol*. 1998;76(6):1039-1050.

115. Chambers SM, Fasano CA, Papapetrou EP, Tomishima M, Sadelain M, Studer L. Highly efficient neural conversion of human ES and iPS cells by dual inhibition of SMAD signaling. *Nat Biotechnol*. 2009;27(3):275-280. doi:10.1038/nbt.1529

116. Oh Y, Cho GS, Li Z, et al. Functional Coupling with Cardiac Muscle Promotes Maturation of hPSC-Derived Sympathetic Neurons. *Cell Stem Cell*. 2016;19(1):95-106. doi:10.1016/j.stem.2016.05.002

117. Saito-Diaz K, Wu HF, Zeltner N. Autonomic Neurons with Sympathetic Character Derived From Human Pluripotent Stem Cells. *Curr Protoc Stem Cell Biol*. 2019;49(1):e78. doi:10.1002/cpsc.78

118. Wu HF, Zeltner N. Efficient Differentiation of Postganglionic Sympathetic Neurons using Human Pluripotent Stem Cells under Feeder-free and Chemically Defined Culture Conditions. *J Vis Exp*. 2020;(159). doi:10.3791/60843

119. Winbo A, Ramanan S, Eugster E, Jovinge S, Skinner JR, Montgomery JM. Functional coculture of sympathetic neurons and cardiomyocytes derived from human-induced pluripotent stem cells. *Am J Physiol Heart Circ Physiol*. 2020;319(5):H927-H937. doi:10.1152/ajpheart.00546.2020

120. Takayama Y, Kushige H, Akagi Y, Suzuki Y, Kumagai Y, Kida YS. Selective Induction of Human Autonomic Neurons Enables Precise Control of Cardiomyocyte Beating. *Sci Rep*. 2020;10(1):9464. doi:10.1038/s41598-020-66303-3

121. Winbo A, Ramanan S, Eugster E, et al. Functional hyperactivity in long QT syndrome type 1 pluripotent stem cell-derived sympathetic neurons. *Am J Physiol Heart Circ Physiol*. 2021;321(1):H217-H227. doi:10.1152/ajpheart.01002.2020

122. Bardsley EN, Davis H, Ajijola OA, et al. RNA Sequencing Reveals Novel Transcripts from Sympathetic Stellate Ganglia During Cardiac Sympathetic Hyperactivity. *Sci Rep*. 2018;8(1):8633. doi:10.1038/s41598-018-26651-7

123. Liu K, Li D, Hao G, et al. Phosphodiesterase 2A as a therapeutic target to restore cardiac neurotransmission during sympathetic hyperactivity. *JCI Insight*. 3(9):e98694. doi:10.1172/jci.insight.98694

124. Lu CJ, Hao G, Nikiforova N, et al. CAPON Modulates Neuronal Calcium Handling and Cardiac Sympathetic Neurotransmission During Dysautonomia in Hypertension. *Hypertension*. 2015;65(6):1288-1297. doi:10.1161/HYPERTENSIONAHA.115.05290

125. Li N, Edel M, Liu K, et al. Human induced pluripotent stem cell-derived cardiac myocytes and sympathetic neurons in disease modelling. *Philos Trans R Soc Lond B Biol Sci*. 2023;378(1879):20220173. doi:10.1098/rstb.2022.0173

126. Roston TM, Haji-Ghassemi O, LaPage MJ, et al. Catecholaminergic polymorphic ventricular tachycardia patients with multiple genetic variants in the PACES CPVT Registry. *PLOS ONE*. 2018;13(11):e0205925. doi:10.1371/journal.pone.0205925

127. Yamamoto T, El-Hayek R, Ikemoto N. Postulated role of interdomain interaction within the ryanodine receptor in Ca(2+) channel regulation. *J Biol Chem*. 2000;275(16):11618-11625. doi:10.1074/jbc.275.16.11618

128. des Georges A, Clarke OB, Zalk R, et al. Structural Basis for Gating and Activation of RyR1. *Cell*. 2016;167(1):145-157.e17. doi:10.1016/j.cell.2016.08.075

129. Im K, Mareninov S, Diaz MFP, Yong WH. An Introduction to Performing Immunofluorescence Staining. *Methods Mol Biol*. 2019;1897:299-311. doi:10.1007/978-1-4939-8935-5_26

130. Rico LG, Bardina J, Bistué-Rovira À, et al. Accurate identification of cell doublet profiles: Comparison of light scattering with fluorescence measurement techniques. *Cytometry A*. 2023;103(5):447-454. doi:10.1002/cyto.a.24690

131. Adams G. A beginner's guide to RT-PCR, qPCR and RT-qPCR. *The Biochemist*. 2020;42(3):48-53. doi:10.1042/BIO20200034

132. Barber RD, Harmer DW, Coleman RA, Clark BJ. GAPDH as a housekeeping gene: analysis of GAPDH mRNA expression in a panel of 72 human tissues. *Physiol Genomics*. 2005;21(3):389-395. doi:10.1152/physiolgenomics.00025.2005

133. Aydin S. A short history, principles, and types of ELISA, and our laboratory experience with peptide/protein analyses using ELISA. *Peptides*. 2015;72:4-15. doi:10.1016/j.peptides.2015.04.012

134. Wu L, Huang C, Emery BP, et al. Förster resonance energy transfer (FRET)-based small-molecule sensors and imaging agents. *Chem Soc Rev*. 2020;49(15):5110-5139. doi:10.1039/c9cs00318e

135. Levitt JA, Poland SP, Krstajic N, et al. Quantitative real-time imaging of intracellular FRET biosensor dynamics using rapid multi-beam confocal FLIM. *Sci Rep*. 2020;10(1):5146. doi:10.1038/s41598-020-61478-1

136. Dani JA. Neuronal Nicotinic Acetylcholine Receptor Structure and Function and Response to Nicotine. *Int Rev Neurobiol*. 2015;124:3-19. doi:10.1016/bs.irn.2015.07.001

137. Barreto-Chang OL, Dolmetsch RE. Calcium Imaging of Cortical Neurons using Fura-2 AM. *J Vis Exp*. 2009;(23):1067. doi:10.3791/1067

138. Thomas CA, Springer PA, Loeb GE, Berwald-Netter Y, Okun LM. A miniature microelectrode array to monitor the bioelectric activity of cultured cells. *Exp Cell Res*. 1972;74(1):61-66. doi:10.1016/0014-4827(72)90481-8

139. Olsen TK, Baryawno N. Introduction to Single-Cell RNA Sequencing. *Curr Protoc Mol Biol*. 2018;122(1):e57. doi:10.1002/cpmb.57

140. Schena M, Shalon D, Davis RW, Brown PO. Quantitative monitoring of gene expression patterns with a complementary DNA microarray. *Science*. 1995;270(5235):467-470. doi:10.1126/science.270.5235.467

141. Margulies M, Egholm M, Altman WE, et al. Genome sequencing in microfabricated high-density picolitre reactors. *Nature*. 2005;437(7057):376-380. doi:10.1038/nature03959

142. Wang Z, Gerstein M, Snyder M. RNA-Seq: a revolutionary tool for transcriptomics. *Nat Rev Genet*. 2009;10(1):57-63. doi:10.1038/nrg2484

143. Tang F, Barbacioru C, Wang Y, et al. mRNA-Seq whole-transcriptome analysis of a single cell. *Nat Methods*. 2009;6(5):377-382. doi:10.1038/nmeth.1315

144. Hu P, Zhang W, Xin H, Deng G. Single Cell Isolation and Analysis. *Frontiers in Cell and Developmental Biology*. 2016;4. Accessed December 23, 2023. https://www.frontiersin.org/articles/10.3389/fcell.2016.00116

145. Mummery C, Ward D, van den Brink CE, et al. Cardiomyocyte differentiation of mouse and human embryonic stem cells. *J Anat*. 2002;200(Pt 3):233-242. doi:10.1046/j.1469-7580.2002.00031.x

146. Mauritz C, Schwanke K, Reppel M, et al. Generation of functional murine cardiac myocytes from induced pluripotent stem cells. *Circulation*. 2008;118(5):507-517. doi:10.1161/CIRCULATIONAHA.108.778795

147. Gai H, Leung ELH, Costantino PD, et al. Generation and characterization of functional cardiomyocytes using induced pluripotent stem cells derived from human fibroblasts. *Cell Biol Int*. 2009;33(11):1184-1193. doi:10.1016/j.cellbi.2009.08.008

148. Mummery CL, Zhang J, Ng ES, Elliott DA, Elefanty AG, Kamp TJ. Differentiation of human embryonic stem cells and induced pluripotent stem cells to cardiomyocytes: a methods overview. *Circ Res*. 2012;111(3):344-358. doi:10.1161/CIRCRESAHA.110.227512

149. Bekhite MM, Schulze PC. Human Induced Pluripotent Stem Cell as a Disease Modeling and Drug Development Platform-A Cardiac Perspective. *Cells*. 2021;10(12):3483. doi:10.3390/cells10123483

150. Aasen T, Raya A, Barrero MJ, et al. Efficient and rapid generation of induced pluripotent stem cells from human keratinocytes. *Nat Biotechnol*. 2008;26(11):1276-1284. doi:10.1038/nbt.1503

151. Alvarez-Palomo AB, Requena-Osete J, Delgado-Morales R, et al. A synthetic mRNA cell reprogramming method using CYCLIN D1 promotes DNA repair, generating improved genetically stable human induced pluripotent stem cells. *Stem Cells*. 2021;39(7):866-881. doi:10.1002/stem.3358

152. Fatima A, Xu G, Shao K, et al. In vitro modeling of ryanodine receptor 2 dysfunction using human induced pluripotent stem cells. *Cell Physiol Biochem*. 2011;28(4):579-592. doi:10.1159/000335753

153. Sallam K, Kodo K, Wu JC. Modeling inherited cardiac disorders. *Circ J*. 2014;78(4):784-794. doi:10.1253/circj.cj-14-0182

154. Yoshida Y, Yamanaka S. Induced Pluripotent Stem Cells 10 Years Later: For Cardiac Applications. *Circ Res*. 2017;120(12):1958-1968. doi:10.1161/CIRCRESAHA.117.311080

155. Herring N, Kalla M, Paterson DJ. The autonomic nervous system and cardiac arrhythmias: current concepts and emerging therapies. *Nat Rev Cardiol*. 2019;16(12):707-726. doi:10.1038/s41569-019-0221-2

156. Takeuchi A, Shimba K, Mori M, et al. Sympathetic neurons modulate the beat rate of pluripotent cell-derived cardiomyocytes in vitro. *Integr Biol (Camb)*. 2012;4(12):1532-1539. doi:10.1039/c2ib20060k

157. Takeuchi A, Shimba K, Takayama Y, et al. Microfabricated device for co-culture of sympathetic neuron and iPS-derived cardiomyocytes. *Annu Int Conf IEEE Eng Med Biol Soc*. 2013;2013:3817-3820. doi:10.1109/EMBC.2013.6610376

158. Larsen HE, Lefkimmiatis K, Paterson DJ. Sympathetic neurons are a powerful driver of myocyte function in cardiovascular disease. *Sci Rep*. 2016;6:38898. doi:10.1038/srep38898

159. Kowalski WJ, Garcia-Pak IH, Li W, et al. Sympathetic Neurons Regulate Cardiomyocyte Maturation in Culture. *Front Cell Dev Biol*. 2022;10:850645. doi:10.3389/fcell.2022.850645

160. Frey N, Katus HA, Olson EN, Hill JA. Hypertrophy of the heart: a new therapeutic target? *Circulation*. 2004;109(13):1580-1589. doi:10.1161/01.CIR.0000120390.68287.BB

161. Nakamura M, Sadoshima J. Mechanisms of physiological and pathological cardiac hypertrophy. *Nat Rev Cardiol*. 2018;15(7):387-407. doi:10.1038/s41569-018-0007-y

162. Zhao MT, Ye S, Su J, Garg V. Cardiomyocyte Proliferation and Maturation: Two Sides of the Same Coin for Heart Regeneration. *Front Cell Dev Biol*. 2020;8:594226. doi:10.3389/fcell.2020.594226

163. Malhotra A, Sharma S. Hypertrophic Cardiomyopathy in Athletes. *Eur Cardiol*. 2017;12(2):80-82. doi:10.15420/ecr.2017:12:1

164. Eghbali M, Wang Y, Toro L, Stefani E. Heart hypertrophy during pregnancy: a better functioning heart? *Trends Cardiovasc Med*. 2006;16(8):285-291. doi:10.1016/j.tcm.2006.07.001

165. Samak M, Fatullayev J, Sabashnikov A, et al. Cardiac Hypertrophy: An Introduction to Molecular and Cellular Basis. *Med Sci Monit Basic Res*. 2016;22:75-79. doi:10.12659/MSMBR.900437

166. Oka T, Akazawa H, Naito AT, Komuro I. Angiogenesis and cardiac hypertrophy: maintenance of cardiac function and causative roles in heart failure. *Circ Res*. 2014;114(3):565-571. doi:10.1161/CIRCRESAHA.114.300507

167. Martin TG, Juarros MA, Leinwand LA. Regression of cardiac hypertrophy in health and disease: mechanisms and therapeutic potential. *Nat Rev Cardiol*. 2023;20(5):347-363. doi:10.1038/s41569-022-00806-6

168. Shimizu I, Minamino T. Physiological and pathological cardiac hypertrophy. *J Mol Cell Cardiol*. 2016;97:245-262. doi:10.1016/j.yjmcc.2016.06.001

169. Müller AL, Dhalla NS. Differences in Concentric Cardiac Hypertrophy and Eccentric Hypertrophy. In: Ostadal B, Dhalla NS, eds. *Cardiac Adaptations: Molecular Mechanisms*. Advances in Biochemistry in Health and Disease. Springer; 2013:147-166. doi:10.1007/978-1-4614-5203-4_8

170. Eschenhagen T, Bolli R, Braun T, et al. Cardiomyocyte Regeneration: A Consensus Statement. *Circulation*. 2017;136(7):680-686. doi:10.1161/CIRCULATIONAHA.117.029343

171. Watkins SJ, Borthwick GM, Oakenfull R, Robson A, Arthur HM. Angiotensin II-induced cardiomyocyte hypertrophy in vitro is TAK1-dependent and Smad2/3-independent. *Hypertens Res*. 2012;35(4):393-398. doi:10.1038/hr.2011.196

172. Yamazaki T, Komuro I, Kudoh S, et al. Angiotensin II partly mediates mechanical stress-induced cardiac hypertrophy. *Circ Res*. 1995;77(2):258-265. doi:10.1161/01.res.77.2.258

173. Hendricks S, Dykun I, Balcer B, Totzeck M, Rassaf T, Mahabadi AA. Higher BNP/NT-pro BNP levels stratify prognosis equally well in patients with and without heart failure: a meta-analysis. *ESC Heart Fail*. 2022;9(5):3198-3209. doi:10.1002/ehf2.14019

174. Matthia EL, Setteducato ML, Elzeneini M, et al. Circulating Biomarkers in Hypertrophic Cardiomyopathy. *J Am Heart Assoc*. 2022;11(23):e027618. doi:10.1161/JAHA.122.027618

175. Feyen DAM, McKeithan WL, Bruyneel AAN, et al. Metabolic Maturation Media Improve Physiological Function of Human iPSC-Derived Cardiomyocytes. *Cell Rep*. 2020;32(3):107925. doi:10.1016/j.celrep.2020.107925

176. Sousa Fialho M da L, Purnama U, Dennis KMJH, et al. Activation of HIF1α Rescues the Hypoxic Response and Reverses Metabolic Dysfunction in the Diabetic Heart. *Diabetes*. 2021;70(11):2518-2531. doi:10.2337/db21-0398

177. Mishima T, Ishikawa T, Imamura K, et al. Cytoplasmic aggregates of dynactin in iPSC-derived tyrosine hydroxylase-positive neurons from a patient with Perry syndrome. *Parkinsonism Relat Disord*. 2016;30:67-72. doi:10.1016/j.parkreldis.2016.06.007

178. Kirino K, Nakahata T, Taguchi T, Saito MK. Efficient derivation of sympathetic neurons from human pluripotent stem cells with a defined condition. *Sci Rep*. 2018;8(1):12865. doi:10.1038/s41598-018-31256-1

179. Capetian P, Müller L, Volkmann J, Heckmann M, Ergün S, Wagner N. Visualizing the Synaptic and Cellular Ultrastructure in Neurons Differentiated from Human Induced Neural Stem Cells—An Optimized Protocol. *Int J Mol Sci*. 2020;21(5):1708. doi:10.3390/ijms21051708

180. Mirza FJ, Zahid S. The Role of Synapsins in Neurological Disorders. *Neurosci Bull*. 2017;34(2):349-358. doi:10.1007/s12264-017-0201-7

181. Guo Y, Pu WT. Cardiomyocyte Maturation: New Phase in Development. *Circ Res*. 2020;126(8):1086-1106. doi:10.1161/CIRCRESAHA.119.315862

182. Burridge PW, Thompson S, Millrod MA, et al. A universal system for highly efficient cardiac differentiation of human induced pluripotent stem cells that eliminates interline variability. *PLoS One*. 2011;6(4):e18293. doi:10.1371/journal.pone.0018293

183. Gaspar JA, Doss MX, Hengstler JG, Cadenas C, Hescheler J, Sachinidis A. Unique metabolic features of stem cells, cardiomyocytes, and their progenitors. *Circ Res*. 2014;114(8):1346-1360. doi:10.1161/CIRCRESAHA.113.302021

184. Malandraki-Miller S, Lopez CA, Alonaizan R, et al. Metabolic flux analyses to assess the differentiation of adult cardiac progenitors after fatty acid supplementation. *Stem Cell Res*. 2019;38:101458. doi:10.1016/j.scr.2019.101458

185. Davis H, Liu K, Li N, Li D, Paterson DJ. Healthy cardiac myocytes can decrease sympathetic hyperexcitability in the early stages of hypertension. *Front Synaptic Neurosci*. 2022;14:949150. doi:10.3389/fnsyn.2022.949150

186. Nanou E, Catterall WA. Calcium Channels, Synaptic Plasticity, and Neuropsychiatric Disease. *Neuron*. 2018;98(3):466-481. doi:10.1016/j.neuron.2018.03.017

187. Südhof TC. Calcium control of neurotransmitter release. *Cold Spring Harb Perspect Biol*. 2012;4(1):a011353. doi:10.1101/cshperspect.a011353

188. Santulli G, Nakashima R, Yuan Q, Marks AR. Intracellular calcium release channels: an update. *J Physiol*. 2017;595(10):3041-3051. doi:10.1113/JP272781

189. Simms BA, Zamponi GW. Neuronal voltage-gated calcium channels: structure, function, and dysfunction. *Neuron*. 2014;82(1):24-45. doi:10.1016/j.neuron.2014.03.016

190. Yoshida S, Miyagawa S, Fukushima S, et al. Maturation of Human Induced Pluripotent Stem Cell-Derived Cardiomyocytes by Soluble Factors from Human Mesenchymal Stem Cells. *Mol Ther*. 2018;26(11):2681-2695. doi:10.1016/j.ymthe.2018.08.012

191. Habecker BA, Anderson ME, Birren SJ, et al. Molecular and cellular neurocardiology: development, and cellular and molecular adaptations to heart disease. *J Physiol*. 2016;594(14):3853-3875. doi:10.1113/JP271840

192. Dokshokova L, Franzoso M, Di Bona A, et al. Nerve growth factor transfer from cardiomyocytes to innervating sympathetic neurons activates TrkA receptors at the neuro-cardiac junction. *J Physiol*. 2022;600(12):2853-2875. doi:10.1113/JP282828

193. Fujiu K, Nagai R. Fibroblast-mediated pathways in cardiac hypertrophy. *J Mol Cell Cardiol*. 2014;70:64-73. doi:10.1016/j.yjmcc.2014.01.013

194. Abbas M, Miles C, Behr E. Catecholaminergic Polymorphic Ventricular Tachycardia. *Arrhythm Electrophysiol Rev*. 2022;11:e20. doi:10.15420/aer.2022.09

195. Pérez-Riera AR, Barbosa-Barros R, de Rezende Barbosa MPC, Daminello-Raimundo R, de Lucca AA, de Abreu LC. Catecholaminergic polymorphic ventricular tachycardia, an update. *Ann Noninvasive Electrocardiol*. 2017;23(4):e12512. doi:10.1111/anec.12512

196. Blackwell DJ, Faggioni M, Wleklinski MJ, et al. The Purkinje-myocardial junction is the anatomic origin of ventricular arrhythmia in CPVT. *JCI Insight*. 2022;7(3):e151893. doi:10.1172/jci.insight.151893

197. Park SJ, Zhang D, Qi Y, et al. Insights into the pathogenesis of catecholaminergic polymorphic ventricular tachycardia from engineered human heart tissue. *Circulation*. 2019;140(5):390-404. doi:10.1161/CIRCULATIONAHA.119.039711

198. Skorska A, Johann L, Chabanovska O, et al. Monitoring the maturation of the sarcomere network: a super-resolution microscopy-based approach. *Cell Mol Life Sci*. 2022;79(3):149. doi:10.1007/s00018-022-04196-3

199. Susuki K. Myelin: A Specialized Membrane for Cell Communication. *Nature Education*. 2010;3(9):59.

200. Fearnley CJ, Roderick HL, Bootman MD. Calcium signaling in cardiac myocytes. *Cold Spring Harb Perspect Biol*. 2011;3(11):a004242. doi:10.1101/cshperspect.a004242

201. Zhang JZ, Waddell HMM, Jones PP. Regulation of RYR2 by sarcoplasmic reticulum Ca(2+). *Clin Exp Pharmacol Physiol*. 2015;42(6):720-726. doi:10.1111/1440-1681.12364

202. Kurebayashi N, Murayama T, Ota R, et al. Cytosolic Ca2+-dependent Ca2+ release activity primarily determines the ER Ca2+ level in cells expressing the CPVT-linked mutant RYR2. *J Gen Physiol*. 2022;154(9):e202112869. doi:10.1085/jgp.202112869

203. Hwang HS, Baldo MP, Rodriguez JP, Faggioni M, Knollmann BC. Efficacy of Flecainide in Catecholaminergic Polymorphic Ventricular Tachycardia Is Mutation-Independent but Reduced by Calcium Overload. *Front Physiol*. 2019;10:992. doi:10.3389/fphys.2019.00992

204. Roston TM, Jones K, Hawkins NM, et al. Implantable cardioverter-defibrillator use in catecholaminergic polymorphic ventricular tachycardia: A systematic review. *Heart Rhythm*. 2018;15(12):1791-1799. doi:10.1016/j.hrthm.2018.06.046

205. Li D, Liu K, Davis H, et al. Abnormal Cyclic Nucleotide Signaling at the Outer Mitochondrial Membrane In Sympathetic Neurons During the Early Stages of Hypertension. *Hypertension*. 2022;79(7):1374-1384. doi:10.1161/HYPERTENSIONAHA.121.18882

206. Ostrom KF, LaVigne JE, Brust TF, et al. Physiological roles of mammalian transmembrane adenylyl cyclase isoforms. *Physiol Rev*. 2022;102(2):815-857. doi:10.1152/physrev.00013.2021

207. Bovo E, Huke S, Blatter LA, Zima AV. The effect of PKA-mediated phosphorylation of ryanodine receptor on SR Ca2+ leak in ventricular myocytes. *J Mol Cell Cardiol*. 2017;104:9-16. doi:10.1016/j.yjmcc.2017.01.015

208. Cooper DM, Schell MJ, Thorn P, Irvine RF. Regulation of adenylyl cyclase by membrane potential. *J Biol Chem*. 1998;273(42):27703-27707. doi:10.1074/jbc.273.42.27703

209. Parker T, Wang KW, Manning D, Dart C. Soluble adenylyl cyclase links Ca2+ entry to Ca2+/cAMP-response element binding protein (CREB) activation in vascular smooth muscle. *Sci Rep*. 2019;9(1):7317. doi:10.1038/s41598-019-43821-3

210. Steegborn C. Structure, mechanism, and regulation of soluble adenylyl cyclases - similarities and differences to transmembrane adenylyl cyclases. *Biochim Biophys Acta*. 2014;1842(12 Pt B):2535-2547. doi:10.1016/j.bbadis.2014.08.012

211. Lerma C, Glass L. Predicting the risk of sudden cardiac death. *J Physiol*. 2016;594(9):2445-2458. doi:10.1113/JP270535

212. Di Pasquale E, Lodola F, Miragoli M, et al. CaMKII inhibition rectifies arrhythmic phenotype in a patient-specific model of catecholaminergic polymorphic ventricular tachycardia. *Cell Death Dis*. 2013;4(10):e843. doi:10.1038/cddis.2013.369

213. Arslanova A, Shafaattalab S, Lin E, Barszczewski T, Hove-Madsen L, Tibbits GF. Investigating inherited arrhythmias using hiPSC-derived cardiomyocytes. *Methods*. 2022;203:542-557. doi:10.1016/j.ymeth.2021.06.015

214. Li D, Paterson DJ. Cyclic nucleotide regulation of cardiac sympatho-vagal responsiveness. *J Physiol*. 2016;594(14):3993-4008. doi:10.1113/JP271827

215. Berisha F, Götz KR, Wegener JW, et al. cAMP Imaging at Ryanodine Receptors Reveals β2-Adrenoceptor Driven Arrhythmias. *Circulation Research*. 2021;129(1):81-94. doi:10.1161/CIRCRESAHA.120.318234

216. Grandi E, Ripplinger CM. Antiarrhythmic mechanisms of beta blocker therapy. *Pharmacol Res*. 2019;146:104274. doi:10.1016/j.phrs.2019.104274

217. Farzam K, Jan A. Beta Blockers. In: *StatPearls*. StatPearls Publishing; 2024. Accessed March 13, 2024. http://www.ncbi.nlm.nih.gov/books/NBK532906/

218. Yao J, Chen SRW. RyR2-dependent modulation of neuronal hyperactivity: A potential therapeutic target for treating Alzheimer's disease. *J Physiol*. Published online March 3, 2023. doi:10.1113/JP283824

219. Kukurba KR, Montgomery SB. RNA Sequencing and Analysis. *Cold Spring Harb Protoc*. 2015;2015(11):951-969. doi:10.1101/pdb.top084970

220. Qian HR, Yang Y. Neuron differentiation and neuritogenesis stimulated by N-acetylcysteine (NAC). *Acta Pharmacol Sin*. 2009;30(7):907-912. doi:10.1038/aps.2009.72

221. Sánchez C, Díaz-Nido J, Avila J. Phosphorylation of microtubule-associated protein 2 (MAP2) and its relevance for the regulation of the neuronal cytoskeleton function. *Prog Neurobiol*. 2000;61(2):133-168. doi:10.1016/s0301-0082(99)00046-5

222. Ribeiro LF, de Wit J. Neuronal Polarity: MAP2 Shifts Secretory Vesicles into High Gear for Long-Haul Transport down the Axon. *Neuron*. 2017;94(2):223-225. doi:10.1016/j.neuron.2017.04.002

223. Henderson CA, Gomez CG, Novak SM, Mi-Mi L, Gregorio CC. Overview of the Muscle Cytoskeleton. *Compr Physiol*. 2017;7(3):891-944. doi:10.1002/cphy.c160033

224. Wu JJ, Weis MA, Kim LS, Eyre DR. Type III collagen, a fibril network modifier in articular cartilage. *J Biol Chem*. 2010;285(24):18537-18544. doi:10.1074/jbc.M110.112904

225. Lenaers A, Lapiere CM. Type III procollagen and collagen in skin. *Biochim Biophys Acta*. 1975;400(1):121-131. doi:10.1016/0005-2795(75)90132-4

226. Uusküla-Reimand L, Wilson MD. Untangling the roles of TOP2A and TOP2B in transcription and cancer. *Sci Adv*. 2022;8(44):eadd4920. doi:10.1126/sciadv.add4920

227. Danson EJ, Choate JK, Paterson DJ. Cardiac nitric oxide: emerging role for nNOS in regulating physiological function. *Pharmacol Ther*. 2005;106(1):57-74. doi:10.1016/j.pharmthera.2004.11.003

228. Klimaschewski L. VIP -- a "very important peptide" in the sympathetic nervous system? *Anat Embryol (Berl)*. 1997;196(4):269-277. doi:10.1007/s004290050096

229. Gagliardi D, Pagliari E, Meneri M, et al. Stathmins and Motor Neuron Diseases: Pathophysiology and Therapeutic Targets. *Biomedicines*. 2022;10(3):711. doi:10.3390/biomedicines10030711

230. Dijkmans TF, van Hooijdonk LWA, Fitzsimons CP, Vreugdenhil E. The doublecortin gene family and disorders of neuronal structure. *Cent Nerv Syst Agents Med Chem*. 2010;10(1):32-46. doi:10.2174/187152410790780118

231. Middeldorp J, Hol EM. GFAP in health and disease. *Prog Neurobiol*. 2011;93(3):421-443. doi:10.1016/j.pneurobio.2011.01.005

232. Yang Z, Wang KKW. Glial fibrillary acidic protein: from intermediate filament assembly and gliosis to neurobiomarker. *Trends Neurosci*. 2015;38(6):364-374. doi:10.1016/j.tins.2015.04.003

233. Sánchez-Navarro A, González-Soria I, Caldiño-Bohn R, Bobadilla NA. An integrative view of serpins in health and disease: the contribution of SerpinA3. *Am J Physiol Cell Physiol*. 2021;320(1):C106-C118. doi:10.1152/ajpcell.00366.2020

234. Jahng JW, Houpt TA, Joh TH, Wessel TC. Expression of catecholamine-synthesizing enzymes, peptidylglycine α-amidating monooxygenase, and neuropeptide Y mRNA in the rat adrenal medulla after acute systemic nicotine. *J Mol Neurosci*. 1997;8(1):45-52. doi:10.1007/BF02736862

235. Chambers KJ, Tonkin LA, Chang E, Shelton DN, Linskens MH, Funk WD. Identification and cloning of a sequence homologue of dopamine beta-hydroxylase. *Gene*. 1998;218(1-2):111-120. doi:10.1016/s0378-1119(98)00344-8

236. Card JP, Lois J, Sved AF. Distribution and phenotype of Phox2a-containing neurons in the adult sprague-dawley rat. *Journal of Comparative Neurology*. 2010;518(12):2202-2220. doi:10.1002/cne.22327

237. Rahim NS, Wu YS, Sim MS, et al. Three Members of Transmembrane-4-Superfamily, TM4SF1, TM4SF4, and TM4SF5, as Emerging Anticancer Molecular Targets against Cancer Phenotypes and Chemoresistance. *Pharmaceuticals (Basel)*. 2023;16(1):110. doi:10.3390/ph16010110

238. Iseki K, Hagino S, Zhang Y, et al. Altered expression pattern of testican-1 mRNA after brain injury. *Biomed Res*. 2011;32(6):373-378. doi:10.2220/biomedres.32.373

239. Dzwonek J, Wilczynski GM. CD44: molecular interactions, signaling and functions in the nervous system. *Front Cell Neurosci*. 2015;9:175. doi:10.3389/fncel.2015.00175

240. Roome RB, Bourojeni FB, Mona B, et al. Phox2a Defines a Developmental Origin of the Anterolateral System in Mice and Humans. *Cell Rep*. 2020;33(8):108425. doi:10.1016/j.celrep.2020.108425

241. Jung K, Choi JS, Koo BM, et al. TM4SF4 and LRRK2 Are Potential Therapeutic Targets in Lung and Breast Cancers through Outlier Analysis. *Cancer Res Treat*. 2021;53(1):9-24. doi:10.4143/crt.2020.434

242. Zhang F, Ye J, Guo W, Zhang F, Wang L, Han A. TYMS-TM4SF4 axis promotes the progression of colorectal cancer by EMT and upregulating stem cell marker. *Am J Cancer Res*. 2022;12(3):1009-1026.

243. Charbonnier F, Chanoine C, Cifuentes-Diaz C, et al. Expression of the proteoglycan SPOCK during mouse embryo development. *Mech Dev*. 2000;90(2):317-321. doi:10.1016/s0925-4773(99)00255-5

244. O'Brown NM, Patel NB, Hartmann U, Klein AM, Gu C, Megason SG. The secreted neuronal signal Spock1 promotes blood-brain barrier development. *Dev Cell*. 2023;58(17):1534-1547.e6. doi:10.1016/j.devcel.2023.06.005

245. Roszkowska M, Skupien A, Wójtowicz T, et al. CD44: a novel synaptic cell adhesion molecule regulating structural and functional plasticity of dendritic spines. *Mol Biol Cell*. 2016;27(25):4055-4066. doi:10.1091/mbc.E16-06-0423

246. Chaerkady R, Kerr CL, Marimuthu A, et al. Temporal analysis of neural differentiation using quantitative proteomics. *J Proteome Res*. 2009;8(3):1315-1326. doi:10.1021/pr8006667

247. Eira J, Magalhães J, Macedo N, et al. Transthyretin Promotes Axon Growth via Regulation of Microtubule Dynamics and Tubulin Acetylation. *Front Cell Dev Biol*. 2021;9:747699. doi:10.3389/fcell.2021.747699

248. Wang X, Cattaneo F, Ryno L, Hulleman J, Reixach N, Buxbaum JN. The systemic amyloid precursor transthyretin (TTR) behaves as a neuronal stress protein regulated by HSF1 in SH-SY5Y human neuroblastoma cells and APP23 Alzheimer's disease model mice. *J Neurosci*. 2014;34(21):7253-7265. doi:10.1523/JNEUROSCI.4936-13.2014

249. Gimelli A, Aimo A, Vergaro G, et al. Cardiac sympathetic denervation in wild-type transthyretin amyloidosis. *Amyloid*. 2020;27(4):237-243. doi:10.1080/13506129.2020.1769059

250. Lim KH, Chen LC, Hsu K, et al. BAFF-driven NLRP3 inflammasome activation in B cells. *Cell Death Dis*. 2020;11(9):1-13. doi:10.1038/s41419-020-03035-2

251. Tada S, Yasui T, Nakatsuji Y, et al. BAFF controls neural cell survival through BAFF receptor. *PLoS One*. 2013;8(7):e70924. doi:10.1371/journal.pone.0070924

252. Yan H, Rao J, Yuan J, et al. Long non-coding RNA MEG3 functions as a competing endogenous RNA to regulate ischemic neuronal death by targeting miR-21/PDCD4 signaling pathway. *Cell Death Dis*. 2017;8(12):3211. doi:10.1038/s41419-017-0047-y

253. Liu X, Hou L, Huang W, Gao Y, Lv X, Tang J. The Mechanism of Long Non-coding RNA MEG3 for Neurons Apoptosis Caused by Hypoxia: Mediated by miR-181b-12/15-LOX Signaling Pathway. *Front Cell Neurosci*. 2016;10:201. doi:10.3389/fncel.2016.00201

254. Tan MC, Widagdo J, Chau YQ, et al. The Activity-Induced Long Non-Coding RNA Meg3 Modulates AMPA Receptor Surface Expression in Primary Cortical Neurons. *Front Cell Neurosci*. 2017;11:124. doi:10.3389/fncel.2017.00124

255. Bosserhoff AK. Melanoma inhibitory activity (MIA): an important molecule in melanoma development and progression. *Pigment Cell Res*. 2005;18(6):411-416. doi:10.1111/j.1600-0749.2005.00274.x

256. Blee AM, Huang H. PMEPA1 guards against TGF-β-mediated prostate cancer bone metastasis. *Asian J Urol*. 2016;3(1):1-3. doi:10.1016/j.ajur.2015.11.002

257. Sharad S, Sztupinszki ZM, Chen Y, et al. Analysis of PMEPA1 Isoforms (a and b) as Selective Inhibitors of Androgen and TGF-β Signaling Reveals Distinct Biological and Prognostic Features in Prostate Cancer. *Cancers (Basel)*. 2019;11(12):1995. doi:10.3390/cancers11121995

258. Sharad S, Dobi A, Srivastava S, Srinivasan A, Li H. PMEPA1 Gene Isoforms: A Potential Biomarker and Therapeutic Target in Prostate Cancer. *Biomolecules*. 2020;10(9):1221. doi:10.3390/biom10091221

259. Ji J, Ding K, Luo T, et al. PMEPA1 isoform a drives progression of glioblastoma by promoting protein degradation of the Hippo pathway kinase LATS1. *Oncogene*. 2020;39(5):1125-1139. doi:10.1038/s41388-019-1050-9

260. Galdos FX, Lee C, Lee S, et al. Combined lineage tracing and scRNA-seq reveals unexpected first heart field predominance of human iPSC differentiation. *Elife*. 2023;12:e80075. doi:10.7554/eLife.80075

261. Cao X, Mircea M, Yakala GK, et al. ETV2 Upregulation Marks the Specification of Early Cardiomyocytes and Endothelial Cells During Co-differentiation. *Stem Cells*. 2023;41(2):140-152. doi:10.1093/stmcls/sxac086

262. Elorbany R, Popp JM, Rhodes K, et al. Single-cell sequencing reveals lineage-specific dynamic genetic regulation of gene expression during human cardiomyocyte differentiation. *PLoS Genet*. 2022;18(1):e1009666. doi:10.1371/journal.pgen.1009666

263. Thomas D, Kim H, Lopez N, Wu JC. Fabrication of 3D Cardiac Microtissue Arrays using Human iPSC-Derived Cardiomyocytes, Cardiac Fibroblasts, and Endothelial Cells. *J Vis Exp*. 2021;(169). doi:10.3791/61879

264. Bargaje R, Trachana K, Shelton MN, et al. Cell population structure prior to bifurcation predicts efficiency of directed differentiation in human induced pluripotent cells. *Proc Natl Acad Sci U S A*. 2017;114(9):2271-2276. doi:10.1073/pnas.1621412114

265. Ho BX, Pang JKS, Chen Y, et al. Robust generation of human-chambered cardiac organoids from pluripotent stem cells for improved modelling of cardiovascular diseases. *Stem Cell Res Ther*. 2022;13(1):529. doi:10.1186/s13287-022-03215-1

266. Lin Z, Garbern JC, Liu R, et al. Tissue-embedded stretchable nanoelectronics reveal endothelial cell-mediated electrical maturation of human 3D cardiac microtissues. *Sci Adv*. 2023;9(10):eade8513. doi:10.1126/sciadv.ade8513

267. Grancharova T, Gerbin KA, Rosenberg AB, et al. A comprehensive analysis of gene expression changes in a high replicate and open-source dataset of differentiating hiPSC-derived cardiomyocytes. *Sci Rep*. 2021;11(1):15845. doi:10.1038/s41598-021-94732-1

268. Ni X, Xu K, Zhao Y, et al. Single-cell analysis reveals the purification and maturation effects of glucose starvation in hiPSC-CMs. *Biochem Biophys Res Commun*. 2021;534:367-373. doi:10.1016/j.bbrc.2020.11.076

269. Biendarra-Tiegs SM, Li X, Ye D, Brandt EB, Ackerman MJ, Nelson TJ. Single-Cell RNA-Sequencing and Optical Electrophysiology of Human Induced Pluripotent Stem Cell-Derived Cardiomyocytes Reveal Discordance Between Cardiac Subtype-Associated Gene Expression Patterns and Electrophysiological Phenotypes. *Stem Cells Dev*. 2019;28(10):659-673. doi:10.1089/scd.2019.0030

270. Schoger E, Bleckwedel F, Germena G, et al. Single-cell transcriptomics reveal extracellular vesicles secretion with a cardiomyocyte proteostasis signature during pathological remodeling. *Commun Biol*. 2023;6(1):79. doi:10.1038/s42003-022-04402-9

271. Siguero-Álvarez M, Salguero-Jiménez A, Grego-Bessa J, et al. A Human Hereditary Cardiomyopathy Shares a Genetic Substrate With Bicuspid Aortic Valve. *Circulation*. 2023;147(1):47-65. doi:10.1161/CIRCULATIONAHA.121.058767

272. Mehrabi M, Morris TA, Cang Z, et al. A Study of Gene Expression, Structure, and Contractility of iPSC-Derived Cardiac Myocytes from a Family with Heart Disease due to LMNA Mutation. *Ann Biomed Eng*. 2021;49(12):3524-3539. doi:10.1007/s10439-021-02850-8

273. Hulme AJ, Maksour S, Glover MSC, Miellet S, Dottori M. Making neurons, made easy: The use of Neurogenin-2 in neuronal differentiation. *Stem Cell Reports*. 2022;17(1):14-34. doi:10.1016/j.stemcr.2021.11.015

274. Chatzidaki A, Fouillet A, Li J, et al. Pharmacological Characterisation of Nicotinic Acetylcholine Receptors Expressed in Human iPSC-Derived Neurons. *PLoS One*. 2015;10(4):e0125116. doi:10.1371/journal.pone.0125116

275. Handel AE, Chintawar S, Lalic T, et al. Assessing similarity to primary tissue and cortical layer identity in induced pluripotent stem cell-derived cortical neurons through single-cell transcriptomics. *Hum Mol Genet*. 2016;25(5):989-1000. doi:10.1093/hmg/ddv637

276. Sarkar A, Mei A, Paquola ACM, et al. Efficient Generation of CA3 Neurons from Human Pluripotent Stem Cells Enables Modeling of Hippocampal Connectivity In Vitro. *Cell Stem Cell*. 2018;22(5):684-697.e9. doi:10.1016/j.stem.2018.04.009

277. Shang Z, Chen D, Wang Q, et al. Single-cell RNA-seq reveals dynamic transcriptome profiling in human early neural differentiation. *Gigascience*. 2018;7(11):giy117. doi:10.1093/gigascience/giy117

278. Lam M, Sanosaka T, Lundin A, et al. Single-cell study of neural stem cells derived from human iPSCs reveals distinct progenitor populations with neurogenic and gliogenic potential. *Genes Cells*. 2019;24(12):836-847. doi:10.1111/gtc.12731

279. Thiry L, Hamel R, Pluchino S, Durcan T, Stifani S. Characterization of Human iPSC-derived Spinal Motor Neurons by Single-cell RNA Sequencing. *Neuroscience*. 2020;450:57-70. doi:10.1016/j.neuroscience.2020.04.041

280. Pokhilko A, Handel AE, Curion F, et al. Targeted single-cell RNA sequencing of transcription factors enhances the identification of cell types and trajectories. *Genome Res*. 2021;31(6):1069-1081. doi:10.1101/gr.273961.120

281. Jerber J, Seaton DD, Cuomo ASE, et al. Population-scale single-cell RNA-seq profiling across dopaminergic neuron differentiation. *Nat Genet*. 2021;53(3):304-312. doi:10.1038/s41588-021-00801-6

282. Silva TP, Sousa-Luís R, Fernandes TG, et al. Transcriptome profiling of human pluripotent stem cell-derived cerebellar organoids reveals faster commitment under dynamic conditions. *Biotechnol Bioeng*. 2021;118(7):2781-2803. doi:10.1002/bit.27797

283. Dong X, You Y, Wu JQ. Building an RNA Sequencing Transcriptome of the Central Nervous System. *Neuroscientist*. 2016;22(6):579-592. doi:10.1177/1073858415610541

284. Armand EJ, Li J, Xie F, Luo C, Mukamel EA. Single-Cell Sequencing of Brain Cell Transcriptomes and Epigenomes. *Neuron*. 2021;109(1):11-26. doi:10.1016/j.neuron.2020.12.010

285. Zhang C, Tan G, Zhang Y, et al. Comprehensive analyses of brain cell communications based on multiple scRNA-seq and snRNA-seq datasets for revealing novel mechanism in neurodegenerative diseases. *CNS Neuroscience & Therapeutics*. 2023;29(10):2775-2786. doi:10.1111/cns.14280

286. Piwecka M, Rajewsky N, Rybak-Wolf A. Single-cell and spatial transcriptomics: deciphering brain complexity in health and disease. *Nat Rev Neurol*. 2023;19(6):346-362. doi:10.1038/s41582-023-00809-y

287. Malla B, Guo X, Senger G, Chasapopoulou Z, Yildirim F. A Systematic Review of Transcriptional Dysregulation in Huntington's Disease Studied by RNA Sequencing. *Front Genet*. 2021;12:751033. doi:10.3389/fgene.2021.751033

288. Humphrey J, Venkatesh S, Hasan R, et al. Integrative transcriptomic analysis of the amyotrophic lateral sclerosis spinal cord implicates glial activation and suggests new risk genes. *Nat Neurosci*. 2023;26(1):150-162. doi:10.1038/s41593-022-01205-3

289. Napierala JS, Li Y, Lu Y, et al. Comprehensive analysis of gene expression patterns in Friedreich's ataxia fibroblasts by RNA sequencing reveals altered levels of protein synthesis factors and solute carriers. *Dis Model Mech*. 2017;10(11):1353-1369. doi:10.1242/dmm.030536

290. Wang TY, Arking DE, Maleszewski JJ, et al. Human cardiac myosin light chain 4 (MYL4) mosaic expression patterns vary by sex. *Sci Rep*. 2019;9(1):12681. doi:10.1038/s41598-019-49191-0

291. Mahadeva R, Sharples L, Ross-Russell RI, Webb AK, Bilton D, Lomas DA. Association of alpha(1)-antichymotrypsin deficiency with milder lung disease in patients with cystic fibrosis. *Thorax*. 2001;56(1):53-58. doi:10.1136/thorax.56.1.53

292. Ikari Y, Mulvihill E, Schwartz SM. alpha 1-Proteinase inhibitor, alpha 1-antichymotrypsin, and alpha 2-macroglobulin are the antiapoptotic factors of vascular smooth muscle cells. *J Biol Chem*. 2001;276(15):11798-11803. doi:10.1074/jbc.M008503200

293. Soman A, Asha Nair S. Unfolding the cascade of SERPINA3: Inflammation to cancer. *Biochim Biophys Acta Rev Cancer*. 2022;1877(5):188760. doi:10.1016/j.bbcan.2022.188760

294. Kalsheker NA. Alpha 1-antichymotrypsin. *Int J Biochem Cell Biol*. 1996;28(9):961-964. doi:10.1016/1357-2725(96)00032-5

295. Zhou ML, Chen FS, Mao H. Clinical significance and role of up-regulation of SERPINA3 expression in endometrial cancer. *World J Clin Cases*. 2019;7(15):1996-2002. doi:10.12998/wjcc.v7.i15.1996

296. Jiang Y, Zhang Y, Zhao C. Integrated gene expression profiling analysis reveals SERPINA3, FCN3, FREM1, MNS1 as candidate biomarkers in heart failure and their correlation with immune infiltration. *J Thorac Dis*. 2022;14(4):1106-1119. doi:10.21037/jtd-22-22

297. Zattoni M, Mearelli M, Vanni S, et al. Serpin Signatures in Prion and Alzheimer's Diseases. *Mol Neurobiol*. 2022;59(6):3778-3799. doi:10.1007/s12035-022-02817-3

298. Vanni S, Moda F, Zattoni M, et al. Differential overexpression of SERPINA3 in human prion diseases. *Sci Rep*. 2017;7:15637. doi:10.1038/s41598-017-15778-8

299. Zhao J, Feng C, Wang W, Su L, Jiao J. Human SERPINA3 induces neocortical folding and improves cognitive ability in mice. *Cell Discov*. 2022;8(1):124. doi:10.1038/s41421-022-00469-0

300. de Mezer M, Rogaliński J, Przewoźny S, et al. SERPINA3: Stimulator or Inhibitor of Pathological Changes. *Biomedicines*. 2023;11(1):156. doi:10.3390/biomedicines11010156

301. Khan MS, Singh P, Azhar A, et al. Serpin Inhibition Mechanism: A Delicate Balance between Native Metastable State and Polymerization. *J Amino Acids*. 2011;2011:606797. doi:10.4061/2011/606797

302. Sánchez-Navarro A, Murillo-de-Ozores AR, Pérez-Villalva R, et al. Transient response of serpinA3 during cellular stress. *FASEB J*. 2022;36(3):e22190. doi:10.1096/fj.202101912R

303. Ko E, Kim JS, Bae JW, Kim J, Park SG, Jung G. SERPINA3 is a key modulator of HNRNP-K transcriptional activity against oxidative stress in HCC. *Redox Biol*. 2019;24:101217. doi:10.1016/j.redox.2019.101217

304. Volpato V, Smith J, Sandor C, et al. Reproducibility of Molecular Phenotypes after Long-Term Differentiation to Human iPSC-Derived Neurons: A Multi-Site Omics Study. *Stem Cell Reports*. 2018;11(4):897-911. doi:10.1016/j.stemcr.2018.08.013

305. Hayashi Y, Ohnuma K, Furue MK. Pluripotent Stem Cell Heterogeneity. *Adv Exp Med Biol*. 2019;1123:71-94. doi:10.1007/978-3-030-11096-3_6

306. Kim YR, Jang SW, Han JH, Na GR, Jang H, Choi HW. The Effects of Co-Culture of Embryonic Stem Cells with Neural Stem Cells on Differentiation. *Curr Issues Mol Biol*. 2022;44(12):6104-6116. doi:10.3390/cimb44120416

307. Doss MX, Sachinidis A. Current Challenges of iPSC-Based Disease Modeling and Therapeutic Implications. *Cells*. 2019;8(5):403. doi:10.3390/cells8050403

308. Wleklinski MJ, Kannankeril PJ, Knollmann BC. Molecular and tissue mechanisms of catecholaminergic polymorphic ventricular tachycardia. *The Journal of Physiology*. 2020;598(14):2817-2834. doi:10.1113/JP276757

309. Bagur R, Hajnóczky G. Intracellular Ca2+ sensing: role in calcium homeostasis and signaling. *Mol Cell*. 2017;66(6):780-788. doi:10.1016/j.molcel.2017.05.028

310. Bers DM, Xiang YK, Zaccolo M. Whole-Cell cAMP and PKA Activity are Epiphenomena, Nanodomain Signaling Matters. *Physiology (Bethesda)*. 2019;34(4):240-249. doi:10.1152/physiol.00002.2019

311. Akbor MM, Kurosawa N, Nakayama H, et al. Polymorphic SERPINA3 prolongs oligomeric state of amyloid beta. *PLoS One*. 2021;16(3):e0248027. doi:10.1371/journal.pone.0248027